Dual-side etched microstructured semiconductor neutron detectors

by

RYAN G. FRONK

B.S., Kansas State University, 2011

AN ABSTRACT OF A DISSERTATION

submitted in partial fulfillment of the requirements for the degree

DOCTOR OF PHILOSOPHY

Department of Mechanical and Nuclear Engineering
College of Engineering

KANSAS STATE UNIVERSITY
Manhattan, Kansas

2017

Abstract

Interest in high-efficiency replacements for thin-film-coated thermal neutron detectors led to the development of single-sided microstructured semiconductor neutron detectors (MSNDs). MSNDs are designed with micro-sized trench structures that are etched into a vertically-oriented *pvn*-junction diode, and backfilled with a neutron converting material, such as ^{6}LiF. Neutrons absorbed by the converting material produce a pair of charged-particle reaction products that can be measured by the diode substrate. MSNDs have higher neutron-absorption and reaction-product counting efficiencies than their thin-film-coated counterparts, resulting in up to a 10x increase in intrinsic thermal neutron detection efficiency. The detection efficiency for a single-sided MSND is reduced by neutron streaming paths between the conversion-material filled regions that consequently allow neutrons to pass undetected through the detector. Previously, the highest reported intrinsic thermal neutron detection efficiency for a single MSND was approximately 30%. Methods for double-stacking and aligning MSNDs to reduce neutron streaming produced devices with an intrinsic thermal neutron detection efficiency of 42%. Presented here is a new type of MSND that features a complementary second set of trenches that are etched into the back-side of the detector substrate. These dual-sided microstructured semiconductor neutron detectors (DS-MSNDs) have the ability to absorb and detect neutrons that stream through the front-side, effectively doubling the detection efficiency of a single-sided device. DS-MSND sensors are theoretically capable of achieving greater than 80% intrinsic thermal neutron detection efficiency for a 1-mm thick device. Prototype DS-MSNDs with diffused *pvp*-junction operated at 0-V applied bias have achieved 53.54±0.61%, exceeding that of the single-sided MSNDs and double-stacked MSNDs to represent a new record for detection efficiency for such solid-state devices.

Dual-side etched microstructured semiconductor neutron detectors

by

RYAN G. FRONK

B.S., Kansas State University, 2011

A DISSERTATION

submitted in partial fulfillment of the requirements for the degree

DOCTOR OF PHILOSOPHY

Department of Mechanical and Nuclear Engineering
College of Engineering

KANSAS STATE UNIVERSITY
Manhattan, Kansas

2017

Approved by:

Major Professor
Douglas S. McGregor

Copyright

Abstract

Over the past several decades, interest in high-efficiency replacements for thin-film-coated thermal neutron detectors led to the development of single-sided microstructured semiconductor neutron detectors (MSNDs). MSNDs are designed with micro-sized trench structures that are etched into a vertically-oriented *pvn*-junction diode, and backfilled with a neutron converting material, such as ^{6}LiF. Neutrons absorbed by the converting material produce a pair of charged-particle reaction products that can be measured by the diode substrate. MSNDs have higher neutron-absorption and reaction-product counting efficiencies than their thin-film-coated counterparts, resulting in up to a 10x increase in intrinsic thermal neutron detection efficiency. The detection efficiency for a single-sided MSND is reduced by neutron streaming paths between the conversion-material filled regions that consequently allow neutrons to pass undetected through the detector. Previously, the highest reported intrinsic thermal neutron detection efficiency for a single MSND was approximately 30%. Methods for double-stacking and aligning MSNDs to reduce neutron streaming produced devices with an intrinsic thermal neutron detection efficiency of 42%. Presented here is a new type of MSND that features a complementary second set of trenches that are etched into the back-side of the detector substrate. These dual-sided microstructured semiconductor neutron detectors (DS-MSNDs) have the ability to absorb and detect neutrons that stream through the front-side, effectively doubling the detection efficiency of a single-sided device. DS-MSND sensors are theoretically capable of achieving greater than 80% intrinsic thermal neutron detection efficiency for a 1-mm thick device. Prototype DS-MSNDs with diffused *pvp*-junction operated at 0-V applied bias have achieved 53.54±0.61%, exceeding that of the single-sided MSNDs and double-stacked MSNDs to represent a new record for detection efficiency for such solid-state devices.

Table of Contents

List of Figures

List of Tables

Acknowledgements

I would like to acknowledge the efforts of many of my peers, friends, and colleagues, without which, this work would not have been possible. Dr. Steven Bellinger, Dr. Douglas McGregor, Dr. William Dunn, Dr. J. Kenneth Shultis, Dr. Larry Weaver, Dr. Benjamin Montag, Michael Reichenberger, Taylor Ochs, Luke Henson, Nathaniel Edwards, Brian Cooper, Colten Smith, Adam Van Bergeijk, and many others from the Semiconductor Materials and Radiological Technologies Laboratory.

Chapter 1 - *Introduction*

Recent years have seen an upsurge of interest in neutron detection technologies and the sensors that compose them. With the ending of the development of new, highly-enriched nuclear materials for weapons, production of the industry standard material, ^{3}He gas, has also come to an end. ^{3}He gas-filled proportional counters have long been used for neutron detection because of its high probability of absorption for thermal-energy neutrons. Further, upon absorption, the resulting charged-particle reaction products could be easily measured, thereby, indicating the presence of the original neutron. However, with the cessation of production of new ^{3}He gas, existing reserves are being depleted, with costs continually increasing. Many new sensor technologies have been investigated over recent years to replace the aging ^{3}He-based detectors.

Research and development of a new type of solid-state thermal neutron counter, the microstructured semiconductor neutron detector (MSND), over the previous decade made progress in developing a sensor for replacing ^{3}He technologies. Early solid-state thermal neutron counters had limited intrinsic thermal detection efficiency at 4-5%, but modern MSNDs showed to have improved detection efficiency with the use of clever three-dimensional structures, and increased neutron conversion material. To date, MSNDs have achieved intrinsic thermal neutron detection efficiencies of 30-35%, depending on their geometry, while maintaining a low per-cm^{2} cost, well below that of ^{3}He-based counters.

To further improve the detection efficiencies of solid-state neutron detector sensors, a brand-new type of MSND has been developed and is reported here. The major weakness of the MSND is that neutrons can pass through the sensor without intersecting neutron conversion material. To solve this problem, the Dual-Sided MSND (DS-MSND) has been developed wherein three-dimensional microstructured are formed onto both sides of the semiconductor diode. For the first time, this ensures that all incident neutrons will intersect conversion material, greatly increasing detection efficiency. The motivation for development of the dual-sided microstructured semiconductor neutron detector (DS-MSND) is explained in this chapter. Topics include the shortcomings of preceding technologies (such as the thin-film-coated diodes and single-sided MSNDs) and advantages of the DS-MSND. This chapter will also include the organization of the thesis as well as a brief synopsis of the author's contributions to the technology.

1.1 Motivation for Development

Development of high-efficiency neutron detectors over recent decades has led to the realization of small-volume, low-power thermal neutron detectors. These detectors are meant to replace aging ^{3}He gas-filled neutron counters commonly found in hand-held instruments. Semiconductor diodes coated with a thin film of neutron converting material, such as ^{10}B or ^{6}LiF, were previously investigated for this role [1-6]. Thin-film-coated diodes operate by counting the charged-particle reaction products emitted by a neutron converting material deposited atop a semiconductor surface, that intersect the semiconductor diode depletion region. Upon absorption of a thermal neutron within either a ^{10}B or ^{6}LiF neutron-reactive film, induced fission of the parent nucleus will produce charged-particle reaction products,

$$^{6}Li + {}^{1}_{0}n \rightarrow {}^{4}He(2.07\ MeV) + {}^{3}H(2.73\ MeV) \qquad \text{(Eq. 1.1.1)}$$

$$^{10}B + {}^{1}_{0}n \rightarrow \begin{cases} {}^{7}Li(1.02\ MeV) + {}^{4}He(1.78\ MeV) & \eta = 6\% \\ {}^{7}Li(0.84\ MeV) + {}^{4}He(1.47\ MeV) + \gamma(0.48\ MeV) & \eta = 94\%\,, \end{cases} \qquad \text{(Eq. 1.1.2)}$$

where η represents the branching ratio of the reaction. The reaction products are emitted in opposite directions, potentially depositing energy into the semiconductor depletion region. Energy deposited into the depletion region will excite electron-hole pairs that can be drifted across the semiconductor device by an applied bias. The resulting induced current can be amplified, measured, and recorded by supporting counting electronics. Self-absorption of the reaction products and solid-angle limitations on their trajectories reduces the amount of energy that can be deposited into the depletion region, and low neutron absorption of the thin-film coatings limit the intrinsic thermal neutron detection efficiency of these devices to 4-5% for both ^{10}B and ^{6}LiF films [7, 8].

It was suggested that the inclusion of microstructures that are backfilled with neutron conversion material within the semiconductor diode could increase the thermal neutron detection efficiency [9, 10]. The trenches increase the amount of neutron converting material present within the system, thereby, both increasing neutron absorption and probability that reaction products will enter the semiconductor. Microstructured semiconductor neutron detectors (MSNDs) were first formed from a GaAs-based Schottky diode, etched with micro-sized holes and backfilled with ^{10}B

neutron converting material [7]. More recently, MSNDs are formed from *pn*-junction diodes on Si substrate with rectangular trenches etched as deep as 495 μm and backfilled with ^{6}LiF powder [11]. The intrinsic thermal neutron absorption efficiency is increased by the deeper-etched trenches and where the additional neutron conversion material increases the absorption probability of an incident neutron, and the high-aspect ratio trenches yield a higher probability that reaction products will enter the semiconductor [12]. These improvements have yielded MSNDs with greater than 30% intrinsic thermal neutron detection efficiency [11, 13-15]. Neutrons streaming through the bare semiconductor regions limits the intrinsic thermal neutron detection efficiency of an MSND to approximately 45% [12].

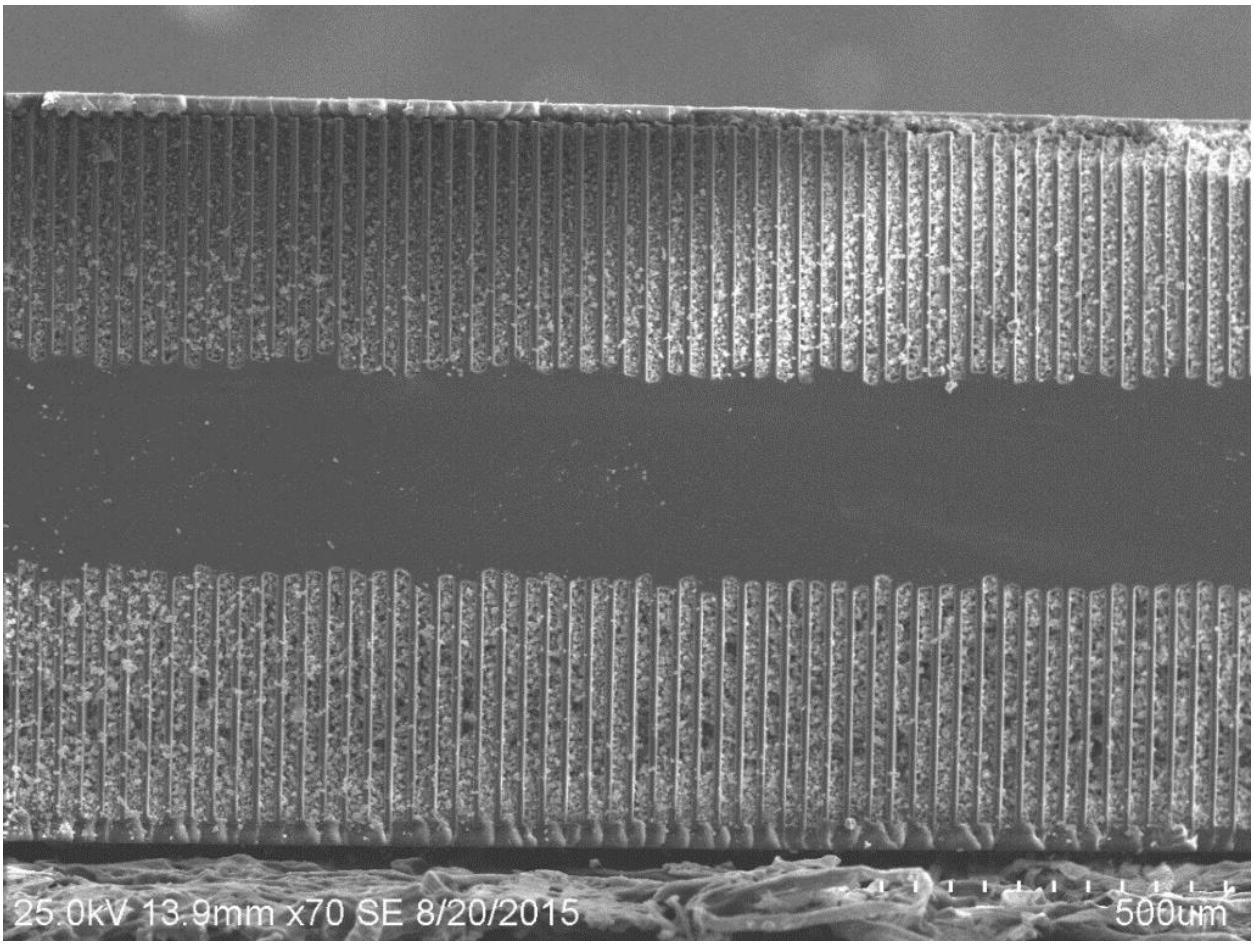

Fig. 1.1. Shown is a cross-section of a dual-sided microstructured semiconductor neutron detector (DS-MSND) backfilled with nano-sized ^{6}LiF neutron converting material. Trenches are etched to approximately 350-μm deep, and 20-μm wide. Trenches are repeated every 30 μm and the bottom-side trenches are offset from the top-side by 15 μm to minimize the possibility of neutron streaming paths.

Previous work on reducing neutron streaming involved stacking and off-setting two detectors such that neutrons streaming through the first detector can be counted by the second [16]. For instance, two MSNDs with 21% intrinsic thermal neutron detection efficiency were double-stacked, aligned, and integrated to count as a single sensor yielding ~42% detection efficiency [16-18]. However, achieving the correct alignment of the stacked MSNDs proved difficult, which is not conducive to mass production. Furthermore, inconsistent leakage current and diode capacitance led to device mismatch and produced poor reaction-product pulse-height spectra. These combined problems necessitate an unusually-high setting of the lower-level discriminator (LLD). Described in the present work is a new device designed after the microstructured semiconductor diode that improves efficiency and performance. The dual-sided microstructured semiconductor neutron detectors (DS-MSNDs) are a recent embodiment of the MSND architecture, and thus feature perforations etched into opposite sides of a semiconductor diode, backfilled with neutron converting material, as shown in Fig. 1.1. The back-side trenches of a DS-MSND are aligned with the front-side fins, as with the stacked MSND design, thereby, capturing and counting neutrons that stream through the front-side semiconductor fins. Fabrication of these sensors is simple and similar to single-sided MSNDs, but are easier to build than double-stacked MSNDs because the front- and back-side alignment is performed with a photolithographic process.

Early DS-MSNDs were produced with trenches etched into both the front- and back-side surfaces that were then doped to form a vertically-operated *pvn*-type diode [19, 20]. The front-side fins were doped with a semi-conformal *p*-type contact while the bottom-side were similarly doped *n*-type. Unfortunately, this method of diode operation had minimal success due to the limited depletion depth in the back-side fins. The back-side n-type contact stopped the depletion region from extending completely into the back-side fins. These *pvn*-type DS-MSNDs yielded less than 30% intrinsic thermal neutron detection efficiency for a 0.5-mm thick device, less than its simulated efficiency of nearly 40% [REF&]. A new generation of DS-MSND has been developed with p-type contacts on both the front and back sides, forming *pvp*-type devices. The thin fins are fully depleted by the device built-in potential, allowing the devices to operate with 0-V bias. The self-depletion of the fins and the built-in potential works to drift holes excited from charged-particle reaction product interactions to the contact where they recombine and produce a voltage pulse at the anode and cathode. In this manner, reliable DS-MSNDs can be fabricated that yield greater than 50% intrinsic thermal neutron detection efficiency. Presented in the following work

are designs, fabrication methods, and evaluation tests of the new generation DS-MSNDs. These modern-day neutron detectors can be deployed in numerous scenarios from personal dosimetry, to neutron source location, detection, and identification, to reactor flux monitoring. Neutron detection systems that are used for personal dosimetry and neutron radiation measurements both require that the detector sensor have a high intrinsic thermal neutron detection efficiency, i.e., recording a high percentage of neutrons intersecting the detector. Many neutron detection systems are designed with a high intrinsic gamma-ray discrimination. Gamma rays are usually present in neutron detection scenarios and incident gamma rays must not be mistaken as neutron counts. The sensors populating these instruments (be they gas-filled proportional neutron counters, doped scintillators, or solid-state neutron detectors) will ultimately affect the overall performance of a neutron detector system, including efficiency and gamma-ray rejection ratio.

1.2 Contribution to knowledge of DS-MSND

Contributions described in this dissertation that advance of the knowledge of MSND-based science and technologies, most notably the introduction and development of the DS-MSND, and related instruments include:

- Development of simulation for ^{6}LiF- and ^{10}B backfilled DS-MSNDs, thereby predicting intrinsic thermal neutron detection efficiencies with varying trench geometries along with their resulting optimal pulse-height spectra.
- Development of simulations of charge transport within DS-MSNDs and the development of the pulse-height characteristics.
- Simulation of internal electric field formation with respect to junction formation on the DS-MSND fins, including type and shape of the junction formed.
- Initialization and advancement of dual-sided etching of microcavities into bulk semiconductor material using aligned, preferential etching of Si using wet KOH-etch methods.
- Adaptation of present backfilling methods for filling dual-sided microcavities etched into bulk semiconductor material with neutron-reactive converting material.
- Testing and characterization of the first ever DS-MSNDs, including measurement of the highest intrinsic thermal neutron detection efficiency ever recorded for such

devices. The gamma-ray rejection for DS-MSNDs is also reported.

- Design, simulation, construction, and testing of a second-generation ^{3}He-replacement technology populated with single-sided MSNDs that matched the performance of a 2-in. diameter, 6-in. long ^{3}He tube, pressurized to 4 atm.
- Design, simulation, construction, and testing of various arrayed MSND-based detector systems, including the man-portable Briefcase Neutron Detector and stationary 1-m x 1-m Neutron Detector Array.
- Design, simulation, construction, and testing of a small-form-factor third-generation ^{3}He-replacement technology populated with DS-MSNDs to compete with 0.75-in. diameter, 4.5-in. long ^{3}He tubes, pressurized to 10 atm.

1.3 Organization of Thesis

The dual-sided microstructured semiconductor neutron detector (DS-MSND) represents a significant advancement in solid-state thermal neutron detection sensor technology. The DS-MSND offers performance advantages over single-sided MSNDs and their predecessors through a more intimate coupling of semiconductor and neutron conversion material. The need for reducing neutron streaming and improving overall thermal neutron sensitivity is motivation for the development of the DS-MSNDs. Many of the fabrication hurdles for developing the DS-MSND were overcome during previous projects [21, 22]. Fabrication of MSND-based sensors is similar to standard very-large scale integration (VLSI) fabrication techniques, and much of what was learned previously was applied to this work. However, the added complication of a second-set of microcavities etched into the back-side of a bulk semiconductor diode required the development of a new methods for junction doping and device operation. Discussed within this work is the development of models for predicting DS-MSND performance (Chapter 3), modifications and advancements in junction doping techniques necessary for fabrication of the DS-MSNDs (Chapter 4). These discussions are preceded by introductory background material necessary for understanding the functionality of the DS-MSNDs (Chapter 2), followed by discussions regarding new instruments that incorporate these new DS-MSND (Chapter 5). DS-MSND and Instrument testing and results and discussion follow (Chapter 6 and Chapter 7).

Chapter 2 - *Background*

Presented in the following chapter are relevant topics to assist the reader with a proper background of the research material. Different types of radiation, their interactions in media, the detection of said radiation, and a more in-depth review of neutron detector systems are reviewed in the following chapter.

2.1 Introduction to Radiation

The discovery of the 'x-ray' was made in 1895 by Röntgen with the use of a Crooke's tube and a fluorescing plate. The experiment had originally been intended to investigate cathode rays (later determined to be electrons) emitted by passing a high current through a cathode and made to intersect a fluorescing layer within a vacuum tube. Röntgen discovered that a fluorescent plate several feet away would also respond to the operation of the Crooke's tube, even when the tube was covered with paper. Further experimentation led Röntgen to conclude that a new, more penetrating ray was responsible. Later renamed x-rays, it was determined that they were emitted by the deceleration of electrons within the Crooke's tube.

The 1890's would see rapid advancements in the field of radiation physics. Becquerel would discover natural radioactivity by absentmindedly exposing photographic plates with a sample of radioactive uranium salts. Later, Perrin would deduce that cathode rays were, in fact, negatively charged. Expanding on this, Thompson would find that by deflecting cathode rays using magnetic and electric fields and measuring the angle of deflection, he could deduce the mass of the rays. Thompson then concluded that cathode rays were particles, rather than rays, and took the name 'electrons' from Stoney, an early theorizer of the particles. Later, Rutherford's aluminum leaf experiment studied particles emitted by radioactive uranium samples [23]. Rutherford noted that by incrementally stacking thin foils of aluminum between the sample and the measuring instrument to block emissions, that there was a major change in particle emissions with few foils initially, and then a long gradual decrease in attenuation following that (from Fig. 2.1.1). Rutherford concluded that the sample of uranium was emitting two types of rays, alpha rays and beta rays.

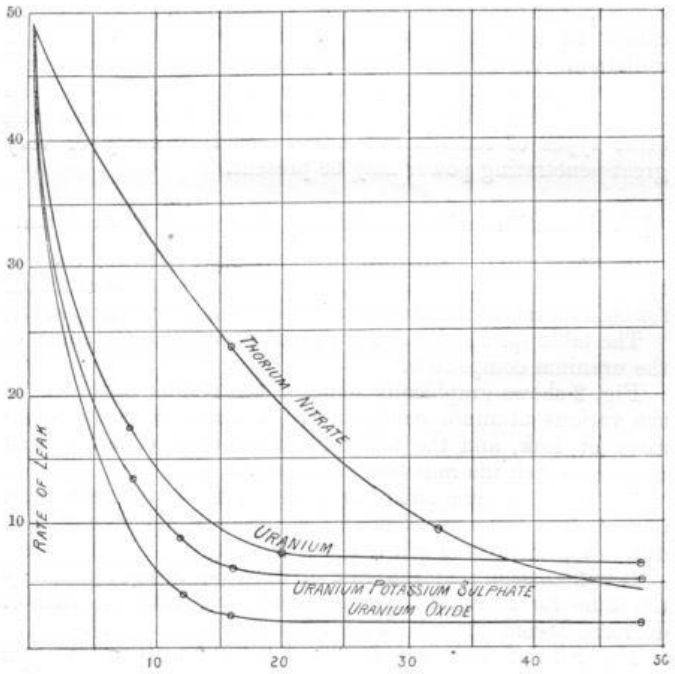

Fig. 2.1.1. Shown is Rutherford's original data from his gold-leaf experiment that determined that the uranium samples were emitting two different types of 'rays', dubbed 'alpha' and 'beta' rays. Note the initially-steep drop off with the later gradual secondary decrease [23].

Rutherford's further studies of the mass of atomic nuclei suggested that another, neutrally-charged particle existed in the nucleus alongside the proton of atoms larger than hydrogen. His student, Chadwick, conducted an investigation of this idea wherein a sample of boron was irradiated with a radioactive polonium source. The bombardment of the boron nuclei with alpha particles induced fission and subsequent emission of an unknown particle. Chadwick measured the particle's mass and found that it had a neutral charge and a mass similar to that of a proton, confirming Rutherford's hypothesis. This particle, the neutron, was seemingly the final piece of the puzzle in atomic physics.

Radiation has since been well characterized, yielding two primary groups of particles, ionizing and non-ionizing radiation. Non-ionizing radiation is composed of photons with a wavelength of greater than 10 nm (<125 eV), including radio waves, microwaves, infrared and the visible spectrum [24]. Ionizing radiation is composed of the remaining particles, charged and uncharged, such as alpha particles, beta particles, neutrons, x-rays, and gamma rays [24]. The important distinction between the two classes of radiation is that ionizing radiation is capable of ionizing matter through direct or indirect interactions with the atoms of the material.

Direct ionization of radiation interacting in matter is the basis by which a detector system measures said radiation. The detection of radiation emitted by some unknown source can provide clues to its material composition. An investigator can determine the composition of a target with great accuracy based on these emissions. Whether the material is naturally radioactive or if the material must be provoked to emit radiation by bombardment of energetic primary particles, the type and energy of the emissions, and the quantities of the emissions can provide clues to its composition. Though the field of study for radiation is broad, the focus of this chapter will be on the neutron, from its creation to its capture and detection.

2.2 The Neutron

The neutron is a neutrally-charged constituent particle of a nucleus, consisting of two down quarks and one up quark [25]. Neutrons are unstable when free from a nucleus and will undergo radioactive decay (with a half-life of 10.23 minutes) with one down quark decaying into an up quark. The decay process will convert the neutron into a proton, electron, and electron neutrino. The neutron is difficult to detect when free from the nucleus [24, 26]. Neutrons are classified by their kinetic energy, with 'thermal' neutrons being at thermal equilibrium with their surroundings (generally kT = 0.0254 eV), epithermal neutrons having on the order of 10-100's keV, and fast neutrons having greater than 1 MeV, but these definitions vary from discipline to discipline. A neutron's energy is the primary characteristic that determines its rate of interaction with a medium.

The study of neutrons and their emission, whether through natural or induced emission, is of great concern to modern research. Free neutrons are born through fission of a parent nucleus, either spontaneously or through induced fission. In spontaneous fission, a nucleus in an excited state can decay into two more-or-less equal fission fragments [27]. These fission fragments exist as highly energetic, ionized, excited nuclei that are emitted in opposite directions, ionizing the matter through which they travel. The secondary nuclei begin to return to their ground state via gamma-ray and neutron emission, as shown in Fig. 2.2.1 [28]. The neutrons emitted from the fission fragments are said to 'evaporate' from the secondary nuclei. These 'evaporation' neutrons are emitted shortly after the initial fission of the parent nucleus and are thus often incorrectly associated with the original fission.

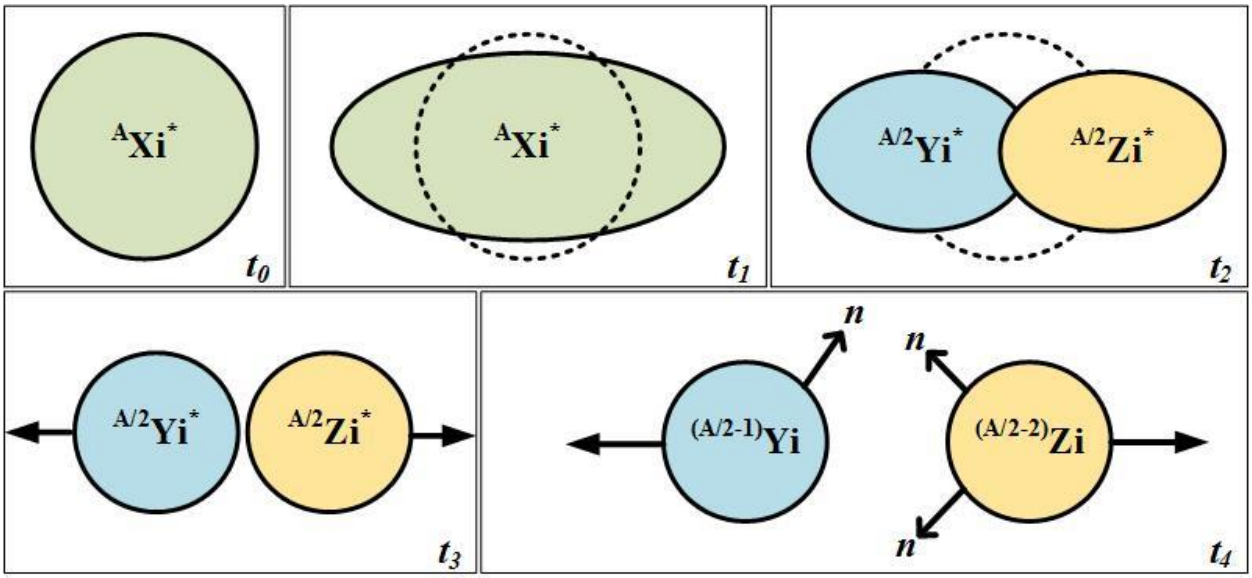

Fig. 2.2.1. Depicted is a schematic of the rain-drop model of spontaneous fission. An excited nucleus (t_0) split in to nearly even nuclei (t_2). The excited nuclei carry kinetic energy (t_3) and de-excite by emission of, among other things, neutrons (t_4).

The spontaneous fission process typically occurs in only the largest nuclei, such as Cf, U, and Pu, where excitation energies can overcome the Coulombic barriers necessary for fission [28]. The de-excitation and emission of neutrons can reveal the identity of the parent material. The number of neutrons emitted per fission is not constant across all materials. Furthermore, the number of neutrons emitted per fission follows a multiplicity distribution and proper study of the number of neutrons emitted per fission can yield the identity and concentration of the isotope [27, 29]. Additionally, the distribution and mean value of the kinetic energy of fission neutrons is also dependent on the parent isotope. The distribution of neutron energies can be measured to determine the isotope's identity [30, 31]. Thus, proper study of free neutrons is important for materials identification and characterization.

Not all large nuclei decay by spontaneous fission at a significant rate that can allow for passive identification. Many nuclei can be made to fission by bombardment with primary particles, thereby, inducing fission. Bombardment of nuclei with an energetic particle can force the nucleus to overcome the Coulombic barrier [28]. Such examples include high-energy gamma rays undergoing inelastic scatter, alpha particles bombarding the nucleus, or absorption of a free neutron within the nucleus. In the case of neutron-induced fission, certain isotopes will exhibit an energy level 'cut-off' wherein a neutron of some minimum energy is required to properly couple

with the nucleus before absorption can occur. ^{235}U, an isotope commonly used as the principle fissile material within a reactor core, can fission by absorption of neutron with thermal energy (i.e. less than 1 eV). ^{238}U, however, must absorb a neutron with kinetic energy of at least 1.4 MeV before fission of ^{239}U* can occur [28].

2.3 Neutron Detection

Neutrons interact in matter differently from photons and charged particles. Gamma rays and charged particles can directly ionize a material through interactions with the bound electrons. Gamma rays can interact through a number of direct interactions with electrons, while charged particles interact at a distance through Coulombic repulsion or attraction [24]. Neutrons typically only interact within the nucleus of an atom, as its neutral charge makes them unlikely to interact with electrons. This lack of interaction requires special attention for neutron detection as direct ionization of a detection medium is unlikely [30]. There are two primary methods of neutron interaction of concern with this work; scattering, and absorption, both of which can produce ionization within a radiation detector.

2.3.1 Neutron Capture

To detect a free neutron, it is often necessary to capture the neutron through nuclear absorption and convert it to a secondary particle that is more easily detected [24, 26]. ^{3}He, ^{6}Li, and ^{10}B are common neutron converting materials and are found in numerous neutron detectors. Upon absorption of a free neutron, the compound nucleus briefly exists in an excited state prior to de-excitation by fission. Fission produces charged-particle reaction products with some kinetic energy, as with the ^{3}He(n,p)^{3}H, ^{6}Li(n,t)^{4}He, and ^{10}B(n,α)^{7}Li reactions. The probability of this absorption occurring depends on several factors; the energy of the neutron (E), the macroscopic cross section (Σ), and the thickness of the material (t). If a beam of parallel neutrons, with intensity I_0 are made incident on a slab of material (Fig. 2.3.1), the intensity of the beam will be reduced in an exponential manner [30]:

$$I(t) = I_0 e^{-\Sigma t}. \qquad \text{(Eq. 2.3.1)}$$

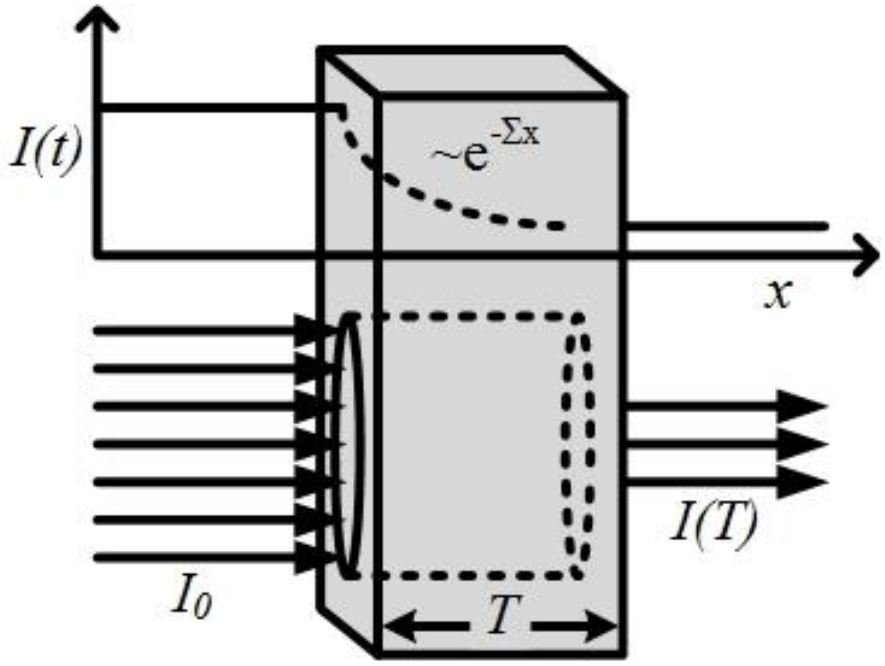

Fig. 2.3.1. Depicted is a drawing of a slab of arbitrary thickness. A beam of neutrons is made incident on the slab which is attenuated in an exponential fashion based on the attenuation coefficient and the thickness of the slab.

As previously discussed, there are two primary modes of interaction of a neutron within a medium, either absorption or scattering. The probability of these two interactions are summed to determine the total probability of interaction within a medium [30]:

$$\Sigma = \Sigma_{tot} = \Sigma_{abs} + \Sigma_{scat}, \qquad \text{(Eq. 2.3.2)}$$

where Σ_{abs} is the macroscopic absorption cross section and is the probability of nuclear absorption per unit length traveled in the material. Σ_{scat} is the macroscopic scattering cross section and refers to the probability that the neutron will undergo some sort of scattering interaction with a nucleus. There are many types of absorption and scattering interactions that a neutron can undergo, such as (n,p), (n,α), or (n,t) nuclear absorption reactions and elastic and inelastic scattering [30]. Neutron detection tends to utilize materials where the absorption is the dominant mode of interaction. The ^{10}B isotope, for example, has a high (n,α) absorption cross section ($\Sigma_a \approx 500$ cm^{-1}) [32]. Therefore, small layers of ^{10}B can be used to attenuate a large percentage of incident low-energy neutrons which is useful in neutron detection and shielding.

The macroscopic cross-section of any material may be calculated by considering the constituent isotopes and their atomic density (atoms cm^{-3}) [30]:

$$\Sigma = \sigma N, \qquad \text{(Eq. 2.3.3)}$$

where, σ, is the microscopic cross section and has units of cm^2 $atom^{-1}$, giving rise to the cross-section analogy from classical motion [28, 33]. The microscopic cross section is a property intrinsic to the isotope and is a function of the kinetic energy of the incident neutron. The atomic density of the material, N, can also be calculated:

$$N = \frac{\rho N_a}{A}, \qquad \text{(Eq. 2.3.3)}$$

where ρ is the material density, N_a is Avogadro's number, and A is the atomic mass of the material. The macroscopic cross section of a material is therefore extrinsic to the material and is dependent on the nuclide density as well. The plotted microscopic cross-sections of some isotopes of interest can be found in Appendix A. Of specific interest are the plots for ^{3}He, ^{6}Li, and ^{10}B. The large capture cross section of the aforementioned absorbing materials and the resulting charged-particle secondary reaction products make them ideal for neutron detection.

Certain compounds improve the atomic density of an absorbing medium, enhancing that material's neutron absorption efficiency. Calculating the macroscopic cross-section of a compound, such as $^{10}B_4C$, is a sum of the cross section of the constituent atoms, i, weighted by their mass fraction [24]:

$$\Sigma_{Total} = \sum_i \sigma_i N_i = \sum_i \sigma_i w_i \frac{\rho N_a}{A_i}, \qquad \text{(Eq. 2.3.5)}$$

where w_i is the weight fraction of the constituent atom. For example, the macroscopic absorption cross section of ^{6}Li is calculated to be approximately 46.1 cm^{-1} while the commonly used ^{6}LiF compound is roughly 57.5 cm^{-1}.

2.3.2 Measuring the Charged-Particle Reaction Products

Once the neutron is absorbed, the charged-particle reaction products emitted must in turn be captured and counted for the event to be recorded by detector electronics. The detection medium will cause the reaction products to lose energy through Coulombic force interactions [24]. The rate of energy loss in the detector gas by a large ion is complex, but can be generalized as [24]:

$$\frac{dE}{dx}(MeV/m) \propto z^2 NZ, \qquad \text{(Eq. 2.3.6)}$$

where z is the charge of the interacting particle, N is the atomic density of the detection medium, and Z is the atomic number of the target material. The Coulombic forces between the reaction products and the electrons in the medium creates ionization or the excitation of electron-hole pairs [24]. This charge is drifted out of the detector by an electric field established by the applied bias, thereby, inducing an electronic pulse on the electrical contacts, which is then amplified and counted. The overall goal of a neutron detection system is to capture the energy from the energetic reaction products such that an electronic pulse can be generated above background noise, recognizable as a count from an incident neutron (Fig. 2.3.2).

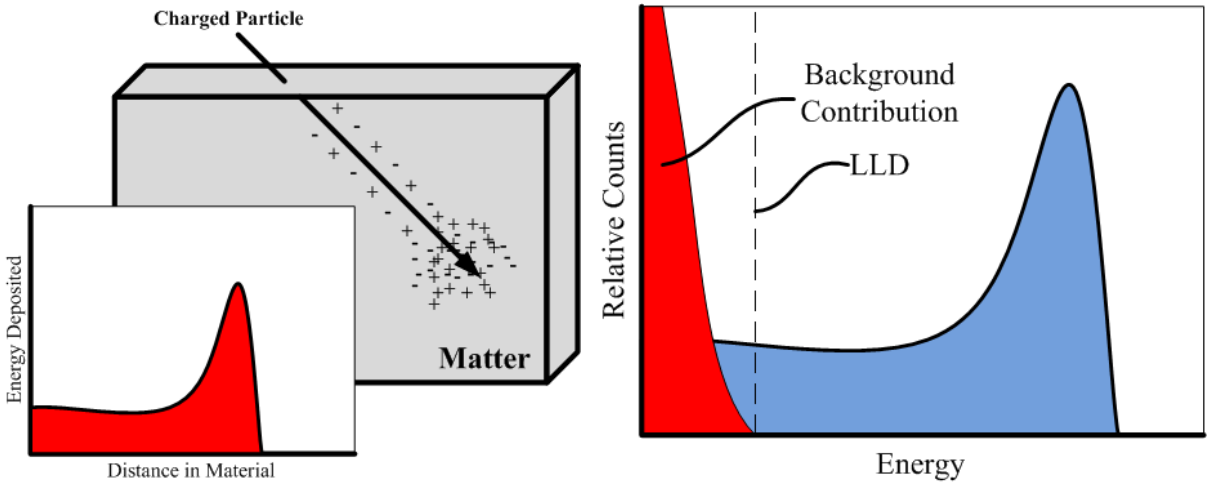

Fig. 2.3.2. Depicted (left) is a typical energy-deposition event from a small charged particle, such as an alpha particle. A majority of the particle's energy is deposited at the end of its travel. Shown (right) is an example pulse-height distribution from a neutron detection system. Pulses from events that rise above a lower-level discriminator (LLD) setting are 'counted' as neutron capture events.

2.3.3 Gamma-Ray Discrimination

A secondary, but important, goal of neutron detectors is to discriminate possible counts due to gamma-ray interactions within the detector volume. Gamma rays can undergo any number of interactions, but primarily only induce ionization through photoelectric absorption, Compton scattering, or pair production [26]. Photoelectric absorption occurs when the incident photon is absorbed by a bound electron, freeing it from the atom. The electron will travel with kinetic energy of the gamma ray (less the binding energy of the electron to the atom) and potentially further ionize the matter through which it travels. Compton scattering deposits energy into the detector volume in a similar manner, however the gamma ray only imparts a portion of its energy to the electron and 'scatters' away in a different direction. The recoil electron can also produce ionization in the detector volume. Pair production occurs when the gamma ray interacts within the potential field of a nucleus and is converted into an electron-positron pair. Here, the minimum energy for pair production is the rest mass, E_{mass}, of the two particles (1.022 MeV) where the remaining energy, E_{γ} - E_{mass}, is conserved in the transport of the new particles. Neutron detectors are generally made from materials that have low probabilities for gamma-ray interactions, thus minimizing energy deposition from these photons.

2.4 Semiconductor Physics

Semiconductors have been used for radiation detection for several decades because of numerous qualities that make them ideal for detecting many types of radiation [34]. Semiconductors are a class of materials with an electrical resistivity between insulators and conductors. Generally speaking, a conductor is a material wherein its conduction band (the energy band wherein electrons are free to move under an applied potential) and its valence bands overlap. Such a material allows for current to pass under an applied potential. In non-conductors, the two energy bands no longer overlap, forming a region devoid of electrons, the energy band gap (E_g). For insulators, the magnitude of E_g is such that electrons are rarely excited into the conduction band, thereby, greatly increasing the resistivity of the material. Semiconductors, however, have an energy band gaps that is sufficiently large to inhibit conduction (i.e. $E_g > 0$ eV), but small enough ($E_g < 4$ eV) such that radiation interactions can easily excite electrons into the conduction band thereby, allowing current to flow under an applied bias. Outlined in the following sections is

pertinent information regarding the physics of operation of a semiconductor and semiconductor diode, such as the dual-sided microstructured semiconductor neutron detector (DS-MSND).

2.4.1 Energy Band Gap

During the early 20th century, Bohr conducted studies to determine why H gas emitted light upon heating and subsequent cooling, which only found to emit at specific wavelengths [35]. Bohr postulated that the single bound electron of the atom must be restricted to certain well-defined energy levels of excitation, or orbitals, and emitted light upon de-excitation [35]. He assumed that the electron's momentum took a quantized value when bound to the H nucleus. Precise measurements of the emitted light and comparison to calculated momentum values confirmed his hypothesis, ultimately giving rise to the concept of the valence energy band (E_V), conduction energy band (E_C), and the energy band gap (E_g) calculated by $E_G = E_C - E_V$. Though many semiconducting materials exist, only Si will be considered in this section.

The electrons constituting a Si atom are also bound to certain energy levels. Most are permanently bound to lower levels, but four exist in the atom's valence band and are relatively free to move and bind with other atoms. These four electrons tend to occupy the lowest energy states available in the Si atom. Given many unassociated Si atoms, but in close proximity, finely split to form a quasi-continuum of energy states, appearing as an energy band (shown in Fig. 2.4.1) [36]. The bending is caused primarily due to the Pauli exclusion principle, which dictates that no two electrons can occupy the same quantum state in a system simultaneously [37]. As the Si atoms become bound to the same system, the Pauli exclusion principle forces the discrete energy levels to each shift slightly, forming quasi-continuous bands of discrete energy levels [36].

The use of semiconductors as radiation detectors relies heavily on these bandgap properties. Ultimately, the goal of any detector system is to produce a signal that is greater than any noise inherent to the system. Semiconductor radiation detectors will produce a signal when an electron is excited across the bandgap (into the conduction band) and drifted using an applied bias, and sensed by amplifying electronics. The smaller the energy band gap of the semiconductor, the higher the likelihood thermal energy will be able to excite electrons into the conduction band, thereby, inducing electronic noise (generation leakage current) [38]. DS-MSNDs are fabricated using Si substrates, with a band gap (1.12 eV) that is large enough to operate at room-temperature (or nearly room-temperature) environments while maintaining low background noise.

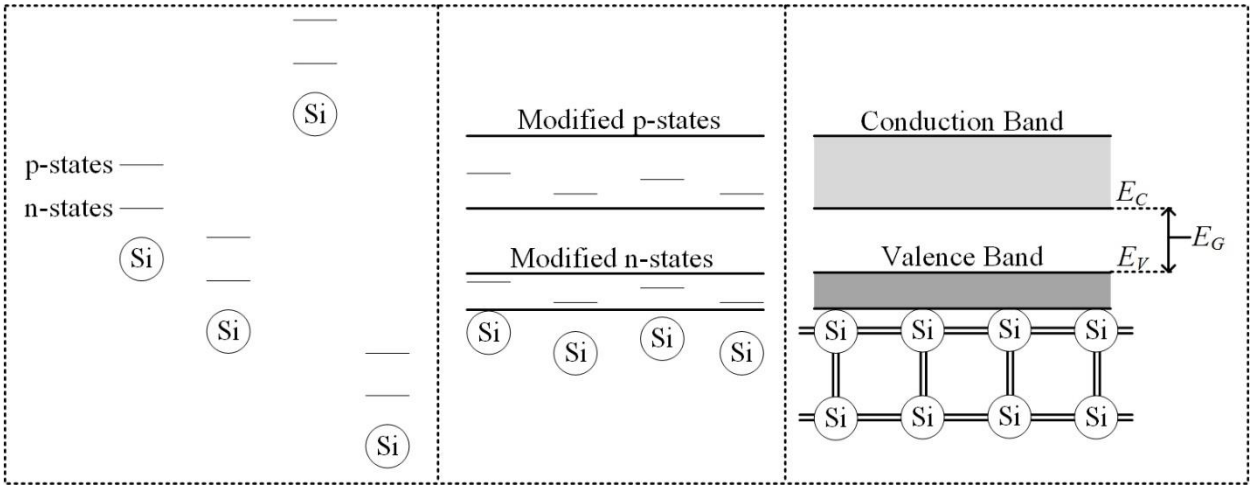

Fig. 2.4.1 Shown (left) are many unassociated Si atoms, each with lower-level n-state and higher-level p-states. As the atoms are brought together (middle) these states are split about the energy level. Finally, once bound (right), the energy states form quasi-continuous bands separated by the energy band gap.

The band structure of a bulk semiconductor is a function of temperature and lattice spacing of the constituent atoms. The band structure can also be altered by the doping concentration in degenerately-doped semiconductors [39]. In the case of an intrinsic semiconductor at zero temperature, the valence band is usually fully occupied, leaving the conduction band completely empty. However, at room temperature, thermal energy will excite some electrons into the conduction band in semiconductors with $Eg < 4$ eV. The probability that a particular electron is occupying a given energy state is defined by the Fermi-Dirac distribution [40]:

$$F(E) = \frac{1}{1 + e^{(E-E_F)/kT}}, \qquad \text{(Eq. 2.4.1)}$$

where E_F is the Fermi energy level for the material, k is Boltzmann's constant, and T is the temperature of the material. The Fermi energy level represents the level above which no electrons will be found at $T = 0$ K. For an intrinsic semiconductor, E_F is nearly midway between E_C and E_V. However, commonly available substrates are often doped with background dopants which adjusts the Fermi level [39].

Semiconductors used in radiation-detector fabrication are often intentionally doped with impurities to modify the resistivity of the material. However, modifying the impurity concentration

of a semiconductor also affects its Fermi energy level. A semiconductor doped with background impurities is considered to be extrinsic, where the majority carrier concentrations are [39]:

$$n = n_i e^{(E_f - E_i)/kT}, \quad \text{(Eq. 2.4.2)}$$

and

$$p = n_i e^{(E_i - E_f)/kT}, \quad \text{(Eq. 2.4.3)}$$

where n and p are the majority carrier concentrations in cm^{-3}, n_i is the intrinsic carrier concentration of the material, and E_i is the Fermi energy level for the intrinsic semiconductor. E_F shifts towards the top E_V for p-doped semiconductors, and shifts towards the bottom of E_C for n-doped semiconductors (shown in Fig. 2.4.2). Typically, for a room-temperature operated semiconductor device, the carrier concentrations can be assumed to be fully ionized (i.e. electrically active within the device) and thus the electron concentration is said to equal the donor concentration, N_D, and

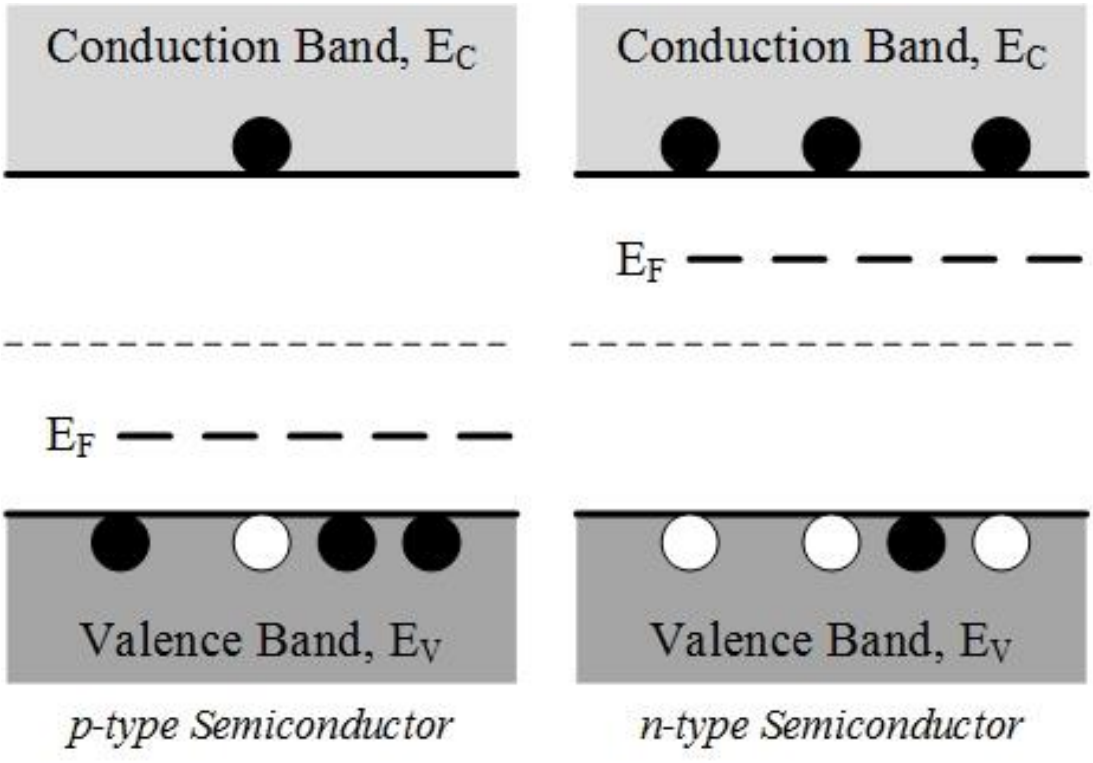

Fig. 2.4.2. Shown are two cases of Fermi energy level adjustment in a semiconductor. (left) A p-type, acceptor-heavy material, E_F is adjusted towards E_V, and (right) for an n-type, donor-heavy material, E_F is adjusted towards E_C.

the hole concentration, p, to equal the acceptor concentration, N_A. Thus, substituting and rearranging the two equations provides [39]:

$$E_f = E_i + kTln\left(\frac{N_D}{n_i}\right), \quad \text{(Eq. 2.4.4)}$$

and

$$E_f = E_i - kTln\left(\frac{N_A}{n_i}\right). \quad \text{(Eq. 2.4.5)}$$

It should be noted that typically, impurities are present in such quantities that either N_D or N_A dominates, but cases can be considered where both types of impurities are present [39]. However, the dopant concentration is above the background dopant concentration in the present work, hence background impurities are not considered.

2.4.2 Charge Carrier Transport

Signal from the detector is produced when electron-hole pairs (excited by an incident charged particle) are drifted towards the electrical contacts. This charge motion induces a current at the detector contacts which can be used to charge a capacitor in parallel with the detector. The voltage measured across the capacitor increases with the excited charge. The shape of the voltage 'pulse' that is tallied by the counting system is a function of time, resistance, and capacitance of the total circuit. Typically, there are only two contacts present on a semiconductor: the anode and cathode, but there can be more in more complex systems [41, 42]. An electrical potential must be produced between these two electrical contacts, thus establishing an electric field, which can drift the excited charges. For semiconductors with high resistivity (~10^9 ohm-cm), a simple metal layer is deposited across the detector face, which forms an electrical contact [34]. Shown in Fig. 2.4.3 is perhaps the simplest semiconductor detector setup possible. Non-blocking contacts are applied to either end of a high-resistivity semiconductor substrate and a voltage is applied. Assuming that no free charge exists in the conduction band, this detector will hold the applied potential indefinitely because it represents a perfect capacitor. The presence of the electrical potential (V) across the semiconductor produces an electric field described by [43]:

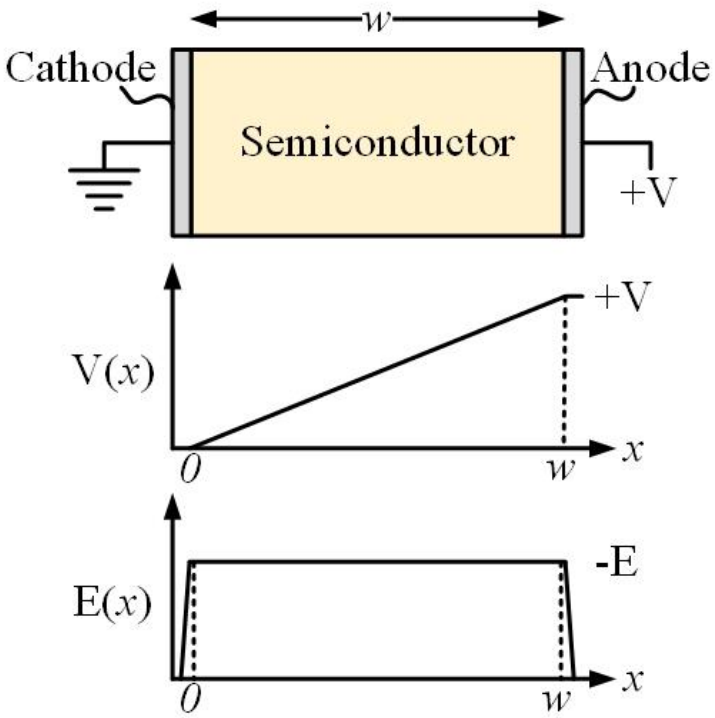

Fig. 2.4.3. Shown is a schematic of a planar detector. Contacts are applied to each end of a perfect semiconductor detector with a positive bias applied to the anode. The potential field increases linearly with distance from the cathode due to the contact geometry. The electric field is constant, with a direction pointed towards cathode.

$$\frac{\partial^2 V}{\partial x^2} = -\frac{\partial E}{\partial x} = \frac{\rho}{\varepsilon_s}, \qquad \text{(Eq. 2.4.6)}$$

where the partial derivative of the electric field, *E*, is equal to the second partial derivative of the potential, *V*, which is also equal to the ratio of the charge density, ρ, to the dielectric constant of the semiconductor, ε_s. In the case of the perfect semiconductor, the detector volume is free of charge, and the magnitude of the electric field is constant.

Current can then be induced from the motion of electron-hole pairs by the established electric field. Fig. 2.4.4 depicts this process in three steps. First, Fig. 2.4.4(a) shows some ionizing particle incident on the detector. The particle deposits its energy into the semiconductor substrate through excitation of electron-hole pairs shown in Fig. 2.4.4(b). The applied potential (and thus the established electric field) drifts the charge to the contacts in Fig. 2.4.4(c) with a force equal to:

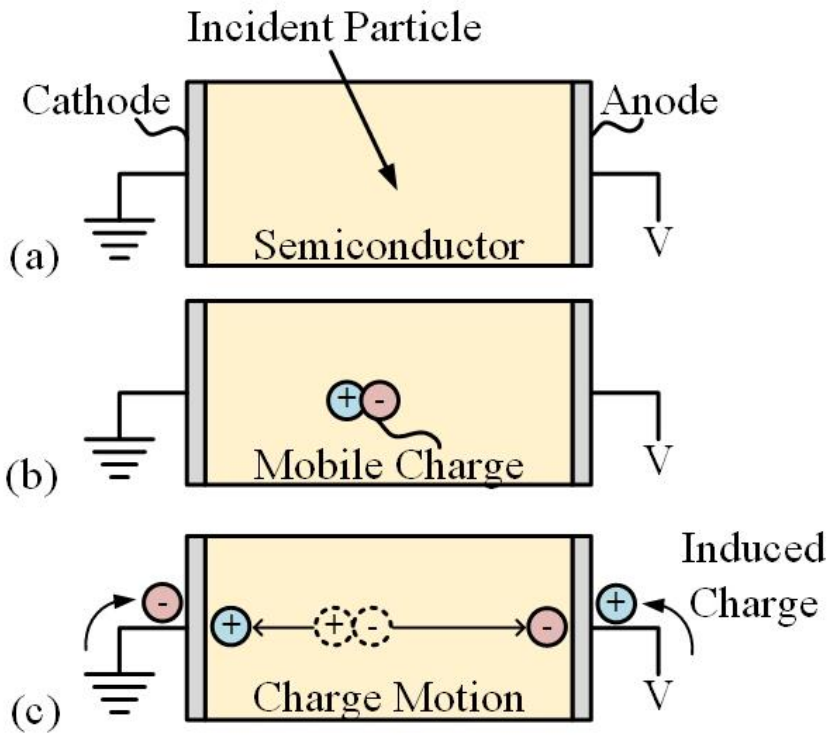

Fig. 2.4.4. Depicted are the three major steps in inducing and measuring charge from a particle incident on a semiconductor detector (a). The excited electron-hole pairs (b) are drifted to the contacts (c), thereby, inducing current that is measured by the counting electronics.

$$\boldsymbol{F} = q\boldsymbol{E}, \qquad \text{(Eq. 2.4.7)}$$

where q is the elementary charge of the electron (and subsequently, the hole as well), and $\boldsymbol{E}$ is the electric field vector. The electrons and holes are quickly accelerated, with velocity given by:

$$\boldsymbol{v}_i = -\mu_i \boldsymbol{E}, \qquad \text{(Eq. 2.4.8)}$$

where μ_i represents the mobility for a given charge carrier (either electron or hole) in the semiconductor under consideration. Mobility of a charge carrier is both a characteristic of the charge carrier itself, as well as that of the material [39].

The current generated by the motion of the charge carriers within the semiconductor can be understood by combining the prior subjects while considering other sources of current. Charge carrier motion within a semiconductor pertinent to this work occurs mainly by two mechanisms,

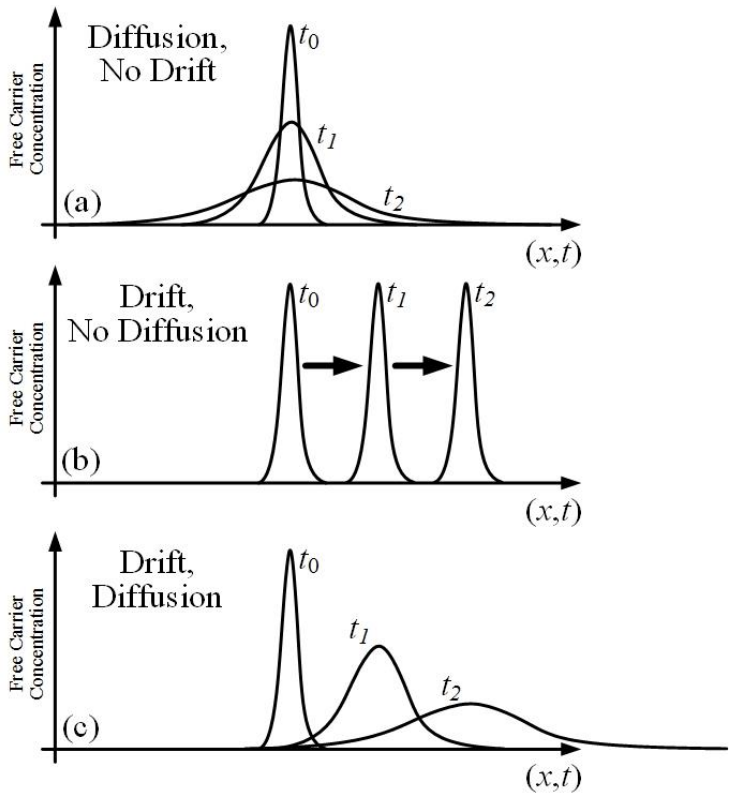

Fig. 2.4.5. Shown are three cases of charge carrier motion within a semiconductor: (a) carrier diffusion occurs due to a concentration gradient and lack of electric field, (b) charge carrier drift, where charge motion is driven entirely by the presence of an electric field, and (c) the case where both carrier drift and diffusion are present.

those being drift and diffusion. Diffusion of a concentration of charge carriers occurs when there is a concentration gradient between the charge carriers and the bulk semiconductor. The diffusion of charge carriers occurs due to the net direction of the Brownian motion being outwards from the area of high concentration (or rather, in the negative direction of the gradient, shown in Fig. 2.4.5(a)). Carrier drift occurs when the charge is in the presence of an applied electric field, as shown in Fig. 2.4.5(b). The current measured by the detector circuit is therefore a combination of the two sources (Fig. 2.4.5(c)) of charge carrier motion, as both occur simultaneously in the presence of an electric field. The current contribution, J_i, from drift is calculated as the amount of charge moving at some group velocity, described by:

$$J_{n,drift} = qn\boldsymbol{v}_n = qn\mu_n\boldsymbol{E}, \qquad \text{(Eq. 2.4.9)}$$

for electrons, and for holes:

$$J_{p,drift} = qp\mu_p \boldsymbol{E}, \quad \text{(Eq. 2.4.10)}$$

where *n* and *p* are the number of electrons and holes present, respectively. The values for *q* will be opposite for one another (*-q* for electrons, +q for holes), however, their opposite direction of motion in an applied electric field offset the need to differentiate this point. The current contribution from the diffusion of charge carriers is dependent on the concentration gradient *dn/dx*, which is important for understanding the formation of *pn*-junction contacts [40]. Here, the current from carrier diffusion for electrons and holes are defined as [40]:

$$J_{n,diffusion} = qD_n \frac{dn}{dx}, \quad \text{(Eq. 2.4.11)}$$

$$J_{p,diffusion} = -qD_p \frac{dp}{dx}, \quad \text{(Eq. 2.4.12)}$$

where D_i is the diffusivity of a carrier in a given semiconductor [39], and *dn*/*dx* and *dp*/*dx* is the change in the population of free charge carriers in the system due to generation and recombination. Generation current, or thermal generation leakage current, is present in any device at a temperature whereby electrons can be excited across the band gap. The generation rate is highly proportional to temperature [34]. The increase to the device current equations from generation stems from the increase in carrier population, thereby, affecting the *n* and *p* terms in Eq. 2.4.11 and Eq. 2.4.12. The recombination rate describes the loss of electrons and holes as electrons fill unoccupied states in the valence band. Generally, recombination is rare in Si, the pertinent material for this work, due to its indirect band-gap structure. Finally, the total current is the sum of J_{drift} and $J_{diffusion}$:

$$J_n = J_{n,drift} + J_{n,diffusion} = qn\mu_n \boldsymbol{E} + qD_n \frac{dn}{dx}, \quad \text{(Eq. 2.4.13)}$$

$$J_p = J_{p,drift} + J_{p,diffusion} = qp\mu_p \boldsymbol{E} - qD_p \frac{dp}{dx}, \quad \text{(Eq. 2.4.14)}$$

where then the total device current is simply the sum of Eq. 2.4.13 and Eq. 2.4.14.

2.4.3 The pn-Junction

Many semiconductor materials, Si in particular, have a band gap and background impurity concentration that require blocking contacts to limit the leakage current [34]. From Ohm's law, voltage is reduced over a resistor inversely proportional to its current. Leakage current through the detector will reduce the overall resistance in the bias circuit, and force a voltage drop across the bias resistor, thereby, diminishing the applied bias across the detector. A lower bias across the diode limits the detector depletion region depth, thereby, reducing the charge-sensitive area and increasing detector capacitance, and decrease charge carrier drift velocity [34, 38].

The ability of a semiconductor to support an applied bias is typically defined by the bulk resistivity of the material. The bulk resistivity, ρ (Ω-cm), of a semiconductor is largely a function of the impurity concentration and carrier mobility [40]. Even high-resistivity Si (~10 kΩ-cm), such as that used to manufacture the dual-sided microstructured semiconductor neutron detectors (DS-MSNDs), has insufficient resistivity to sustain a substantial bias for detector operation. A blocking contact must be formed with the Si surface to reduce current flow in the reverse direction (rectification), as shown in Fig. 2.4.6. In the forward direction, the diode junction 'turns on', thereby, allowing current to flow freely, also shown in Fig. 2.4.6. There are two primary types of blocking contacts used in semiconductor devices, Schottky contacts and *pn*-junction contacts [34]. Only *pn*-junction contacts are considered here.

Recall from Section 2.4.1, that an *n*-type semiconductor has an excess of electron-donor atoms that increase the probability of electrons being excited into the conduction band, thereby, pushing E_F higher. Conversely, the addition of acceptor atoms in a *p*-type semiconductor will reduce the number of free electrons, while increasing the hole population. When bringing an *n*-type and a *p*-type semiconductor into direct contact with each other, the Fermi energy levels of the two materials are brought into alignment, as shown in Fig. 2.4.7 [40]. The excess hole concentration of the *p*-type material, mirrored by the excess electron concentration of the *n*-type material, induces a diffusion current upon contact. The free mobile carriers will diffuse to the opposing region, were concentration is low. The diffusion of charge carriers leaves behind regions of stationary ions, causing a buildup of space charge in these regions. The space charge regions produce an electric field opposing the diffusion force, thereby, inducing drift of the minority carriers in the opposite direction of diffusion. At equilibrium, a balance between the carrier diffusion and carrier drift is reached, whereupon Eq. 2.4.13 and Eq. 2.4.14 are zero [40].

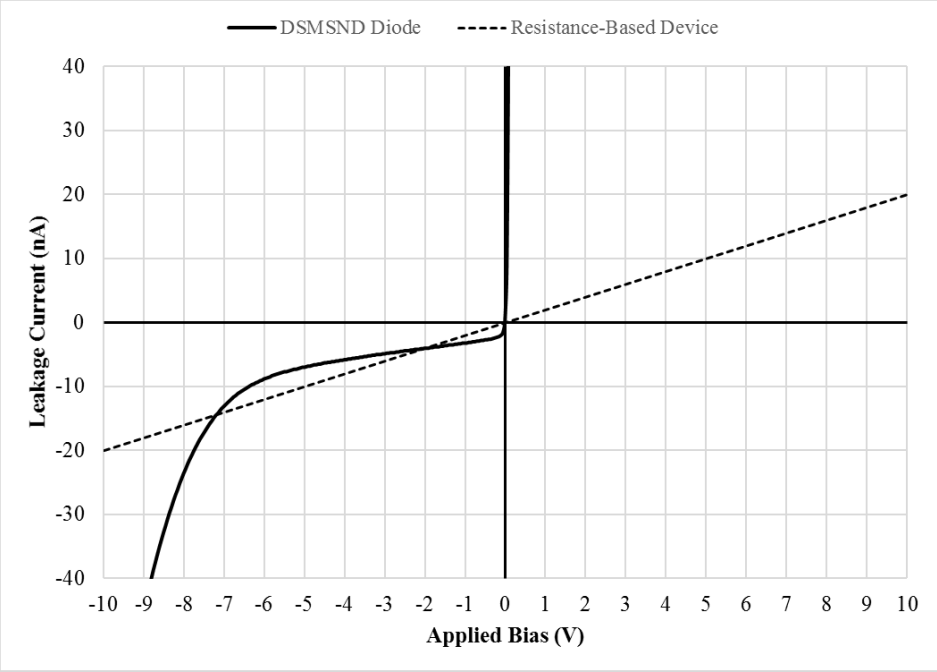

Fig. 2.4.6. Plotted is the current-voltage curve for a DS-MSND rectifying diode and a theoretical 1/R semiconductor detector. Although a 1/R semiconductor may have lower leakage current than a pn-junction diode, there are many benefits to applying a blocking contact to more common materials, such as Si, rather than working with high-cost, high-resistivity materials.

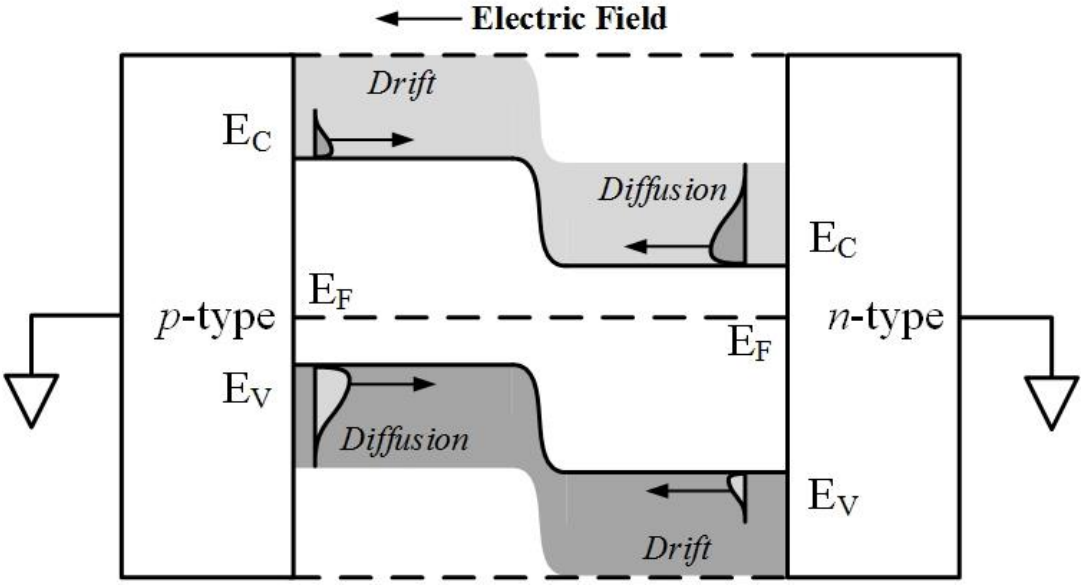

Fig. 2.4.7. Shown is a schematic of p- and n-type semiconductors being brought into contact with one another, forming a pn-junction. The high concentration of holes in the p-type material and electrons in the n-type material will cause carrier diffusion upon contact. The diffusion of carriers establishes space charge regions from the ionized impurities, thereby, producing an electric field. This electric field induces drift in the minority carriers, opposite to diffusion.

In the case of MSNDs and DS-MSNDs, the *pn*-junction contacts are formed during the contact diffusion steps of fabrication [44]. Rather than joining two semiconductor materials directly, a natively-doped target Si wafer is exposed to a secondary dopant source [40]. A Si wafer with a light *n*-type background dopant (often on the order of 10^{12} cm^{-3}) is loaded into a furnace and is exposed to a solid BN *p*-type source at a high temperature for a period of time. The BN source reacts with the process gasses to transport B material to the source of the wafer. The drive-in diffusion process forces B atoms to diffuse into the bulk material and occasionally displace an Si atom within the Si crystal lattice (with a final concentration of ~10^{16} cm^{-3}). The B atoms, and their missing valence electron, act as an acceptor impurity site within the lattice, thereby, locally reducing the Fermi level of the Si (Fig. 2.4.8). The newly formed *p*-type Si layer is in direct contact with the *n*-type bulk Si, thus forming a blocking contact. Further details regarding this type of process can be found elsewhere [40, 45].

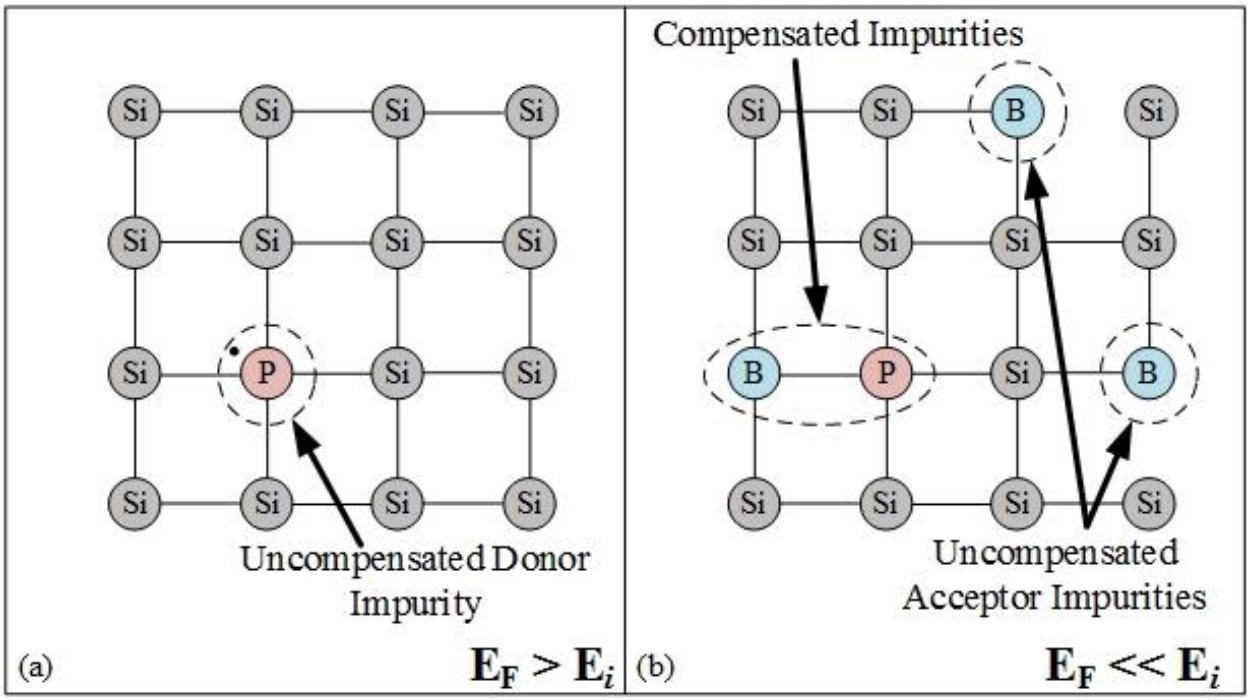

Fig. 2.4.8. Shown (a) is a representation of the crystal lattice of a lightly-doped n-type Si wafer. A low concentration of background P dopant serves to increase the Fermi level slightly from the intrinsic level. Following contact diffusion, Si atoms are displaced by acceptor-type B atoms, forcing the local Fermi level much lower, thereby, making the material p-type.

2.4.4 Depletion Region

The Fermi equilibrium condition that occurs when joining *p*-type and *n*-type semiconductors produces a region of space charge that is devoid of mobile charge carriers called the depletion region. The depletion region is comprised of the ionized, immobile, uncompensated impurity sites of the *p*-type and *n*-type doped regions of the junction. Poisson's equation dictates that a region of enclosed charge produces an electrostatic potential that is given by [40]:

$$\psi_p = -\frac{kT}{q} ln\left(\frac{N_A}{n_i}\right), \qquad \text{(Eq. 2.4.15)}$$

$$\psi_n = \frac{kT}{q} ln\left(\frac{N_D}{n_i}\right), \qquad \text{(Eq. 2.4.16)}$$

for the *p*-type and *n*-type regions, respectively. N_D and N_A are the carrier concentrations within the region, as shown in Fig. 3.4.1(b). Summing these two electrostatic potentials provides a useful potential, the built-in potential, given by:

$$V_{bi} = \psi_n - \psi_p = \frac{kT}{q} ln\left(\frac{N_D N_A}{{n_i}^2}\right), \qquad \text{(Eq. 2.4.17)}$$

and represents the net electrical potential between the two materials of the *pn*-junction with zero applied bias.

As previously discussed, an important characteristic for semiconductor detectors is the ability to drift charge excited by an interacting particle to produce an electrical pulse. A continually changing electrical potential produces an electric field that is capable of drifting said charge. A location-dependent electric field is established within the depletion region based on the space charge distribution [39]. The magnitude of the electric field is governed by Poisson's equation and is defined as:

$$E(x) = -\frac{d\psi_p}{dx} = -\frac{qN_A(x + x_p)}{\varepsilon_s}, \qquad -x_p \leq x < 0, \qquad \text{(Eq. 2.4.18)}$$

and

$$E(x) = -E_m + \frac{qN_D x}{\varepsilon_s} = -\frac{qN_D(x - x_n)}{\varepsilon_s}, \qquad 0 < x \leq x_n, \qquad \text{(Eq. 2.4.19)}$$

where the values for x_p and x_n are the distances into the semiconductors that the depletion region extends into the respective semiconductors. The most important characteristic of the depletion region is that this is the only region in the semiconductor volume where an electric field exists. This is important for semiconductor radiation detectors as this is the only region wherein excited charge can be drifted and produce a measureable electrical pulse.

The case shown in Fig. 2.4.9 is representative of a scenario wherein two semiconductors with equal or nearly equal dopant concentrations are joined. However, a scenario more pertinent to DS-MSNDs is the case wherein one semiconductor has a much higher dopant concentration. Often, the background dopant level of a bulk semiconductor can vary (from 10^{12} -10^{15} cm^{-3}) [39]. The *pn*-junction formed during device fabrication can produce a region of impurity concentration

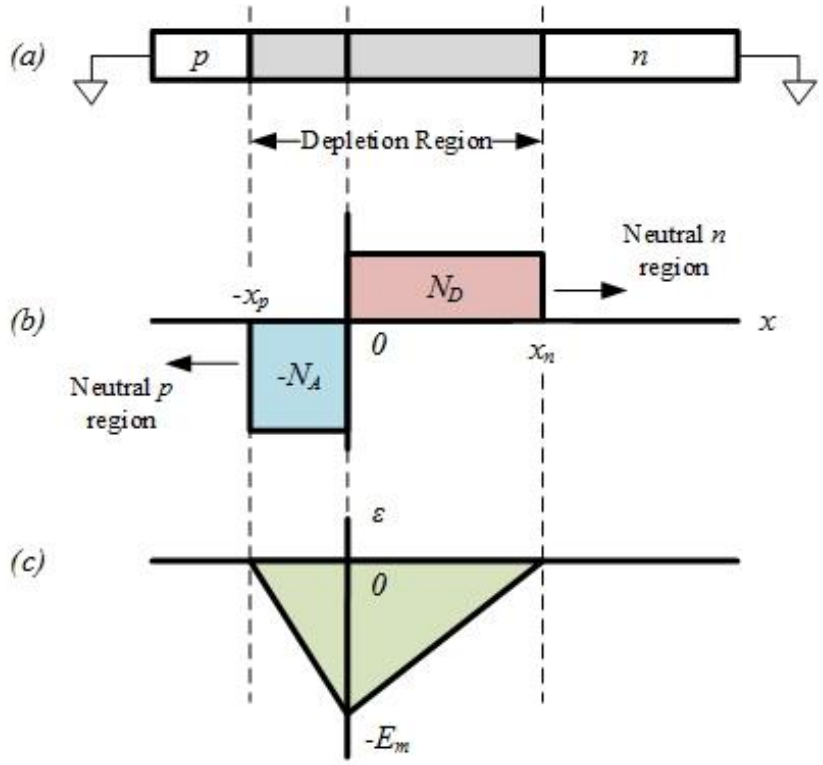

Fig. 2.4.9. Shown (a) is the junction between p-type and n-type semiconductors with no applied bias. In reaching the Fermi equilibrium condition, the depletion of the mobile charge carriers produces (b) space-charge regions of uncompensated impurity ions, whose summed electrical potential produces an (c) electric field.

of 10^{16} cm^{-3} or more. The joining of two such semiconductors forms an abrupt junction (Fig. 2.4.10) which has more desirable characteristics for use in radiation detectors [38]. This shallow, but highly-doped *p*-type contact allows for the depletion to reach much deeper into the bulk semiconductor, thereby, increasing the charge-sensitive semiconductor volume.

The total depth of the depletion region, *W*, is the sum of the depth into the respective semiconductors ($x_p + x_n$). However, for the case where N_A is much greater than N_D, such as the case in the abrupt junction, a majority of the depletion region reaches into the bulk of the semiconductor, rather into the diffused region. Therefore, the depletion depth approaches x_n, and can be related to the built-in potential by [39]:

$$W \cong x_n = \sqrt{\frac{2\varepsilon_s}{qN_D} V_{bi}}, \qquad \text{(Eq. 2.4.20)}$$

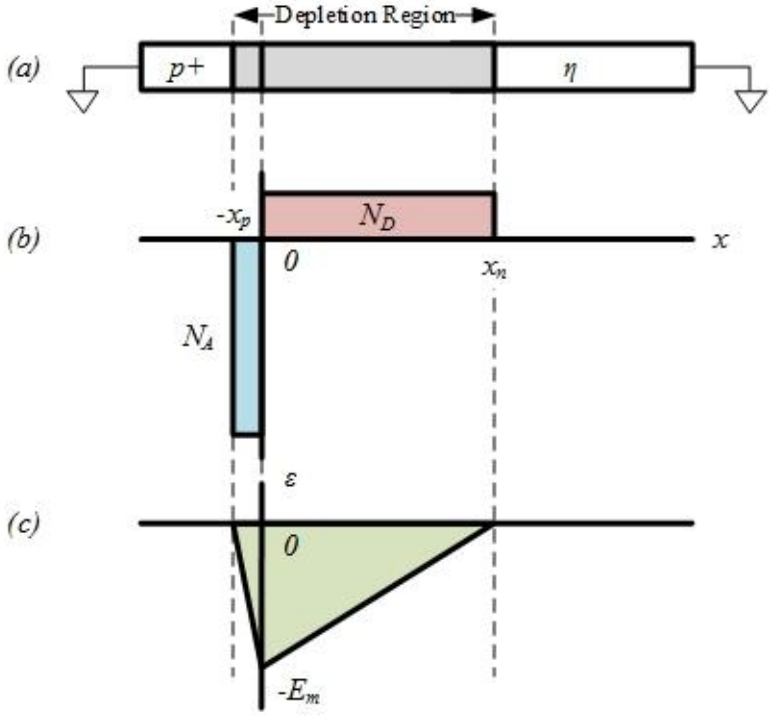

Fig. 2.4.10. Depicted is an (a) abrupt junction, commonly used in semiconductor radiation detectors due to the increased electric field strength. The (b) high-concentration p^+-type contact allows for greater depletion depths within the lightly η-type doped bulk semiconductor. (c) Greater electric fields are possible as well for increased detector performance.

where V_{bi} is the built-in potential from electrochemical potential between the heavily-doped *p*-type regions of the contact layers, and the *n*-type background-doped bulk material. An external bias applied across the device will modify the depletion depth by modifying the carrier drift component of the Fermi equilibrium. An applied reverse bias will widen the depletion region whereas a forward bias will narrow the region, and is calculated by [39]:

$$W \cong \sqrt{\frac{2\varepsilon_s}{qN_D}(V_{bi} - V)}, \qquad \text{Eq. 2.4.21}$$

where V is positive for a forward bias and negative for a reverse bias. Breakdown of the junction occurs when a forward bias equal to V_{bi} is applied, thereby, dropping the depletion depth to zero. Breakdown of the device generally occurs when the depletion depth reaches a conductive region, generally represented by ohmic metal contacts [39].

2.5 Solid-State Thermal Neutron Detectors

Many common detector systems utilize a gas-filled chamber operated in the ionization or proportional region [24]. For some systems, the gas acts as both the neutron conversion material and the proportional gas, such as the case with ^{3}He and $^{10}BF_3$ detectors [26]. For others, a secondary material is placed inside the gas chamber to convert incident neutrons into measureable reaction products, as with ^{10}B-coated or ^{6}Li-foil counters [46-49]. Most gas-filled detectors have extremely low gamma-ray-detection efficiencies, a desirable trait for neutron counters. Other systems utilize coated or doped scintillators wherein neutron interactions with neutron conversion material works to induce scintillation that can be read with a photomultiplier tube (PMT) or photodiode (PD) [50, 51]. Scaling these systems down to portable, low-power, mass-producible devices is often difficult. Large-volume gas-filled detectors are necessary to fully capture the energy of reaction products resulting from a thermal neutron capture. However, smaller gas-filled detectors are available. To maintain absorption efficiencies, the pressure of the gas must be increased to counter the reduced volume. The consequences of increased gas pressure are generally reduced energy resolution of pulses produced from the detector, increased operating voltages, and reduced sensitivity. Taking the concept to the extreme, reducing a gas-filled detector to the size of

a wearable badge requires impractical gas pressures and consequently poor detection efficiency.

Scintillator-based neutron detector systems can be made quite small, but the limiting factor then becomes the design of the photon collection system, be it a PMT or PD. The photodiode and silicon-photomultiplier (SiPM) are the only systems presently available that can be made small enough and cheaply enough to be used for personal-dosimetry applications [52, 53]. Scintillation-based neutron detectors are often sensitive to gamma-ray background, thus pulse-shape discrimination must be implemented to separate out neutron signal from gamma-ray background [50, 51]. The alternative to these technologies are semiconductor-based thermal neutron counters.

Thin-film-coated solid-state semiconductor neutron detector diodes were developed as a means of filling the need for smaller, rugged, low-cost neutron detectors, shown in Fig. 2.5.1 [8, 54, 55]. A common semiconductor diode, often a *pn*-junction Si diode, is coated with a thin film of neutron conversion material, such as ^{10}B or ^{6}LiF, to convert incident neutrons into charged-particle reaction products that could be measured. A neutron intersecting the conversion material could be absorbed in the ^{10}B or ^{6}Li coating, resulting in the generation of charged-particle reaction products. The energetic reaction products travel away from each other in opposite directions

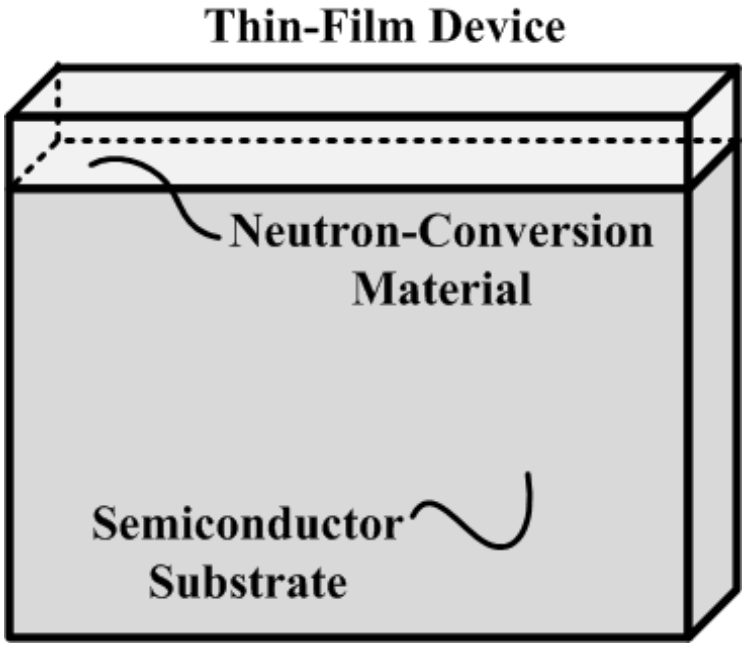

Fig. 2.5.1. Depicted is a simplified diagram of a thin-film-coated thermal neutron detector. A thin film of neutron converting material is applied to a semiconductor diode to convert neutrons into reaction products that can be counted by the diode.

where one of the reaction products may intersect the semiconductor depletion region. The reaction products would then transfer their residual kinetic energy into the depletion region, generating electron-hole pair charge carriers. Similar to the electron-ion pairs of a gas-filled counter, the electron-hole pairs are then drifted under an electric potential and measured by the counting electronics. If the reaction products deposited sufficient energy into the depletion region, the resulting signal can be above any gamma-ray or electronic noise level background present in the system and register as a neutron 'count'.

Geometric and material attenuation of the reaction products within the conversion film (along with the poor neutron absorption efficiency of the thin conversion material) limits detection efficiencies to no greater than 4-5% [55]. The coating thickness must be kept thin enough to allow the escape of the charged-particle reaction products into the diode volume, but still thick enough to absorb a sufficient portion of incident thermal neutrons. Furthermore, the neutron conversion material is often evaporated or sputtered onto the substrate, resulting in poor materials adhesion and leading to flaking and peeling of the conversion film [54]. However, the thin-film-coated semiconductor neutron detectors were easy to mass-produce using typical very-large-scale integration (VLSI) fabrication techniques and used common semiconductor materials with low sensitivity to gamma-ray background. Additionally, the devices were more compact than their gas-filled counterparts due to the diode's greater density and greater reaction-product stopping power. Thin-film-coated devices required little power for operation, often less than 5V, which benefits portable and/or long-term remote detector systems. Though the poor detection efficiency could be somewhat compensated with detector stacking, these devices have seen limited use in industry. There existed a need to develop a neutron detector system that combined the high detection efficiency of larger gas-filled and scintillator detectors with the low-power consumption and mass-producibility of the thin-film-coated devices was desired. This led to the advent of the microstructured semiconductor neutron detector (MSND).

The MSND, shown in Fig. 2.5.2, was suggested and later developed to meet all of the aforementioned goals [9, 12, 56-60]. MSNDs were produced with VLSI fabrication techniques in conjunction with microelectromechanical systems (MEMS) etching techniques. Microstructures were etched perpendicularly into a semiconductor diode using either wet-chemical or dry-etching

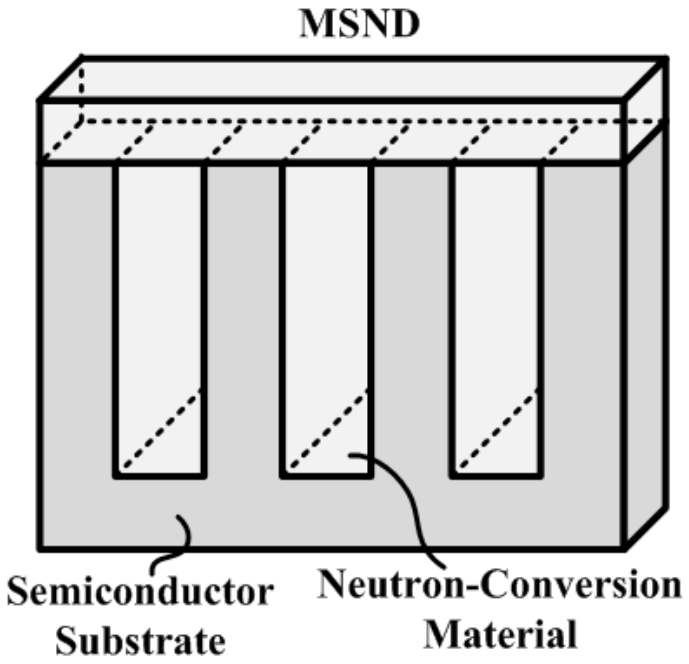

Fig. 2.5.2. Depicted is a microstructured semiconductor neutron detector (MSND) wherein backfilled trenches improve neutron detection efficiency over thin-film-coated counterparts with increased neutron absorption and charged-particle counting efficiency.

methods [61]. The perforations were then backfilled with the same neutron conversion material as is used with thin-film-coated devices. The additional neutron conversion material (on the order of 100's of microns compared to thin-film-coated devices with 10's of microns of thickness) greatly increased the likelihood of absorbing an incident thermal neutron, as shown in Fig. 1.1.3. Additionally, reaction products produced within the perforations had a much higher probability of being counted by the diode due to the greatly improved solid angle, also shown in Fig. 2.5.3. Combined, these factors lead to an order-of-magnitude increase in intrinsic thermal neutron detection efficiency over a thin-film-coated device to nearly 45% for some designs [12]. These devices were produced with great success over the following years, as their repeatability and ruggedness were continually improved. However, the devices could not achieve the comparable efficiencies realized with ^{3}He-based counters.

A major weakness of the MSND was the streaming of neutrons between the perforations without being absorbed within the conversion material. A neutron intersecting the detector on the semiconductor sidewalls could pass through the sensor undetected. These 'streaming paths' arise from the low neutron interaction cross-section of most semiconductor materials, such as Si ($\sigma_{Si} \approx$

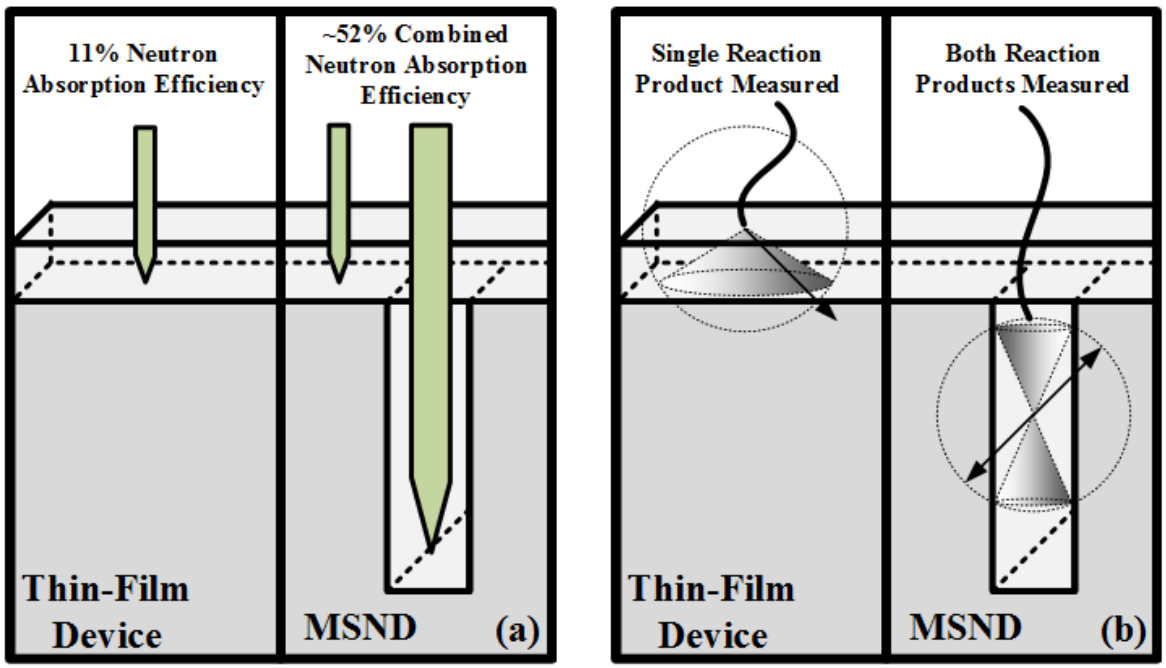

Fig. 2.5.3. Depicted (left) is a diagram of the increased neutron absorption efficiency from backfilling trenches with neutron converting material. Shown (right) is a sketch of the difference in solid angle of the reaction products produced in a thin film and within etched trenches.

0.17 b) [62]. To mitigate the streaming problem, the widths of the semiconductor fins can be reduced, thereby, limiting possible streaming paths. However, doing so reduces reaction-product energy deposition into the semiconductor detector, limiting the signal-to-noise ratio.

Efforts to eliminate neutron streaming were conducted by stacking two similar MSNDs and offsetting them such that any streaming paths in the first detector were eliminated by the second, as shown in Fig. 2.5.4 [17, 18, 63, 64]. Stacking two MSNDs was successful, and proved that the efficiency of a single MSND could be doubled. Unfortunately, properly stacking the two devices was problematic in that the MSNDs would be minutely misaligned, resulting in a non-opaque system. Additionally, if the detectors were not electrically identical, a smearing effect of their output signal would arise, leading to difficulties in setting the lower-level discriminator (LLD) of the system; a small change in their LLD would result in a large change in their detection efficiency. Both effects were detrimental to the commercial potential of the technology. The need for a single-chip design of the double-stacked MSND arose, and the dual-sided microstructured semiconductor neutron detectors (DS-MSNDs) were therefore developed and introduced in this work.

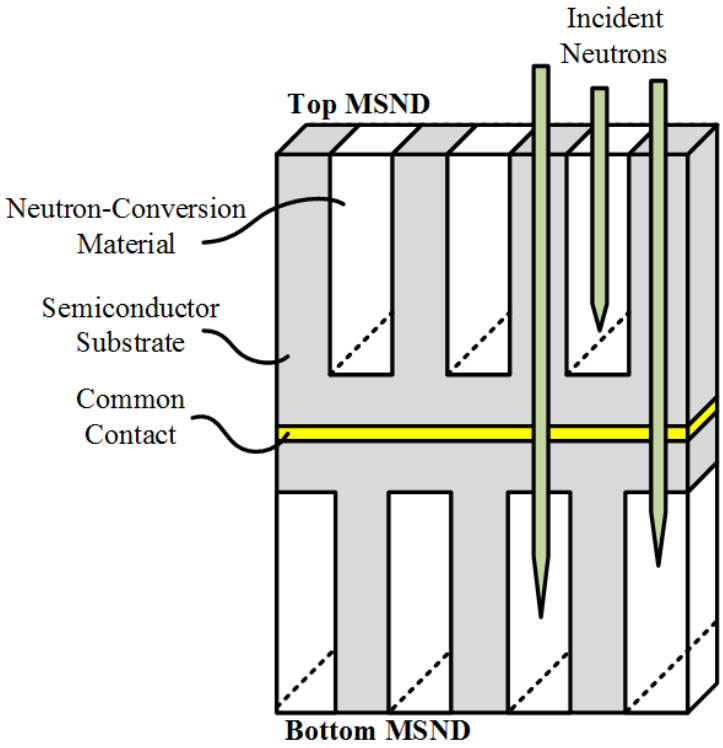

Fig. 2.5.4. Depicted is a double-stacked, off-set pair of MSNDs. Neutrons streaming through the first device can be counted by the second device, effectively doubling their detection efficiency.

The DS-MSND was designed to combine the ease of manufacture of a single-sided, single-die MSND, and the high intrinsic thermal neutron detection efficiency of the double-stacked MSND. DS-MSNDs offer all of the benefits that the MSND holds over their thin-film-coated counterparts while providing a device that is nearly opaque to normally-incident thermal neutrons, all while solving the issue with alignment of the top and bottom trenches. The DS-MSNDs use the same trench structure as is found in the MSNDs but trenches are etched into both the top and the bottom of the device simultaneously, effectively mimicking a double-stacked MSND (Fig. 2.5.5). Misalignment is greatly reduced as alignment of the microstructures is done at the photolithographic stage, as advancements in dual-side optical alignment have rendered the technique straight forward. Signal matching is also no longer an issue as the DS-MSND is a single, larger device. The development of the DS-MSND represents what is likely the final iteration of the microstructured semiconductor neutron detector technology. In the present work, design considerations of the DS-MSND will be described, and prototype sensors achieving greater than 54% intrinsic thermal neutron detection efficiency will be presented and discussed.

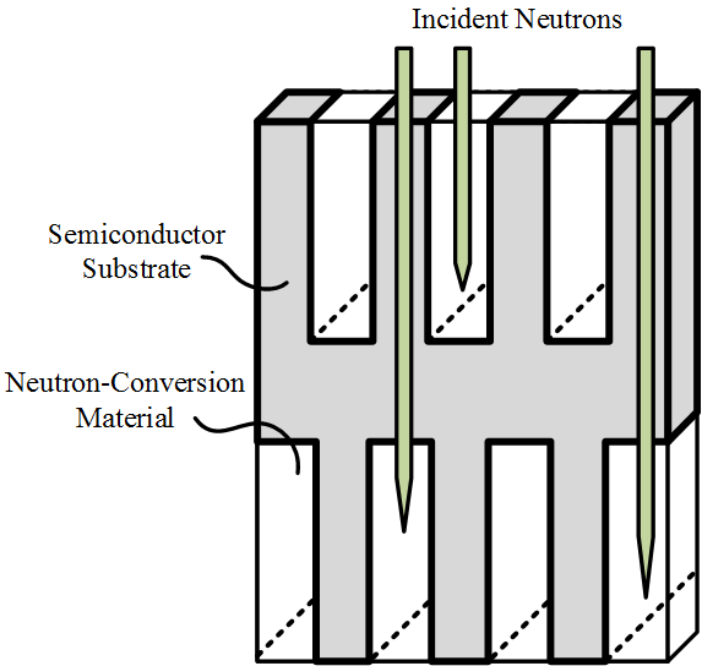

Fig. 2.5.5. Depicted is a dual-sided microstructured semiconductor neutron detector (DS-MSND). Similar to a double-stacked MSND, neutron streaming is unlikely. Trenches are easily aligned and off-set by photolithographic printing.

Chapter 3 - *Design of Dual-sided Microstructured Semiconductor Neutron Detectors (DS-MSNDs)*

The development of the dual-sided microstructured semiconductor neutron detector (DS-MSND) is a significant advancement in solid-state thermal neutron detection technologies. Previously, the highest intrinsic thermal neutron detection efficiency achievable by a single-sided MSND was less than 45%. This efficiency is higher than some other alternative technologies (such as BF_3 gas-filled proportional counters), it is much less than that of ^{3}He proportional counters and newer ^{6}Li- and ^{10}B based scintillators. The DS-MSND is capable of detection efficiencies matching expensive and relatively large ^{3}He counters with a single, 1-mm thick chip that can be produced for under ten U.S. dollars. Outlined in the following chapter is the development and modeling of the DS-MSND and its variants.

3.1 MCNP Modeling of DS-MSND

Simulation modeling of the DS-MSNDs is possible through the use of Monte Carlo Neutral Particle (MCNP6) software, which combines the neutral particle transport of MCNP5 and the charged-particle tracking and energy deposition of MCNPX [65]. The software utilizes Monte Carlo methods to find solutions to radiation transport problems [66]. Prior to MCNP6, custom scripts were developed to model detector performance [12, 21, 22]. These scripts were limited to single- or double-stacked MSND systems and only for specialized cases wherein neutrons did not interact with the surrounding world. MCNP6 allows for more sophisticated models to be developed than previous editions, ranging from a single DS-MSND sensor, to an entire detector instrument populated with hundreds of DS-MSNDs in a room with various real-life geometries. Modeling the DS-MSND sensors (and instruments populated from these sensors) is relatively easy, compared to previous modeling techniques. An input card (an example of which can be found in Appendix B) is fed into MCNP6 that defines all problem geometries and physics necessary for finding the solution. A description of the general process for radiation transport is described here.

3.1.1. Monte Carlo Particle Transport

Monte Carlo modeling of the transport of neutrally-charged particles relies on the Law of Large Numbers in order to converge on a correct answer [66]. The stochastic nature of radiation emission and transport dictates that particle interactions are probabilistic. Random sampling of particle emission, transport, and interactions with matter can be used to predict these interactions to develop accurate predictions of detector performance. Generally, these predictions are determined by performing many histories wherein a particle is first born, randomly given a direction of travel, and transported until it reaches a new body or interacts in some medium. Upon interacting within a medium, the type of interaction can also be sampled. This section will detail the general method for modeling the transport of neutrons into a detector, the testing for interactions, and then the testing and tracking of the charged-particle reaction products. For the purposes of this discussion, a uniform, collimated disk source is considered (Fig. 3.1.1) that that is analogous to a collimated beam of neutrons, such as a beam port of the TRIGA Mk II research reactor used to determine intrinsic thermal neutron detection efficiencies [67].

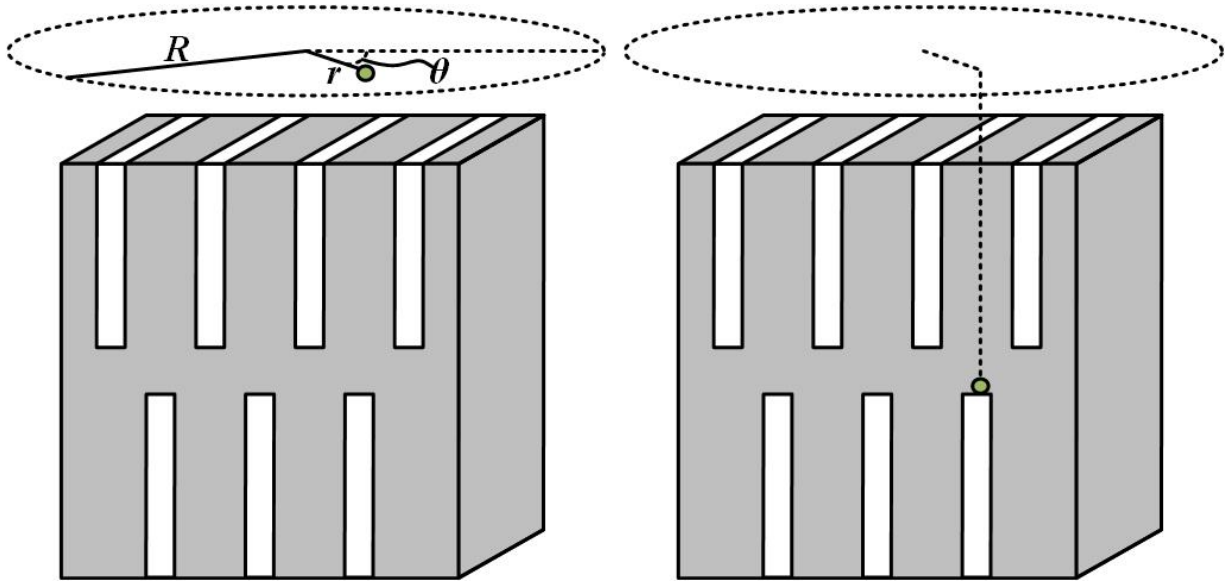

Fig. 3.1.1. (left) A neutron is randomly assigned a starting location on the surface of a disk source defined by radius R. The starting radial position is sampled uniformly between 0 and R while θ is sampled between 0 and 2π. (right) The neutron is then transported to the next important surface, where an interaction can possibly occur.

The modeling of neutron transport begins with the birth of the neutron, by pseudo-randomly selecting a point on the source (Fig. 3.1.1). The point is chosen by randomly selecting values r from a uniform distribution over the radius of the source, R, and θ in the range of 0 to 2π. Often, the neutron is assigned a direction of travel that is normal to the surface of the disk (as is the case for any collimated source), also shown in Fig. 3.1.1. Generally, over short distances air is a poor attenuator of neutrons ($\Sigma_{\text{Total}} \approx 5.2 \times 10^{-4}$ cm^{-1} for 0.0254-eV neutrons), thus the disk is often assumed to be in contact with the surface of the device being investigated. Once born, the neutron is transported through the material it intersects. MCNP6 then samples its transport through the material, testing for an interaction [66]. The test for an interaction is modeled as exponential attenuation from Eq. 2.3.1, using the total interaction cross-section. A pseudo-random number, ρ, is selected and used to determine if the neutron interacts in the medium [66]:

$$l = -\frac{1}{\Sigma} ln(\rho), \qquad \text{Eq. 3.1.1}$$

where l is the randomly-calculated distance of travel through the material. Σ is total macroscopic neutron interaction cross-section of the material, and ρ is a pseudo random number sampled uniformly between 0 and 1. This function is derived from Eq. 2.3.1, where l is analogous of x, and ρ is analogous of the ratio of the initial intensity to the intensity at x. Should l be less than the thickness of the medium, then an 'interaction' event occurs. Often, one interaction type dominates the total interaction cross-section. Thus, Σ is approximated as Σ_a for absorbing materials (such as ^{10}B or ^{6}Li) or Σ_s for scattering materials (such as C or H).

If the neutron is absorbed in the conversion material, then the appropriate charged-particle reaction products are born at the point of absorption. They are assigned the proper kinetic energy and transported in opposite directions (Fig. 4.1.2). The sampling of the charged particles can be approximated as a zero-sum-momentum problem due to the low kinetic energy of the incident neutron, thus the direction of the emitted particles can also be sampled uniformly:

$$\theta = -1 + 2\rho_i, \qquad \text{Eq. 3.1.2}$$

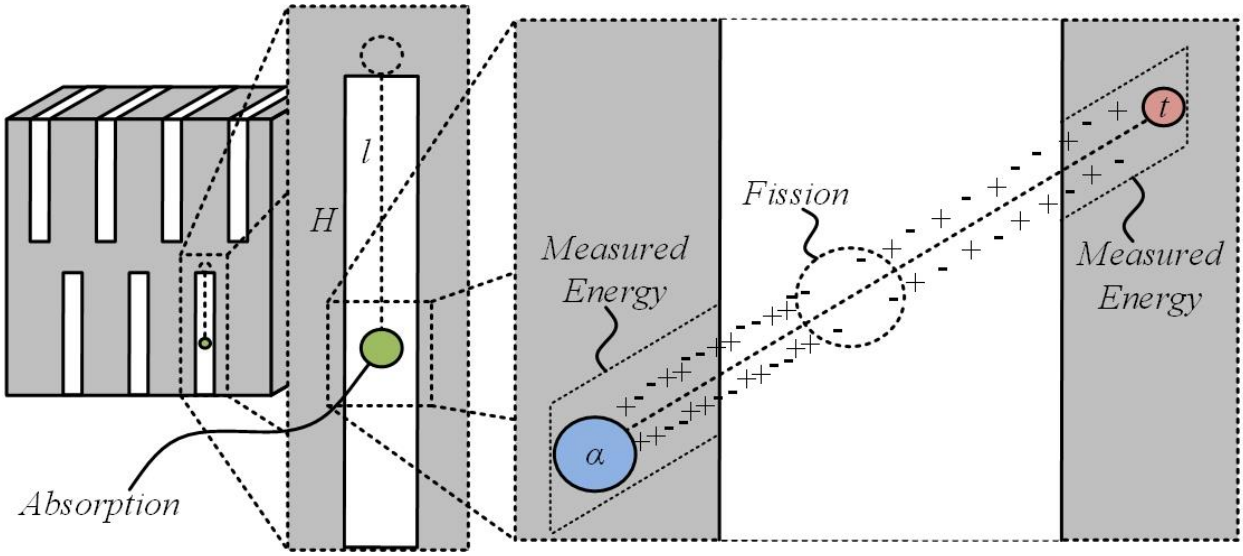

Fig. 3.1.2. Shown (left) is a neutron intersecting the neutron converting material in the bottom side of the DS-MSND. Its path length, l, is determined as sampled from Eq. 4.1.1, shown (middle), and if found to be less than H, a pair of charged-particle reaction products are produced from the origin of the neutron capture. The charged particles are tracked until their energy is depleted. Energy deposited in the semiconductor volume is assumed to be counted and is tallied.

$$\psi = 2\pi\rho_j, \qquad \text{Eq. 3.1.3}$$

where θ and ψ dictate the direction of the first charged particle (as in Fig. 3.1.3), and ρ_i and ρ_j are two pseudo random numbers selected from a uniform distribution. The second particle from the reaction is given a direction opposite of the first particle to conserve momentum.

As the particles are transported through the medium, Coulombic energy deposition is tracked for the duration of the particles' travel. Energy reduced from the particle in the conversion material is deducted and ignored. Energy deposited into detection volume (often, the Si material) is summed for that history and binned into the appropriate energy bin, not unlike a common MCA during real-world measurements, as shown in Fig. 3.1.4. All energy deposited into the detection volume are tallied without considering charge-carrier loss through ballistic deficit (i.e. recombination, insufficient charge integration time, etc.), charged-particle straggling effects, or Gaussian smoothing of the spectral features and is therefore considered to be the optimized result. All tallies recorded that exceed some user-defined lower-level discriminator (LLD) value are summed and reported as the intrinsic thermal neutron detection efficiency [12, 67].

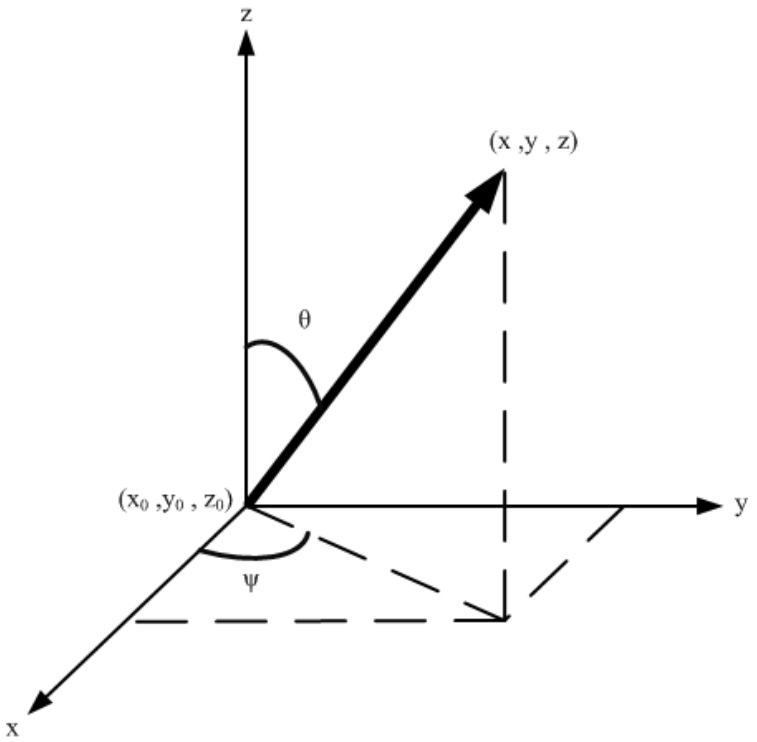

Fig. 3.1.3. Shown is the directional coordinate system used to direct the motion of the charged-particle reaction products in the specialized Monte Carlo code and MCPN6 scripts. Generally, these values are sampled uniformly in all directions due to the relatively-small momentum contribution of thermal neutrons.

3.1.2. Device Geometry Considerations

There are three primary geometric dimensions that are of importance for any given MSND-type solid-state neutron detector: 1) perforation depth, 2) perforation width, and 3) width of the remaining bulk semiconductor (i.e. the unit cell area minus the perforation dimensions). The effect that each of these dimensions has on the device performance can be manipulated to optimize the device performance [12].

Trench depth has two major contributions to overall device performance, these being neutron absorption efficiency, and charge-carrier integration time. As the trench depth is increased, the neutron absorption efficiency also increases. However, because the absorption probability of an incident neutron follows an exponential dependence, the increase in absorption diminishes with depth. Furthermore, as charge-collection time is dependent on fully collecting excited electron-hole pairs, the linear increase in distance traveled by the charge carriers leads to an increased drift time, thereby, increasing the detector dead time.

Trench width and width of the semiconductor side-walls also play an important role on the overall device performance. Increasing the width of the conversion-material backfilled trenches increases the probability of absorbing normally-incident neutrons. However, this causes two major issues: increased distance of travel for the resulting charged-particle reaction products before they can reach the semiconductor material, and reduced charge-sensitive volume for a given unit cell. Fig. 3.1.4 shows the effect of increasing the trench width for a unit cell 40-µm wide. The resulting charged-particle reaction products must travel further through the conversion material prior to intersecting the charge-sensitive semiconductor. The increased distance through the conversion material continuously reduces the energy of the reaction products available for deposition within the semiconductor fins [55, 68]. The result is a reduction in the magnitude of a majority of the pulses output by a device, thereby, downshifting the overall pulse-height spectrum along the energy domain. These factors must all be considered simultaneously in order to both optimize detector performance (as discussed in the remainder of Chapter 3) as well as maintain good producibility (Chapter 4).

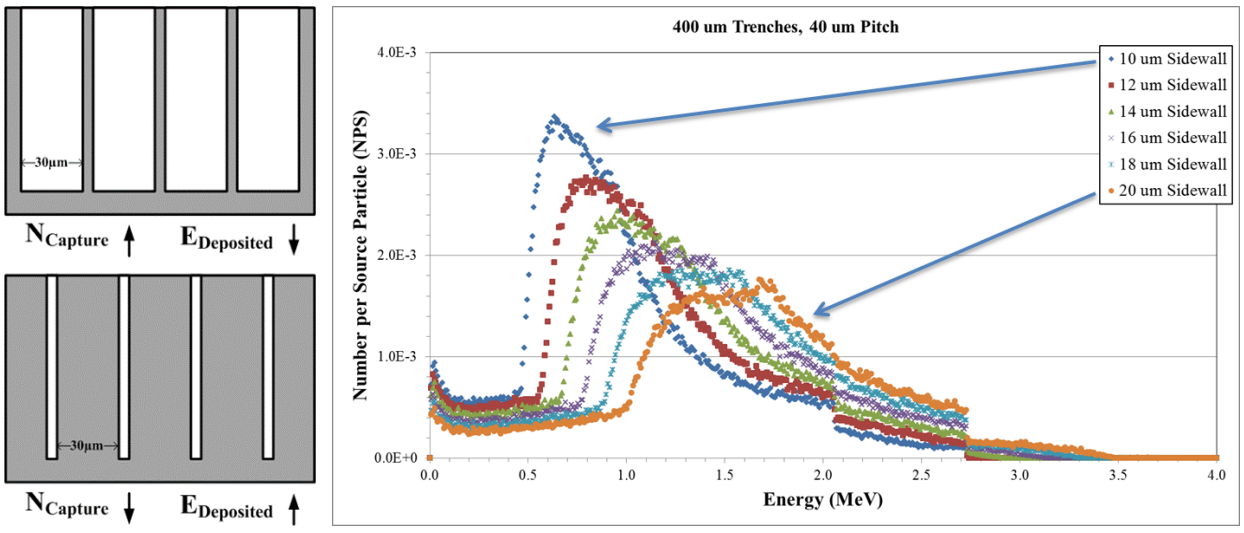

Fig. 3.1.4. Shown (left) is a schematic of the effect of etching wider trenches in MSND-type devices. Increased trench width greatly increases the probability of neutron capture at the cost of reduced semiconductor absorber, thereby, reducing energy deposition from reaction products in the semiconductor regions. Plotted (right) is the effect of reduced energy deposition (but increased neutron capture) on the pulse-height spectrum.

3.1.3. The DS-MSND Model

The design of a DS-MSND begins with modeling and optimization of detector performance. To determine the possible intrinsic thermal neutron detection efficiency for a DS-MSND, features such as trench depth, width, and unit-cell width must be varied and modeled as defined in Fig. 3.1.5. A collimated beam source of thermal neutrons with a circular aperture was used to meet the accepted standard for efficiency determination [67]. At the onset of the problem, a neutron is born at a random xy-coordinate on the surface of the DS-MSND. The origin of the neutron is chosen by sampling a point on the aperture by first choosing a point, (θ, r) from the origin, on the disk as shown in Fig. 3.1.1. Neutrons born on the surface of the Si fins had a high likelihood of streaming through the material, without interaction, to the backside trenches where an absorption is likely. The trench and fin dimensions were varied using a custom Python script (Appendix B) that iterated through unit-cell widths, trench widths and depths, and alternated absorption materials. This process was repeated for circular hole, circular pillar, and straight trench geometry types. Intrinsic thermal neutron detection efficiency tables were constructed using MCNP6 and can be found in Appendix C. An excerpt can be found in Table 3.1.1.

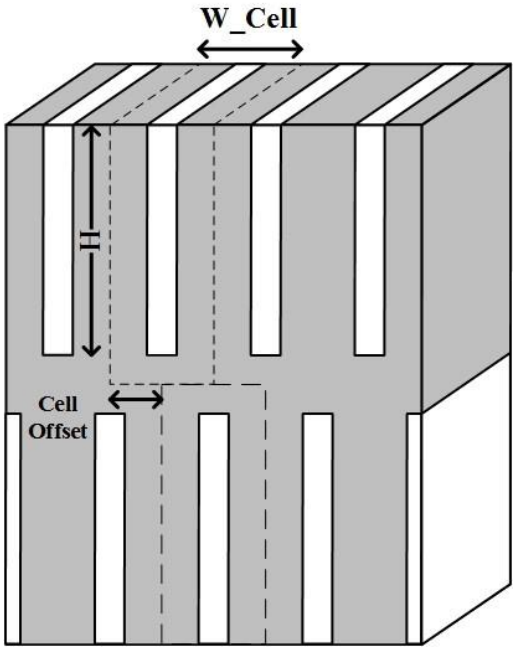

Fig. 3.1.5. Shown is a diagram of a DS-MSND. The trench depth, H, the unit-cell width, W_Cell, and unit-cell offset were defined by the user via the MCNP6 input card. Other geometries were considered, such as circular pillars, circular holes, in addition to the straight trenches.

Table 3.1.1. MCNP6 thermal neutron detection efficiency results for a 1-mm thick DS-MSND. Additional solutions, including varied trench depths and alternate trench geometries can be found in Appendix B.

Off-Set Dual-Sided MSND, Straight Trench, 6-LiF					
T/W_Cell	***Cell width W_Cell (um)***				
	20	**40**	**60**	**80**	**100**
	Trench depth H = 350 um				
0.10	16.7%	16.2%	15.7%	15.1%	14.5%
0.20	32.2%	30.1%	28.1%	26.1%	24.1%
0.30	46.6%	42.0%	37.6%	33.1%	28.8%
0.40	59.9%	52.0%	44.1%	36.4%	29.5%
0.50	72.3%	59.9%	47.8%	36.9%	30.0%
0.60	70.8%	54.8%	39.1%	28.7%	22.4%
0.70	70.2%	51.3%	34.1%	24.4%	18.9%
0.80	61.3%	47.5%	30.5%	22.1%	17.8%
0.90	31.4%	32.3%	28.0%	21.5%	17.5%

This method for determining the intrinsic thermal neutron detection efficiency is computationally heavy. Transport of neutral particles (such as neutrons and gamma rays) is simple and can be performed quickly by modern CPUs. Furthermore, methods exist for reducing the number of histories necessary to achieve good certainty of the solution [66]. However, the generation and transport of the charged-particle reaction products is more time consuming. The reaction products do not interact probabilistically with matter but rather continuously through Coulombic-force interactions [24]. The rate of energy deposition in the medium by the charged-particle is not constant, but rather is dependent on many factors, most notably of the particle's own velocity. As a particle traverses a material, its remaining energy must be recalculated through integration over its path of travel [68, 69]. This calculation leads to longer simulation times per particle history, resulting in problems that can take hours to solve with good statistical accuracy; the aforementioned variance reduction techniques cannot be applied.

A method for approximating the detection efficiency was developed to bypass the need for transporting the charged-particle reaction products [31]. This approximate-model method for device simulation uses a cell-averaged flux modifier tally that does not involve the generation or tracking of the reaction products. Instead, the average flux within the backfilled-trench cells is calculated and a tally modifier is applied. The modifier is dependent on the volume of the cell. Each approximate model must be recalibrated upon changing the trench dimensions or neutron

energy. The approximation model allows for problems to be solved in a small fraction of the time of the charged-particle tracking method.

The greatly reduced computing time permits scripts to be developed that produce large amounts of batch-processed information with good accuracy, as shown in Fig. 3.1.6. Here, two batches of simulations were performed to compare the charged-particle tracking method to the approximation-model method. The normally-incident beam of collimated neutrons was rotated about the front face of the detector in 5-degree increments and the intrinsic thermal neutron detection efficiency was reported. Both models were in good agreement with one another. The charged-particle tracking model required an average of approximately 32 minutes per iteration, while the approximation-model required only 20 seconds. This is largely beneficial for large-scale batch-processed models or complex models of populated instruments, as will be further discussed in Chapter 4.4 of this work.

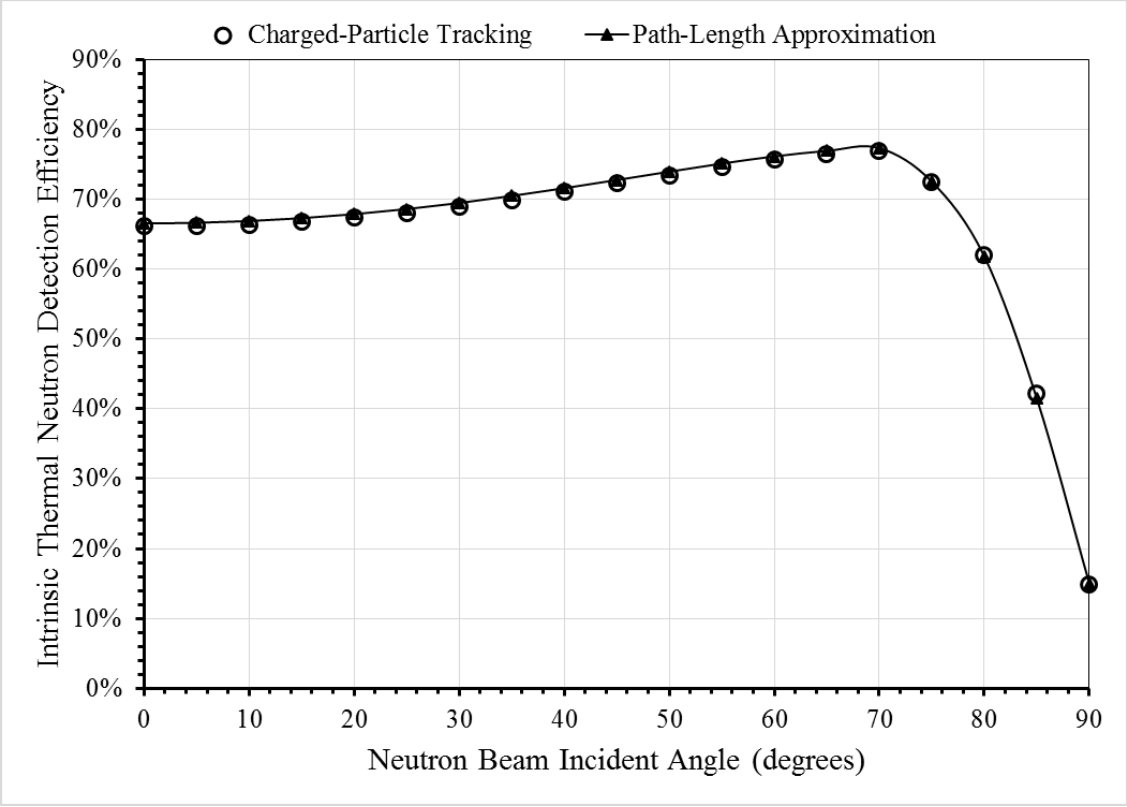

Fig. 3.1.6. Plotted are two MCNP6 models of the same DS-MSND. One model tracks charged-particle reaction products and their energy deposition and the other uses a neutron path-length modifier approximation. Each are irradiated with a collimated beam of 0.0254 eV neutrons with an incident angle varying from 0° to 90° to normal of the detector face.

3.2 Modeling of Charge-Carrier Transport

The aforementioned MCNP models and results can compensate for a non-zero lower-level discriminator value to better predict real-world detection efficiencies. MCNP cannot compensate for imperfect charge transport within the semiconductor. In a real-world device, excited electron-hole pairs are drifted towards the contacts by the electric field established by the built-in potential or applied bias. However, charge-carrier recombination or trapping can occur that consequently reduces the amount of charge that reaches the electrical contacts, thereby, reducing the electrical signal measured by the counting electronics. Furthermore, as will be presented in Chapter 6, ballistic deficit occurs when the amplifier integration time is shorter than the time necessary to fully drift all excited charge to the contacts. This cutting-off of the integration period stops the formation of the pulse for that event, thereby, limiting its amplitude. The results of this effect are shown in Fig. 3.2.1 which compares a real-world pulse-height spectrum to the idealized MCNP pulse-height spectrum.

Models can be adjusted to account for this ballistic deficit such that more accurate predictions can be made regarding the performance of MSND-type devices. Specialized MCNP models were developed to approximate the ballistic deficit effect by horizontally segmenting the tally regions of the MSND and considering the charge collection efficiency of each segment separately (Fig. 3.2.2). Here, many segments were formed determine the probability of reaction product interaction and energy deposition within the fins at each segment. A maximum ballistic deficit can be assigned to the top section, wherein the pulse height is reduced by that fraction and re-added to the overall tally. The effect of this correction is shown in Fig. 3.2.3 wherein a maximum ballistic deficit of 20% was assumed. Fig. 3.2.4 shows the overall effect that the ballistic deficit can have on the intrinsic thermal neutron detection efficiency. Although ballistic deficit will be addressed in Chapter 6, a value of 20% was chosen based on experimental measurements. The results of the model appear to match well to the effect shown in Fig. 3.2.1.

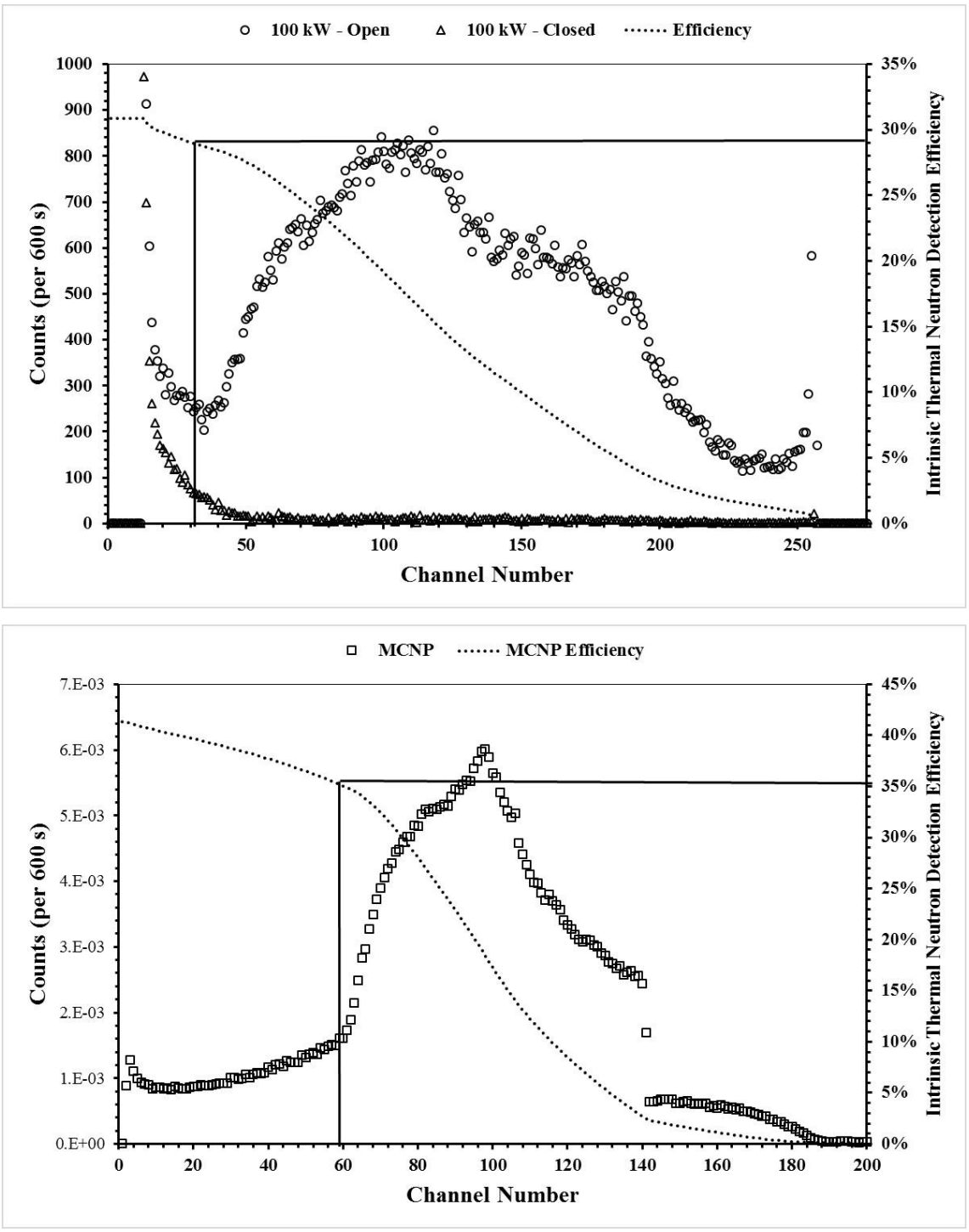

Fig. 3.2.1. Shown (top) is a measured charged-particle reaction product spectrum collected from a DS-MSND compared to a (bottom) simulated reaction product spectrum produced from MCNP6. Smearing effects and incomplete induced-charge collection reduced the resolution of the features in the measured spectrum and is not accounted for in the MCNP6 spectrum.

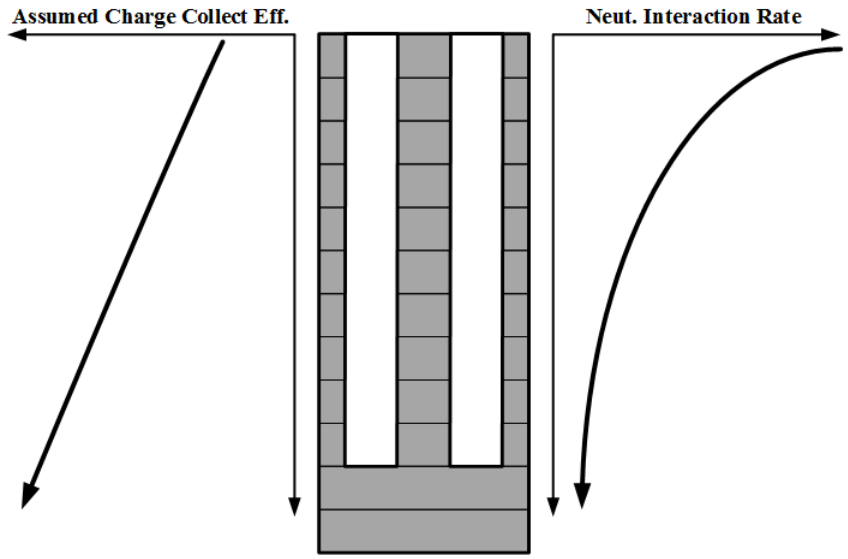

Fig. 3.2.2. Shown is a cross-section of two unit cells of an MSND wherein the tally volume has been segmented into vertical segments. Energy deposition into each segment was tallied separately, thereby, allowing for post-processing to model ballistic deficit. The neutron interaction rate (and thus rate of reaction-product interaction) reduces exponentially down the trench, while the charge collection efficiency is assumed to linearly increase in lower sections of the diode.

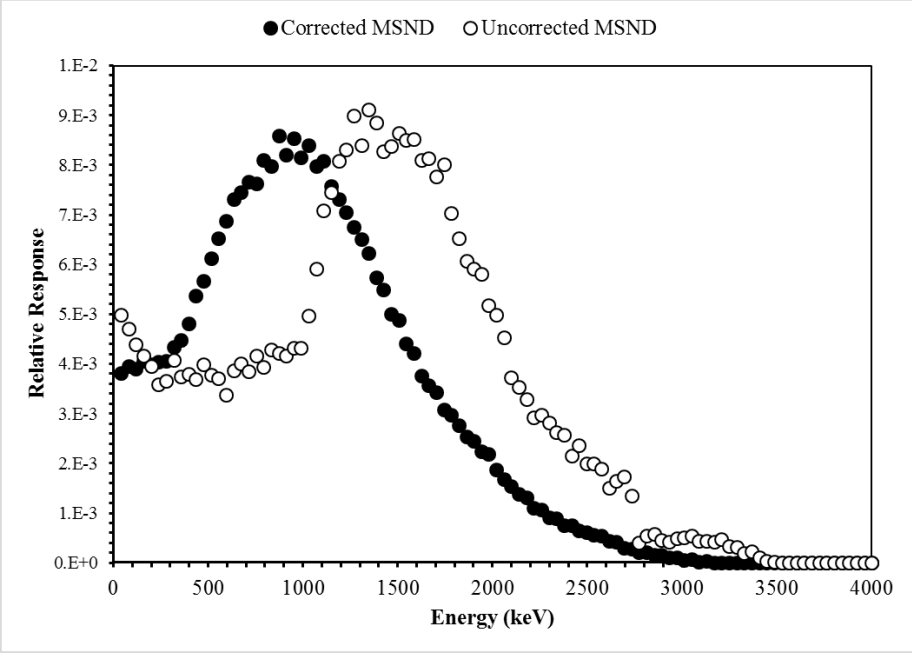

Fig. 3.2.3. Plotted are the simulated pulse-height spectra for two MSND cases where the 'Corrected MSND' represents the model that accounts for ballistic deficit and the 'Uncorrected MSND' does not account for ballistic deficit.

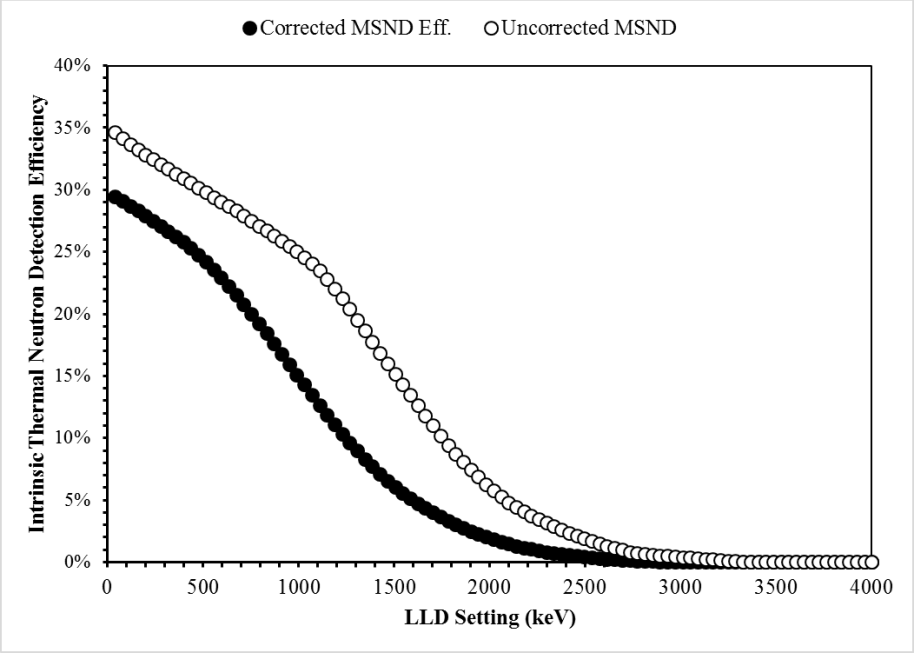

Fig. 3.2.4. Plotted are the simulated intrinsic thermal neutron detection efficiency for the ballistic-deficit corrected MSND model and the uncorrected model vs. LLD setting. Note the reduced efficiency that closely resembles real-world measurements.

3.3 DS-MSND Variants

There are numerous geometries that have been considered in the fabrication of single-sided microstructured semiconductor neutron detectors [12]. These varied geometries each have their benefits and drawbacks. Specifically, some geometries are simple to fabricate using chemical-wet etching while others must be fabricated using dry-etching techniques [61]. Further, some geometries yield greater charged-particle reaction product counting efficiency, while others benefit from greater neutron absorption efficiency [12]. Dual-sided MSNDs (DS-MSNDs) similarly have numerous possible geometric configurations, each having their own characteristics.

Presented in the following sections are different sample geometries that are possible for DS-MSNDs, along with some initial findings for expected device performance. Three basic designs are investigated here: (1) a lateral matrix of straight, parallel trenches (the "trench design"), (2) a square matrix of cylindrical hole perforations (the "hole design"), and (3) a square matrix of cylindrical pillars that remain after etching the bulk semiconductor material (the "pillar design"). An alternative method of producing a DS-MSND is to have the front-side pattern aligned to an inverse image of the front-side pattern. Three basic designs are investigated for this inverse opaque

design: are investigated here: (1) a lateral matrix of straight, parallel trenches (the "trench design"), (2) a square matrix of circular hole perforations on the front-side (the "hole design") and circular substrate pillars on the back-side, and (3) a square matrix of circular pillars on the front-side (the "pillar design") with back-side circular-hole pattern.

3.3.1. Opposing Pattern Straight Trenches

Most MSNDs and DS-MSNDs that are presently fabricated have the straight-trench pattern, similar to those shown in Fig. 3.3.1 [15, 20]. The pattern is simple to manufacture using common wet-etching techniques and allows for easy junction doping for good diode characteristics. The pattern also allows for simple formation of opaque DS-MSNDs as the pattern can be made to completely overlap itself on the opposing face. Reaction products generated within the trenches have a good probability of depositing energy into the substrate, provided that the width of the trenches does not exceed that of the summed ranges of the Li and α ions, as depicted in Fig. 3.3.1. Here, the reaction products from the $^{10}B(n,\alpha)^{7}Li$ or $^{6}Li(n,t)^{4}He$ reactions can be emitted in any number of directions. Shown in Fig. 3.3.1 are the main directions: (1) along the length of the trenches where no energy will be deposited into the semiconductor and fail to produce a 'count', (2) along the height of the trenches where no energy will be deposited into the semiconductor and fail to produce a 'count', (3) where one or both reaction products are fully stopped in the semiconductor medium, likely producing a 'count', (4) where one or both reaction products can traverse the semiconductor into another absorber, depositing little energy into the substrate, possibly producing a 'count', and (5) where similar reactions can occur in the back-side trenches. Cases (3), (4), and (5) are preferred. Numerous variations of the offset, straight-trenched DS-MSND were modeled by varying the trench depth, width, and unit cell thickness to determine optimal intrinsic thermal neutron detection efficiency with a lower-level discriminator (LLD) value of 300 keV. Efficiency values for this geometry are listed in Table D.1 of Appendix D. Plots of intrinsic thermal neutron detection efficiency versus LLD setting can be found in Fig. D.1-D.6.

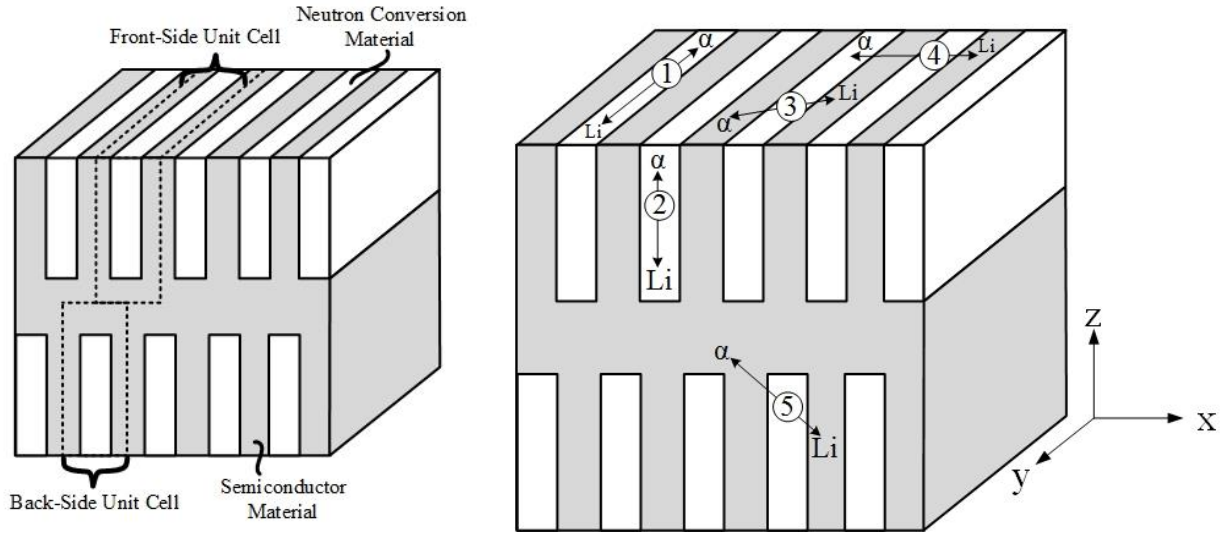

Fig. 3.3.1. (left) The basic concept for a straight-trenched dual-sided microstructured semiconductor neutron detector (DS-MSND). Shown are two typical unit cells for the structure. (right) Several of the trajectories for reaction products in a trench design DS-MSND. Here, (1) and (2) show complete misses where reaction products are not measured, (3) one or both reaction products are measured, (4) with small dimensions, one or both reaction products traverse another absorber, consequently reducing energy deposited into the semiconductor. Also, (5) shows a reaction that can occur in the backside trenches.

3.3.2. Opposing Pattern Circular Hole-Shaped Perforations

Circular-hole shaped perforations were the first type of MSNDs produced to replace thin-film-coated neutron detectors (Fig. 3.3.2) [7]. Devices using these perforations are simple to fabricate using standard ICP-RIE etching techniques that do not require alignment to specific crystal faces for etching. Diffusion and contact formation on these devices is simple and the electric field established with the device often assures good charge-collection efficiency. However, due to the nature of the circular pattern, a fully opaque off-set-style device cannot be fabricated as neutrons can potentially miss the etched holes on both the front- and the back-side patterns. The pattern benefits from excellent reaction-product detection efficiency for backfilled holes with a diameter less than the combined ranges of the reaction products, leading to devices that can have high LLD-settings without great detriment to the detection efficiency. Shown in Fig. 3.3.2 are the various paths that the charged particle reaction products can follow from an n-capture reaction. Case (1) shows the likely scenarios where complete absorptions of both reaction products occurs.

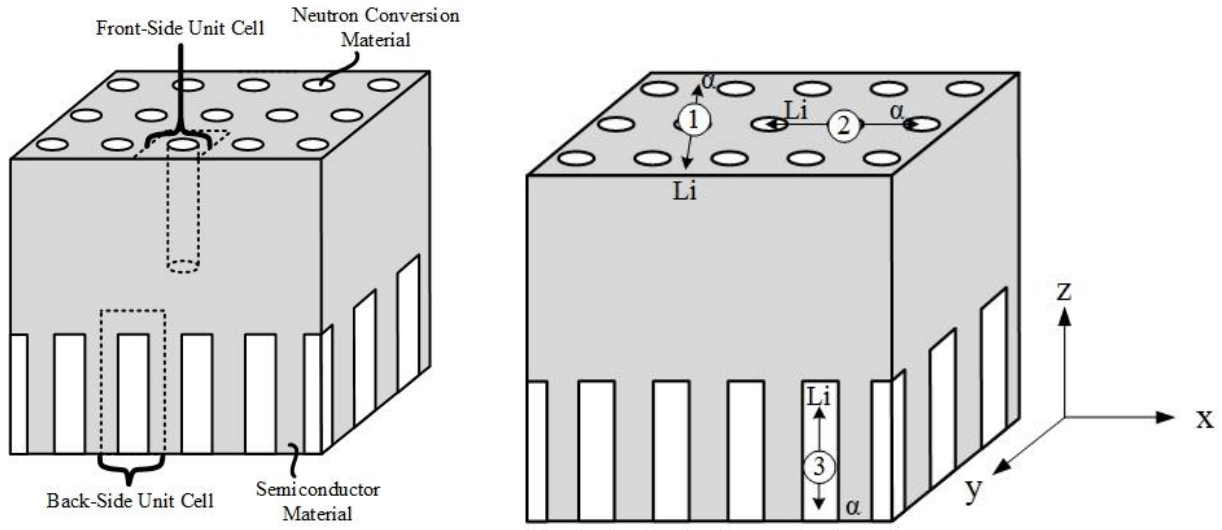

Fig. 3.3.2. (left) The basic concept for a circular-hole dual-sided microstructured semiconductor neutron detector (DS-MSND). Shown are two typical unit cells for the structure. (right) Several of the trajectories for reaction products in a hole design DS-MSND. Here, (1) shows complete absorptions where reaction products are fully measured, (2) one or both reaction products are absorbed in an adjacent hole structure, failing to fully energize the substrate, and (3) with large dimensions, one or both reaction products fail to exit the hole, failing to be counted.

Case (2) depicts one or both reaction products traversing the substrate into an adjacent hole, failing to fully deposit their energies into the substrate, reducing the pulse height. Case (3) is the least likely case to occur, where one or both reaction products being emitted along the length of the hole, being reabsorbed in the conversion material. This this effect reduces hole diameter and depth decreases. Efficiency values for this geometry are listed in Table D.2 of Appendix D. Plots of intrinsic thermal neutron detection efficiency versus LLD setting can be found in Fig. D.7-D.12.

3.3.3. Opposing Pattern Circular Pillar-Shaped Perforations

Circular-pillar shaped semiconductor formation are a variation with limited success. Devices using these perforations are difficult to fabricate using standard ICP-RIE etching techniques due to the high probability of etching away structures and the large amount of bulk material that must be removed (Fig. 3.3.3). Diffusion and contact formation on these devices is also difficult because a large amount of the bulk material is consumed by the doped contact regions rendering them insensitive to incident reaction products. However, the large amount of neutron conversion material present can produce devices with high neutron absorption efficiencies and relatively low LLD settings.

Unlike the circular-hole shaped pattern, pillar-type DS-MSNDs typically do not have neutron streaming paths present due to the large amount of neutron conversion material present. However, the pattern suffers because of poor reaction product detection efficiency from the poor solid angle geometries for reaction products. Fig. 3.3.3 also shows the various paths that the charged reaction products can follow from an n-capture reaction. Case (1) depicts the unlikely scenario where both reaction products are measured to some extent. Case (2) depicts one or both reaction products traversing the substrate and being absorbed in the conversion material, failing to fully deposit their energies into the substrate. Case (3) shows one or both reaction products being emitted away from the pillar structures, being reabsorbed in the conversion material, failing to count that reaction product. Efficiency values for this geometry are listed in Table D.3 of Appendix D. Plots of intrinsic thermal neutron detection efficiency versus LLD setting can be found in Fig. D.13-D.18.

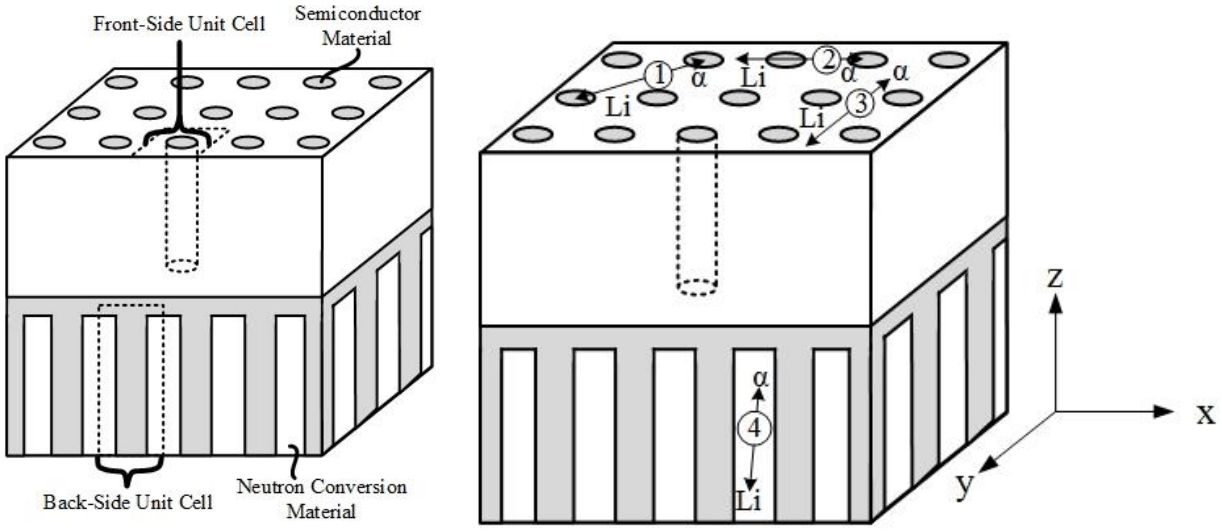

Fig. 3.3.3. The basic concept of a circular-pillar dual-sided microstructured semiconductor neutron detector (DS-MSND). Shown are two typical unit cells for the structure. Depicted are several of the trajectories for reaction products in a pillar design DS-MSND. Here, (1) shows where both reaction products are measured, (2) one reaction product is absorbed in conversion material, (3) no energy is deposited into the silicon substrate due to complete absorption within the conversion material, and (4) an interaction in the back-side conversion material.

3.3.4. Opaque Pattern Straight Trenches

The straight-trenched, opaque-type pattern utilizes aligned and off-set trenches on the top- and back-side semiconductor surfaces whose dimensions are inverse of one-another (Fig. 3.3.5). The pattern is simple to manufacture using common wet-etching techniques and allows for easy junction doping for good diode characteristics. Similar to the Opposing Pattern Straight Trenches, reaction products generated within the trenches have a good probability of depositing energy into the substrate, provided that the width of the trenches does not exceed that of the summed ranges of the Li and α ions, as depicted in Fig. 3.3.1. The reaction products from the $^{10}B(n,\alpha)^{7}Li$ or $^{6}Li(n,t)^{4}He$ reactions can be emitted in any number of directions. Shown in Fig. 5 are several notable directions: (1) along the length of the trenches where no energy will be deposited into the semiconductor consequently failing to produce a 'count', (2) along the height of the trenches where no energy will be deposited into the semiconductor and also failing to produce a 'count', (3) where one or both reaction products are fully stopped in the semiconductor medium, likely producing a 'count', (4) where one or both reaction products can traverse the semiconductor into another absorber, depositing little energy into the substrate, possibly producing a 'count', and (5) where

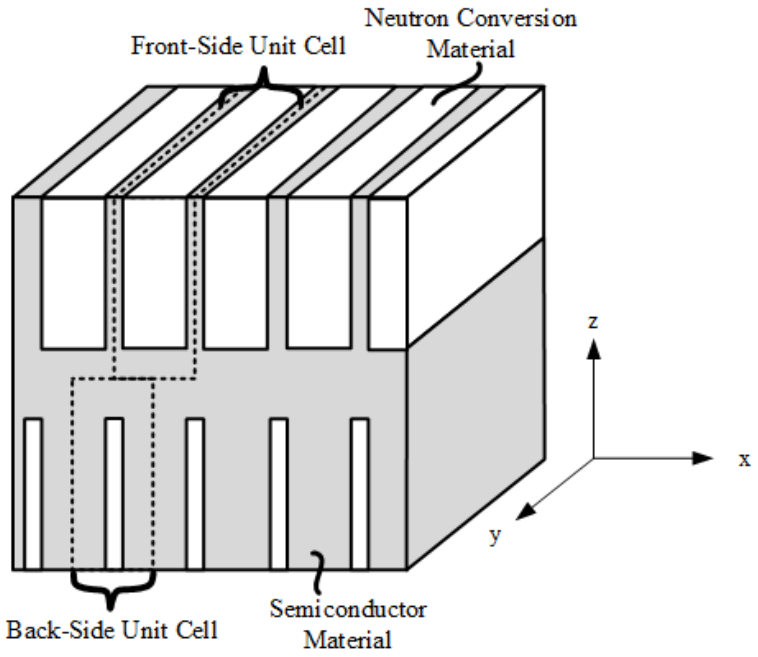

Fig. 3.3.5. The basic concept for an opaque-type straight-trenched dual-sided microstructured semiconductor neutron detector (DS-MSND). Top-side and back-side unit-cells are identical in width, but are off-set. The trench dimensions are such that total device opaqueness is achieved, but no overlapping occurs.

similar reactions can occur in the back-side trenches. Cases (3), (4), and (5) are preferred. Efficiency values for this geometry can be found in Table D.4 in Appendix D. The calculated efficiencies for the opaque-type straight trench patterns were not plotted, because the 0.50-ratio trench-width to unit-cell width is identical to the off-set type pattern, whose results can be found in Figs. D1-D6.

3.3.5. Opaque Pattern Circular-Hole Pattern

Circular-hole-shaped opaque DS-MSNDs represent devices that have a circular hole etched into the front-side of the semiconductor substrate and have a semiconductor pillar representing the back-side structure which are backfilled and surrounded, respectively, with neutron converting material. Devices using these perforations are simple to fabricate using standard ICP-RIE etching techniques that do not require alignment to specific crystal faces for etching. Proper alignment of the two patterns will result in a device that is entirely opaque to incident thermal neutrons, similar to a stacked straight-trench pattern device (Fig. 3.3.6). This geometry is different from the off-set pattern where neutrons may still stream through the device without intersecting conversion material (Fig. 3.3.6). Diffusion and contact formation on the front-side these devices are simple but can be difficult to achieve on the back-side pillars. The pattern benefits from excellent reaction-product detection efficiency for holes with a diameter less than the combined ranges of the reaction products, but is somewhat off-set by the lack of reaction-product detection efficiency of the back-side pillars. Efficiency values for this geometry are listed in Table D.5 of Appendix D. Plots of intrinsic thermal neutron detection efficiency versus LLD setting can be found in Fig. D.19-D.24.

The circular-hole opaque pattern will produce different detection efficiencies if irradiated from the opposite side given identical structure geometries. Though the device is identical to the previously discussed device, significant difference in detection efficiency exist form back-side irradiation (Fig. 3.3.6). The change in detection efficiency is caused by an increase in neutron absorption near the tops of the pillars, where reaction product counting efficiency is minimized. The reaction product spectra experience a suppression effect wherein pulses are generally lower in magnitude, thereby, reducing overall detection efficiency. Efficiency values for back-side irradiation of this geometry are listed in Table D.6 of Appendix D. Plots of intrinsic thermal neutron detection efficiency versus LLD setting can be found in Fig. D.25-D.30.

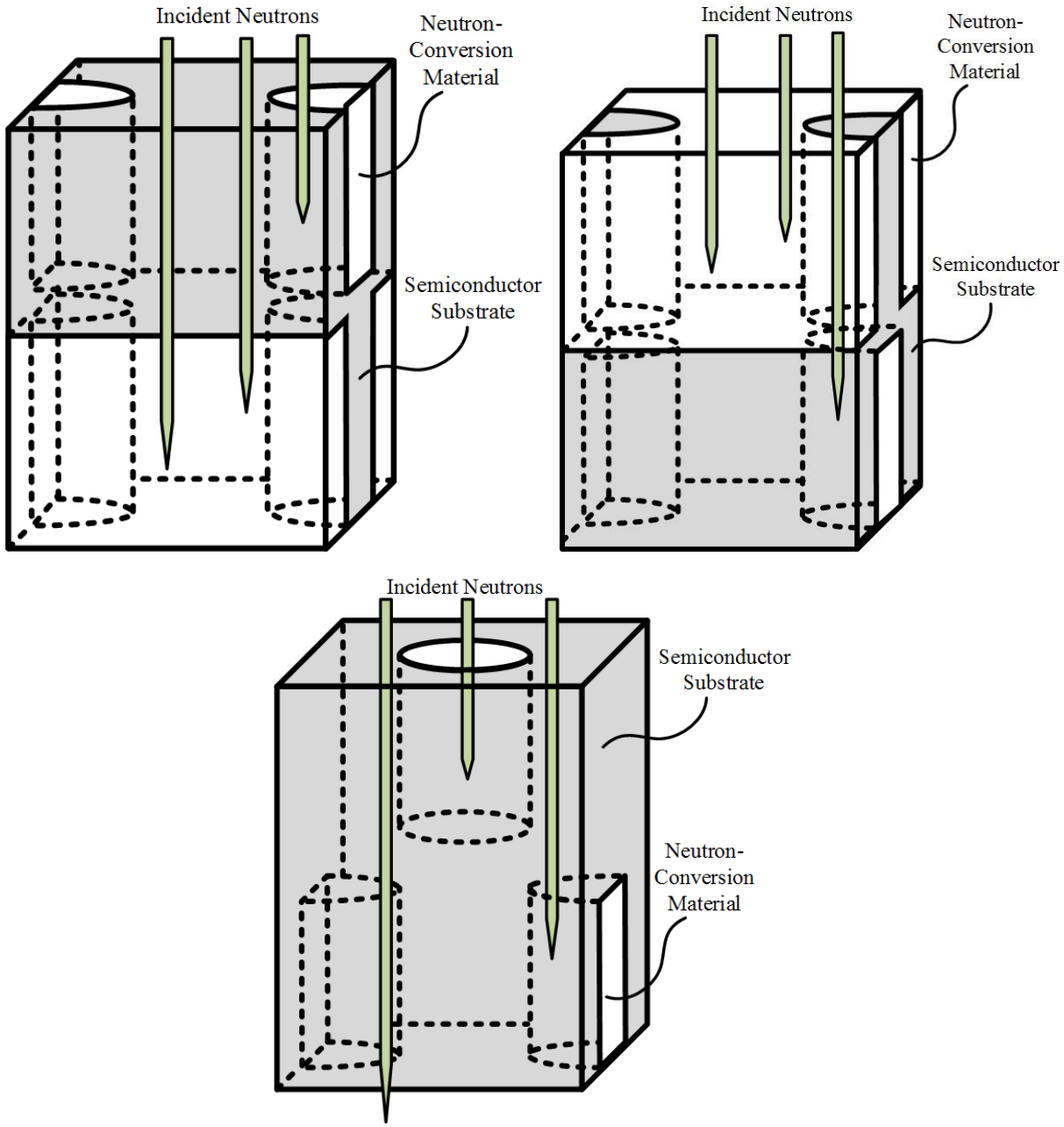

Fig. 3.3.6. Depicted (top-left) is an opaque-type DS-MSND where the front side of the device is perforated with circular holes and the back-side with aligned circular pillars backfilled and surrounded, respectively, with neutron converting material. Also shown (top-right), is the same device irradiated from the back-side. This geometry eliminates possible neutron streaming paths through the semiconductor unlike the opposing-hole design DS-MSND (bottom) wherein the front- and back-side patterns allow neutron streaming paths.

Chapter 4 - *Fabrication of DS-MSNDs*

Fabrication of the dual-sided microstructured semiconductor neutron detector (DS-MSND, Fig. 4.1.1) is a relatively simple process that involves common VLSI fabrication techniques and traditional wafer processing equipment. Many fabrication techniques developed previously for the single-sided MSND were applicable to the fabrication of the DS-MSND, however some advancements were made to effectively produce the back-side trenches and contacts. At present, 4-cm^2 active-area DS-MSNDs can be fabricated twelve at a time on commercially-available (110)-oriented 100-mm diameter silicon wafers. More than fifty 1-cm^2 DS-MSNDs can be fabricated on a same-sized wafer. Wafers can be batch processed resulting in the production of hundreds of DS-MSNDs in a short period of time in a relatively small laboratory setting. The following chapter covers in detail the methods of fabrication implemented on the DS-MSNDs.

In general, a thin, wet thermal oxide layer (SiO_2) is grown on a Si wafer. The wafer is then patterned with the straight trench pattern using photoresist. The pattern is etched into the SiO_2 layer using a wet buffered-oxide etch (BOE) and then the photoresist is removed. The (110)-

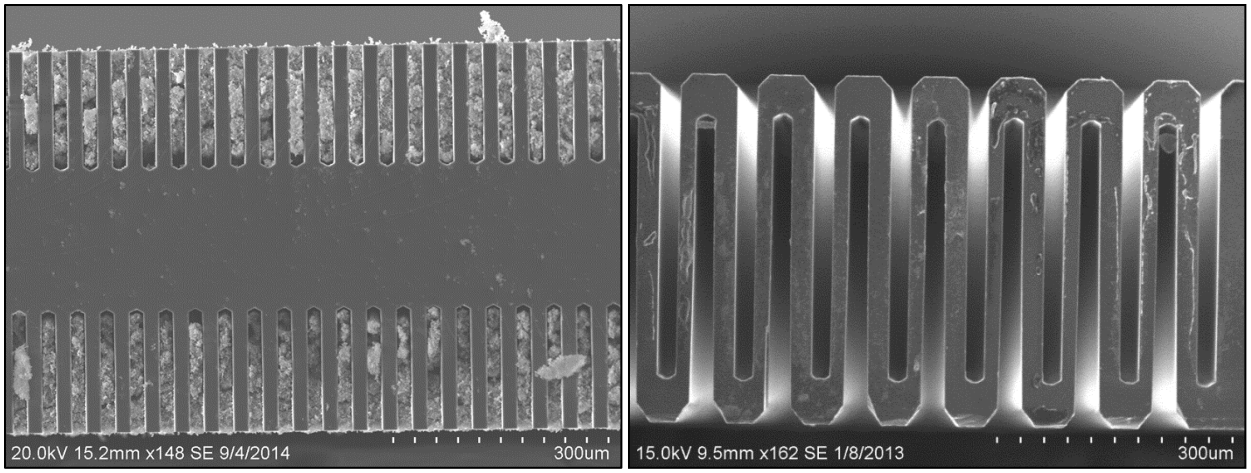

Fig. 4.1. Shown (left) is a cross-section of a 500-µm thick DS-MSND wherein the front- and back-side trenches are identical and aligned such that they are offset by one-half unit cell, thereby, reducing the neutron streaming path in the Si substrate. Shown (right) is an alternative DS-MSND design wherein the interdigitated trenches serve to reduce the charge-carrier drift length between the anode and cathode of the device, thereby, reducing charge-collection time and dead time.

oriented wafer is then wet-etched in aqueous potassium hydroxide (KOH) until the microstructures are formed. The wafer is then cleaned, diffused with the *p*- and/or *n*-type contacts, backfilled with ^{6}LiF, diced, mounted, and then tested for functionality and neutron sensitivity. The following chapter will cover this process in greater detail.

4.1 Silicon Wafer Processing

There are numerous semiconductor materials that can be used to fabricate DS-MSNDs. However, silicon and its many benefits allows for low-cost mass-producibility and rugged operational capabilities. The band gap of silicon (Si, E_g = 1.12 eV) allows for room-temperature operation of the DS-MSNDs, which is important in many detector applications [34]. Si is also chemically stable at room temperature in most atmospheric conditions found on Earth, mechanically rugged, and is widely available due to its abundant usage in the electronics industry. Most importantly, however, is the ease at which Si can be processed in a clean-room environment to alter its electronic and mechanical characteristics. All research contained within this work therefore utilized Si as the base semiconductor material. Devices were fabricated exclusively using 100-mm-diameter, 500-µm- or 1000-µm-thick, (110)-oriented wafers. The primary flat was cut to coincide (±0.25°) with the (111) plane oriented in the <111> directions to the wafer surface. Both the top and the bottom faces of the wafer were polished by the manufacturer.

4.1.1 Wafer Cleaning and Oxidation

A blank silicon wafer is cleaned using a common RCA-cleaning process[70]. Two sets of chemicals are used to clean the polished wafer of both organic and inorganic contaminants. First, the wafer is placed in a Piranha bath heated to 130°C, consisting of sulfuric acid (H_2SO_4), hydrogen peroxide (H_2O_2), and deionized (DI) water in a 1:1:1 mixture to remove any organic contaminants from the surface and subsurface of the wafer. The wafer is then moved to a BOE bath to remove the thin thermal oxide that grows during the cleaning process. A second heated bath is kept at 90°C and consists of H_2O_2, Baker Clean solution (a proprietary chemical), and DI water mixed in a 1:5:25 ratio to remove any inorganic contaminants. From here, the wafer is then rinsed and dried in a spin-rinse-dryer for several minutes.

Following cleaning, the wafer is loaded into an oxidation furnace where an oxygen-

hydrogen burn produces a wet thermal-oxide growth on the surface of the wafer. The thermal oxidation process is typically used (over that of an evaporation deposition or similar) because the method produces the highest-quality, lowest trap-inducing thin film possible [40]. The process of growing a wet thermal-oxide goes as:

$$Si\ (solid) + 2H_2O\ (gas) \rightarrow SiO_2\ (solid) + 2H_2\ (gas), \qquad \text{Eq. 4.1.1}$$

Eq. 4.1.1 shows that a portion of the Si wafer is consumed by the oxide during growth. The consumption of the Si occurs at a rate of roughly 0.44 nm of Si per 1 nm of SiO_2 grown, depicted in Fig. 4.1.1. The process is often performed at temperatures between 900°-1200°C [40]. Here, care must be taken to control the rate of temperature increase in the wafer as rapid increases in temperature can induce traps from furnace slip [45]. A wet-thermal oxide is preferred over the denser, but slower growing, dry oxide due to the ease at which a thick (+3 μm) thin film can be grown in a relatively short period of time. This oxide thickness is sufficient for serving as an etch mask during the trench-etching and subsequent contact diffusion steps of fabrication.

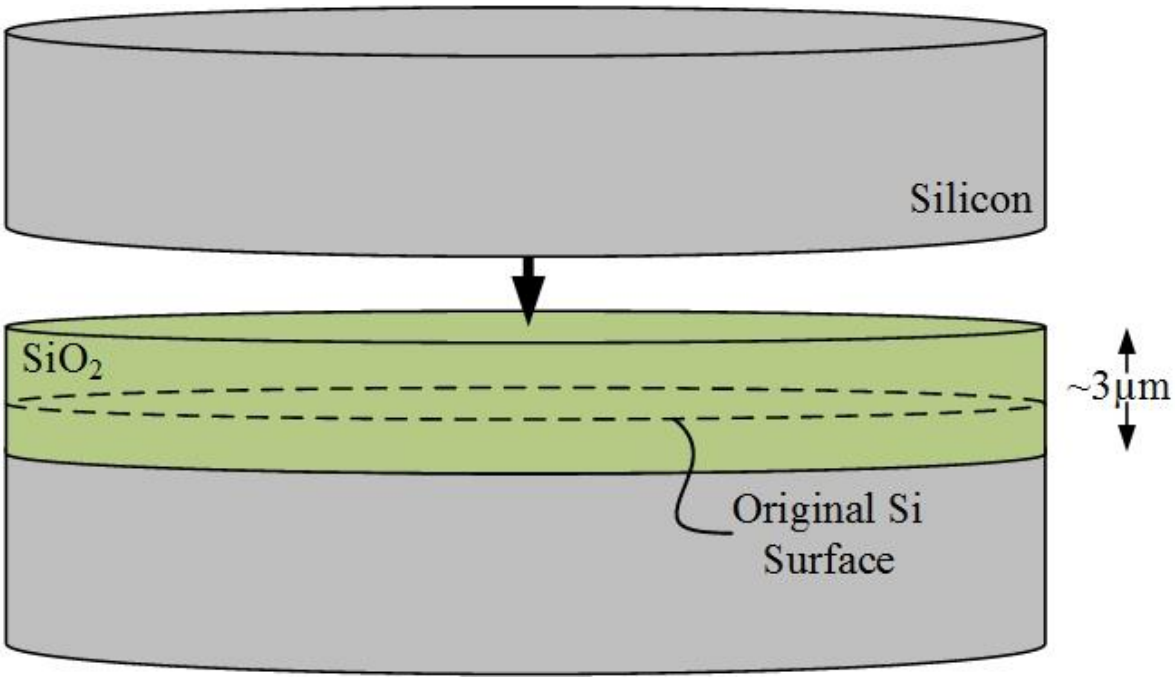

Fig. 4.1.1. Depicted is a schematic of the consumption of the Si bulk material during the oxidation process. The layer of SiO_2 can extend nearly 1.3 μm into the original Si surface, forming a good semiconductor-oxide interface.

4.1.2 Wafer Preparation

Prior to patterning the oxidized wafer with photoresist, the surface of the wafer must be prepared by dehydration and treated with a photoresist adhesion promoter, such as hexamethyldisilazane (HMDS). During the oxidation process, residual water molecules can become trapped in the low-density SiO_2 film (either during film growth or when remaining in atmosphere for a period of time) that must be baked out. Batches of wafers are kept in a clean-room oven at a temperature of 100°C in order to dehydrate the thin-film oxide. Wafers should be kept at this temperature for more than one hour prior to treatment with HMDS. Following baking, HMDS is vapor-deposited onto top and bottom surfaces of the wafer. HMDS works by molecularly polarizing the oxide layer which greatly benefits the adhesive properties of the photoresist [40]. Improving photoresist adhesion is important for reducing pattern undercut, which reduces the resolution capabilities of the printed pattern, and therefore improving the patterning capabilities of the photoresist. Extremely poor photoresist adhesion can lead to pattern lift off, decreasing overall device throughput and yield.

4.1.3 Photolithography

Photoresist is a photo-sensitive material that is patterned onto the surface of a wafer to mask portions from subsequent fabrication processes. The process for printing a pattern into photoresist is similar to the exposure and development of photographic film, wherein exposure to ultra-violet (UV) light causes a chemical change to the photoresist that can be defined using a chemical developer. Liquid photoresist is first spun onto a wafer substrate, with the resist's viscosity and wafer spin velocity determining the final film thickness. Control of the film thickness is important for maintaining good pattern characteristics (such as controlling pattern resolution) and pattern repeatability. The photoresist is then hardened with a pre-bake (or soft-bake) step wherein the solvent used to reduce the photoresist's viscosity is baked out of the system. A pattern is then exposed into the photoresist using ultra-violet light using a blocking mask. The UV light that intersects the photoresist either promotes cross-linking (in the case of negative photoresist) or inhibits cross-linking (in the case of positive photoresist). Cross-linked photoresist is typically resilient against wet chemical etches including buffered oxide wet etches and dry plasma (ICP-RIE) etches. The non-cross-linked photoresist is dissolved using a photoresist developer, leaving

behind the intended mask pattern. In this fashion, the pre-designed pattern can be imprinted onto the surface of a wafer for further processing. After the necessary process is completed, the photoresist is easily removed using ammonium hydroxide based photoresist strippers and O_2-based plasma ashers, thus allowing the wafer to undergo further patterning.

In common MEMS devices, there can be a dozen or more patterns or masks used during processing for the various layers of the devices, however, the DS-MSNDs are relatively simple and require only three primary photo masks; a trench pattern, a diffusion-window pattern, and a bond-pad window pattern. The diffusion window and trench patterns are designed to coincide with the dimensions determined from the optimization models of the trench structures with the Monte Carlo simulations, outlined in Chapter 4. These patterns are designed and drawn using L-Edit, a commercially-available software package. The mask pattern is then printed onto a soda-lime glass which allows for MSND-scale (~10 μm resolution) patterns to be drawn for low cost.

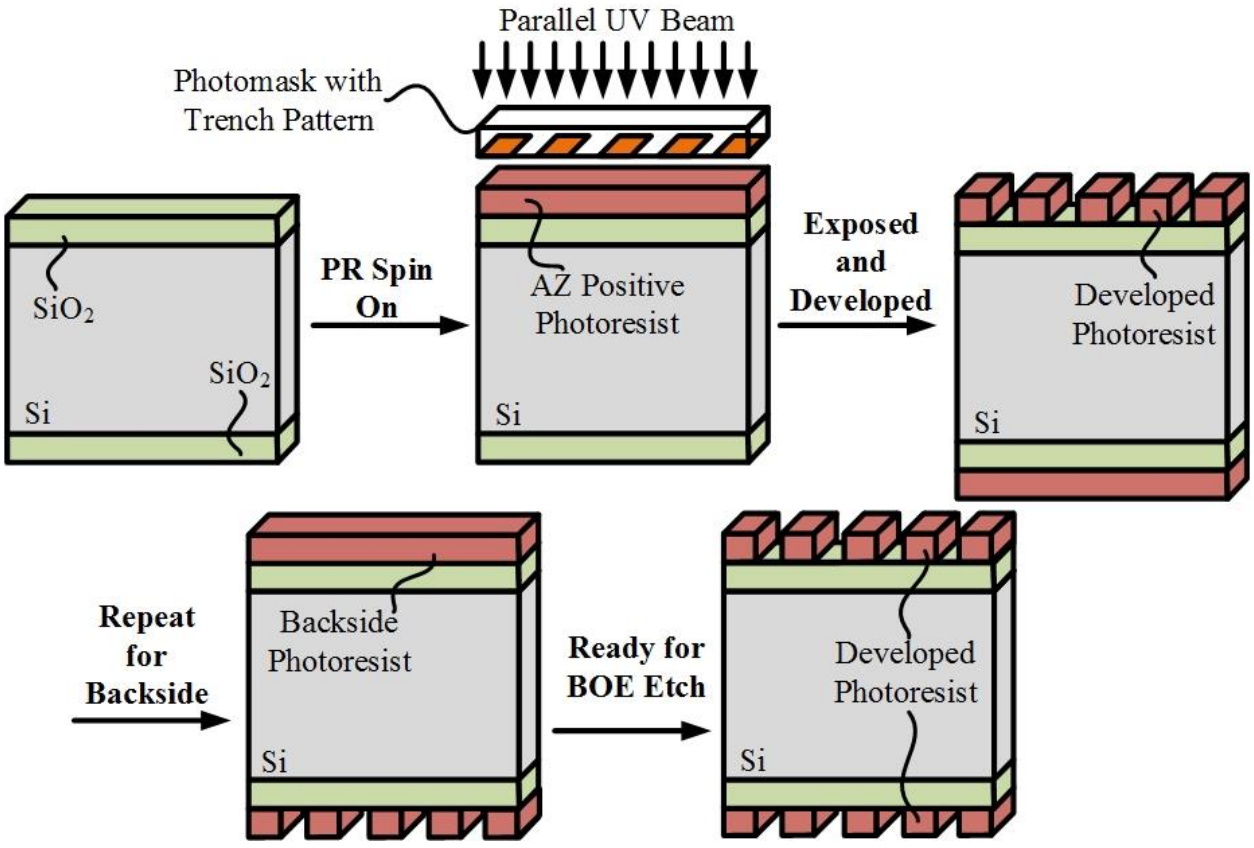

Fig. 4.1.2. Depicted are the main steps in photolithographic printing of the dual-sided MSNDs. The oxidized wafer is coated with a thin film of photoresist which is exposed with the trench pattern. The exposed regions are developed away and the process is repeated for the back side features.

The primary purpose of the photoresist is to protect regions of the SiO_2 layer during the wet oxide etch process (as described in section 4.1.4); hence, the photoresist must withstand dilute-HF etches and produce a high-resolution duplicate of the mask pattern of the wafer. There are two primary patterns used to produce the DS-MSND; the straight trench structure, and the diffusion window pattern. The straight trench pattern is first produced on a blank, oxidized Si wafer by aligning a series of straight trenches along the (111) plane. Alignment of the pattern is accomplished by aligning the mask pattern to the primary flat of the Si wafer. The developed pattern exposes the SiO_2 as shown in Fig. 4.1.2. This process is repeated following etching of the trench pattern into the SiO_2 layer for the diffusion window. In both cases, the back-side pattern is repeated and off-set from the front-side pattern by a factor equal to one-half of the unit-cell width. The back-side pattern is inherently aligned to the (111) plane when aligned to the front-side pattern. Alignment of the diffusion window pattern to the (111) plane is not crucial as this pattern is not etched during the micro-structuring process.

4.1.4 Chemical Wet Etching of the Barrier Oxide

The DS-MSNDs undergo two primary chemical wet etches to form the trench and diffusion window structures. The first process is an etch of the SiO_2 protective layer, described in section 4.1.1, followed by an etch of the bulk Si itself. As described in section 4.1.3, a protective photoresist layer is applied to the oxidized Si wafer and patterned with the straight-trench pattern. The developed pattern yields exposed regions of SiO_2 in the photoresist film where the trench structures will ultimately be located (Fig. 4.1.3). The pattern is then repeated on the back side of the wafer, off-set by one-half of the unit cell. The wafer is then submerged in a bath of room-temperature buffered-oxide etch (BOE). BOE consists of roughly 6:1 ratio of buffering agent (NH_4F) and HF. The mixture is reduced in H_2O to achieve an HF concentration of approximately 5%. The HF consumes the SiO_2 layer at a controlled rate [45]:

$$SiO_2 + 6HF \rightarrow H_2 + SiF_6 + 2H_2O, \qquad \text{Eq. 4.1.2}$$

where the SiF_6 is water soluble and is removed by the solution. The wet-etch process is economical, repeatable, and many wafers can be processed simultaneously, allowing for batch processing of devices. A fallback of this method for oxide removal is that the etch is isotropic in nature. There-

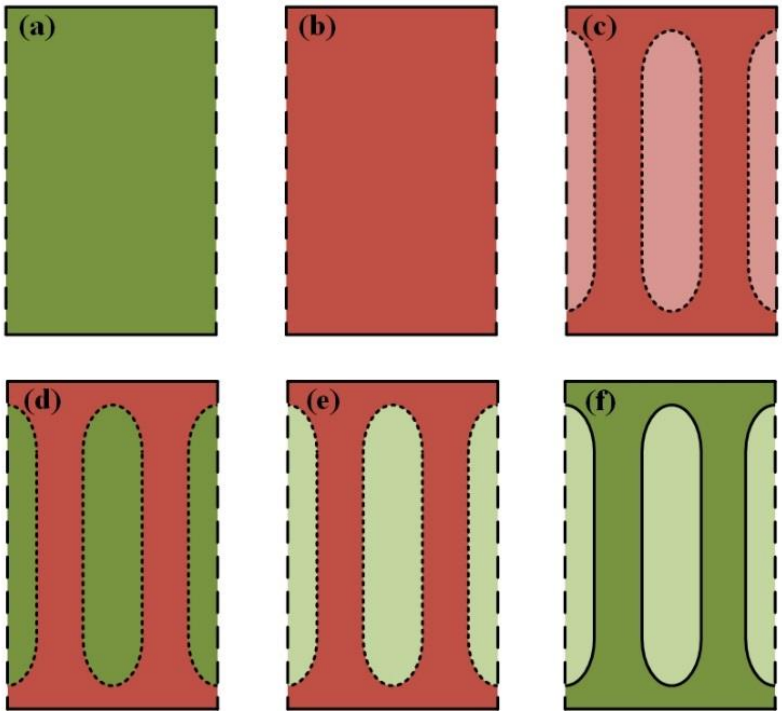

Fig. 4.1.3. Shown is a top-down view of the trench patterning process. An oxidized Si wafer (a) is coated with a thin film of photoresist (b), and is then exposed with the pattern (c). The pattern is developed away (d), thereby, exposing the underlying SiO_2. The exposed oxide is partially removed (e) by BOE etch. The wafer is then stripped of photoresist (f).

fore, every micrometer of vertical etch will yield a micrometer of horizontal (or lateral) etch [45]. This consequently leads to undercutting of the photoresist for the deep oxide layers used for the DS-MSNDs. However, the mask pattern can be designed to account for the lateral etching of the oxide by prematurely reducing the pattern size.

A diffusion window is then patterned into the remaining SiO_2 layer (Fig. 4.1.4), which protects different regions of the SiO_2 from the BOE process. The diffusion window pattern serves two functions; to expose the Si where the trenches will eventually be etched, and reduce the oxide thickness which will later be removed (post etch) and diffused with a *p*- or *n*-type blocking contact. At this point in the process, there are three different thicknesses of oxide present on the Si wafer: 1) thin, native oxide in the regions that will be trenched, 2) an intermediate oxide level in the diffusion window that will be removed post etch for contact diffusion, and 3) the barrier oxide, which is often the full original oxide thickness to serve as a diffusion barrier between the active area of the diode and the edge of the di post dicing. After these steps, the wafer is ready for etching of the microstructures into the Si substrate.

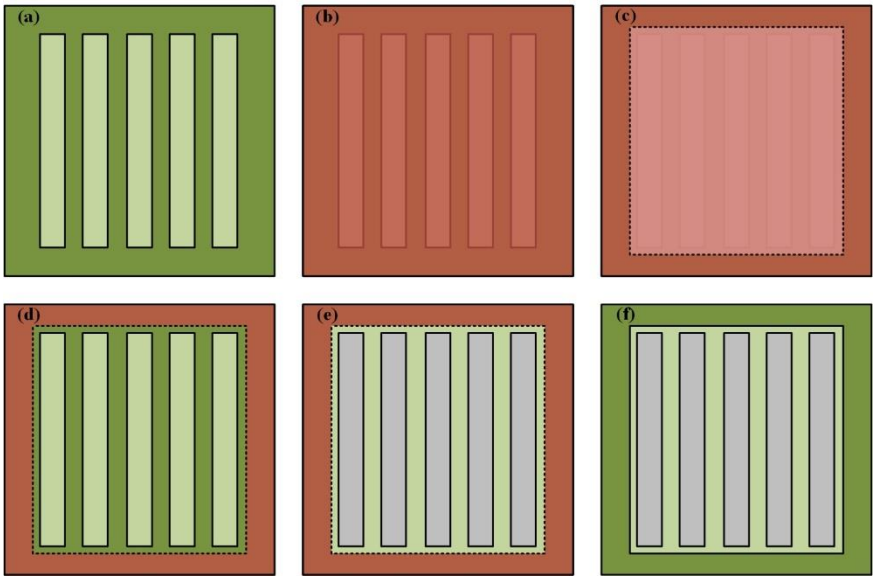

Fig. 4.1.4. Shown is a top-down view of the diffusion window patterning process. A patterned, oxidized Si wafer (a) is coated and patterned with photoresist (b, c). The pattern is developed away (d), where the exposed oxide is then partially removed (e) by BOE etch. The wafer is then stripped of photoresist (f). Bare Si is exposed in the trench regions for KOH etch.

4.1.5. Chemical Wet Etching of the Bulk Si

Microelectromechanical systems (MEMS) are common in industry and have numerous uses [45]. Often, micrometer-sized structures are etched into bulk semiconductor devices such that they may be used as a physical sensor. Minute changes in the structure post-fabrication modifies the electrical characteristics of the material, thereby, allowing measurement of some change via the piezoelectric effect [45].

The methods and technologies used to fabricate these devices are directly adaptable to the microstructured semiconductor neutron detector (MSND) technology [61]. Early MSNDs were fabricated through inductively-coupled plasma, and reactive ion etching (ICP-RIE). ICP-RIE relies on heated etch gasses propelled to the surface of the exposed Si. Typically, two different gasses are alternated, the first softening the semiconductor and the second removes the material [45]. However, issues with ICP-RIE etching, including mechanical damage following the etching process, low device throughput, and high expense per etch, ultimately led to the adoption of the wet etch method [21, 44]. Furthermore, in order to be adapted for use with the dual-sided MSNDs, multiple runs would be necessary; the front-side trenches would need to be etched where then a second photolithographic step would be needed to pattern and then etch the back-side trenches.

An alternative method for forming the microstructures was explored and later fully implemented in the fabrication of MSND-type sensors. Wet chemical etching of the substrate using aqueous KOH was found to be superior to the dry ICP-RIE of previous generations. Aqueous KOH etches Si preferentially along the (111) plane in a highly-anisotropic manner; KOH can achieve 100:1 aspect ratio or better when etching along the plane versus into it [71]. Unlike ICP-RIE etching, the wet KOH wet yields good surface characteristics, with minimal damage [72, 73]. Furthermore, because the wafers are etched in a heated bath, the number of wafers that can be processed simultaneously is limited only by the size of the bath. Many wafers can be processed simultaneously by this repeatable, low cost, low maintenance method. However, alternative chemicals exist that have various benefits and drawbacks [74].

As discussed previously, the Si wafer was patterned with parallel, straight trenches that populated each detector on the wafer. The straight trenches must be aligned with the (111) plane of the Si wafer (Fig. 4.1.5). Typically, this etch method is used to etch straight-trench patterns, but other geometries are possible and have been demonstrated with some success (see Fig. 4.1.5) [75]. Up to fifty wafers can be loaded in batches into a heated bath between 50-55°C with a KOH concentration of approximately 45%. Trenches etch at a rate of roughly 20-30 μm per hour under these conditions.

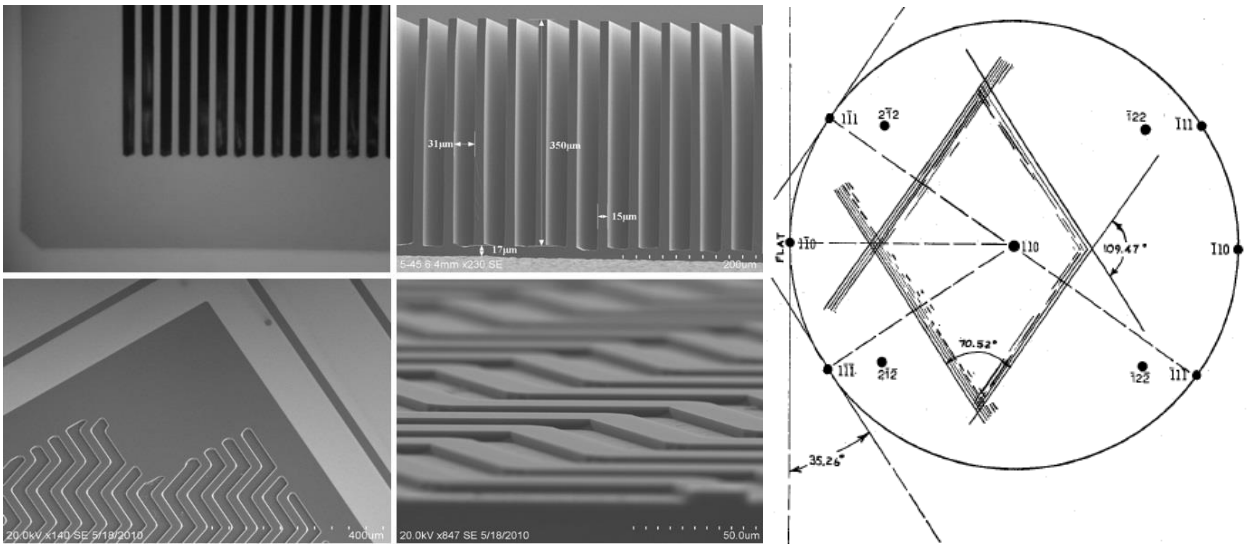

Fig. 4.1.5. Shown (left) a few patterns possible with wet KOH etching. Patterns are limited to the orientation of the (111) planes (right) perpendicular to the (110) surface of the Si wafer.

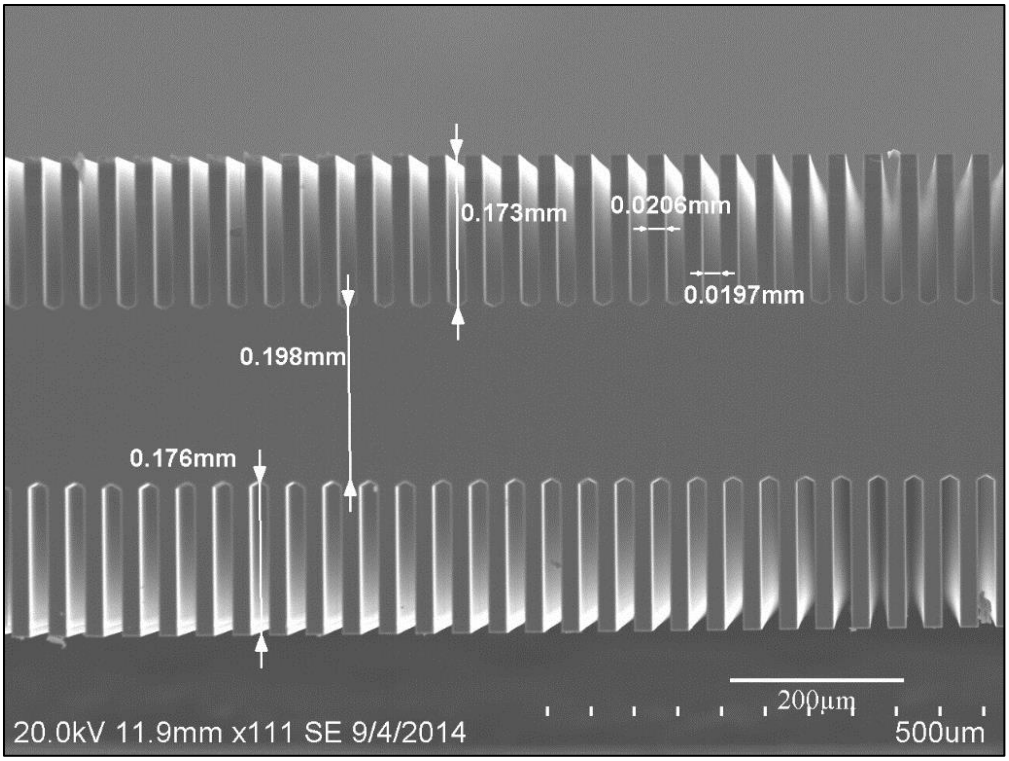

Fig. 4.1.6. Shown is a cross section of a DS-MSND etched in a heated KOH bath. A trench depth of approximately 175 µm was achieved in roughly 8 hours. Both sets of trenches were etched simultaneously, thereby, maximizing device throughput.

An additional benefit of etching the trenches by a heated KOH bath is that both the front- and back-side trenches can be etched simultaneously (Fig. 4.1.6). Etching both sets of trenches simultaneously reduces the overall time needed to produce the trenches by a factor of two, and is equal to that of the single-sided MSNDs; the total amount of bulk Si removed can be doubled without any appreciable increase in the total etch time required. Furthermore, because both sets of trenches are etched simultaneously (a feat that is not possible with common ICP-RIE reactors), both sets of trenches can have nearly identical etch characteristics, and therefore uniform properties. The device throughput during the trench etching step does not change with respect to the single-sided MSNDs, a benefit that is appealing from a commercialization standpoint.

An issue that arises, however, with the use of KOH as the Si etchant is the residual K^+ ions that remain present following the removal of bulk Si (Fig. 4.1.7). The residual K^+ ions can serve as fast diffusers and can contaminate the Si, thereby, changing the device electrical properties [40, 45]. However, the residual K^+ ions are removed by an intermediate HCl + H_2O_2 bath, typically lasting for several hours. The HCl reacts with the K^+ ions, producing KCl, which is water soluble.

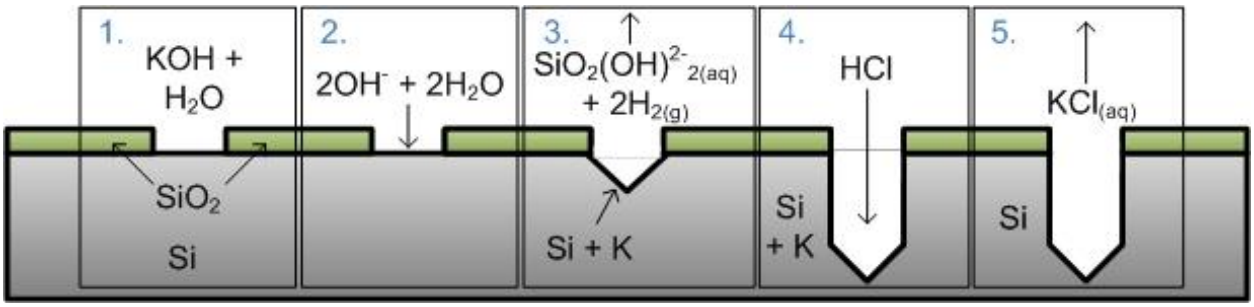

Fig. 4.1.7. Depicted are the five major steps for wet KOH etching of Si-based microstructures. 1) A Si wafer (patterned with an SiO_2 etch mask) is submerged in a heated, hydrous-KOH bath where 2) the K^+ ion is easily separated from its OH^- ion, producing free OH^-. Afterwards, 3) the OH^- reacts with the Si, quickly forming $SiO_2(OH)^{2-}$ and H_2 gas. Following the etch, the wafer is then 4) cleaned of residual K^+ ions in an HCl bath, which 5) forms water-soluble KCl.

4.1.6. Blocking Contact Diffusion

In the case of MSNDs and DS-MSNDs, the *pn*-junction contacts are formed during the contact diffusion steps of fabrication [44]. A natively-doped target Si wafer is exposed to a secondary dopant source [40]. Most often, wafers used in the fabrication of DS-MSNDs are lightly-doped *n*-type substrates, with a phosphorous background dopant (often on the order of 10^{12} cm^{-3}). Prior to the diffusion process, the wafers are again cleaned using the RCA cleaning process described in Chapter 4.1.1. The wafers are then rinsed thoroughly and dried thoroughly in a slightly pressurized nitrogen atmosphere. Following cleaning, the wafers are loaded into a furnace and exposed to a solid BN *p*-type source at a high temperature for a period of time, as in Fig. 4.1.8. The heated furnace transports an H_2-N_2 mixture, or forming gas, along with O_2 across the source wafer-wafer pair (Fig. 4.1.8(a)). The solid BN source reacts with H_2 and the O_2, thereby, producing $B((OH)_3)$ which then makes contact with the wafer surface. The acid reacts with surface of the Si wafer and forms a thin-film B_2O_3 layer (Fig. 4.1.8 (b)). The temperature is then increased to the drive-in temperature, wherein the B disassociates from the oxide. The released B atoms diffuse into the Si lattice, doping a thin layer of Si near the surface, thereby, forming a *p*-type contact (Fig. 4.1.8 (c)) and a *pn*-junction at the bulk Si interface. The B atoms displace an Si atom within the Si crystal lattice, and with their missing valence electron, act as an acceptor impurity site within the lattice (Fig. 4.1.8(d)). Further details regarding this type of process can be found elsewhere [40, 45].

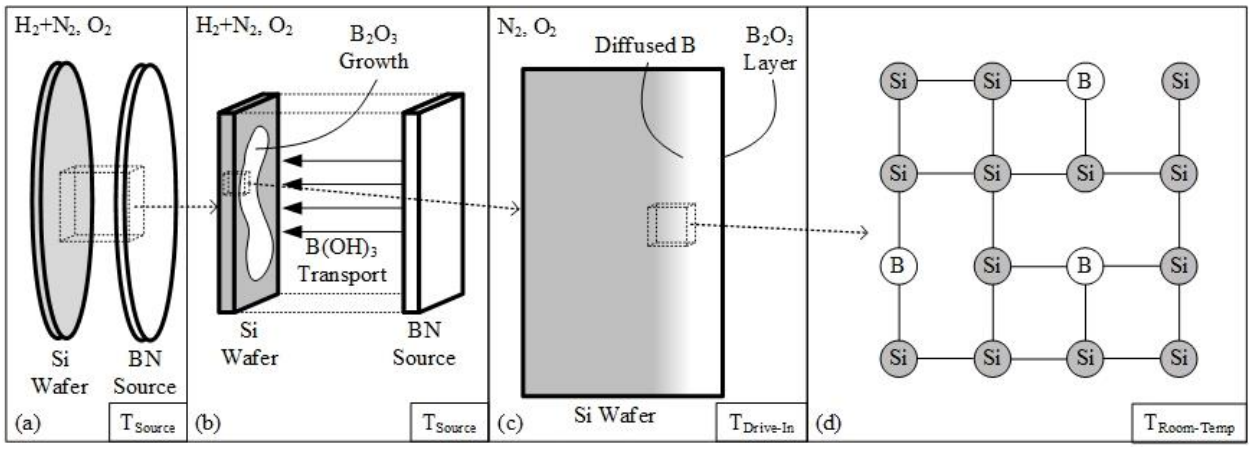

Fig. 4.1.8. Shown is the basic process by which a p-type contact is formed on an n-type Si substrate. (a) The Si substrate and the BN source wafers are heated to the sourcing temperature in an H_2 + N_2 + O_2 atmosphere, (b) causing the release of the B from the wafer which deposits on the surface of the Si wafer. (c) The temperature is elevated to the drive-in temperature, thereby, promoting diffusion of the high-concentration of B at the surface into the bulk Si. (d) During the drive-in, B atoms displace Si atoms in the lattice, thereby, altering the Fermi level.

Reported here are two variations of the DS-MSND that were fabricated with the described process: the vertically operated *pvn*-type DS-MSND (Fig. 4.1.9), and the laterally operated *pvp*-type DS-MSND (Fig. 4.1.10). The first to be considered is the vertically-operated *pvn*-type DS-MSND with trenches etched into a lightly-doped *v*-type Si substrate. The top-side fins were doped with the aforementioned *p*-type contact as previously described. During this process, a sacrificial dummy wafer was mated directly to the back-side surface of the DS-MSND wafer, thereby, shielding the back-side fins from the *p*-type dopant. The DS-MSND wafers were then briefly dipped in a BOE bath, and loaded into the *n*-type diffusion furnace. Here, a heavy *n*-type contact is formed on the back-side fins in a similar fashion as the *p*-type contact formation on the front-side fins. However, the source wafer is a P-based source wafer, thereby, doping the back-side fins with a heavy dose of P. As described in Chapter 3, this heavy back-side contact was hoped to allow for an applied bias and vertical-operation of the device similar to single-sided MSNDs of similar design. However, issues arose with this method of *pvn*-DS-MSND device fabrication, wherein the electric field strength within the back-side *n*-type fins did not allow for a fully developed signal formation from induced charge carrier motion [19].

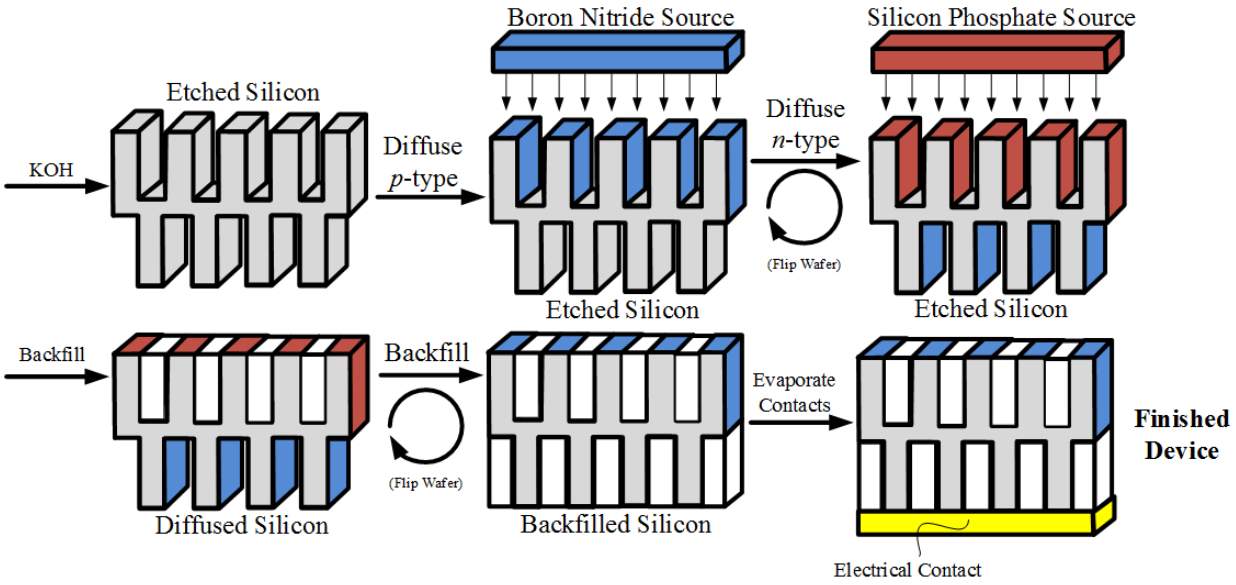

Fig. 4.1.9. Shown is the basic process whereby a pvn-type DS-MSND is finished following etching of the trenches. The p-type contact is formed on the front-side fins, where then the wafer is moved to a n-type diffusion furnace to form the back-side n-type contact. The wafer is this completed by a two-step backfill process that will be further discussed in Chapter 4.2.

To overcome this issue, an alternative method of device fabrication was implemented to eliminate the poor electric field characteristics in the back-side fins. These new devices are produced by forming identical *p*-type contacts on both sets of fins, thereby, forming *pn*-junctions on all fins, yielding a *pvp*-type device. The chemicalpotential of the differently doped regions establishes a built-in potential and natively depletes the fin of excess charge carriers, as described in Chapter 3. Fabrication of the *pvp*-DS-MSNDs is simpler than with the *pvn*-DS-MSNDs. Similar to the first diffusion process for the formation of the *p*-type contact on the *pvn*-DS-MSNDs, the *pvp*-DS-MSNDs are exposed to, and diffused with B with the same process as described before (Fig. 4.1.10). However, the aforementioned sacrificial shielding wafer is removed and the *p*-type material is allowed to expose the back-side fins as well. This simultaneously forms the blocking contact on both sides of the wafer, thereby, reducing the required contact formation time by a factor of two and greatly simplifying the overall process. These devices greatly enhanced the detection efficiency of the DS-MSND technology, thereby, serving as the solution to the issue of back-side fin depletion and signal formation [76]. The wafers are then removed and etched briefly with BOE prior to advancing to the next process.

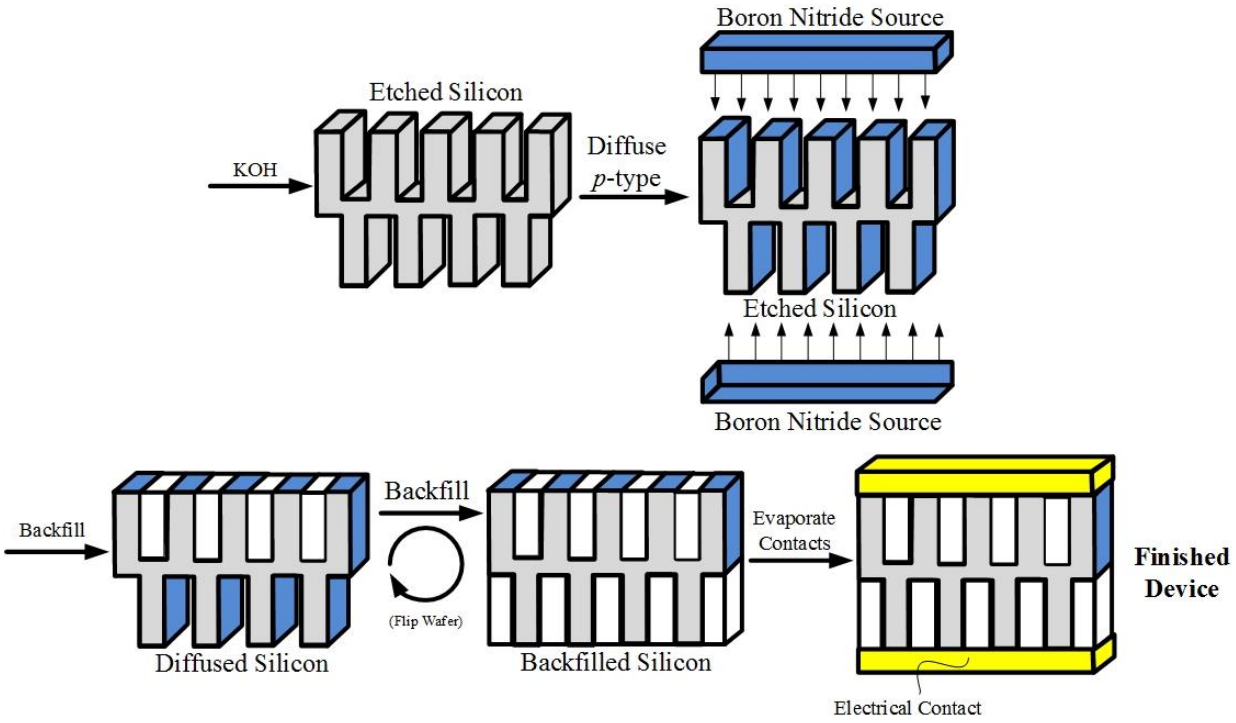

Fig. 4.1.10. Depicted is the basic process whereby a pvp-type DS-MSND is finished following etching of the trenches. The p-type contact is formed on both the front-side and back-side fins. Device fabrication is completed by a two-step backfill process, discussed in detail in Section 4.2.

4.2. Neutron Conversion Material Backfilling

Following the formation of the blocking contacts, the device trenches must be backfilled with a neutron converting material. As discussed in Chapter 3, most MSND-type neutron sensors utilize ^{6}LiF as the preferred neutron converting material. ^{6}LiF powder is produced by first reacting pure, enriched ^{6}Li metal with highly-deionized water, thereby, forming a solution of ^{6}LiOH. ^{6}LiF is then precipitated out of the solution by reacting diluted HF acid with the ^{6}LiOH, thereby, producing ^{6}LiF and H_2O. The powder is recovered with great efficiency and dried. ^{6}LiF powder is a solid at room temperature and is mostly inert to other chemicals [77]. The challenge of filling a micro-sized cavity with a powder was not simple. However, a method was recently developed for backfilling single-sided MSND devices [44]. There are two primary issues that arise when backfilling the trenches: first, the powder often forms particulates larger than the microcavities themselves (Fig. 4.2.1) due to the method of ^{6}LiF titration, and second, use of force to fill the microcavities with powder forms a blockage that limits the depth at which the powder can reach.

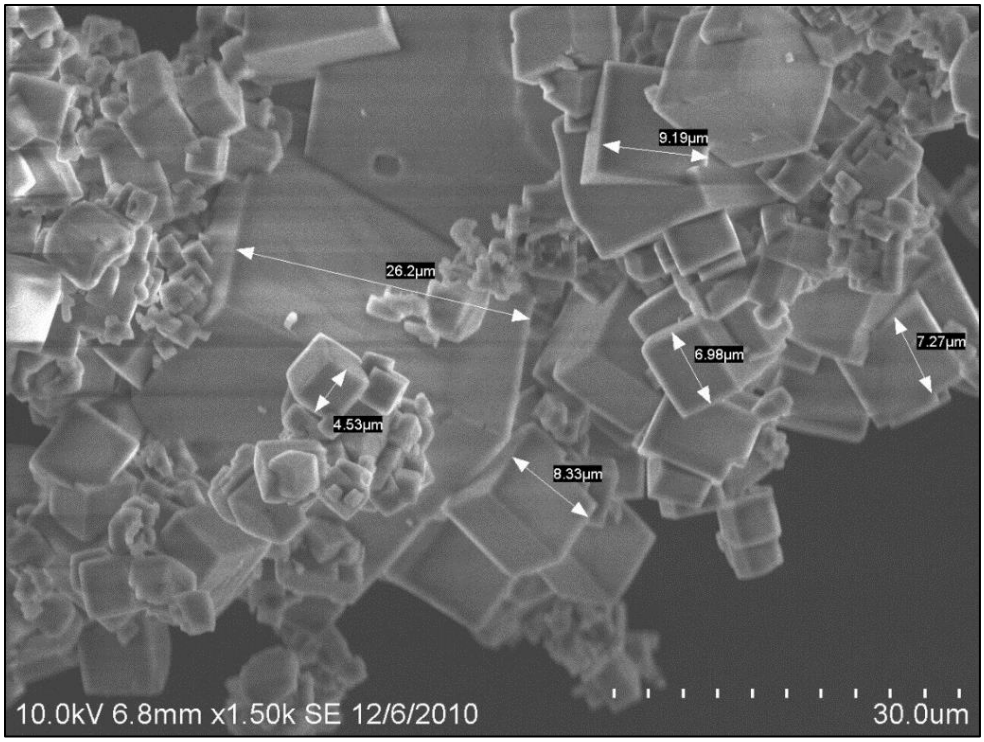

Fig. 4.2.1. Shown is a common distribution of the LiF crystals following simple HF-LiOH titration. There is a large distribution of particle sizes, ranging from sub 1 µm to nearly 30 µm. Particles larger than the trench features (i.e. greater than 20 µm) can become lodged in the trenches, inhibiting backfilling of the trenches [21].

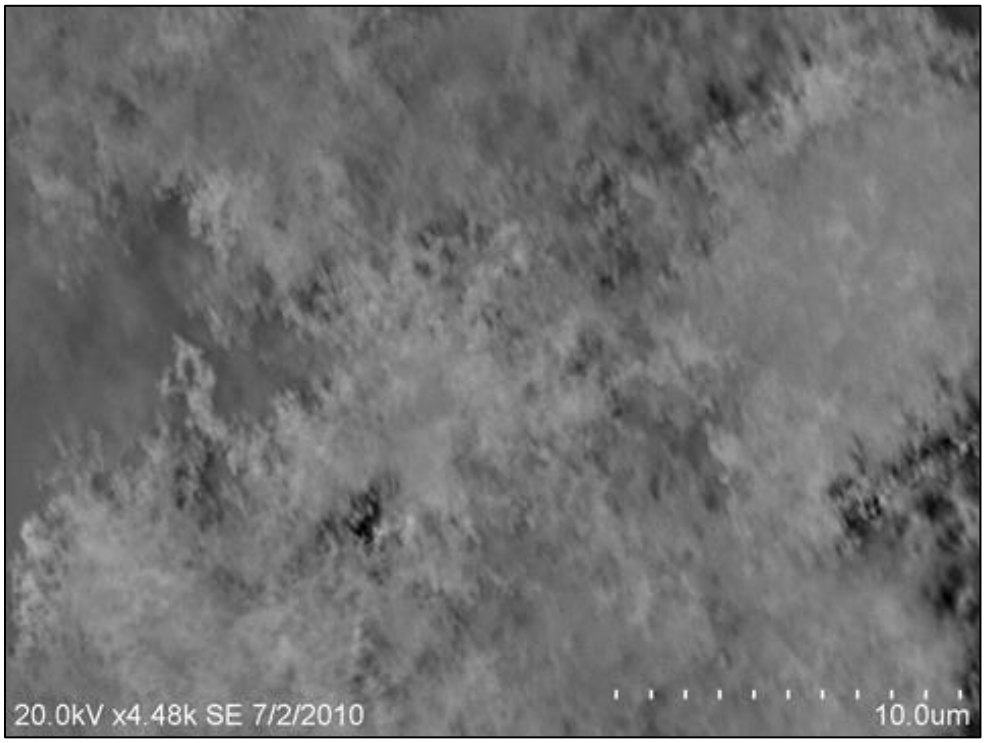

Fig. 4.2.2. LiF that has been nano-sized has a much narrower distribution in particle sizes which are more conducive to completely backfilling the trenches of a DS-MSND [21].

The first issue of the ^{6}LiF being too large to fit into the microcavities is caused largely due to the relatively slow process by which the ^{6}LiF powder precipitates from ^{6}LiOH solution. Post-processing of the ^{6}LiF powder is necessary to reduce its overall size. There are various methods for this, including evaporation and rapid condensation of the ^{6}LiF vapor which yields good results (Fig. 4.2.2), but has low yield [44]. More recently, a method for reducing the particle size by direct-contact ball milling has been implemented, thereby, greatly improving throughput. The second issue regarding the backfilling trenches with ^{6}LiF powder involves the mechanical friction between the powder and the Si fins. As the powder is pressed into the trenches, the powder becomes compacted, thereby, disallowing further material to be added into the trenches. This issue was resolved by suspending the ^{6}LiF powder in a solution of methanol and H_2O_2 and driving the suspended powder into the trenches by centrifugal force [21, 44].

These methods were found to be largely applicable for the DS-MSNDs and required little modification to properly implement. Because only one side of trenches may be backfilled per run, all DS-MSND wafers must be processed twice to backfill both sets of trenches. It was found that by allowing the front-side trenches to 'cure' post backfill, the friction coefficient of the backfill in the cavities would largely sustain the centripetal force felt upon filling the back-side trenches; in other words, the original backfill did not dislodge as (see Fig. 4.2.4 and Fig. 4.2.5).

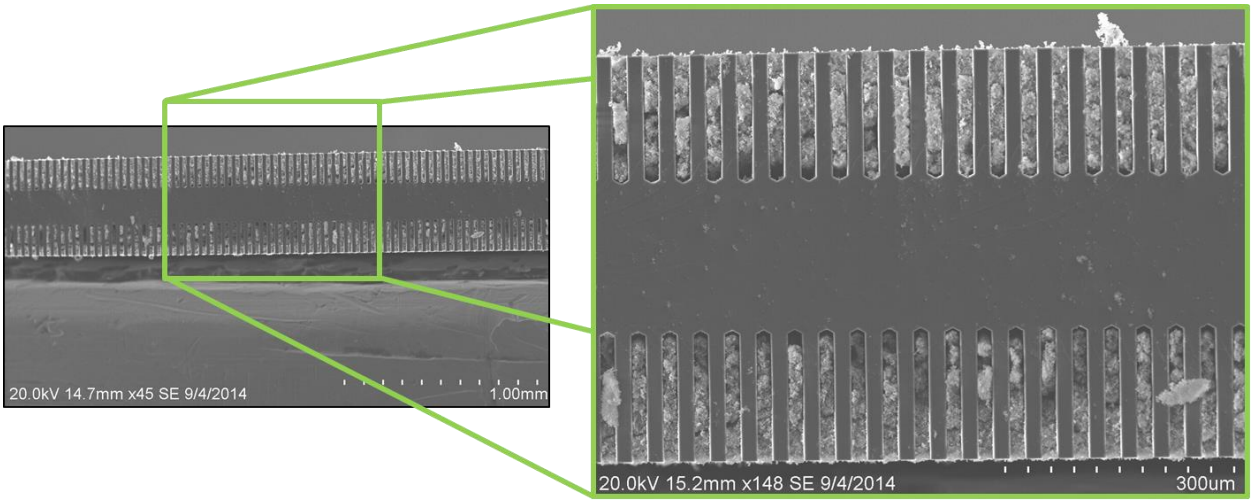

Fig. 4.2.4. Shown (left) is an early DS-MSND that has been backfilled with nano-sized ^{6}LiF on both the front- and back-side trenches thereby, completing the device. (right) Also shown is an exploded view of the trenches.

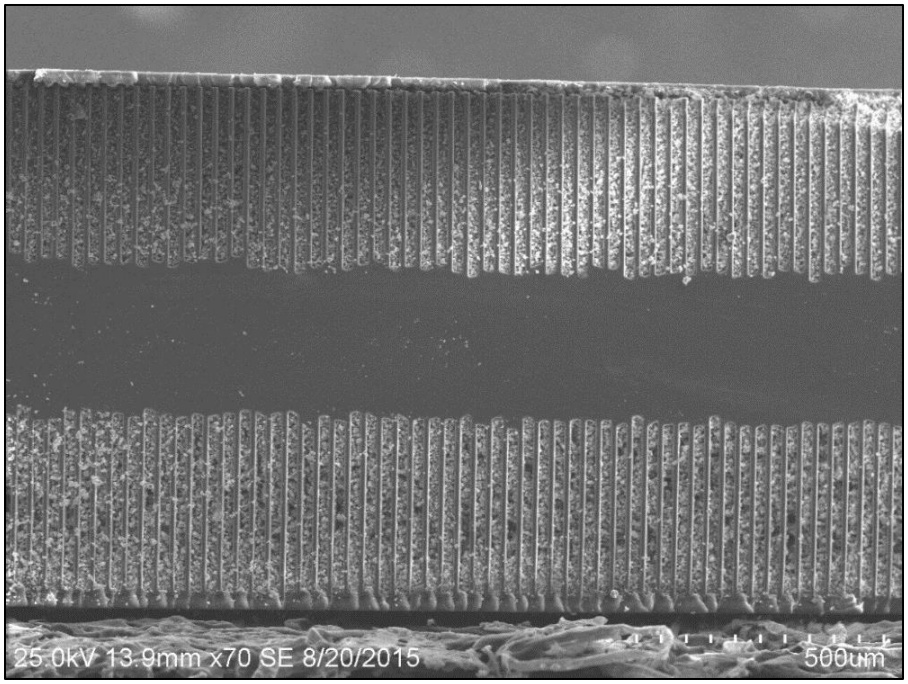

Fig. 4.2.5. Trenches as deep as 400 µm have been backfilled using the described centripetal method of powder backfilling with great success on even the DS-MSND-type sensors.

4.3. Wafer Dicing

Post backfilling, the DS-MSNDs are cut and removed from the wafer for individual testing and mounting. To accomplish this task, the wafers are mounted to dicing tape that has an adhesive layer to hold the wafer stationary. Wafers are diced using a reciprocating process whereby a diamond-coated, silicon carbide-coated blade is spun at 30kRPM and passed through the wafer [78]. A mixture of cutting fluid and water is injected at the cut site to wash away removed material. To achieve a good cutting edge devoid of damage, a balance between the wafer feed rate, rate of saw fluid injection, cut depth, and blade dimensions and characteristics must be met [79]. Backside damage to the diodes occurs when some portion of the dicing parameters fall out of balance (Fig. 4.2.6). Most commonly, the physical damage manifests as chipping on the backside of the diode, where grit can become lodged, causing fractures rather than a uniform cut. Furthermore, as the dicing blade begins to wear, the point most susceptible to breaking are the edges of the blade, leading to damage of the back-side of the diode. These issues were resolved by using pre-dressed blades, increasing the wafer feed rate to 120 mm/s (Fig. 4.2.6), and improving the saw fluid feed rate. Eliminating back-side chipping worked to improve the stability of the vertical *pvn*-DS-MSNDs, however, the issue was not as important for the lateral *pvp*-DS-MSNDs.

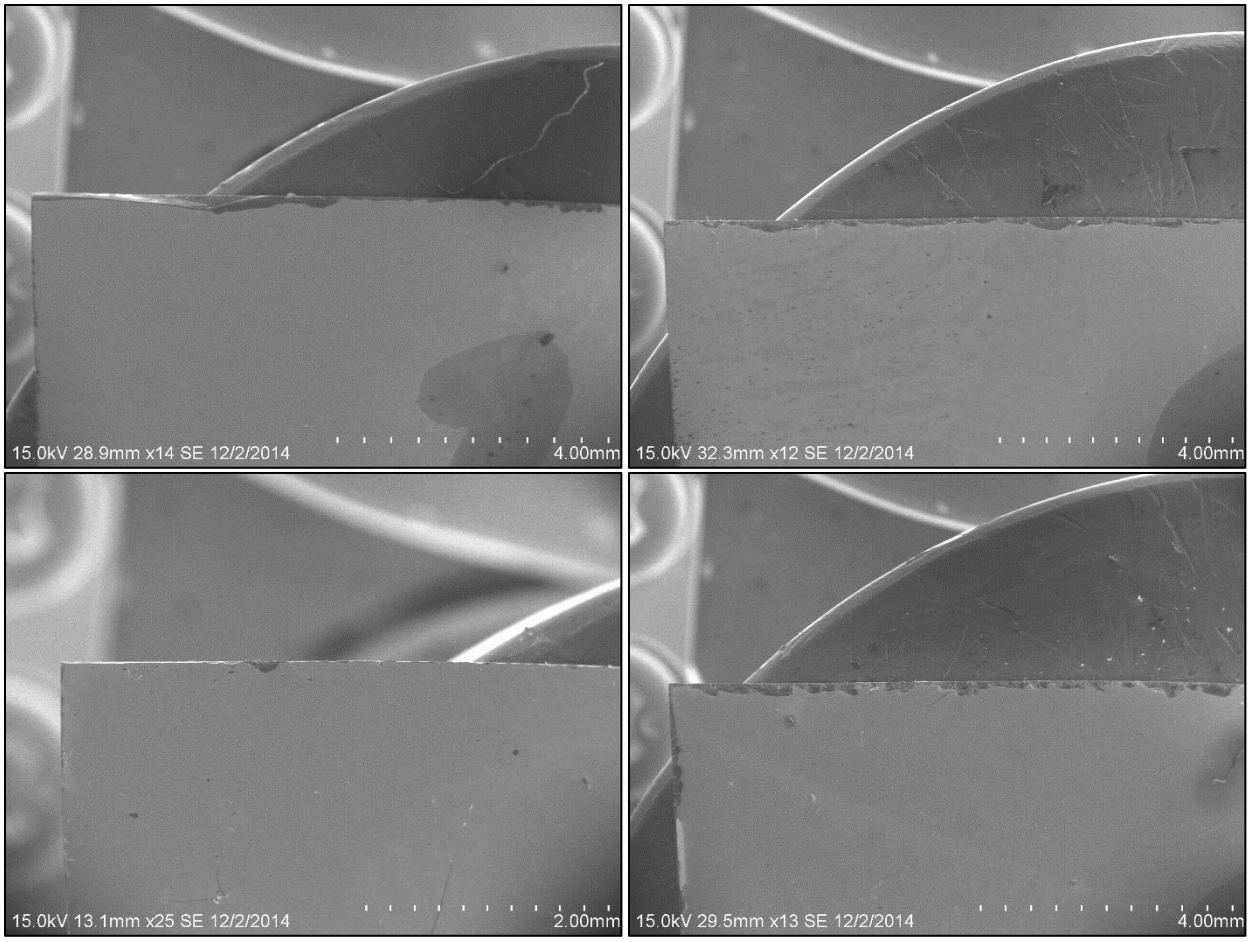

Fig. 4.2.6. Shown here are four instances of the back side of the diode post dicing. Shown (top left) is a relatively slow feed rate of 25 mm/s where large chipping is observed. The (top right) device was fed at 60 mm/s and shows marked improvement. The (bottom left) shows the best results at 120 mm/s, while damage reappears for the (bottom right) case at 220 mm/s.

4.4 Diode Mounting

After dicing the diodes from the wafer, they are removed from the adhesive tape and tested for electrical characteristics (Chapter 7). 'Good' diodes are chosen by their low capacitance and leakage current at the operating bias (Chapter 7). However, diodes are not directly mounted to the electronics package that they will populate; 'good' diodes are mounted to a low-cost, modular ceramic detector board (CDB, Fig. 4.4.1) for neutron and gamma-ray sensitivity testing which can then be mounted to any number of instruments. Furthermore, the advent of the CDB allows for diodes to be removed from an instrument and re-used, should the instrument be made obsolete or become damaged. The CDB package also serves to hermetically seal the DS-MSND and its wire-

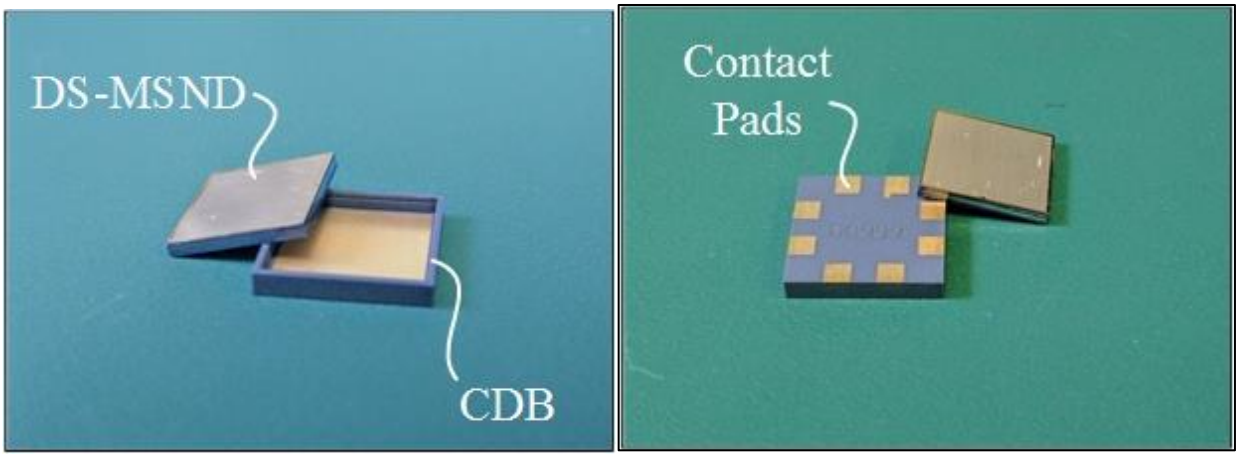

Fig. 4.4.1. Shown are a DS-MSND-CDB pair. The DS-MSND is mounted into the CDB package (left) by a two-part conductive silver epoxy which serves to form both the electrical and mechanical contacts. The top-side is then wirebonded to the top-side CDB contact, thereby, completing the electrical contact to the back-side contact pads (right).

bond from external conditions. The diced diode is secured into the CDB by a two-part, conductive silver epoxy thereby, forming both a mechanical and electrical contact of the sensor to the CDB back-side contact. The top-side contacts are formed by a wedge-style wirebond between the DS-MSND electrical bond pad and the CDB contact pedestal. The finished product is a rugged, and inexpensive package that connects the DS-MSND electrical contacts for use in detector systems.

The CDB is then tested for electrical continuity by applying a small bias and measuring the resulting current across the electrical contacts, as seen in Fig. 4.4.1. From here, a small lid is applied to the top of the CDB and glued into place, thereby, completing the hermetically-sealed package. This process can be repeated in large batches of devices (up to several-hundred concurrently) by a single process engineer.

Chapter 5 - *Sensor Instrumentation*

MSND sensor technology has great neutron detection and gamma-ray rejection capabilities but suffer from low absolute detection efficiency due to its small size. Diode leakage current and capacitance limits the overall size that an MSND or DS-MSND can be (often no more than 4 cm^2 in total active area) [64]. The device leakage current reduces the maximum applied bias to the device to limit the electronic noise level. Lower bias reduces the depletion depth which leads to an overall decrease in the sensor's detection efficiency. An increase in device capacitance reduces the overall pulse height produced by the device for a given detection event. Thus, in order to produce larger neutron detectors using the MSND technology, it is necessary to produce instruments that are populated with many MSNDs. MSNDs and DS-MSNDs can be mass produced, shown in Fig. 5.1, allowing for thousands of sensors to be produced in a short time. The intrinsic thermal neutron detection efficiency of MSNDs and DS-MSNDs increases with the neutron angle of incidence (Fig. 5.2 and Fig. 5.3). Instruments populated with MSNDs are designed to combine detectors to perform as a single device. Methods of combining detector into such instruments are presented in the following chapter.

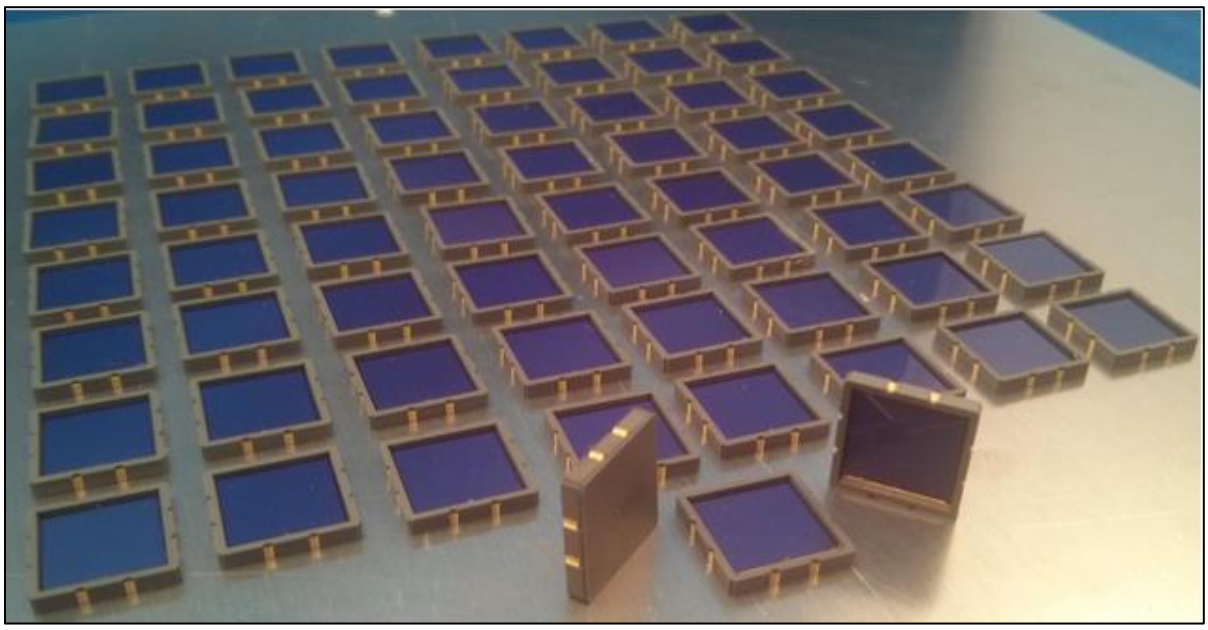

Fig. 5.1. The mass-producibility and ruggedness of the MSND and DS-MSND sensor packages makes them ideal for use in populating larger instruments or highly-specialized instruments.

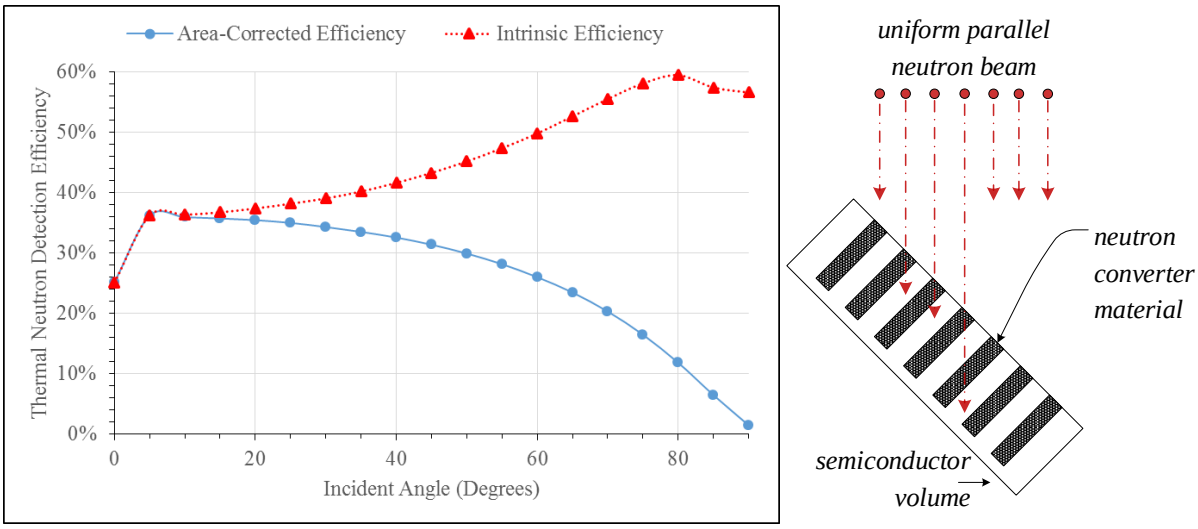

Fig. 5.2. Plotted (left) are MCNP6 calculated results for the intrinsic thermal neutron detection efficiency for a given single-sided MSND as the incident angle of the beam of thermal neutrons is rotated away from normal. Note the early sharp increase in detection efficiency as the streaming paths are closed off.

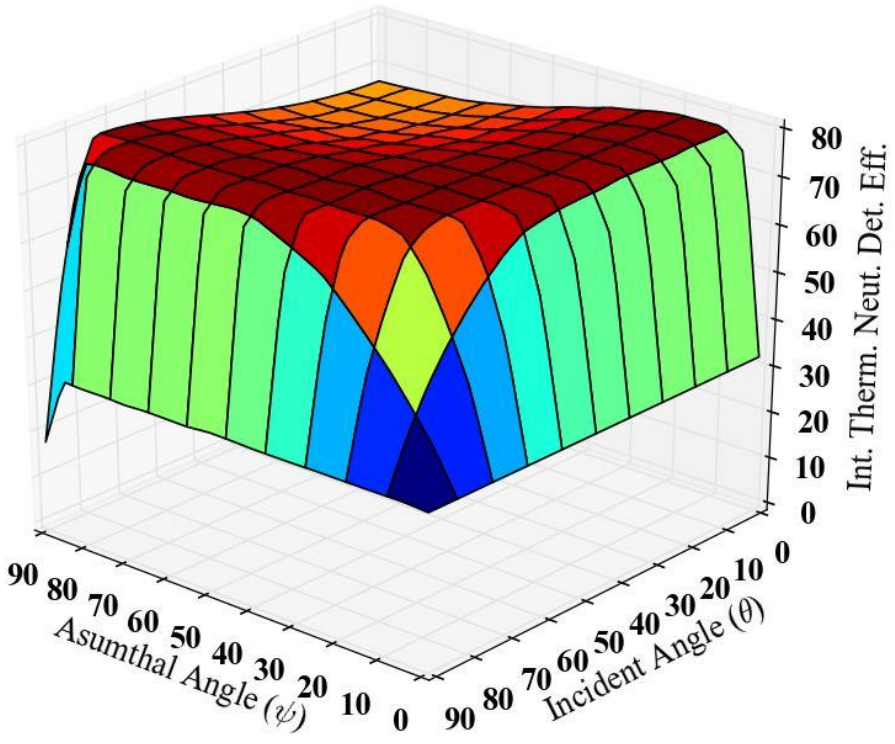

Fig. 5.3. Plotted is the intrinsic thermal neutron detection efficiency for an arbitrary DS-MSND device as the incident neutron angle is varied in both θ and ψ. Note the relatively small change in detection efficiency over a wide range of data points.

5.1. Arrayed MSND Detector Instruments

There is a need for radiation detection systems capable of determining the presence of low-activity and/or shielded radiation sources from a distance. These passive-type radiation detection systems require that the target under investigation naturally emit radiation and is often subject to low radiation emission rates, making detection of the materials difficult [29]. 'Stand-off' radiation detection is made difficult by three primary factors that each work to reduce the number of particles that can potentially reach a detection system. These factors include (1) time spent measuring the source, which is often short [80], (2) shielding between the source and the detector, which reduces the overall number of particles that can leave into the environment [30], and (3) the distance from the source to the detector, which geometrically reduces the number of particles that ultimately reach the detector system [30].

The two goals of a radiation detector system are: (1) to provide an accurate observation of a radiation source, possibly identifying where the source is and its composition and (2) should also determine whether to raise an alarm if required by the operator. These goals are accomplished by maximizing the number of counts reported. Uncertainty in a count rate measurement is inversely related to the square root of the counts recorded. In order to maximize the reported number of counts (and therefore minimize the uncertainty of the measurement), the detector must either increase the amount of time spent investigating the target, remove shielding from the target, and/or increase its fractional solid angle with respect to the target. In most cases, the investigator will not be in control of these factors and must work to improve the detection system itself. This is generally accomplished by using highly sensitive radiation detection systems or larger detection systems, both greatly increasing the response to a radiation source.

Until recently, MSNDs and DS-MSNDs were limited to small-area detector systems (as described previously in this Chapter). Although the intrinsic thermal neutron detection efficiency of these sensors is high, their small size (1 cm^2 or 4 cm^2 for single chips) inhibits their overall extrinsic neutron detection efficiency. Therefore, numerous MSNDs were arranged into arrays of devices, whereby all sensors were integrated together to function as a single, large-area detector system [21, 64]. An arrayed neutron detector was designed with two arrays of 1 cm^2 active-area MSNDs, each arranged in a 6 x 6 layout, and stacked to reduce streaming [21]. This single detector system, having an active area of 36 cm^2, was the first in a series of designs. The progression of this type of technology and the design importance are described in the following section.

5.1.1. The Panel Array Mk I (Year 2011)

The MSND-based Panel Array Mk I was developed as a successor to the stacked, arrayed neutron detector to both further increase the active area of the element and allow for tiling of the elements themselves, thereby, producing a large-area, modular detector system [81]. Each element of the Panel Array composed of sixteen 4 cm^2 single-sided MSNDs, each with an intrinsic thermal neutron detection efficiency of approximately 5-10%, arranged in a 4 x 4 configuration (Fig. 5.1.1) for a total active area of 64 cm^2. These elements could then be tiled laterally to increase the total active area, thereby, increasing the system's solid angle and extrinsic detection efficiency, or vertically to increase the intrinsic thermal neutron detection efficiency (Fig. 5.1.2).

The Panel Array Mk I assembly was composed of nine individual 4 x 4 elements arrayed in a 3 x 3 large-area array (Fig. 5.1.3), with a total of 144 cm^2 of active neutron detection area. The MSNDs were each mounted directly to FR4-based electronics boards which house the pre-amplifiers, amplifiers, discriminators, and digital-pulse forming electronics for the entire detector system (Fig. 5.1.3). Each diode has an associated pre-amplifier with a gain of 0.33 mV fC^{-1} charge

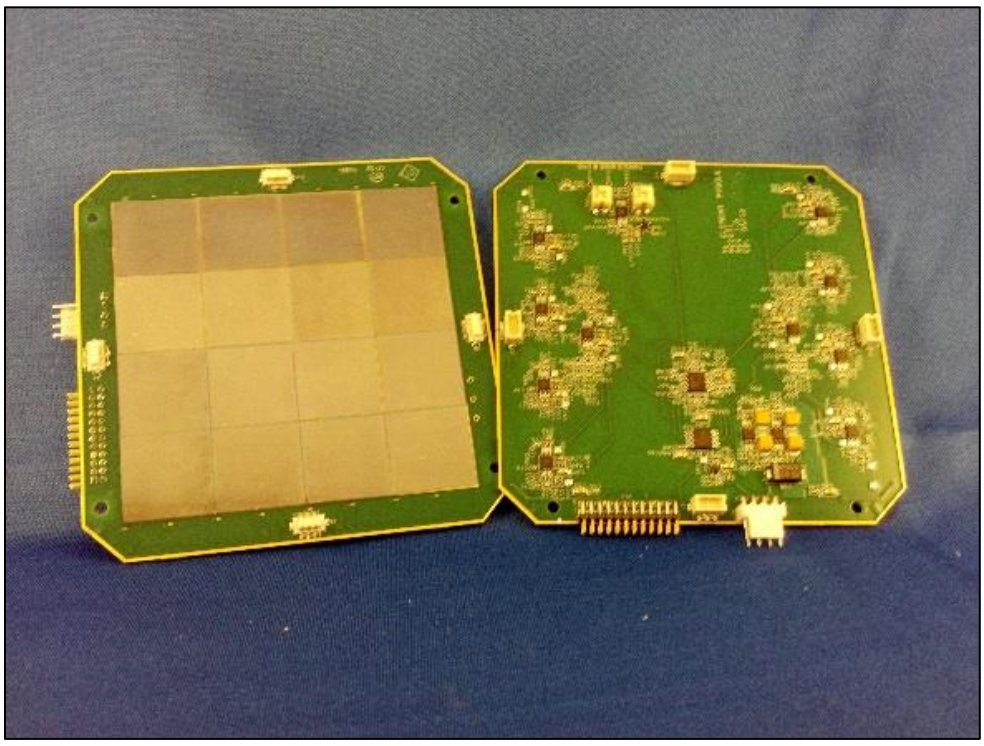

Fig. 5.1.1. Shown are two elements of the Large-Area Panel Array, front and back. Each element was populated with sixteen single-sided MSNDs, each with an active area of 4 cm^2. Shown (left) is the front side of the element and (right) the backside of the element. A single element contains all necessary signal-processing electronics.

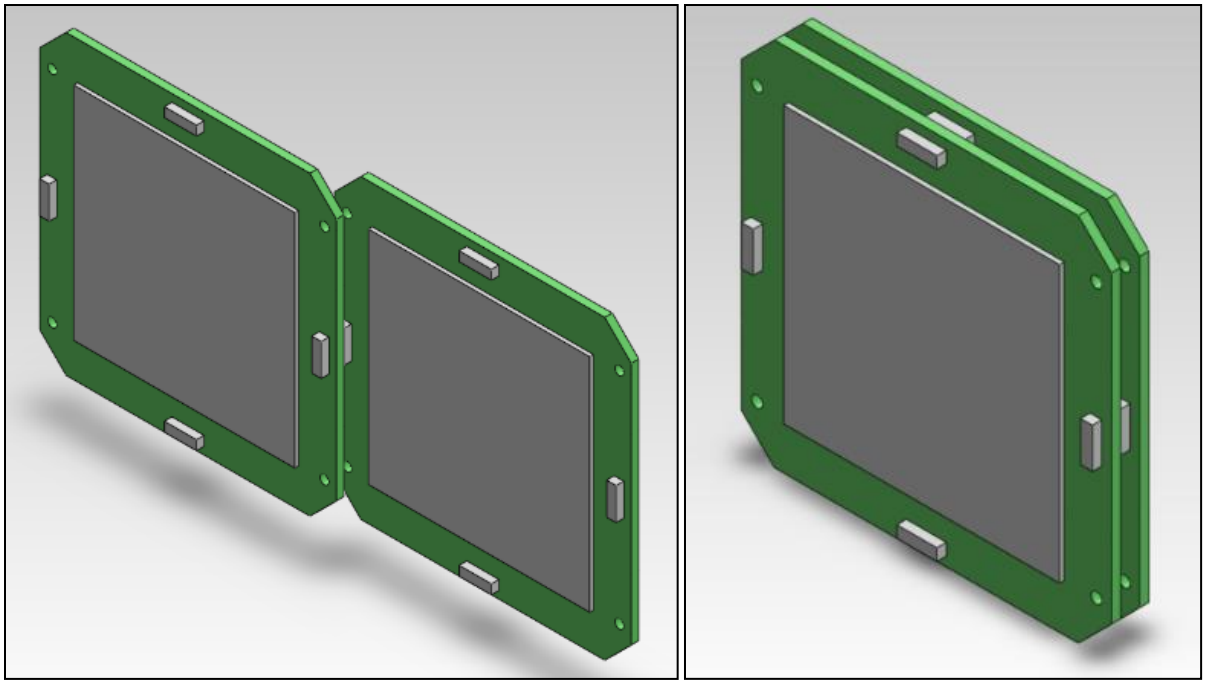

Fig. 5.1.2. (left) Panel Array elements could be tiled together laterally to increase active area, or (right) vertically to increase the intrinsic thermal neutron detection efficiency where large-area arrays may not be practical.

amplification [81]. On each detector element, the output pulses from four diode- preamplifier pairs were coupled to a single amplifier, reducing circuit complexity and power consumption. The charge amplifiers operated with a 43.3 V V^{-1} shaper gain and 15 μs time-constant [81]. In total, there were sixteen pre-amplifiers and eight amplifiers per 4x4 detector element with a total gain of 14.3mV fC^{-1}. Each diode of the detector elements was biased with -1V, and could be varied by the user from 0 volts to -5 volts. The on-board pulse-height discriminator provided a -3.3V logic level pulse when the analog output from an amplifier exceeded a user defined lower-level discriminator (LLD) value, and for the purposes of the described prototype, was set at 350 mV. The detector elements were powered by ±8V with a current draw of 4mA during operation, for a total current draw of 36mA for the Panel Array Mk I during operation.

The nine-element Panel Array Mk I were paired with a master signal summing board that combined the digital signal of each of the elements into a single digital output signal, and also served to condition and distribute power to the Panel Array Mk I. The digital outputs were accumulated by the motherboard where the digital signal was interpreted and read out on a physical display. The motherboard also transmitted its signal to an Android handheld device via Bluetooth using a proprietary phone application (Fig. 5.1.4).

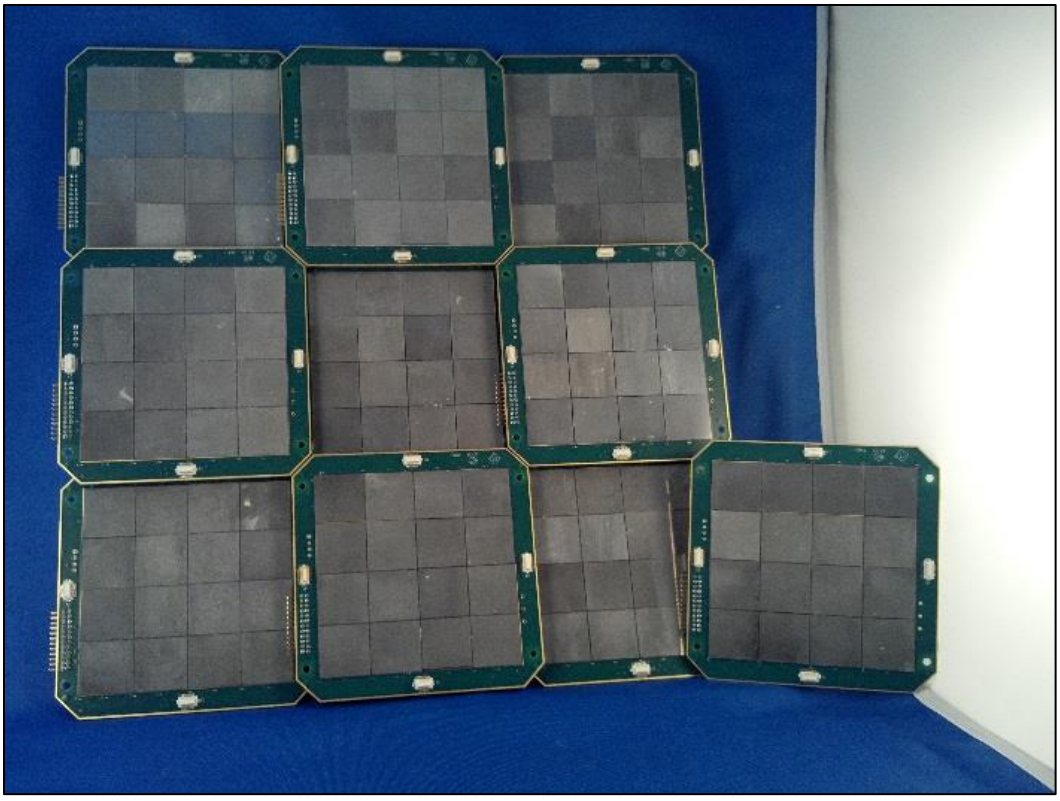

Fig. 5.1.3. The individual 4x4 elements were tiled into a 3 x 3 array and made to function as a single, large area detector with a total active neutron detection area of 144 cm^2.

The Panel Array Mk I suffered from performance issues related to poor detector efficiency and poor chip-assembly method. The single-sided MSND chips themselves were of low quality, in that most chips suffered from chipping of the fins (thereby, piercing and nullifying the blocking *pn*-junction contact), and excessive *p*-type contact dosage. The chipped fins and excessive doping of the top-side contacts greatly increased leakage current, which was often beyond 1 μA cm^{-2}, thereby, reducing the working applied bias. The greatly-reduced bias decreased the depletion depth of the device, both increasing device capacitance, and reducing sensitivity to incident reaction products. These effects combined to yield devices with a low intrinsic thermal neutron detection efficiency (σ_{th} < 5%), and poor signal-to-noise ratio. Furthermore, because the MSNDs were mounted directly to the electronics boards, forming the top-side electrical contact was difficult (Fig. 5.1.4), leading to intermittent connections and broken wirebonds. However, the advent of the Android phone application and Bluetooth capabilities allowed the device to be remotely operated up to 50 feet away, placing the user far from the irradiated zone, a feature that was new to this type of technology (Fig. 5.1.5).

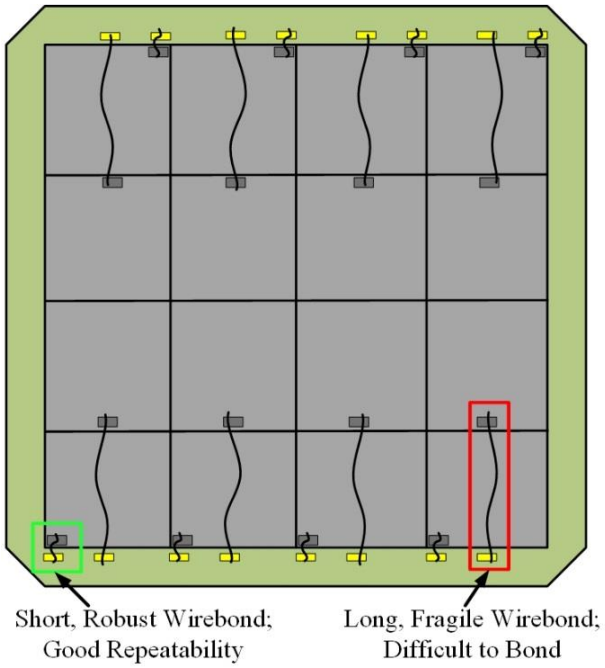

Fig. 5.1.4. Depicted are the two methods by which the top-side electrical contact was formed for each of the 4 x 4 detector elements. The short wirebond was easy to form and robust, while the longer wirebond was prone to breaking or forming intermittent connections.

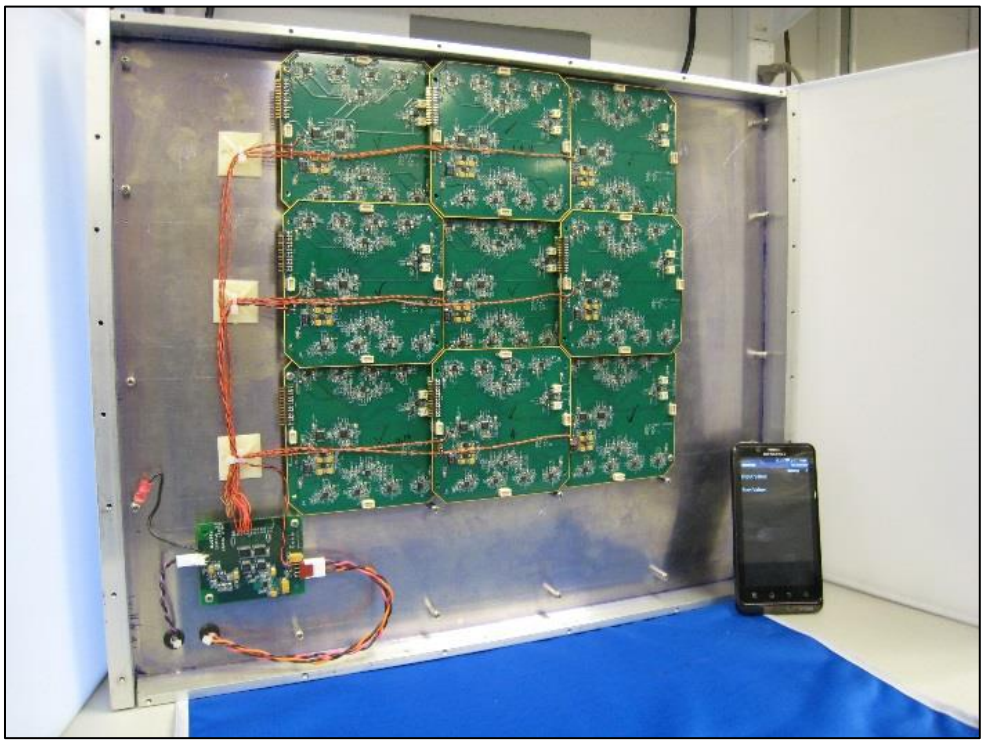

Fig. 5.1.5. The detector elements were powered using a separate power board, which also served to collect the counts reported by the detectors. Count rate information was transmitted to a handheld Android device via Bluetooth.

5.1.2 The Domino

Recent interest in scalable neutron detector instruments has motivated research for replacements of aging and expensive ^{3}He-base counters. ^{3}He proportional counters have historically been used for most neutron-detection instruments, from small hand-held counters, to large stationary portal monitors. Thus, the need for a small, scalable, ultra-low power, modular neutron detector package drove the development of the Domino [15, 82]. The Domino is a mass-producible, ultra-low power, compact, modular thermal neutron counter developed to deploy MSND sensors into detector instruments. The 'Domino' is a modular neutron detector system that is populated with four 1-cm^2 active-area MSNDs and all necessary supporting electronics (Figs. 5.1.7, left). The MSNDs are mounted to ceramic mounting packages and soldered directly to the Domino board (Fig. 5.1.7, right).

The Domino board is powered by a 2.9-5-volt input and contains pre-amplifying, amplifying, shaping, and pulse discrimination electronics, and TTL-driver for output signal. Output signal from the MSND is amplified and converted to a driven TTL pulse with a nominal width of 5-50 μs, and 5-volt amplitude. The Domino measures 2.5 cm wide by 3.8 cm tall and 0.47 cm thick, weighs 9.5 g, and has an active neutron-detector area of 4 cm^2. The compactness of the electronics package makes the Domino well suited for small hand-held detector instruments. The small detector volume allows for insertion into neutron moderator or arraying with other sensors.

Fig. 5.1.7. Shown (left) is the Domino™ modular neutron detector with its front-facing RF shield removed, and (right) displaying the four underlying 1-cm^2 active area MSNDs.

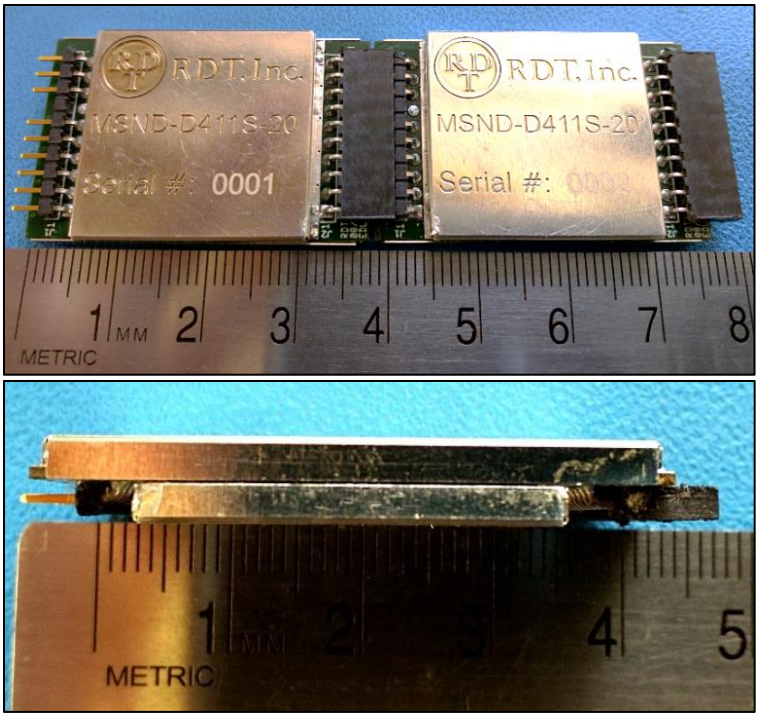

Fig. 5.1.8. The Domino™ can be linked (top) with other Dominoes™ to form long strings of detector systems up to 1 m. (bottom) Their low profile aids in instrument population.

Dominoes can be connected end-to-end (Fig. 5.1.8) to form long strings of detectors up to 1 m in length, which behave as a single detector. The strings of detectors can be tiled laterally to form an array of detectors up to 1 m^2 in area (Fig. 5.1.9) at a lower cost than modern ^{3}He instruments. There have been many iterations of the Domino™ neutron detector technology, each iteration leading to reduced power consumption, cost, and improved efficiency performance. Improvements in the amplification circuitry have reduced the power consumed by the detector by a factor of 3x, down to approximately 300 µW at maximum draw. Furthermore, the amplifier modification has produced better detector-to-electronics coupling, yielding better signal-to-noise performance. Finally, the bias and threshold electronics have been replaced with Inter-Integrated Circuit (I^2C)-based controllers, that reduces detector cost and complexity over the prior generations. These newer versions allow detector bias and counting threshold values to be adjusted digitally rather than replacing a physical resistor. Digital programming of these values simplifies the manufacturing process, thereby, promoting greater mass-producibility. The greatly reduced power, and simplification of device calibration represent a large advancement in MSND-based technology and for the Domino. The cost of the Domino has been reduced and performance greatly improved, indicating that the Domino will be capable of directly competing with ^{3}He counters.

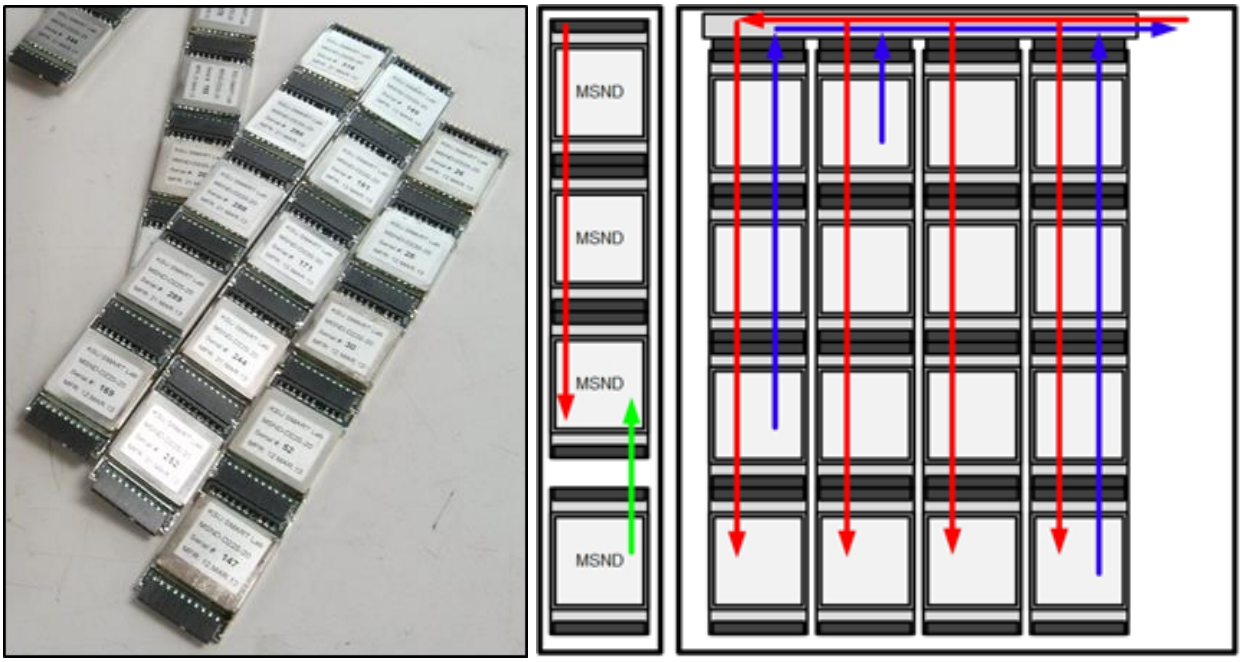

Fig. 5.1.9. Shown (left) is the Domino's capability to tile end-to-end and form a string of detectors. (middle) Power is provided to all Doiminoes in the string via a power pass through line (RED). If a count is produced within a Domino, then the signal is passed up the string (GREEN) and across any laterally tiled devices (BLUE).

The Domino's light weight and low power makes them ideal for deploying into environments where these factors are important. Dominoes were paired with a long-range reach back electronics package that could provide power to the Domino and transmit its output signal over large distances via Bluetooth. These versions were paired with a DJI Phantom quadcopter (Fig. 5.1.10). The wireless module (called the NeuStone) contained a single CR123 battery to supply the required 2.9-5 V to the Domino. The early-version Domino would then output its digital pulses that the NeuStone would then transmit to an iOS handheld device via Bluetooth. The prototype was deployed in a laboratory setting, showing that the NeuStone and Domino pair could operate remotely while mounted to a small remote-operated aircraft (Fig. 5.1.11). The aircraft was flown towards a concealed ^{252}Cf until counts were recorded. The craft could then land on the material of interest in order to aggregate more counts, thereby, increasing the certainty of the measurement. Once the investigation was completed, the aircraft was removed from the area, where then the count rate again returned to background. The concept showed that the Domino could be utilized in unique scenarios where other instruments may have difficulty, either due to their large size or due to their less-rugged construction.

Fig. 5.1.10. Shown is a Domino coupled with a wireless Bluetooth electronics package paired with a DJI Phantom drone for remote source investigation.

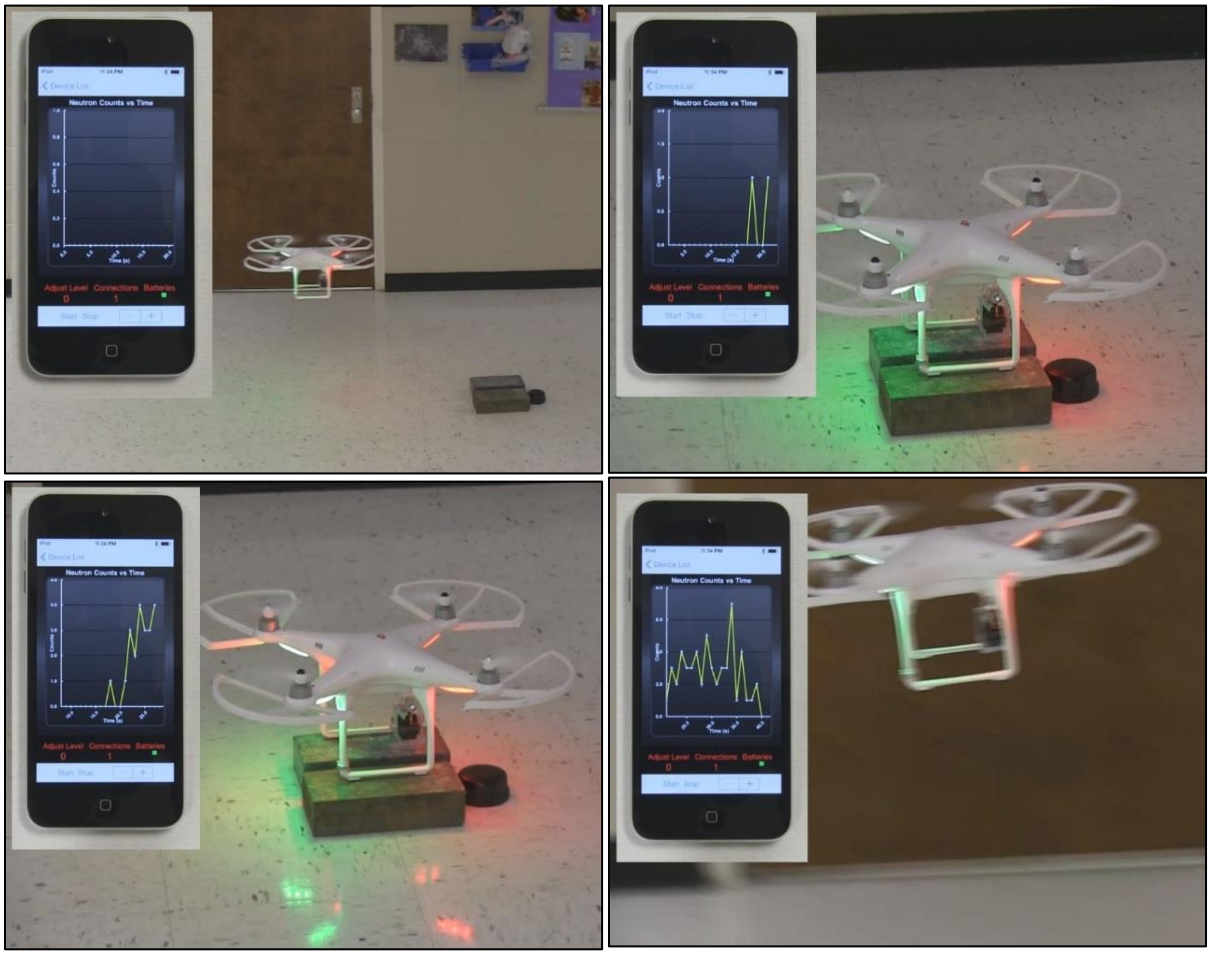

Fig. 5.1.11. (top-left) A DJI Phantom drone approaches a radioactive source with the Domino and NeuStone, reporting a low-background rate. (top-right) The drone has landed on the source and reports counts. (bottom-left) Counts continue until (bottom-right) the investigation is complete and the drone is removed.

5.1.3. The Briefcase Neutron Detector (Year 2013)

The Briefcase Neutron Detector (BND) was developed as a hand-held portable detector system [15, 82]. The BND supports up to 168 Dominoes, arrayed in two layers of twelve strings, each with seven Dominoes (Fig. 5.1.12). This array of Dominoes has an active neutron detection area of 336 cm^2 while maintaining hand-held portability. The Domino array was supported between two 1-in. thick sheets of high-density polyethylene (HDPE) to provide moderation for high-energy neutrons (Fig. 5.1.13) that are commonly emitted by spontaneous fission sources. The dimensions of the BND were 38-cm wide by 30-cm tall with a thickness of approximately 6 cm, including the neutron moderator. The with a total weight of the detector was 21 lbs. The BND utilized motherboards that summed the count rates reported by all of the strings of the system, outputting a single count rate, as described in Chapter 5.1. Presently, the BND is powered with a 5-volt input and has a maximum power draw of 0.3 watts. Based on the Domino detector technology, the BND also outputs a 5-volt TTL pulse. For testing purposes, the BND was powered with a standard wall plug, but could be made to contain its own battery.

Fig. 5.1.12. Depicted is the Briefcase Neutron Detector system. The system uses twelve or twenty-four strings of seven Dominoes tiled laterally to form a large-area, man-portable thermal neutron detector system. The Dominoes are sandwiched between two 1-in. thick sheets of HDPE moderator.

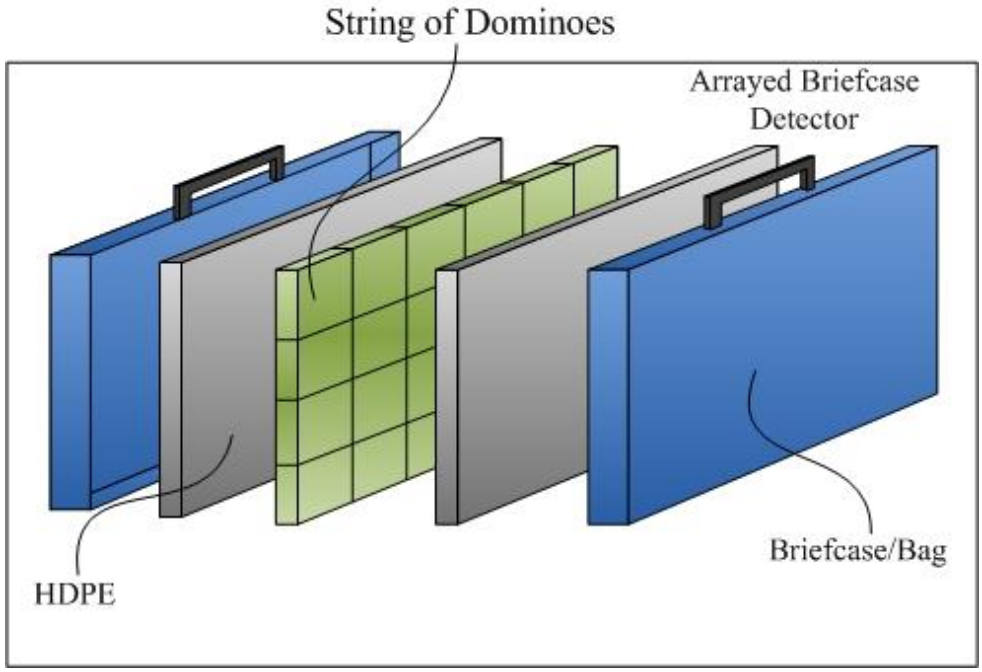

Fig. 5.1.13. Shown is an exploded view of the Briefcase Neutron Detector (BND) system. The array of Dominoes is sandwiched between two layers of HDPE moderator, and encased in a commercially-available briefcase.

5.1.3. The Panel Array Mk II (2013)

The Panel Array Mk II is a large-area, low-power, stationary neutron detector designed for large-distance standoff neutron detection. The array consists of 480 Domino detectors, arranged in 24 strings of 20 devices, 36-in tall by 36-in wide and a total thickness of approximately 2 in. (Fig. 5.1.14) [15, 82]. The Panel Array is sandwiched between and 1-in thick sheet (front) and a 1.5-in thick sheet (back) HDPE for neutron moderation (Fig. 5.1.14). Every four strings of Dominoes are managed by a 'smart' motherboard, forming a 'blade'. Count rate information from each the string is processed at the motherboard level. Counts are stored at that string's memory location on the motherboard until read out by the external LabView program, via an Aardvark I^2C USB interface adapter (Fig. 5.1.15). The counts for that string are then reset.

The program sweeps through each motherboard's string-count rate memory location and reads out the number of counts stored at each position, after which, the memory is cleared of its contents once per second. The program then sums the strings' counts for that one-second period to the histogram and then displayed to the user. 'Total counts recorded' and 'count rate' fields are also updated and displayed to the user. Each string can be read out individually, allowing for the capability to determine the azimuthal location of a neutron source at some distance from the detector.

Fig. 5.1.14. Shown is the Panel Array Mk II neutron detector system that utilized twenty-four strings of twenty Dominoes, sandwiched between two 1-in. thick sheets of HDPE moderator to form a 1 m x 1 m detector array.

Fig. 5.1.15. Shown (left) is the Panel Array Mk II outside of its aluminum housing. The array consists of five blades, each containing four strings of twenty Dominoes. The count rate data from each string is transmitted to a laptop with an Aardvark-controlled I^2C bus.

5.1.4. The Modular Neutron Detector (MND) Mk I

A recent need for low-profile neutron counters has led to development of a sensor package that falls between the Domino and the larger Panel Array systems. Thus, the Modular Neutron Detector (MND) Mk I was developed to fill this role. The MND Mk I is composed of twenty-four 1-cm^2 active area, single-sided MSNDs (Fig. 5.1.16), each with an intrinsic thermal neutron detection efficiency of approximately 30%. Presently, the MSNDs are tightly packed in the arrangement, thereby, reducing the overall dimensions of the sensor (measuring 2.4-in wide, 3.2-in long, by 0.2-in thick). However, the first-generation wireless module was considerably bulkier. The MND Mk I contains all of the necessary pulse-processing electronics to support the twenty-four MSNDs. The digital output signal from the discriminator electronics is communicated to an exchangeable communications board via I^{2}C protocol. The first generation MND was paired with a wireless communications board (Fig. 5.1.16) containing Bluetooth reach back electronics and power source (two CR123 batteries). The communications board wirelessly transmits count rate and detector identification information to the user on a handheld iOS device.

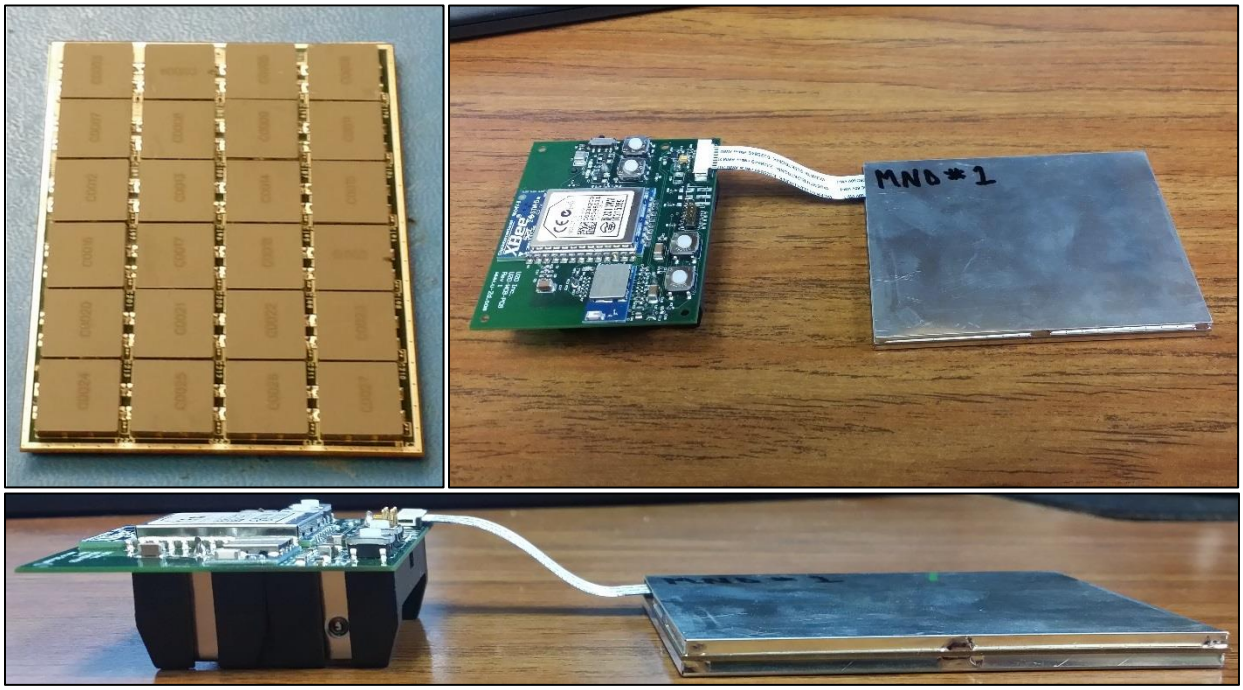

Fig. 5.1.16. The Modular Neutron Detector (MND, left) was designed as a means of filling many roles with a single detector design. Measuring approximately 2.5-in. wide and just over 3-in. long, the 0.2-in thick sensors can be coupled with a wireless electronic readout (right).

5.1.5. The Modular Neutron Detector Mk II (MND)

The Modular Neutron Detector Mk II (MND Mk II) is a technology developed in collaboration between Kansas State University and Alion Science and Technology Corp. as a continuation of the low-profile modular neutron counters. The MND Mk II element maintained its compact (< 5 mm thick), light-weight (< 55 g), low-power (< 4 mW), profile while increasing the detection efficiency and overall capabilities. The MND Mk II contains 24 cm^2 of Microstructured Semiconductor Neutron Detector (MSND) technology, each with a detection efficiency between 25-30%. The MND Mk II length was extended over the MND Mk I (Fig. 5.1.18, left) in order to add the capability to communicate directly with other detectors within a localized network. The interconnect was achieved using a detachable module (Fig. 5.1.18, right) called the Dongle. Each of the detector modules couple and communicate via a Controller Area Network (CAN) bus protocol [83]. Often utilized by automotive manufacturers, CAN bus allows multiple sensors to communicate nearly simultaneously on a single wiring harness, thereby, reducing the number of wires necessary in a wired configuration. CAN bus also provides for sensors to enter and exit the network, thereby, supporting field use where sensors may be added or removed while in service.

Fig. 5.1.18. Shown (left) is a comparison between the MND Mk I and Mk II. The length dimension was increased to accommodate additional communication and information capabilities. Shown (right) is a detachable communications module, the CAN Dongle.

Fig. 5.1.19. Shown (left) are two MND Mk II detectors coupled to CAN Dongles. The CAN Dongles allow the MNDs to connect to a local CAN bus communications network via USB-C cables. (right) The network is controlled and powered by the Master Control and Power Boards.

The CAN Dongle (Fig. 5.1.18) communicates with the I^2C controller on the MND to propagate the detector count rate, temperature, bias, and counting threshold information to a master controller, that then communicates back to the user. Detector bias and counting threshold can also be reprogrammed via the I^2C communications protocol through the CAN Dongle. The CAN Dongle connects to the network wiring harness via a Quad Board hub, a passive USB-C coupler (Fig. 5.1.19). The benefit of using industry-standard USB-C is the availability of the cables, their low cost and complexity, and durability of the cables. The Quad Board then passes the signal to the next Quad Board until, ultimately, the connection is made to the Master Control Dongle (Fig. 5.1.19). There is no difference between the Master Control Dongle or the CAN Dongle in terms of hardware, however, the Master Control Dongle Contains the firmware necessary to initialize the CAN bus and serve as the communications hub for the entire local network (Fig. 5.1.20).

The counts reported by each MND in the network is aggregated once per second at the Master Control Board, which is then organized into a repeated output string, and reported to the handheld Android device. The output string from the Master Controller Board to the handheld contains bytes, occupied by hexadecimal-digits for each MND connected to the network,

$$[\text{Mac ID}][\text{Thresh. Volt.}][\text{Bias Volt.}][\text{Temp}][\text{Cts.}][\text{Spare}], \qquad \text{Eq. 5.1.1}$$

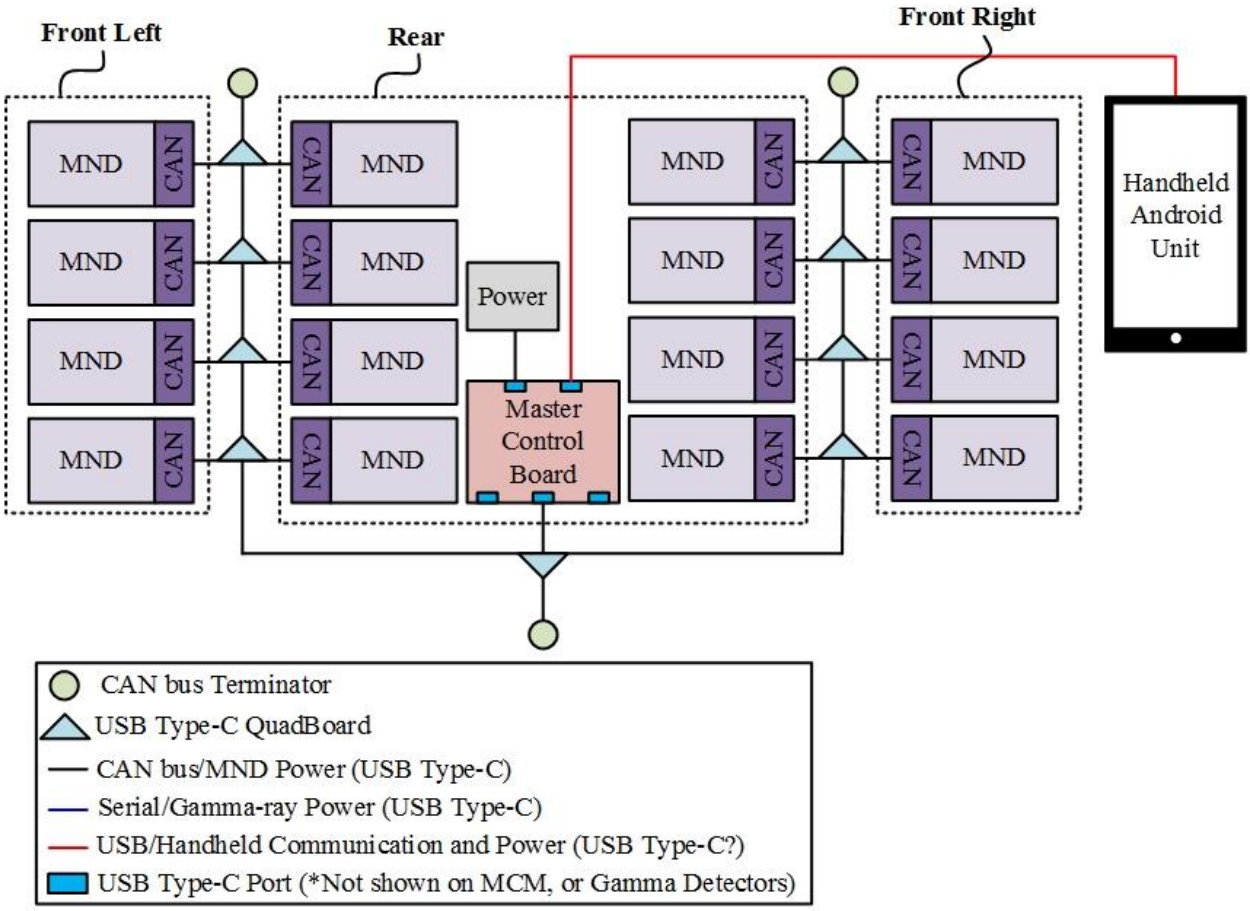

Fig. 5.1.20. Shown is a schematic of a complete network of MNDs arranged into a networked configuration. This configuration contains sixteen MNDs, each paired with a CAN Dongle. Two MNDs are each then connected to a single Quad Board, which then passes the signal upstream, ultimately to the Master Control Board. The Master Control Dongle on the Master Control Board then sends the output string to the handheld Android device.

where [Mac ID] is a four-byte identification number of each individual MND within the network, read from an on-board serialization chip integrated within the MND. The two-byte [Thresh. Volt.] reports that MND's threshold voltage required to trigger a digital count, and the next two-byte field [Bias Volt.] is the global bias applied across each MSND. The MND also reports a two-byte [Temp] field that may be used for threshold and bias adjustment by some algorithm. Finally, there is a two-digit [Cts.] field that reports the number of counts stored on the MND during the one-second integration period and is reset during each reporting period.

5.2. Helium-3 Replacement (HeRep) Instruments

The high cost and waning availability of ^{3}He gas has been steadily driving up the overall costs of the detectors that use this gas. ^{3}He proportional neutron detectors are widely used for everything from stationary, large-area portal monitors to portable handheld REM meters. The recent push for replacements for these ^{3}He-based detector technologies has motivated of the research into developing the high-efficiency, low-cost, low-power Microstructured Semiconductor Neutron Detector (MSND)-based ^{3}He-Replacement (HeRep) detectors.

MSND-based neutron detectors designed to replace ^{3}He counters have the unique benefit of being able to contain moderator material within the detector canister alongside the detectors. ^{3}He proportional counters cannot contain moderator within the gas detection volume, because that area is dedicated for detector gases and electrodes. In other words, putting moderator within the detector volume would eliminate charge collection and render the detector inoperable. Thus, moderator is housed around the outside of the detector, thereby, increasing the bulk of a ^{3}He detector. MSND-based HeRep devices are generally housed in an aluminum casing that can contain granular HDPE, effectively filling the voids between the MSND strings with neutron moderator. Filling the detector voids with neutron moderator acts to scatter neutrons streaming between MSNDs, potentially scattering them back into an MSND to be counted, as shown in Fig. 5.2.1. The additional moderator within the detector also has the added benefit of providing more material with which to thermalize higher-energy neutrons, thereby, reducing the amount of outer moderator material.

5.2.1. The Helium Replacement Mk II (HeRep Mk II, Year 2014)

The MSND-based ^{3}He-replacement (HeRep) Mk II neutron detector is a cylindrical thermal neutron detector designed as an alternative to aging and increasingly expensive ^{3}He proportional neutron detectors, and represents the next iteration of MSND-based ^{3}He-replacement technologies over the HeRep Mk I [14]. The HeRep Mk II was designed to be able to directly replace a Reuter Stokes 6-in. long by 2-in. diameter ^{3}He proportional counter, pressurized to 4 atm (Fig. 5.2.2). The HeRep is populated by thirty MSNDs, each with a tested intrinsic thermal neutron detection efficiency of at least 20%. The MSNDs are tiled onto six strings, five MSNDs per string (Fig. 5.2.2), and then arranged in a hexastrip pattern to minimize neutron streaming through the HeRep

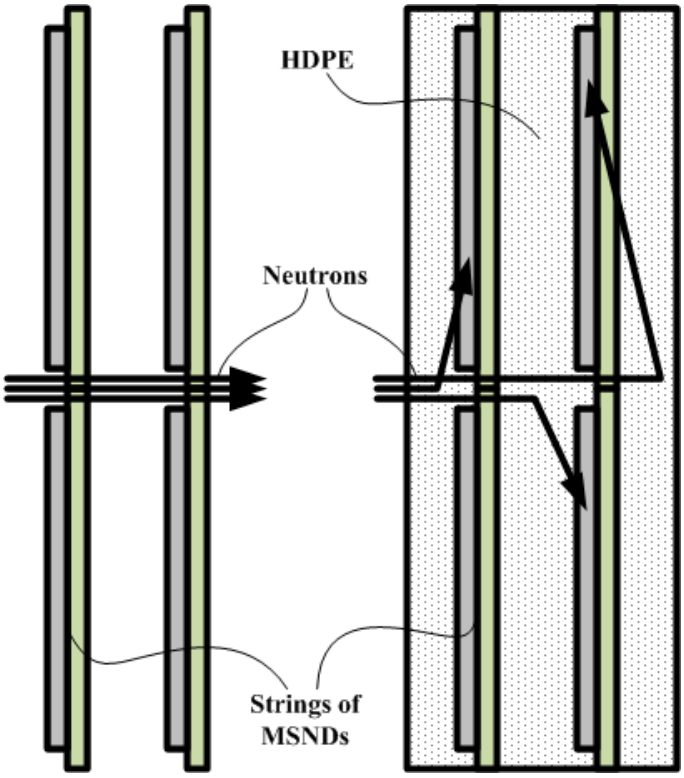

Fig. 5.2.1. (left) Neutrons traversing the HeRep can stream between MSNDs on the strings; however, the void regions within the outer casing can be filled with HDPE moderator (right) to scatter streaming neutrons back into an MSND without compromising detector integrity. The additional material also provides a means to thermalize incident neutrons, thereby, increasing the sensitivity to higher-energy neutrons.

detector (Fig. 5.2.3). The benefit of the hexastrip layout is threefold; the layout increases MSND packing density, eliminates neutron streaming paths through the detector, and provides a uniform angular response to incident neutrons. The HeRep Mk I, in comparison, arranged sixty-four 1-cm^2 MSNDs in a circular pattern for a total active MSND area of 64 cm^2 [84]. The HeRep Mk I was not able to outperform the aforementioned ^{3}He counter, due to poor detection efficiency of each detector and poor packing density of the MSNDs. The HeRep Mk II features an upgraded design that utilizes the same external dimensions, yet improves the sensor density within the device. Although the HeRep Mk II contains only thirty 4-cm^2 MSNDs, a total active MSND area of 120 cm^2 is achieved using larger, 4-cm^2 active area diodes. The total device active area was almost doubled for the Mk II while the number of devices was reduced by half. Fewer MSNDs requires fewer supporting electronics, thereby, greatly reducing detector cost, complexity, and power draw. The HeRep Mk II system is powered with a 12V DC power source and draws a maximum of 130 mA during peak counting rates of 10,000 cps and requires only 30 mA while at rest.

Fig. 5.2.2. The second generation Helium-3 Replacement (HeRep Mk II) detector was developed in 2013 and refined in 2015. The HeRep Mk II was populated with thirty 4-cm^2 active area MSNDs, each with an intrinsic thermal neutron detection efficiency of 20% (and later 30%), arranged in six strips of five sensors each. The detector was intended to directly replace a 2-in. diameter, 6-in. long ^{3}He pressurized to 4 atm.

The bias voltage applied to each MSND and the global counting threshold of the detector are externally adjustable by the user. A control box allows the user to modify the discriminator threshold from 0 volts to 2 volts in increments of 4 mV, and the bias can be adjusted from 0 volts to 5 volts in 200-mV increments (Fig. 5.2.4). Once the device is fully programmed with the threshold and bias settings, the programing box can be removed from the system and the HeRep Mk II device on-board memory maintains the settings until they are again modified. Neutron measurements are made in a similar fashion to the strings of Dominoes that populate the Briefcase Neutron Detector and the Panel Array Mk II systems. Bias is applied across each MSND through the string. A neutron event in a given MSND generates a voltage pulse within that MSND's pre-amplifier. The shaper-amplifier then processes the pulse from the pre-amplifier and a discriminator reads the final voltage of the pulse. A 3.3V TTL positive square pulse is generated by the discriminator, should the pulse exceed the threshold, which aggregates at the motherboard. The motherboard contains an on-board signal driver system that amplifies the TTL pulse to 5 volts and couples it with 50 Ω-impedance systems. The driver unit can drive the final 5-volt TTL pulse through an SMA connector through 15 m of R58 cable.

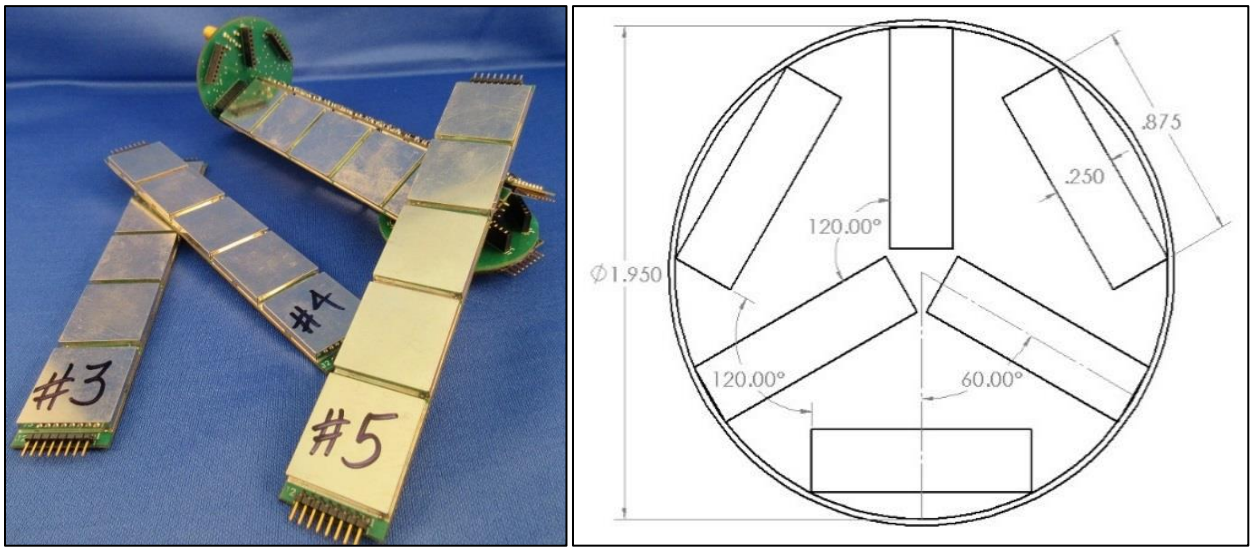

Fig. 5.2.3. The cylindrical design is not optimal for packing MSNDs into a system, however, the arrangement of the six strips reduced the possibility of neutron streaming and allowed for the inclusion of moderator in the gaps between the detectors.

Fig. 5.2.4. The HeRep control box allows for a user to program the applied bias and the threshold settings for the entire HeRep device. Applied bias can be globally adjusted from 0 V to 5 V in 0.2 V increments, and the discriminator threshold values from 0 V to 2 V in 4 mV increments. The programing box can be removed from the system following the settings adjustment.

5.2.3. The Helium Replacement Mk III (HeRep Mk III, Year 2015)

A next-generation MSND-based detector was developed to meet a demand for compact, small-diameter ^{3}He replacement. The HeRep Mk III (Fig. 5.4.3) was designed and populated with improved 1 cm^2 active-area dual-sided MSNDs (DS-MSNDs) [19, 20], each with intrinsic thermal neutron detection efficiency, $\varepsilon_{th} \geq 50\%$. The HeRep Mk III has two strips of six detectors each and has overall dimensions of 0.75 in. by 4.5 in. The detector is powered with a 5-volt input, drawing a maximum of 15 mW. Similar to the new-generation Domino, the detector threshold is programmed via an on-board I^{2}C circuit. The built-in potential operates the detectors; hence an external bias is unnecessary for these DS-MSNDs [76]. Counts originating in a DS-MSND are processed in the accompanying pre-amplifier/amplifier electronics. Counts are collected and digitized at the dual-sensing discriminator at the top of the detector package. The dual-polarity nature of the signal produced in the DS-MSNDs necessitates the use of dual-sensing discriminator electronics. Separate discriminators are needed to measure the pulse amplitude for positive and negative pulses, as a single discriminator is unable to measure both. The major drawback of this arrangement is that power and board-footprint area that are required are both increased.

The HeRep Mk III was designed with the intention of filling the intermediate role between modular sensor support (i.e. the Domino) and larger instruments such as the Panel Array or HeRep Mk II. Such an instrument would likely be integrated into a hand-held type unit and integrated with other sensors to provide a compact, ultra-high efficiency radiation detection package. The compact nature of the HeRep Mk IV, the ultra-high efficiency of the DS-MSNDs populating the device, and the low-power operation (i.e. < 15 mW at full counting rate) make this instrument ideal for low-cost handheld instrumentation.

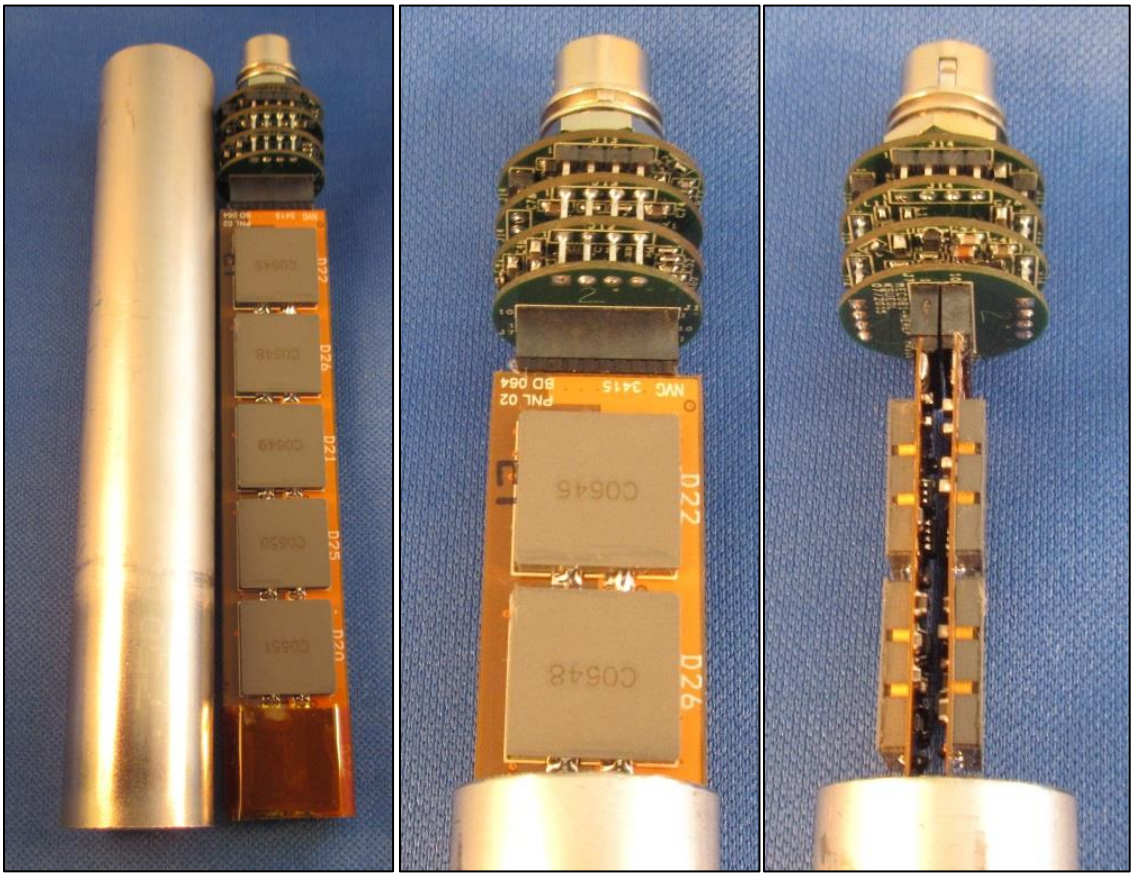

Fig. 5.4.3. The third generation Helium Replacement (HeRep Mk III) was developed primarily as a test bed for the DS-MSND sensor. The HeRep Mk III was populated with twelve DS-MSNDs arranged in two strips of six detectors (left). The detector measured 0.75-in. in diameter by 4.5-in. long, and was intended to match the performance of a 6-atm ^{3}He counter of similar dimensions.

Chapter 6 - *DS-MSND and Instrument Testing*

DS-MSNDs undergo numerous tests throughout fabrication to ensure that they will pair well with signal processing electronics and that they meet neutron detection efficiency requirements. Damage to diodes during dicing, extraction, or handling can cause increased leakage current or otherwise produce mechanically fragile detectors. DS-MSND diodes are tested for leakage current, capacitance, and neutron sensitivity numerous times during fabrication as there are many steps that can possibly destroy a device. Two major generations of DS-MSNDs were produced and tested from *v*-type material, shown in Fig. 6.1: 1) *pvn*-type, wherein a *p*-type contact was formed on the top side of the diode and an *n*-type contact was formed on the bottom side, and 2) the *pvp*-type wherein both the top and bottom surfaces of the diode were doped with *p*-type contact material. Described in the following section are the testing processes for both DS-MSND sensors and instruments.

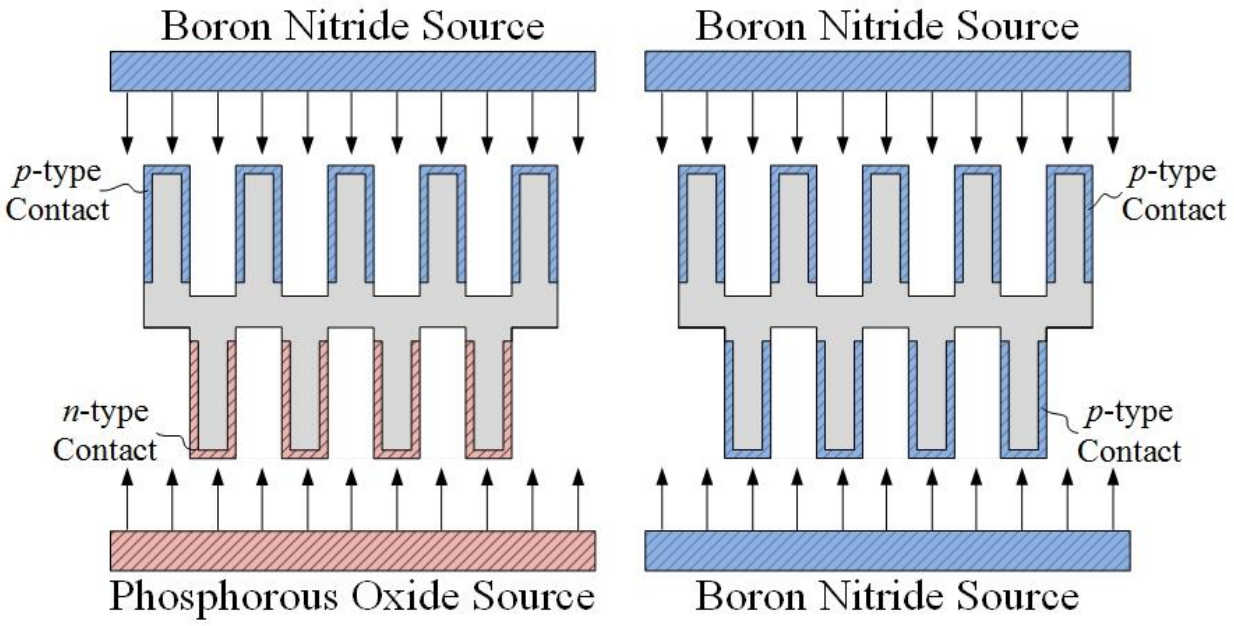

Fig. 6.1. Depicted are generalizations of the two types of DS-MSND explored, (left) the pvn-type wherein top-side fins are doped with B to form a heavy p-type contact, and bottom fins are heavily doped with P to form an n-type contact. (right) The pvp-type DS-MSNDs have both the top-side and bottom-side fins that are doped with heavy p-type B.

6.1. Electrical Characteristics

MSND and DS-MSND sensors must be paired with signal amplifying electronics (such as a pre-amplifier/amplifier pair) in order for the small signal produced by the motion of the charge carriers to be measurable. Design of signal amplifying electronics to match with DS-MSND and MSND sensors is necessary to avoid excessive electronic noise, false counts, signal ringing, and signal oscillation [38]. Thus, it is necessary to understand the electrical characteristics of the MSND and DS-MSND sensors to support proper electronics design.

There are two primary electrical characteristics of concern for solid-state sensors in terms of electronics development: 1) device leakage current (or dark current) and 2) device capacitance. Leakage current, largely a consequence of thermal carrier generation within the bulk of the depletion region, manifests as low-level noise within the detector system. Leakage current also determines the maximum applied bias that the diode can sustain. Higher leakage current yields noisier devices that have a reduced ability to sustain an applied bias. Leakage current is measured and characterized by applying a bias across the diode and measuring the resulting current within an electromagnetically shielded dark box [40]. A current versus voltage (IV) curve can be produced by incrementing the applied bias and subsequently measuring the resulting dark current.

Diode capacitance is important in maintaining a good pulse-height per charge induced within the depletion region, as increased capacitance (C) will reduce the pulse height induced by the charge motion per given amount of excited charge, (Q), where $V = Q/C$. The RC time constant for pulse-processing time is also dependent on the total capacitance [40]. Capacitance measurements are performed by rapidly oscillating an applied bias and measuring the change in the resulting current, thereby, allowing for determination of the device RC constant and thus the capacitance of the device.

6.1.1 Electrical Testing Results

The early generation of DS-MSNDs were fabricated with contact dopant profiles similar to single-sided MSNDs. The top-side fins were heavily doped with *p*-type impurities, while the bottom-side fins were doped with *n*-type impurities. It was hoped that this dopant configuration would be best suited for holding an applied bias, thereby, being able to drift induced charge carriers efficiently. Leakage current and capacitance measurements of these diodes were conducted in the

same manner as common solid-state diodes [40]. These devices showed good electrical characteristics, as depicted in Fig. 6.1.1 and devices from the same wafer yielded similar capacitance characteristics, as shown in Fig. 6.1.2 [19], yielding approximately 5 nA cm^{-2} leakage current and 95 pF capacitance at an operational bias of -3 V.

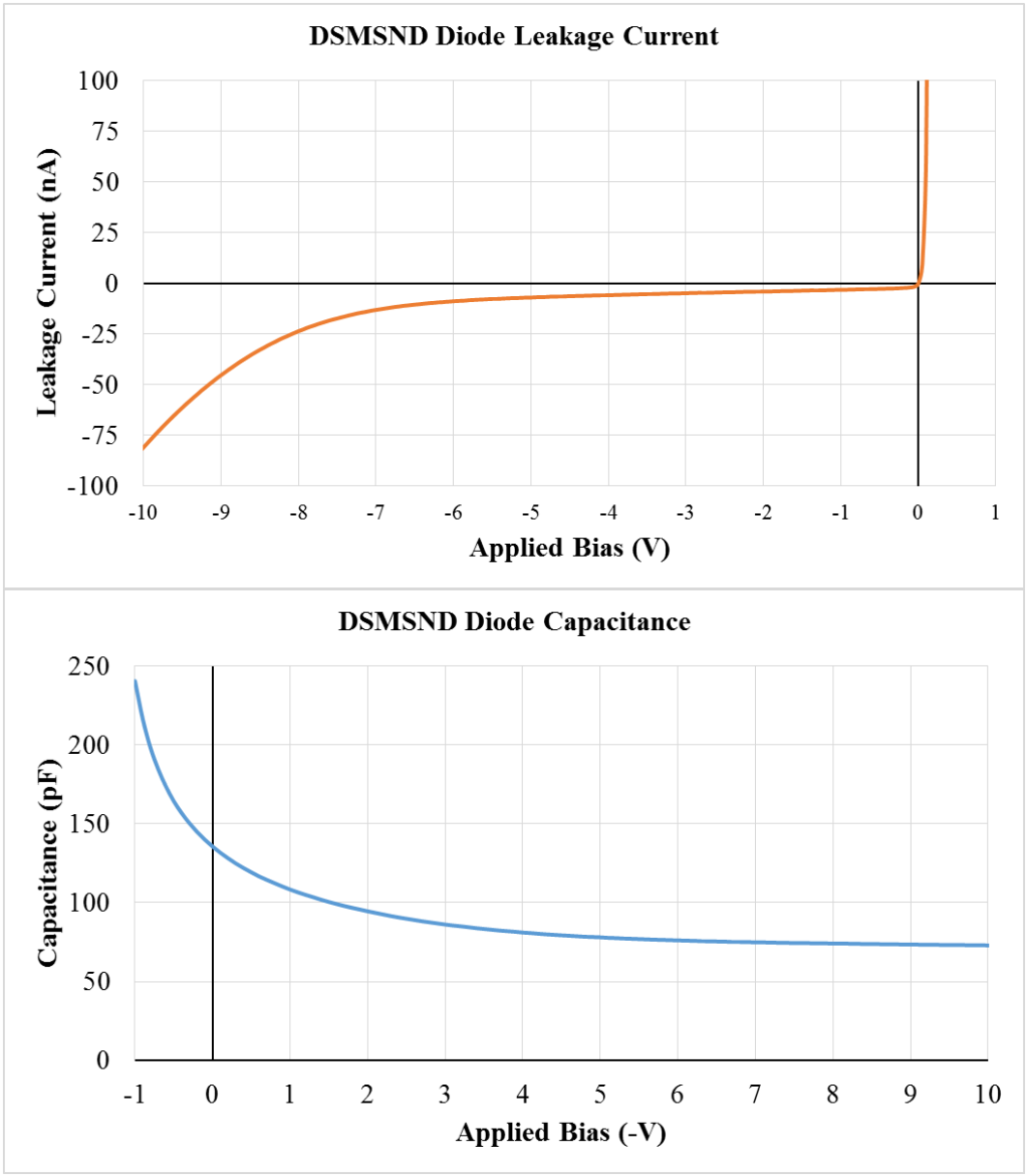

Fig. 6.1.1. Plotted are (top) IV- and (bottom) CV- curves for a typical first-generation pvn-type DS-MSND. These devices had good electrical characteristics, yielding <5 nA cm^{-2} and <95 pF at their -3 V operational bias.

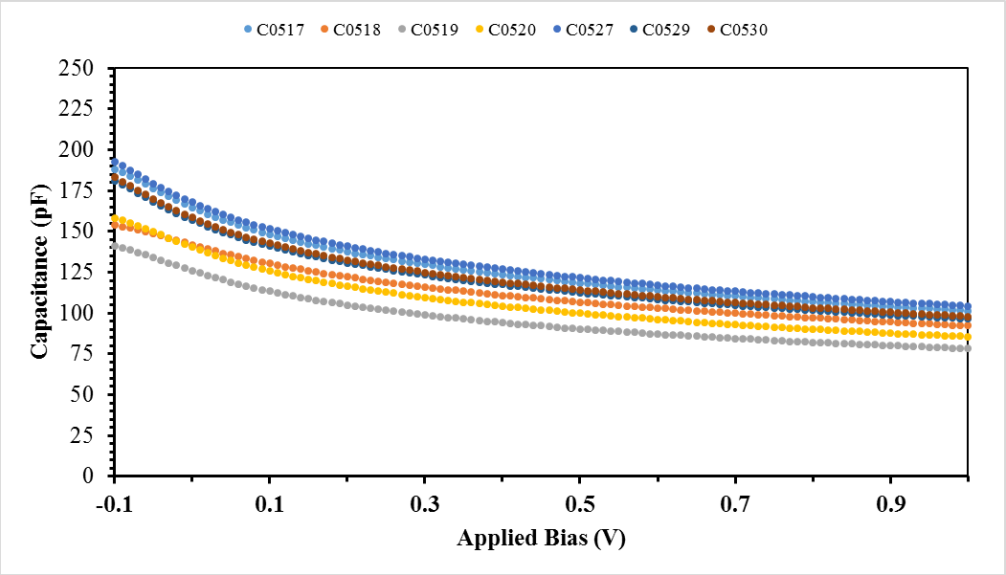

Fig. 6.1.2. Plotted are the CV measurements for several first-generation pvp-type DS-MSNDs sampled from a single wafer. Generally, it is ideal for diode capacitance to be under 100 pF per cm^2 to maintain a good signal-to-noise ratio. Note that these diodes have a generally higher than desired value.

6.2. Charge Collection Efficiency

The basic device structure has microscopic trenches etched into a vertically-oriented *pvn*-junction semiconductor diode which are backfilled with a neutron conversion material. Neutrons absorbed within the conversion material produce energetic charged-particle reaction products with appreciable kinetic energy. When these reaction products intersect the adjacent semiconductor material, they excite electron-hole pairs that subsequently produce an electronic pulse, thereby, indicating a neutron event. The pulse magnitude and rise time is dependent on the charge collection efficiency, charge carrier velocities, and drift distance. Induced current that is terminated prematurely by the shaping time of the counting electronics, commonly referred to as "ballistic deficit", consequently produces smaller pulses than ideal. A collimated alpha-particle source was used to develop a method to characterize the charge collection dependence within the semiconductor materials, shaped as fins, and also the required charge integration times.

Theoretical predictions indicate that MSNDs should be capable of higher efficiencies than presently measured through experimentation, with theoretical values exceeding 32% for a single 0.5-mm thick device [12]. Differences between theoretical and measured values become apparent when comparing theoretical and experimental pulse-height spectra. Measured reaction product

spectra are often shifted to lower energy bins than theoretically predicted, and the spectral features are often broadened as a consequence of non-uniform charge-collection efficiency within the MSND fin, as shown in Fig. 6.2.1. Electron-hole pairs produced within the upper portion of semiconductor fins of the MSND are less likely to reach the anode during a given relatively short shaping time than those electron-hole pairs generated within the lower regions of the semiconductor, closer to the anode, due to finite drift velocities. However, energy deposition in the tops of the fins is more probable, as shown in Fig. 6.2.2, due to increased neutron interaction in the upper portions of the trenches. Neutron interaction rates within the conversion material reduce exponentially for a normally-incident beam of neutrons; therefore, electron-hole pair production rate is higher in the upper portions of the fins. Understanding to what extent this charge loss affects signal output is important in order to provide optimal coupling of MSNDs to counting electronics.

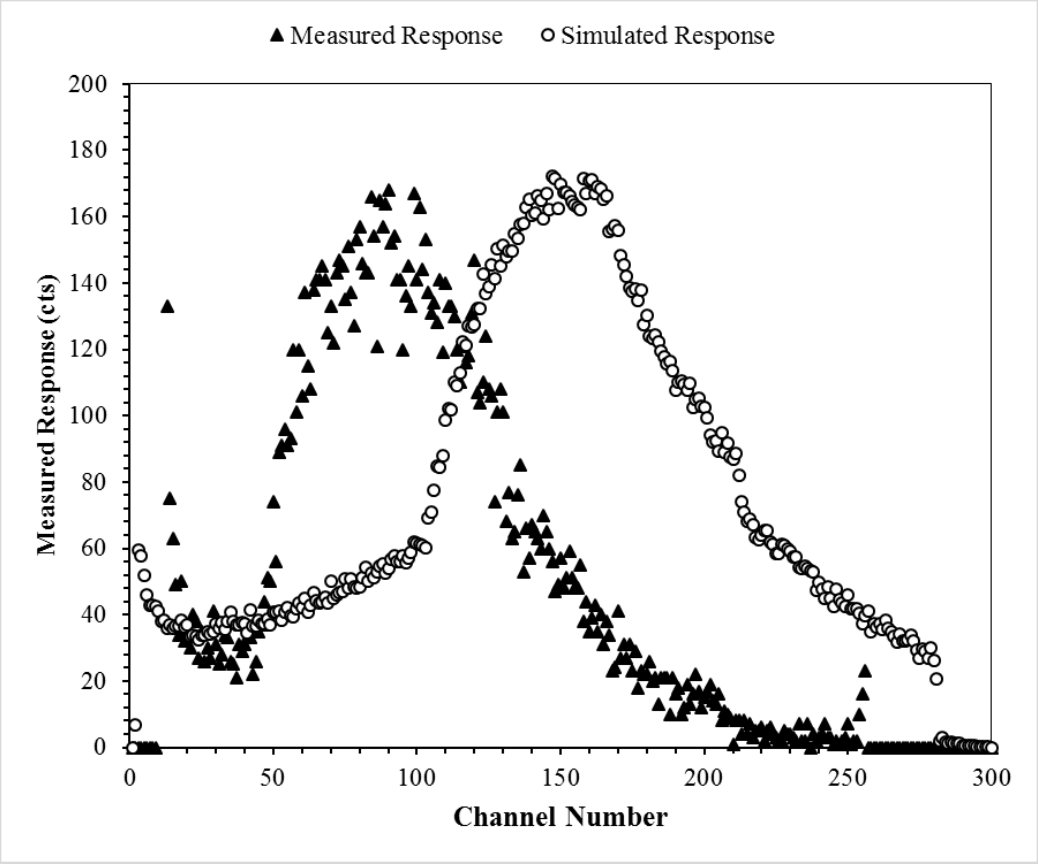

Fig. 6.2.1. Depicted are reaction-product spectra experimentally collected from a thermal neutron measurement using a single-sided MSND (dark) and a MCNP6 simulation (light). Although the predicted features are apparent, the down-shifted measured spectrum indicates charge loss, primarily from ballistic deficit.

A method to measure the charge collection efficiency with respect to the vertical irradiation location along a fin was developed to quantify this phenomenon. This analysis allows for adjustments in theoretical performance models so as to improve predictive models for detection efficiencies. Further, an improved understanding of the pulse shaping dynamics may allow for optimization of detector and electronics performance. Two measurements were conducted in which a MSND without neutron reactive material in the trenches was irradiated with a collimated alpha-particle source at angles of 0° and 45° with respect to the normal face of the detector, as shown in Fig. 6.2.3. At an angle of 0°, alpha particles deposited energy into both the tops of the fins and at the bottoms of the trenches. At an angle of 45°, however, energy was deposited primarily near the tops of the fins without depositing energy deep into the trench.

The initial tests were performed using single-sided MSNDs (although this technique is also applicable to DS-MSNDs). An MSND with leakage-current less than 10 nA cm^{-2} and diode capacitance less than 100 pF was paired with an Ortec 142A pre-amplifier and Canberra 2022 amplifier and biased to -2.6 V. Pulse-height data was collected with an Ortec Easy-MCA. A collimated ^{241}Am alpha-particle source was positioned above the diode to irradiate the surface of

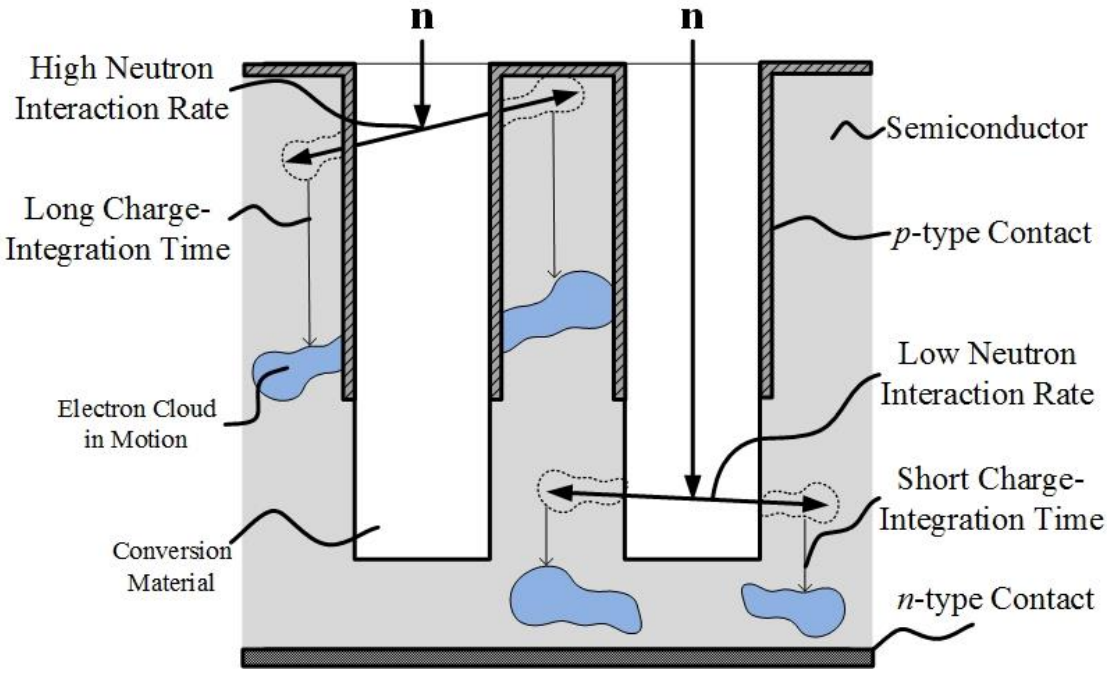

Fig. 6.2.2. Depicted is a cross-section of an MSND, in which two possible neutron interaction cases are shown. Charges excited in the lower portion of the fins, as depicted for the interaction case on the right, are quickly collected by the applied potential.

the MSND, normal to the face of the detector, as shown in Fig. 6.2.3. Pulse shaping times were varied from 0.5 μs to 12 μs to observe the effect of shaping time on the charge collection of the signal that originated in the fins, as shown in Fig. 6.2.2. At the 0° orientation, roughly half of the emitted alpha particles strike the tops of the fins and half strike the bottoms of the trenches. The alpha-particle source was repositioned to the 45° irradiation angle from normal, also shown in Fig. 6.2.3, ensuring that no alpha particles could interact deep in the trenches, but instead were confined to the uppermost regions of the semiconductor fins. A final measurement wherein the trenches of the MSD were backfilled with paraffin wax was conducted with the ^{241}Am source located at the 0° position. All measurements were performed in air in an electromagnetically-shielded and light-shielded container.

During these measurements, it was assumed that all charge carriers excited by α particles impacting the bottoms of the trenches is fully collected for the pulse-shaping times used in the experiment, mainly due to the relatively short drift path to the anode. Thus, those energy peaks

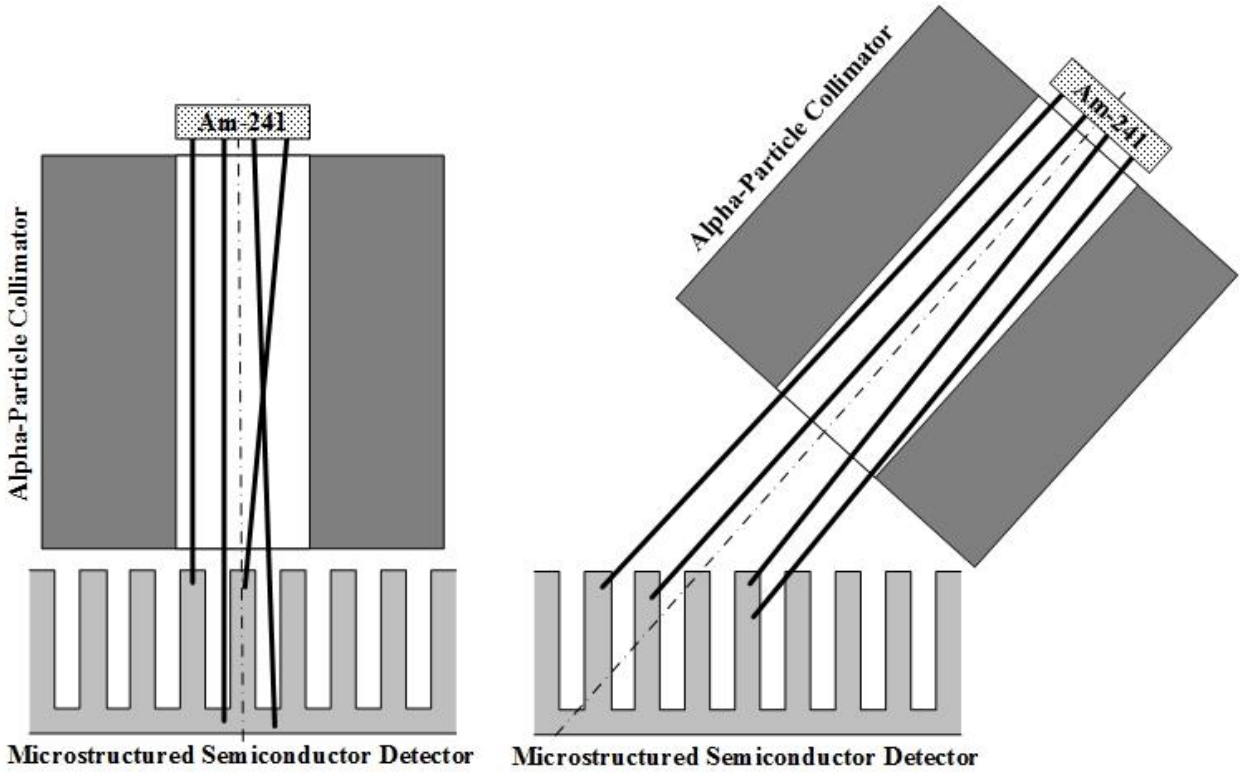

Fig. 6.2.3. Depicted are representative collimated alpha-particle paths for the 0° (left) and 45° (right) irradiation scenarios. For the 0° case, roughly 50% of the emitted particles should interact within the tops of the fins, and 50% at the bottoms of the trenches. For the 45° case, all of the particles interact within the upper portion of the fins.

produced from α-particle interactions at bottom of the 350-μm deep trenches can be considered to be the 'true' full-energy peak, with their pulse heights representing the full energy of the incident particle. Any features generated below this peak are assumed to represent charge loss due to shaping-time cutoff and/or attenuation through the dead diffused regions on the edges of the fins. It is also assumed that there is negligible charge loss due to recombination based on the relatively long charge carrier lifetimes of the material, which are on the order of milliseconds, and also the relatively-high charge carrier mobilities for high purity Si.

The effect that shaping time has on the resulting pulse-height spectrum is shown in Fig. 6.2.4. The 'true' full-energy peak does not shift any appreciable amount for each of the shaping times applied during the experiment, justifying the assumption of negligible charge loss for α-particle interactions occurring at the bottoms of the trenches. However, as the shaping time is incrementally increased from 2 μs to 12 μs, the 'false' full-energy peak rises in channel number, representing higher charge-collection efficiency for long charge-integration times. These results were to be expected because the charge carriers generated within the fins require a longer amount

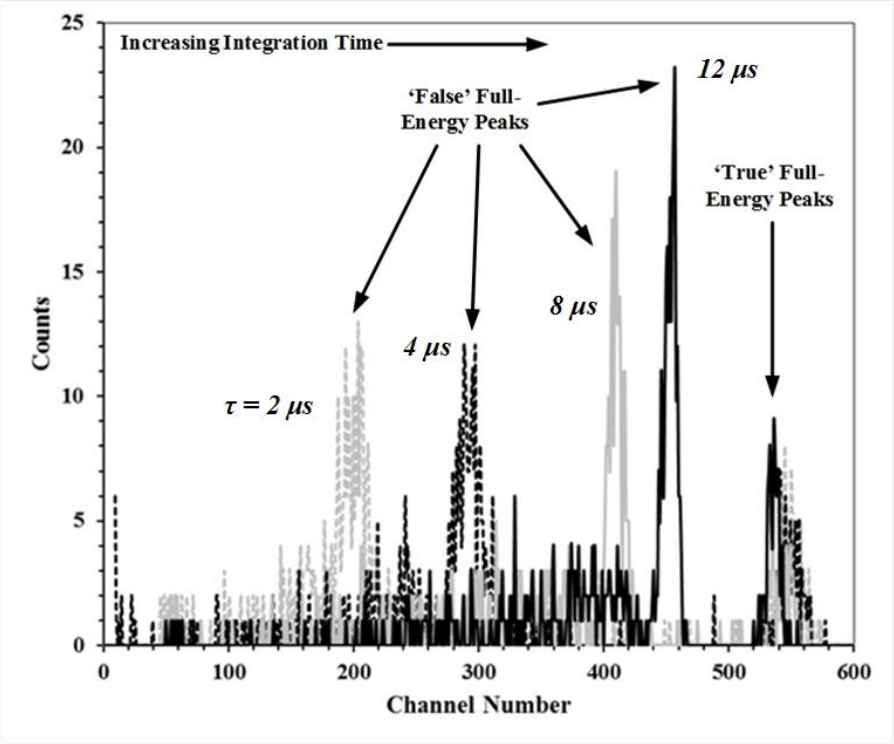

Fig. 6.2.4. Shown are the pulse-height spectra for 2-μs, 4-μs, 8-μs, and 12-μs amplifier shaping times. The high-energy peak produced by reactions at the bottoms of the trenches does not change with increasing shaping time. The lower-energy peaks from interactions at the top of the semiconductor fins are strongly affected by shaping time.

of time to traverse the distance to the anode than events occurring at the trench bottom. Furthermore, it proves that 10 μs (the charge integration time for present-day MSND-based neutron detector systems) is not sufficient to fully integrate the charge deposited into the tops of the fins, giving explanation to the pulse-height spectrum observed in Fig. 6.2.1. The 'percent-charge-fraction' (PCF) is defined as the fraction of the 'true' full-energy peak where the 'false' full-energy peak appears. Thus, the PCF is roughly 35%, 52%, 75%, and 82% for the 2-, 4-, 8-, and 12-μs shaping times, respectively. Following this trend, it can be surmised that a shaping time of roughly 20 μs is necessary to fully collect all charge carriers generated within the upper portion of the fins of this particular MSND design. Fig. 6.2.4. also shows an α-particle punch-through peak below the 'false' full-energy peak, representing α-particles that have punched through the tops of the Si fins and were measured in the next fin.

The results of the 45° irradiation and paraffin-backfilled measurements, shown in Fig. 6.2.6, served to confirm that the higher-energy peaks seen in Figs. 6.2.4 and 6.2.5 were in fact from energy deposited into the bottom of the trenches. At the 45° incident angle, the ~5.5-MeV α

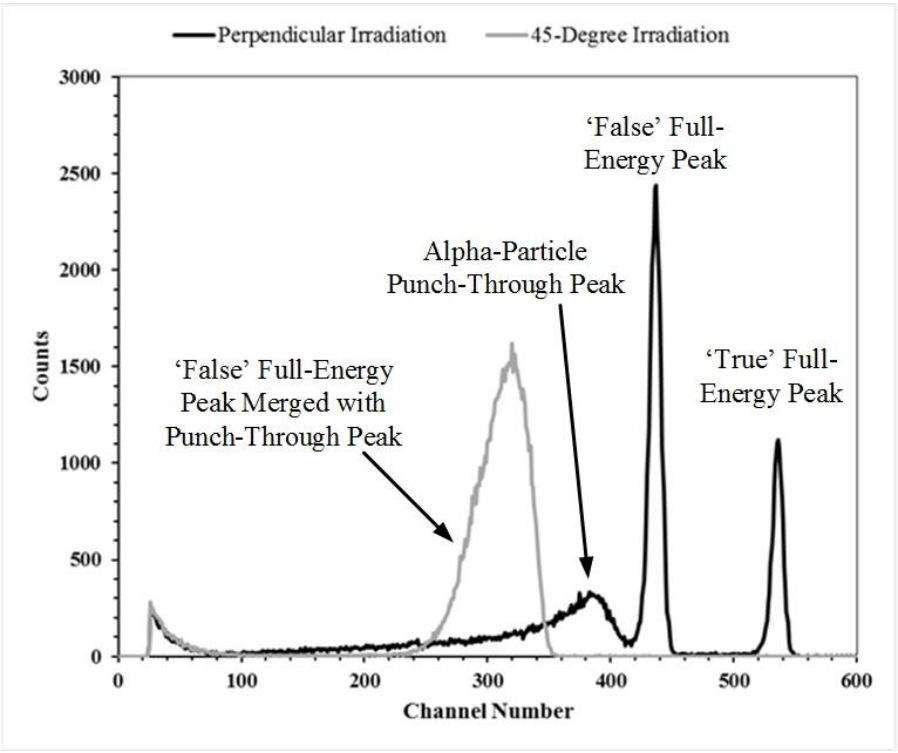

Fig. 6.2.5. Plotted is the MSND pulse-height spectra from perpendicular irradiation (circles) and the 45-degree irradiation (triangles). The high-energy feature of the perpendicular case, generated by interactions at the bottoms of the trenches, is not present in the 45-degree case.

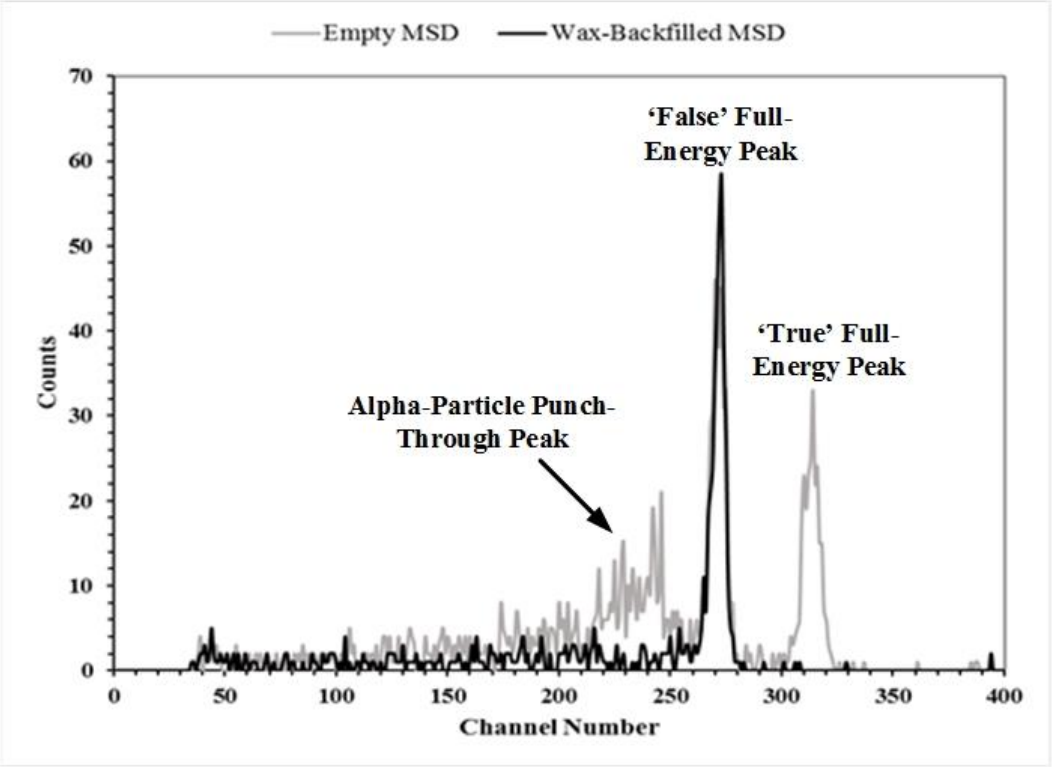

Fig. 6.2.6. Shown are pulse-height spectra measured for the mostly perpendicular irradiation of an empty MSD and one backfilled with paraffin in the trenches. The features predicted to be the 'true' full-energy peaks and the punch-through peak are eliminated by the wax.

particles are almost entirely stopped within the top 35 μm of the detector fins, as shown in Fig. 6.2.3. At an angle of 45°, the hypotenuse (and projected thickness) of the 22-μm wide fins is 31.1 μm, which is greater than the range of 5.5 MeV alpha particles in Si [85]. Confirmation is further achieved with the paraffin-backfilled irradiation experiments. The 350 μm of paraffin is greater than the range of the ^{241}Am alpha particles, and therefore, stops all particles from reaching the bottoms of the trenches. Consequently, the higher-energy peaks in Figs. 6.2.4 and 6.2.5 disappear (see results of Fig. 6.2.6), as well as the small feature just below the 'false' full-energy peak (Fig. 6.2.5). It is speculated that the smaller low-energy feature in Fig. 6.2.5 is from alpha particles that have intersected the small, heavily doped corners of the semiconductor fins. This information is useful for both quality assurances of these neutron detectors, as well as characterization of new prototype devices. Further, proper coupling of these detectors to signal read-out electronics is of utmost importance for optimal device performance.

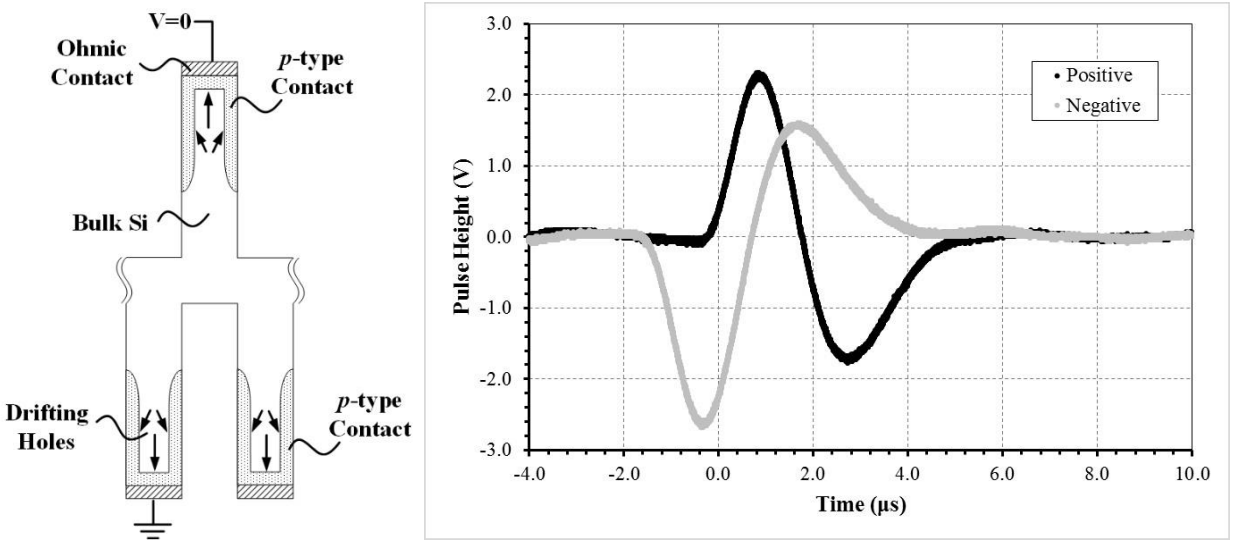

Fig. 6.2.7. Depicted (left) is a cross-section of a pvp-type DS-MSND wherein the top- and bottom-side fins are doped with a p-type contact. The bottom-side contact is grounded while the top-side contact is kept at 0 volts. Electrons excited in either the top-side or bottom-side fins travel towards the center of the diode, contrary to the single-direction motion seen in single-sided MSNDs, while holes travel towards the contacts. The direction of the motion produces either a (right) positive- or negative-polarity pulse, depending on the location of the event, as plotted.

The overall issue of proper charge collection is further complicated in DS-MSNDs by the fact that present-generation *pvp*-type devices operate on a 0-volts applied bias and drift charge by the built-in potential of the heavily-doped *p*-type contacts. In such devices, charge motion is no longer simply a top-to-bottom direction, but rather a dual-direction motion, as depicted in Fig. 6.2.7. Here, the direction of the electric field is no longer driven by the applied bias, and so therefore always points from the lightly-doped *n*-type substrate to the heavily-doped *p*-type contacts. Electron-hole pairs generated within the depletion region of these devices drift in different directions, depending on where the event occurred. Electrons excited in the top-side fins drift down and away from the contact, and holes drift upwards to the contact. In contrast, charge motion is opposite in the bottom-side fins. The positioning of the contacts (i.e. anode and cathode) determines the polarity of the pulse, as one contact will produce a positive-polarity pulse, while the other will produce a negative-polarity pulse.

6.3 DS-MSND Testing

The most important characteristic of DS-MSNDs to determine is the neutron detection efficiency. The overall goal of the research described here is to develop a neutron detector that can rival, and eventually exceed, existing neutron detection technologies. Therefore, it is vital that sensors maintain high neutron detection efficiencies. Neutron detection efficiency is described simply as the number of neutrons counted during a given measurement period, divided by the number of neutrons that intersected the sensor during that time period, shown in Eq. 6.3.1 [67],

$$\varepsilon_{th} = \frac{Counts}{Normal\ Fluence}. \qquad \text{Eq. 6.3.1}$$

Here, the thermal neutron detection efficiency is defined as the counts reported by the detector system (i.e pulses generated above some lower-level discriminator (LLD) value), divided by the number of neutrons that passed through the sensor during the measurement period. It is important to note that neutrons must intersect the sensor perpendicular to the surface of the sensor in order to achieve an accurate measurement of the intrinsic thermal neutron detection efficiency [67], the streaming paths between the backfilled trenches close off rapidly when the incident angle deviates from normal. Further discussion angular dependence can be found in Chapter 5.

Intrinsic thermal neutron detection efficiency is determined using the collimated thermal neutron diffraction beam port, at the Kansas State University TRIGA Mk II reactor facility. A collimated, monoenergetic beam of 0.0254 eV neutrons is produced by diffracting and then collimating a beam of neutrons from a graphite diffractometer [86]. There are three steps to measure the intrinsic thermal neutron detection efficiency of DS-MSNDs, depicted in Fig. 6.3.1[67]: 1) determination of the neutron beam flux, 2) determination of the DS-MSND background counts, and 3) determination of the DS-MSND count rate. A 1.25 cm thermal neutron beam is further reduced to 2.5-mm in diameter with the use of a thick Cd shutter. The flux is determined from two measurements using a calibrated 4-atm Reuter Stokes ^{3}He-gas filled proportional counter with an intrinsic thermal neutron detection efficiency of 81% [22]. The ^{3}He counter is replaced by the DS-MSND apparatus (Fig. 6.3.2) and the process is repeated.

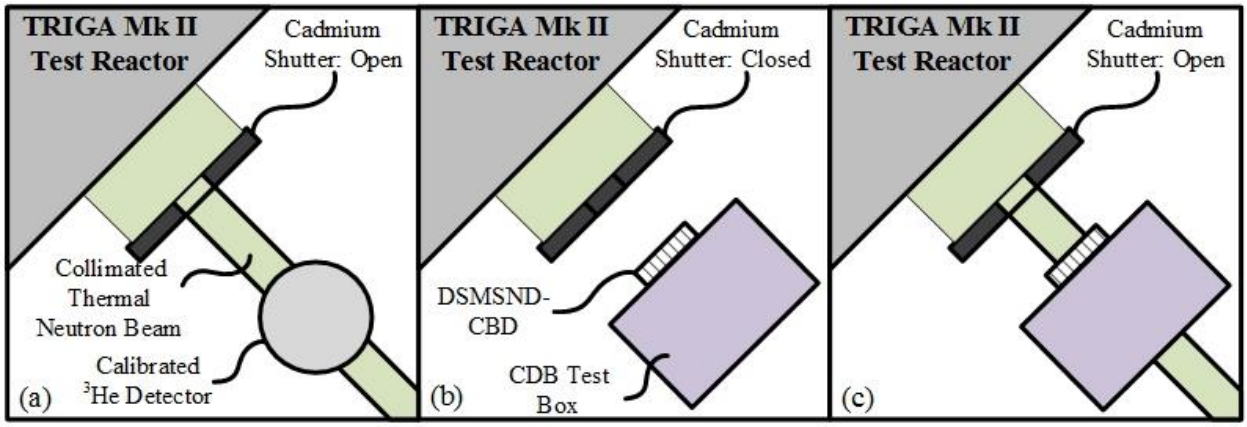

Fig. 6.3.1. Depicted are the three major steps for determining the intrinsic thermal neutron detection efficiency for a DS-MSND. First, (a) the thermal neutron beam is calibrated using a well-known ^{3}He counter. The ^{3}He tube is then replaced by the CDB test box (b) and a background measurement is performed. Finally, (c) the shutter is re-opened and the DS-MSND is exposed to the thermal neutron beam.

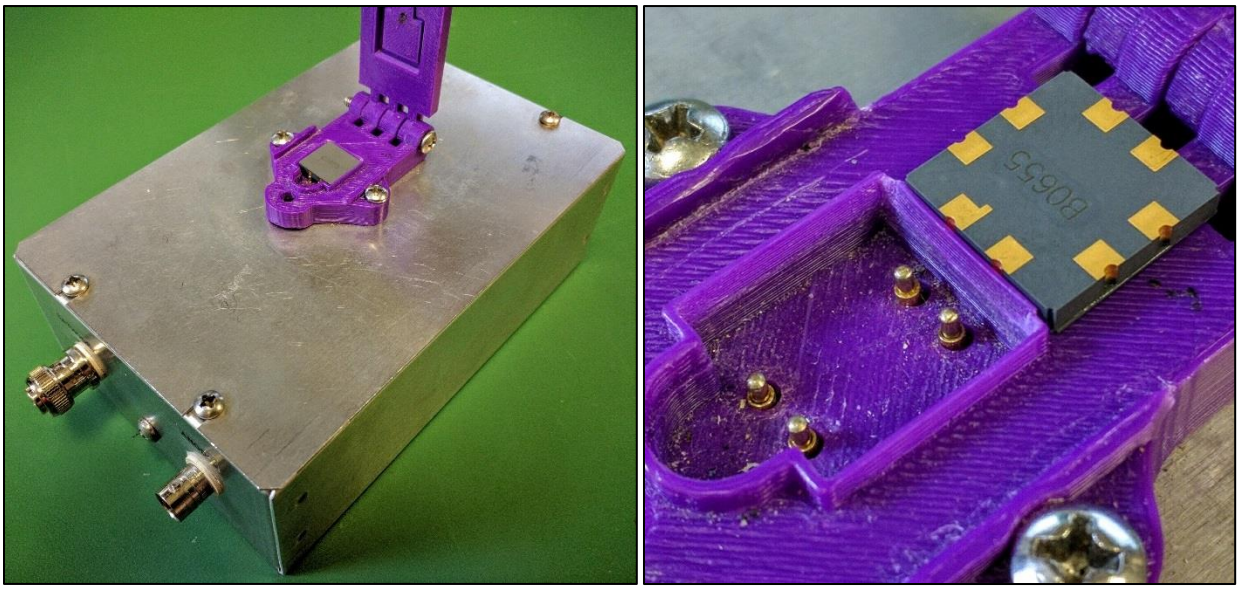

Fig. 6.3.2. Shown (left) is the DS-MSND sensor test box that provides a means of coupling the DS-MSND with counting electronics, such as a pre-amplifier, amplifier, and multi-channel analyzer (MCA). (right) The DS-MSND is coupled to the electronics via signal feed-through pins located within the light shield, mimicking the electronic connections of the instruments described in Chapter 6.

6.3.1. DS-MSND Testing Results

DS-MSND intrinsic thermal neutron detection efficiencies were determined, as described in the previous section, at the Kansas State University TRIGA Mk II diffracted thermal neutron beam port. DS-MSNDs were each mounted to a serialized ceramic detector board (CDB), and placed into the DS-MSND test box for the neutron test. All sensors were tested with an open-shutter beam diameter of 2.5 mm, nominally yielding approximately 750 n s^{-1} through the shutter aperture at room temperature. All devices were calibrated and tested against a well-characterized 4-atm ^{3}He proportional counter [67]. The intrinsic thermal neutron detection efficiency for the ^{3}He counter was found to be approximately 80.5% [22]. The purple lid of the DS-MSND testing apparatus depicted in Fig. 6.3.2 causes a reduction of the thermal neutron flux by approximately 30%, either by absorbing or scattering incident neutrons. The intrinsic thermal neutron detection efficiency is thus determined by Eq. 6.3.2,

$$\varepsilon_{th,corrected} = \frac{\varepsilon_{th}}{0.7} = \left(\frac{Counts}{Normal\ Fluence}\right)\left(\frac{1}{0.7}\right). \qquad \text{Eq. 6.3.2}$$

6.3.1.1. First-Generation pvn-type DS-MSNDs

First-generation DS-MSNDs were fabricated with *pvn*-type dopant contacts wherein the top-side fins were doped conformally with a *p*-type dopant and the bottom-side fins were conformally doped with an *n*-type contact material. Trenches were etched 175-μm deep, and approximately 20-μm wide, with a 40-μm wide pitch (Fig. 6.3.3). The top-side was grounded and a 2.7-V positive bias was applied to the bottom-side fins. Initially, eight *pvn*-DS-MSNDs were produced and tested for neutron sensitivity. Select results are listed in Table 6.3.1.

The measured data in Table 6.3.1 suggests that there was a major issue with the first-generation DS-MSNDs. The devices fell far short of their predicted efficiency values of 43.5% (Table D.1, Appendix D). It is clear that there are two primary issues contributing to the poor detection efficiency: 1) poor signal-to-noise ratio, and 2) lower than expected count rates in the upper energy channels. From Fig. 6.3.4, the shape and strength of the electric field in the fins is less than ideal. Unfortunately, these regions are also where energy deposition by the charged-particle reaction products is most likely to occur. Electrons excited to the conduction band drift

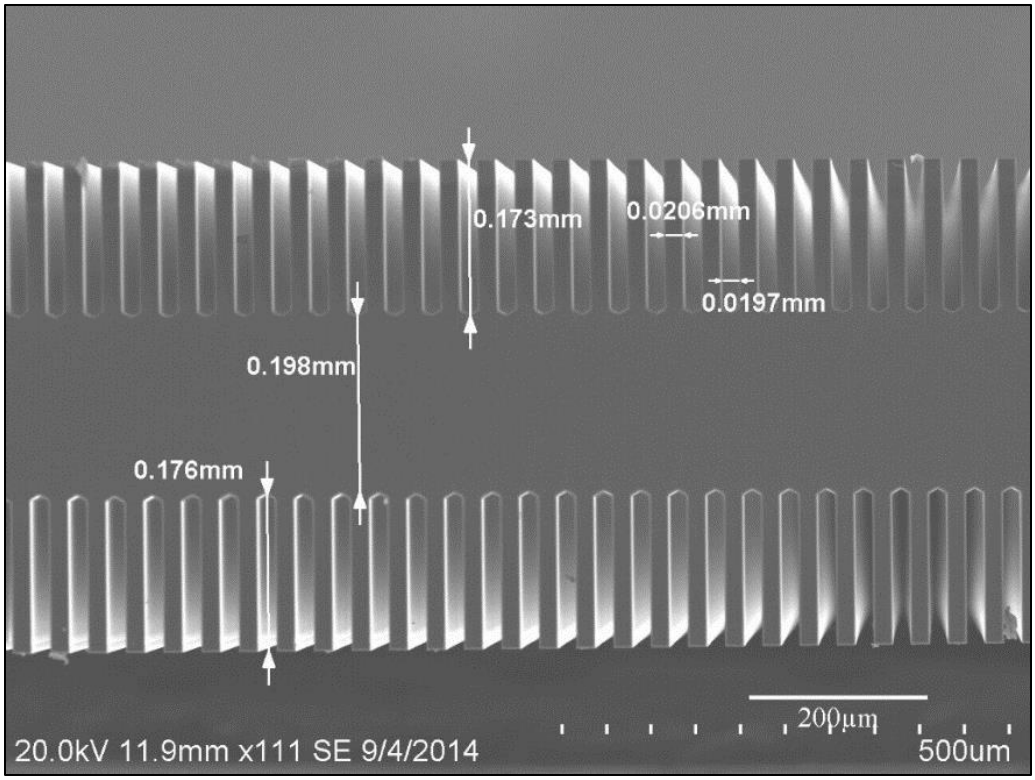

Fig. 6.3.3. Shown is a SEM image of the cross-section of the first-generation pvn-DS-MSNDs. Trenches were etched approximately 175-μm deep, 20-μm wide, with a 40-μm wide pitch.

Table 6.3.1. Measured data for a select group of detectors at the calibrated thermal neutron beam port. Devices with a D designation are DS-MSNDs. Detector S1 is a single-sided MSND. The ^{3}He counter is a calibrated 4-atm proportional counter [19].

Device	**Counts with Shutter Open**	**Counts with Shutter Closed**	**Net Counts**	ε_{th}
^{3}He	22,111	4,127	17,974	**80.5%**
D9	2,263	52	2,211	14.15 ± 0.30%
D10	1,523	30	1,493	9.56 ± 0.25%
D11	2,640	45	2,595	16.60 ± 0.33%
D12	1,850	35	1,815	11.61 ± 0.27%
S1	5,124	69	5,055	32.34 ± 0.45%

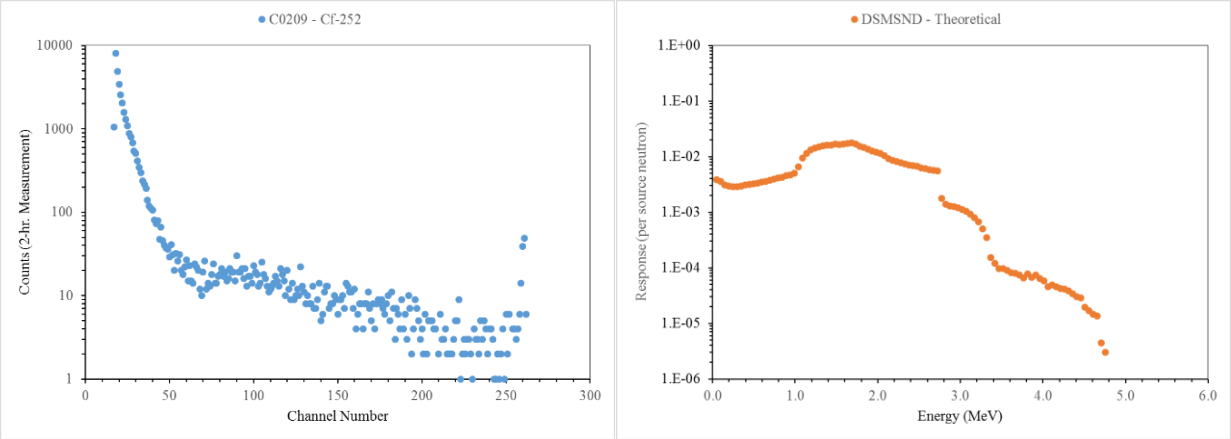

Fig. 6.3.4. Shown (left) is a measured pulse-height spectrum (PHS) for a first generation pvn-type DS-MSND compared to a PHS simulated with MCNP6 (right) where charge collection efficiency is assumed to be 100%. To note, the features present in the simulated spectrum are instead greatly smeared in the measured spectrum, most likely a consequence of poor charge collection efficiency.

under the influence of the internal electric field and thus follow the direction of the electric field. Their velocity of travel is also directly proportional to the strength of the electric field (in V/cm). Electron motion within the conduction band cannot continue in regions where the field strength has reduced to zero; a zero-strength electric field seems to be an inevitability for vertically-operated, conformally-diffused device. This situation is evident in the TCAD-simulated pulse generation for energy within these regions, shown in Fig. 6.3.4. The measured pulse-height spectrum of Fig. 6.3.3 provides additional evidence. The poor detector count rate is also partially caused by this phenomenon, as many counts that would otherwise be included above the lower-level threshold were rejected by the counting system.

The lack of full device depletion is the primary contributor to the poor detection efficiency of these DS-MSNDs. Full 'depletion' of a device, in the traditional sense and as seen in single-sided MSNDs, implies that the depletion layer extends well into the bulk material, making the device sensitive to energy deposition from the eaction products. However, with the *pvn*- type DS-MSNDs, the backside *n*-type conformal contact acts as a depletion sink, stopping the depletion layer from reaching completely to the backside of the device. This truncated active volume reduces charge sensitivity within the backside fins.

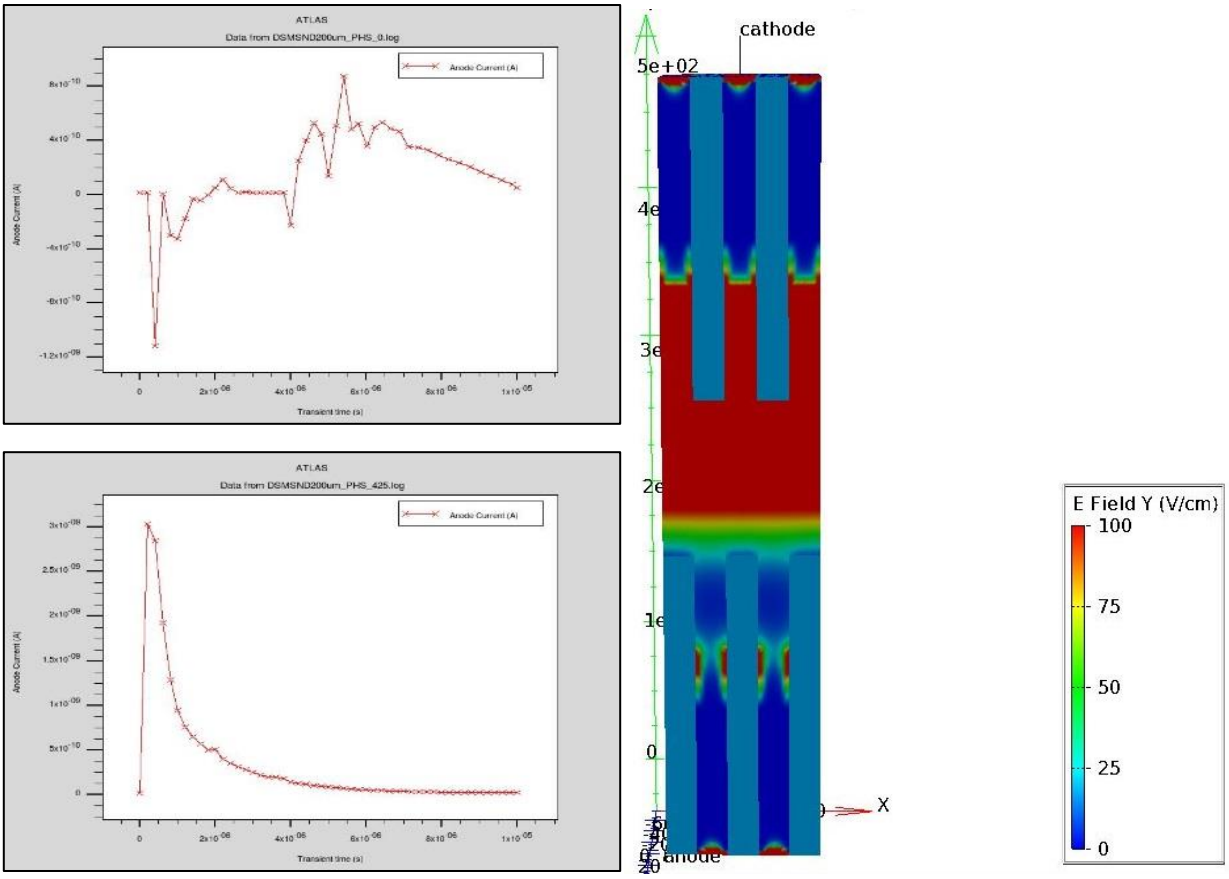

Fig. 6.3.4. Shown (top left) is a simulated pulse generated from free charges moving in the bottom fins of the DS-MSND where the n-type contact forms irregular electric fields. The pulse shown (bottom left) is generated from charge motion within the top fins. For clarity, electric field strength is mapped (right) within the DS-MSND.

6.3.1.2. Second-Generation pvn-type DS-MSNDs

The goal to extend the depletion region into the backside fins drew attention to the back-side *n*-type contact [20]. Shown in Fig. 6.3.5 is the effect that depletion depth has on the intrinsic thermal neutron detection efficiency of 500-μm thick MSND and DS-MSND devices. With the depletion depth ending somewhere in the central bulk Si region, models indicate that the intrinsic thermal neutron detection efficiency is less than 20%, even with perfect charge collection efficiency. Therefore, it is required that the depletion depth extend across the entire device for DS-MSND technology to succeed. A second generation of *pvn*-DS-MSND was developed to address this issue.

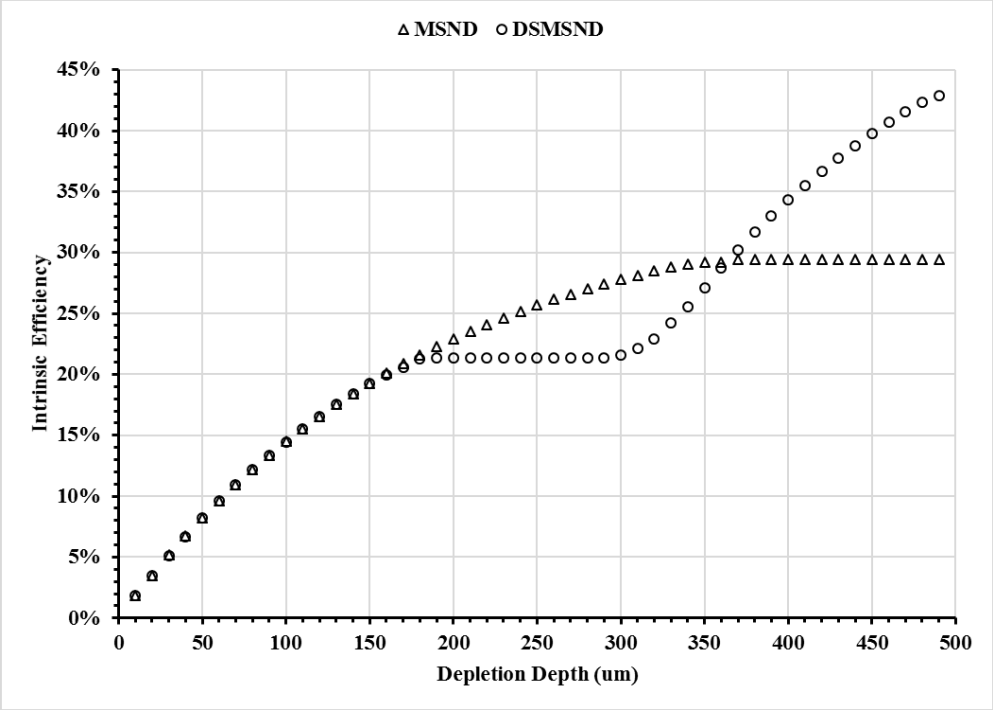

Fig. 6.3.5. Plotted are the theoretical intrinsic thermal neutron detection efficiencies for a single-sided MSND and a DS-MSNDs with respect to the active depletion depth as modeled in MCNP and Python. DS-MSND trenches were etched to 175 µm in both directions, and the MSND trenches were etched to 350 µm. Achieving good depletion depth is required to produce good DS-MSNDs.

Because the stoppage of the depletion region was entirely due to the depletion sink found in the conformal *n*-doped surface of the back-side fins, it was advantageous to reduce the conformalness of the dopant profile. Many trials were performed to reduce the conformalness of the back-side contact, with the ideal case yielding a completely planar *n*-type contact. However, even simply reducing the conformalness of the contact yields improved electric-field characteristics, as shown in Fig. 6.3.6. Unfortunately, the front-side and back-side contacts are formed during the diffusion process (as described in Chapter 4) with solid-source B and P wafers, and therefore control of the shape of the dopant contacts is difficult. In order to reduce the conformalness of the back-side *n*-type contacts, the diffusion time was reduced. The difficulty in accomplishing this goal is that dopant sourcing occurs throughout the duration of the *n*-type diffusion process, thereby, making it difficult to find a balance between good electrical characteristics (i.e. well-activated P dopant atoms), and a non-conformal contact pattern. However, by carefully controlling the backside profile, the second-generation devices were capable of greater device depletion, shown in Fig. 6.3.8.

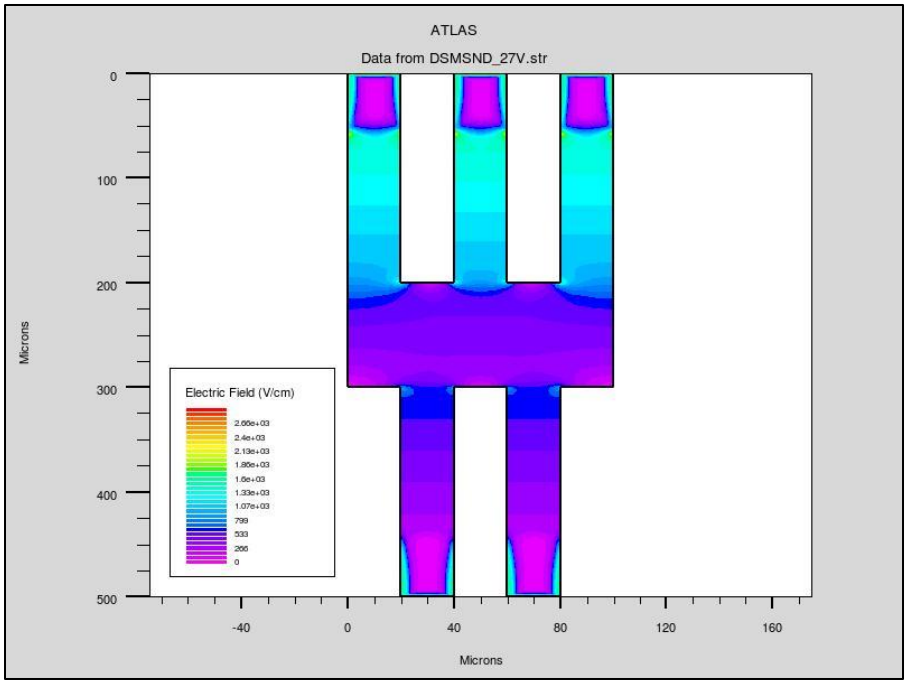

Fig. 6.3.7. Shown is a TCAD simulation of the internal electric field for a DS-MSND section for a partially-conformal n-type diffusion profile. The electric field within the device is improved over the first-generation devices by eliminating the choke points in the back-side fins (as seen in Fig. 6.3.4).

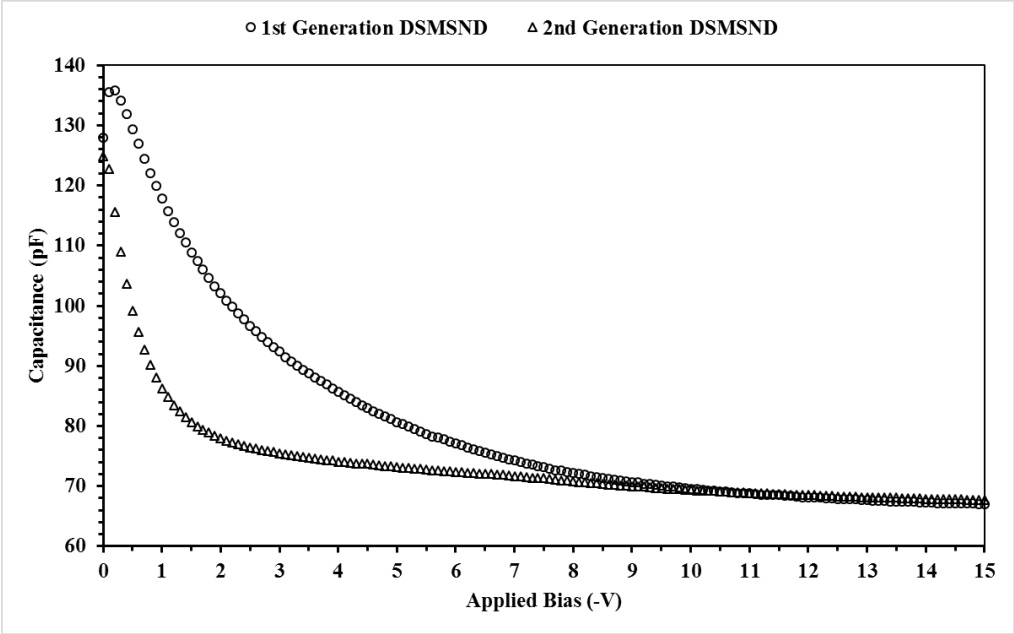

Fig. 6.3.8. Plotted are the CV-curves for a first-generation, conformally-doped pvn-type DS-MSND and a second-generation, less-conformally-doped pvn-type DS-MSND. Capacitance of a device is reduced with increasing depletion depth, and shown here is the low-voltage required by the second-generation device to obtain full depletion, relative to a similar first-generation device.

The resulting improvements in both reducing the electric field complexity as well as increasing the possible depletion depth as shown in Fig. 6.3.7. The conformal-shape of the back-side *n*-type contact was reduced, thereby, eliminating much of the dead electrical dead space within the fin region. The improved depletion depth was evidenced by TCAD models and the CV curves in Fig. 6.3.8. The resulting neutron detection efficiency from second-generation DS-MSNDs was improved over first-generation devices (Table 6.3.2). Shown in Fig. 6.3.9 is a reaction product pulse-height spectrum that appears to resemble a MCNP-modeled pulse-height spectrum (Fig. 6.3.10). The results provide evidence that the detector had relatively good charge-collection capabilities. However, the detection efficiency of this device (and those also fabricated as *pvn*-type devices) still did not achieve predicted values, with efficiencies often close to 30%, rather than the expected 35% (see Fig. 6.3.10). This discrepancy can be explained by the lack of complete device depletion. Shown in Fig. 6.3.8, the device capacitance at -2.7 V bias was approximately 76 pF, compared to 68 pF at full depletion, implying incomplete device depletion. The measured efficiency represents about 85% of the expected efficiency, thereby, also suggesting incomplete device depletion.

Table 6.3.2. Measurement data for a select group of second-generation pvn-DS-MSNDs at the calibrated thermal neutron beam port. All measurements were performed with a reactor power of 100 kW using a 2.5 mm diameter collimated beam of thermal neutrons.

Device	**Measurement Duration**	**Net Counts**	ε_{th}
^{3}He	300 s	229,466	**80.5%**
C0501	100 s	19,081	28.87 ± 0.21%
C0502	100 s	18,696	28.28 ± 0.21%
C0503	100 s	18,256	27.62 ± 0.20%
C0504	100 s	17,562	26.57 ± 0.20%
C0505	100 s	18,680	28.26 ± 0.21%
C0506	100 s	17,099	25.87 ± 0.20%
C0507	100 s	17,301	26.17 ± 0.20%
C0508	100 s	17,381	26.29 ± 0.20%
C0509	100 s	18,093	27.37 ± 0.20%
C0510	100 s	17,029	25.76 ± 0.21%

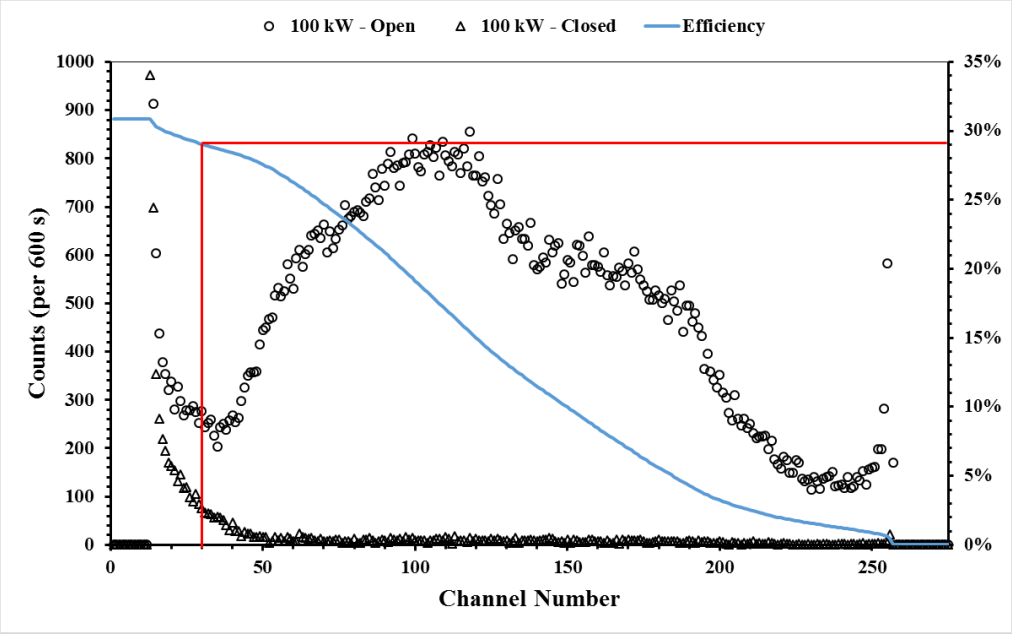

Fig. 6.3.9. Plotted is the reaction-product spectrum output by the detector. Red lines indicate the LLD threshold for the calculation of the neutron detection efficiency. The blue line indicates the detection efficiency for a given LLD. The clearly-defined characteristic valley and hump spectral features show that charge collection issues have been largely resolved.

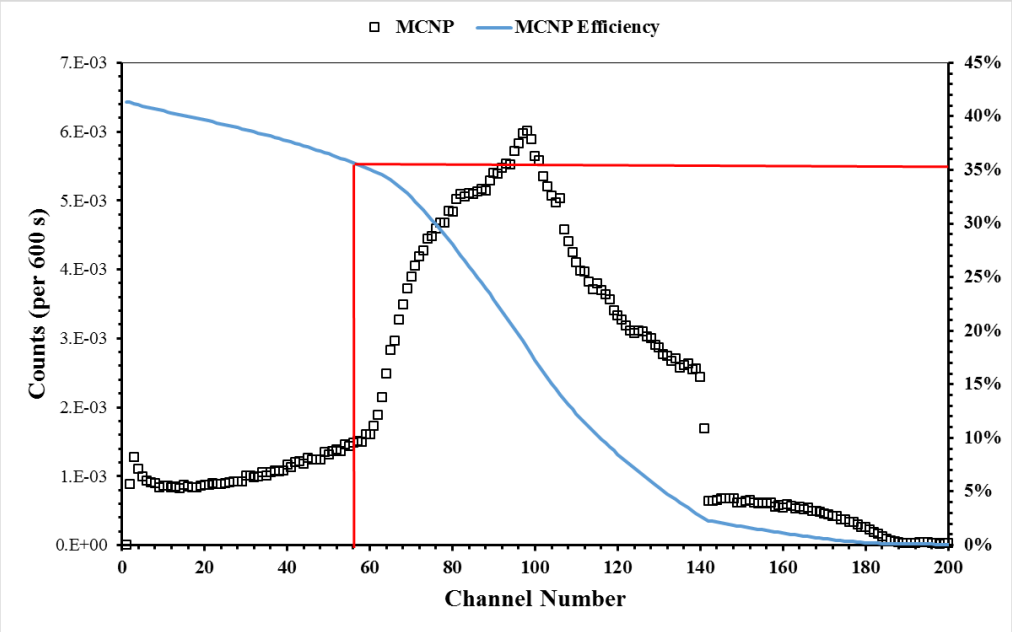

Fig. 6.3.10. Plotted is the simulated reaction-product spectrum for a DS-MSND device with similar spectral features to those in Fig. 6.3.9. A LLD threshold was set approximately in the same location as was set in the real-world measurement and compared for detection efficiency. From this model, the detection efficiency should be close to 35%, indicating that the count rate from the experimental device is lower than expected.

6.3.1.3 pvp-type DS-MSNDs

In order to achieve complete device depletion, a new type of DS-MSND was designed and fabricated. Difficulty in advancing the depletion region into the back-side fins arose with *pvn*-type DS-MSNDs was due to the heavy concentration of *n*-type dopant material along the periphery. The back-side *n*-type contact restricted the depth of the depletion region to the start of the doped region, often 100-µm or more from the end of the fin. A new generation of DS-MSNDs were fabricated with *p*-type contacts on the front- and back-side fins, thereby, forming a *pvp*-type device. The purpose of the back-side *p*-type contact is to intrinsically deplete the fins of excess charge carriers, thereby, activating that region to energy deposition with no applied bias. However, because there is no applied bias, excited charges resultant from a neutron event have a directional drift based on the the electric field established by the electrochemical potential between the contact and bulk Si carrier concentration. Formation of *p*-type contacts generally requires that dopant concentrations greater than that of the background *n*-type dopant level be diffused into the fin surface. Given a background donor concentration of $4x10^{11}$ cm^{-3} for 5 kΩ-cm *n*-type Si, a *p*-type contact of approximately 10^{16} cm^{-3} formed on the surface of the fin establishes a built-in voltage of nearly 0.5 V. A built-in potential of this magnitude will produce a depletion width of approximately 35 µm, sufficient to fully deplete the fins [39].

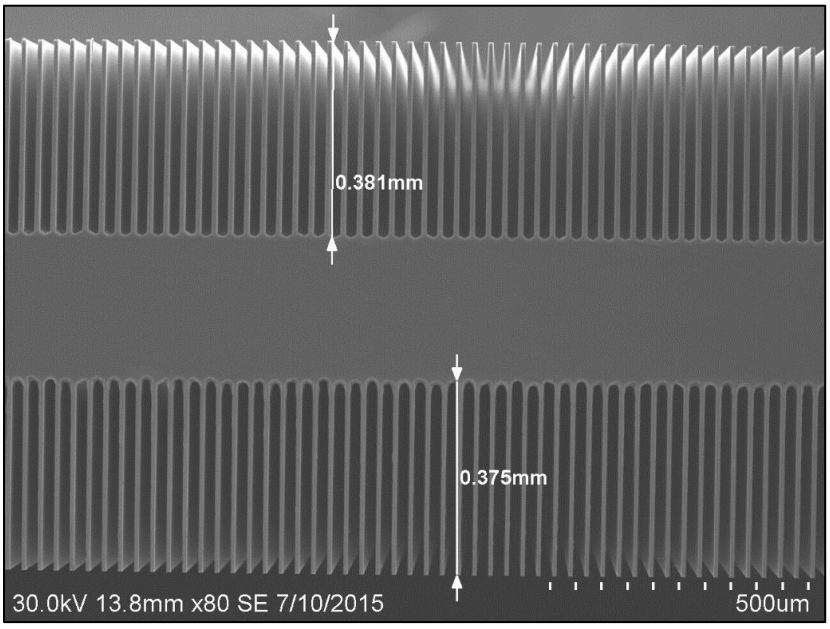

Fig.6.3.11. Shown is a SEM image of a cross-section of a pvp-type DS-MSND. Here, trenches are offset one-half unit cell and etched to approximately 375-µm deep from each surface.

During initial testing of *pvp*-type devices, it appeared as though the devices suffered from poor neutron detection efficiency, although good pulse-height spectra were produced. It was determined that events in the back-side fins were not being measured by the pre-amplifier/amplifier pair. Upon inspection, that the dual-polarity nature of the devices was discovered [20]. To remedy the problem, the amplifier was operated in dual-polarity mode, thereby, producing a measurable positive-going pulse for all incoming pulses regardless of their initial polarity. However, the initial dual-polarity results indicated that these devices had good charge-collection characteristics, denoted by the relatively large valley between the noise level and the features generated by the charged-particle reaction products. The reaction product spectra of device B0552, a part of a batch of devices listed in Table 6.3.3, is plotted in Fig. 6.3.12. Device B0552 yielded an intrinsic thermal neutron detection efficiency of 38.12 ± 0.24%. Device B0553 yielded an intrinsic thermal neutron detection efficiency of 40.18 ± 0.25%, which, at the time of the measurement, was the world record for solid-state semiconductor neutron detectors. However, the device still fell well short of the theoretically-predicted value of 60.7% determined by MCNP6.

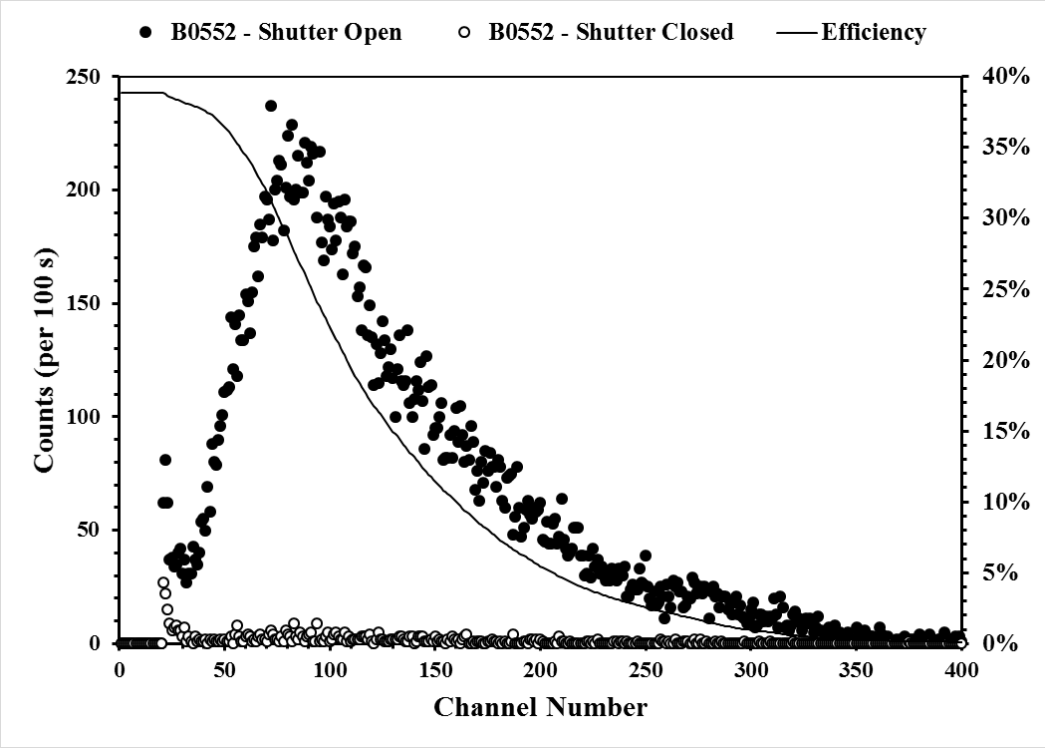

Fig. 6.3.12. Plotted are the charged-particle reaction product spectra produced by B0552 for both Cd shutter open and shutter closed cases. The intrinsic thermal neutron detection efficiency is plotted on the secondary axis. The LLD was set to Channel 25, where an intrinsic thermal neutron detection efficiency of 38.5% was achieved.

Table 6.3.3. Measurement data for a select group of first-generation pvp-DS-MSNDs at the calibrated thermal neutron beam port. All measurements were performed with a reactor power of 100 kW using a 2.5 mm diameter collimated beam of thermal neutrons. B0553 yielded a world record detection efficiency at the time of the measurement.

Device	**Measurement Duration**	**Net Counts**	ε_{th}
^{3}He	300 s	227,855	**80.5%**
B0547	100 s	23,993	36.54 ± 0.24%
B0548	100 s	25,113	38.54 ± 0.24%
B0549	100 s	24,690	37.74 ± 0.24%
B0550	100 s	24,231	37.12 ± 0.24%
B0551	100 s	24,400	37.21 ± 0.24%
B0552	100 s	24,891	38.12 ± 0.24%
B0553	**100 s**	**26,348**	**40.18 ± 0.25%**

There were two major issues that were observed with the measurement, not accounted for with the MCNP6 model: 1) reduced magnitude of pulses generated in the back-side fins, and 2) incomplete fin depletion due to limited *p*-type diffusion profile. The method by which negative-polarity pulses are inverted causes a reduction in the amplitude of the outgoing pulse by 30% [86]. The attenuation of the outgoing pulse results in a downshift of the pulse-height spectrum for events occurring in the back-side trenches and fins, as seen and successfully modeled in MCNP6 by applying a multiplier of 0.7 on the F6 card for the back-side fins. Shown in Fig. 6.3.13 is the effect on the back-side spectrum produced due to this phenomenon. However, models still indicate that the neutron detection efficiency could be as high as 60.8%, with a LLD of 300 keV. It was assumed that charge collection was good for these devices in the models, which is not entirely true in this actual devices (indicated by the narrow valley between the electronic noise and neutron detection signal). It was theorized that a second contributor to the reduced efficiency must exist. The issue was likely caused by lack of complete fin depletion of both front and back-side fins. The 0-volt applied-bias condition relies entirely on the conformalness of *p*-type junction. Thus, a junction profile that is not fully conformal (i.e. does not reach to the bottoms of the trenches) cannot entirely deplete the fins. Therefore, increasing the depth of the *p*-type contact profile was necessary.

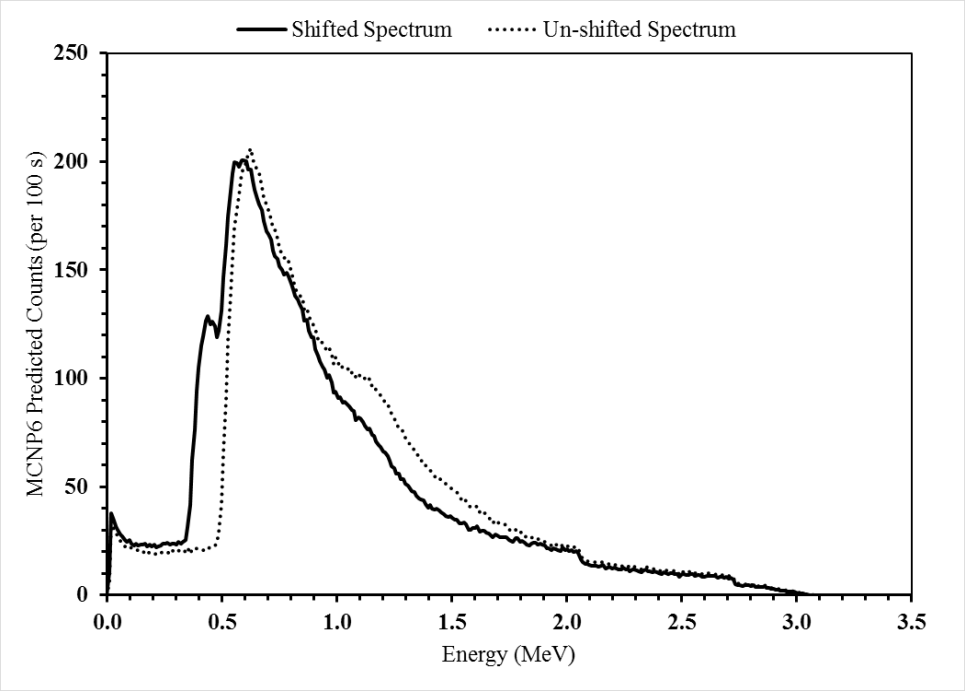

Fig. 6.3.13. Shown is the theoretical spectrum as predicted by MCNP6 wherein events occurring in the back-side trenches and fins yielded a pulse-height reduced by 30% in magnitude. Also, 100% charge-collection efficiency was assumed for the model.

A second-generation of *pvp*-DS-MSNDs were produced with a more conformally-diffused junction profile. This was accomplished by increasing the dopant source time and reducing the activation/drive-in duration. The increased sourcing time allowed for a greater amount of B to reach the bottoms of the fins, and the reduced activation/drive-in time compensated for the greater dose imparted on the substrate. The increased conformalness of the doped region had competing effects on the detection efficiency of the sensors; the increased depletion depth increased the counting efficiency of the devices, but charge collection efficiency was reduced. However, a net gain in the intrinsic thermal neutron detection efficiency was observed, with most devices yielding between 44-54% detection efficiency. The overall average pulse height reduced from Ch. 100 (as seen in the first generation DS-MSNDs, Fig. 6.3.12) to Ch. 60 (Fig. 6.3.14). A select group of devices and test data can be found in Table 6.3.4. Device B0749 produced a detection efficiency of 53.54 ± 0.47%, which at the time of writing this report is the world-record holding solid-state thermal neutron detector. The charged-particle reaction product spectrum produced by the device is shown in Fig. 6.3.14. Further attempts to increase conformalness of the junction produced poor reaction product spectra, almost indistinguishable from noise and other background.

Table 6.3.4. Measurement data for a select group of second-generation pvp-DS-MSNDs at the calibrated thermal neutron beam port. All measurements were performed with a reactor power of 50 kW using a 2.5 mm diameter collimated beam of thermal neutrons. B0749 represents the current neutron detection efficiency world record for semiconductors.

Device	Measurement Duration	Net Counts	ε_{th}
^{3}He	300 s	87,669	**80.5%**
B0749	100 s	13,183	53.54 ± 0.47%
B0750	100 s	12,401	50.36 ± 0.45%
B0751	100 s	12,978	52.71 ± 0.46%
B0752	100 s	12,462	50.61 ± 0.45%
B0753	100 s	11,897	48.32 ± 0.44%

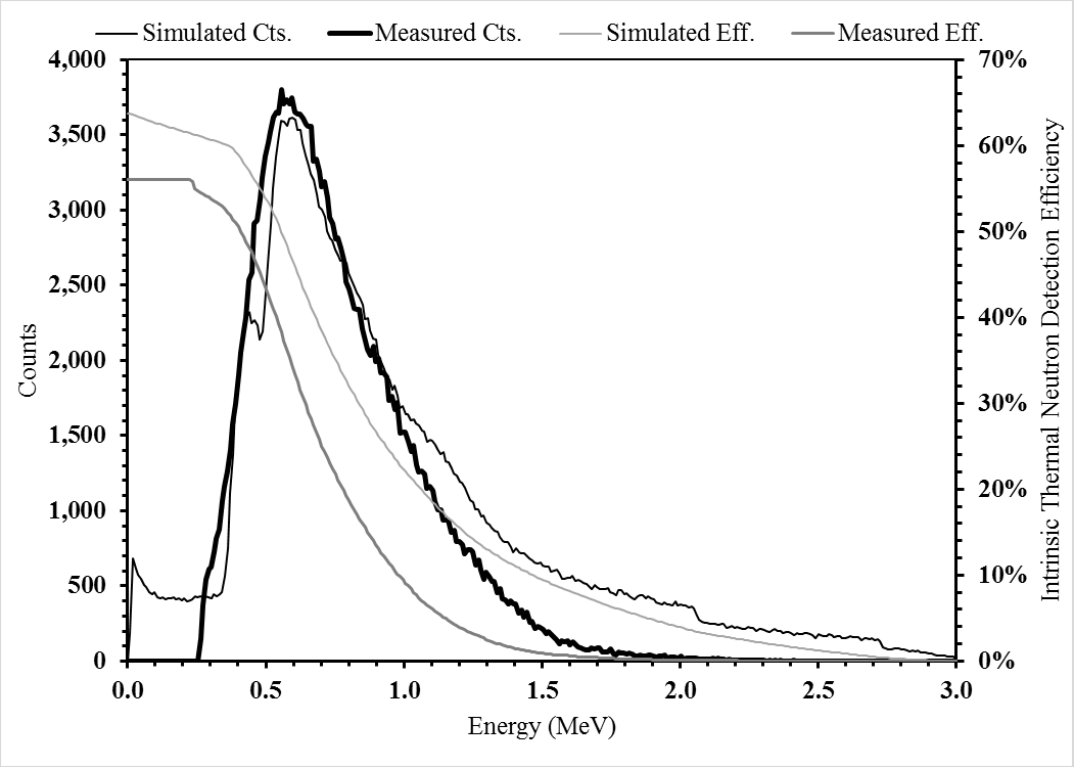

Fig. 6.3.14. Plotted are the charged-particle reaction product spectra produced by B0749 for conditions with the Cd shutter open and the shutter closed. The intrinsic thermal neutron detection efficiency is plotted on a secondary axis. The LLD was set to Channel 20 (~250 keV), where an intrinsic thermal neutron detection efficiency of 53.4% was achieved.

6.4. Instrument Testing

The numerous instruments built and populated with MSNDs and DS-MSNDs were tested and characterized in various ways. Typically, instruments were categorized in one of three types of detectors: hand-held man-portable arrays, stationary arrays, and ^{3}He replacement sensors. Instruments were introduced and described in Chapter 5; however, the testing methods, data, and results are presented here. In general, large-area stationary arrays are intended for long-distance stand-off measurement of shielded and/or moderated sources, thereby, necessitating high-intrinsic and extrinsic neutron detection efficiency. The mid-range man-portable array devices are intended to maximize neutron sensitivity while maintaining a good level of portability, with the intention of passively measuring sources from nearby to 10's m distance. ^{3}He replacement instruments are typically small instruments with ultra-high intrinsic thermal neutron detection efficiency, with the hopes of being able to directly replacing existing ^{3}He sensors, or displacing them from future hand-held instruments.

6.4.1. Panel Array Mk I (2013) Testing

The Panel Array Mk I was the first generation, large-area, stationary MSND-based detector array and was tested in the first few years of instrument development [81]. The array was composed of nine elements, each populated with sixteen 4-cm^2 active area MSNDs, arranged in a 4x4 arrangement. Each of the MSNDs populating the elements were tested at the TRIGA Mk II thermal neutron diffraction beam port at Kansas State University [67]. The MSNDs were found to have an intrinsic thermal neutron detection efficiency between 10-15%. Upon assembly, the MSNDs were biased to -1 volt, with an LLD setting of approximately 350 mV and a 15 µs shaping time. The array was placed between two 2-in. thick sheets of HDPE and tested for neutron sensitivity with a bare 1x10^7 n s^{-1} ^{252}Cf source at a distance of 2 m (Fig. 6.4.1) [81]. The intrinsic detection efficiency was found to be 2.21±0.02%, or 0.164 cps ng^{-1} of ^{252}Cf, for the un-moderated ^{252}Cf source using the larger area of the HDPE as the cross-sectional reference for the detector (rather than the active area of the MSND-based array). Ultimately, this array concept was abandoned due to inability to swap out damaged or poorly-performing MSNDs and the high rate of failure for the elements. Each element contained several dead or otherwise inoperable MSNDs from poor wire-bonds and long signal traces, which were difficult to repair or replace.

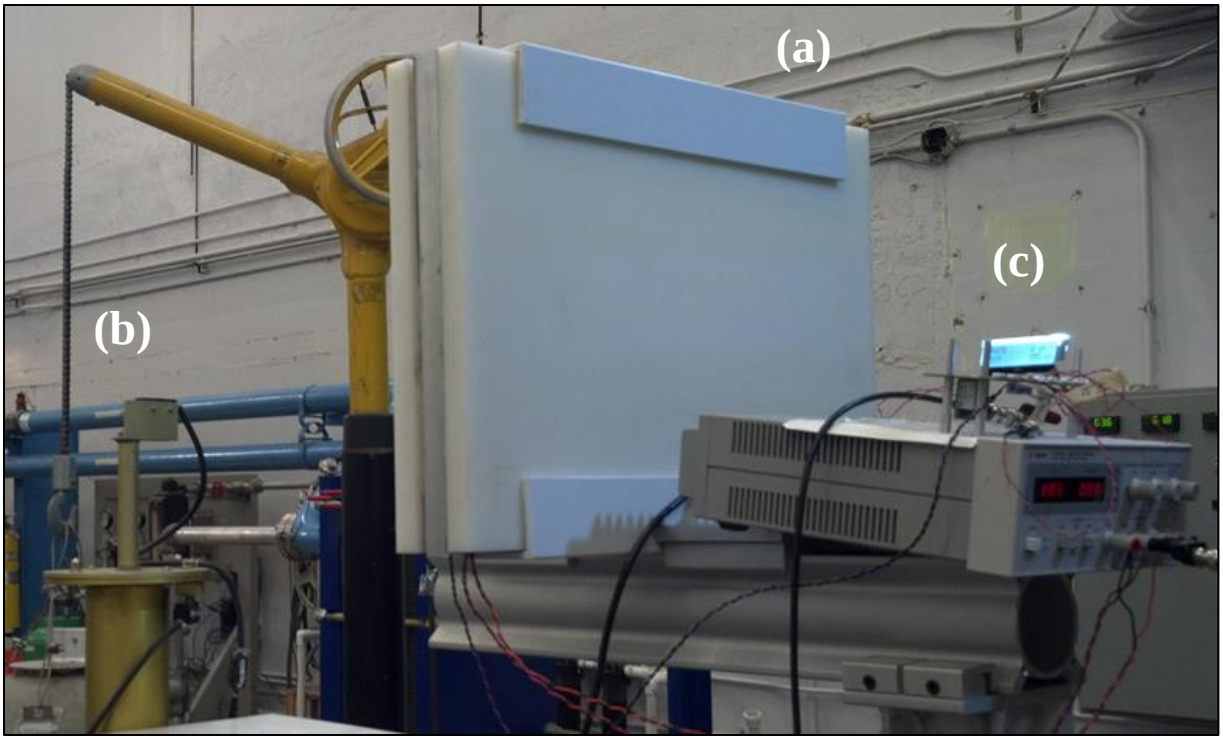

Fig. 6.4.1. Depicted is the (a) Panel Array Mk I assembled and sandwiched between two 1-in thick sheets of HDPE. The detector was placed 2 m from the (b) roughly 1x10^{7} n s^{-1} ^{252}Cf source that could be raised or lowered into a cask to effectively 'turn' the source on or off. Counts could be read directly from (c) a nearby display or from a remote handheld device (not shown).

6.4.2. Briefcase Neutron Detector Testing

The Briefcase Neutron Detector was a part of a second-generation set of tileable and expandable arrays based on the Domino neutron detector technology. This array was designed to be a highly-sensitive, man-portable array. The Briefcase Neutron Detector was populated with 84 Dominoes, each housing a single 4 cm^2 MSND with an intrinsic thermal neutron detection efficiency of approximately 15%. Lower-level threshold values were set by a 100-kΩ threshold resistor (roughly 160 mV, equivalent pulse-height rejection), with a shaping time of 20 μs. The detector system was capable of operating a total of 168 Dominoes, however, due to constraints on available sensors, the system was only populated to 50% capacity. The array of Dominoes was sandwiched between two 1-in. thick sheets of HDPE, for a total weight of approximately 9.5 kg. For all tests, the Briefcase Neutron Detector system was powered using 12 volts via a wall adapter with a total power draw of 0.25 W during full operation.

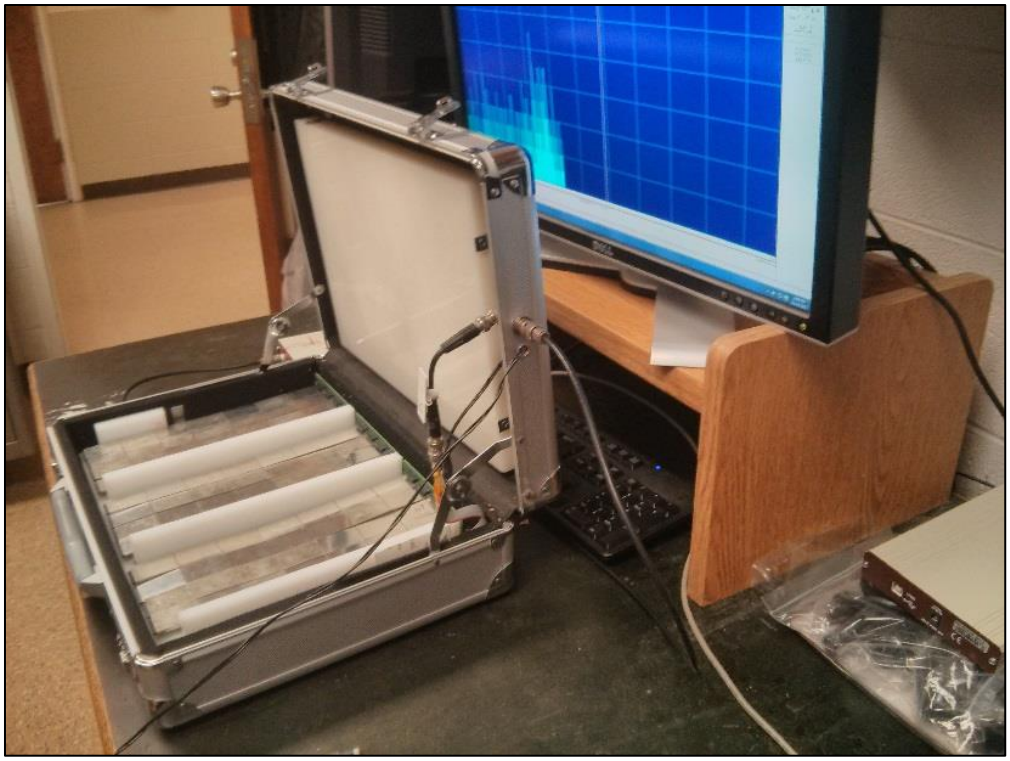

Fig. 6.4.2. Shown is the Briefcase Neutron Detector during a 24-hour-long background measurement. The test was intended to measure the long-term background stability of the detection system by conducting a measurement of the supposedly stable neutron background.

Detector testing occurred in two primary stages, the first of which was intended to be a long-term background measurement conducted over a 24-hour period to test for long-term stability in a relatively low radiation background (Fig. 6.4.2). The measurement data can be found in Fig. 6.4.3. The output TTL pulse was fed into a 50-Ω terminated Multi-Channel Scalar (MCS) which recorded pulses on a desktop computer. The long-term background measurement yielded low-level measurements of the reactor operation, initially thought to be detector noise or a change in the background. Indeed, the Briefcase Neutron Detector was sensitive enough to remotely observe the operation of the TRIGA Mk II research reactor at a distance of over 50 yards, even through the concrete shielding, earth shielding, and numerous walls of offices. Careful calibration of the detector system would allow for remote tracking of the reactor power levels for future projects or investigations. The second set of measurements were performed using a small, portable ^{252}Cf source at various distances from the instrument. Measurements were conducted at distances of 1m, 2m, and 5m down the length of a concrete hallway using a bare 54-ng ^{252}Cf source. The results of these measurements can be found in Table 6.4.1.

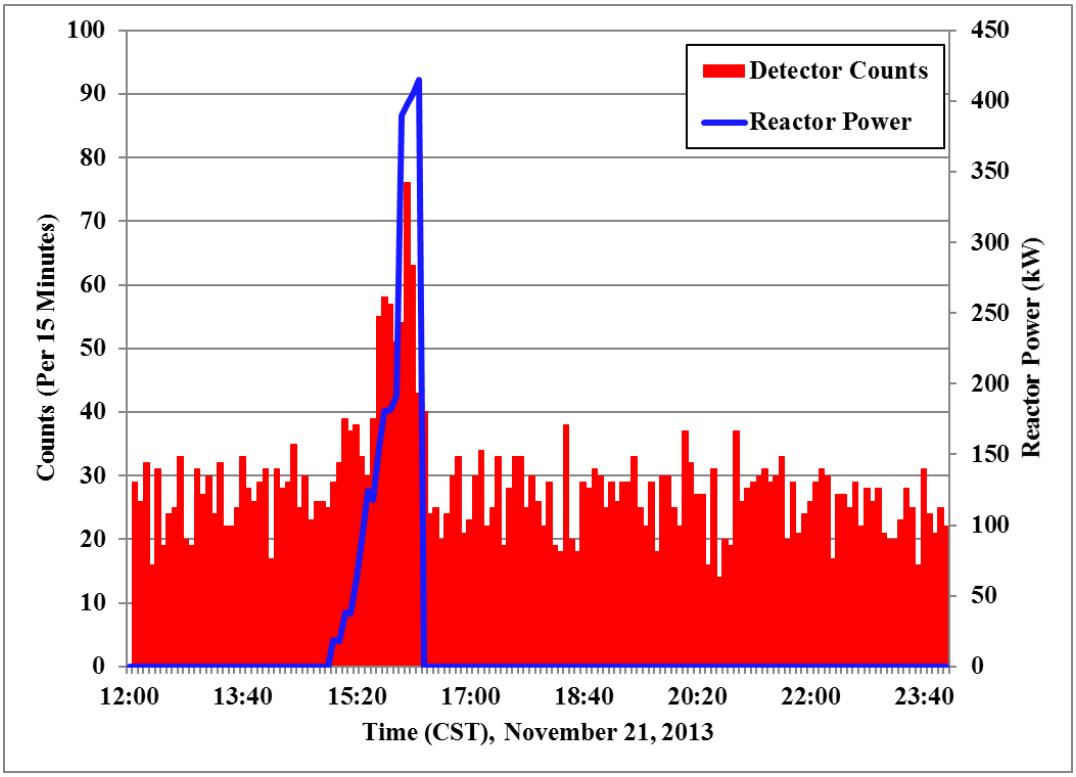

Fig. 6.4.3. Plotted here are two data sets from different sources. The counting response of the Briefcase Neutron Detector is on the primary axis in counts per 15-minute period. A consistent background level is seen at most intervals, with the exception of a period during the late afternoon, when the TRIGA Mk II nuclear reactor was operated at various power levels (secondary axis).

Table 6.4.1. Listed are the net count rates for the Briefcase Neutron Detector in response to a bare 60-ng ^{252}Cf source at various distances. Measurements were conducted in a concrete hallway.

Distance (m)	Bare ^{252}Cf Net Count Rate (s^{-1} ng^{-1})
1.0	0.54 ± 0.02
2.0	0.27 ± 0.01
5.0	0.08 ± 0.01

6.4.3. Panel Array Mk II (2014) Testing

The Panel Array Mk II was the second-generation large-area array based on the MSND technology. The Panel Array Mk II was populated with twenty-four strings of twenty Dominoes, for a total of 480 Domino neutron detectors, thereby, forming an array roughly 1 m^2 in area. The array was powered with a 12-volt input and operated at a total power of 1.5 W. Each of the

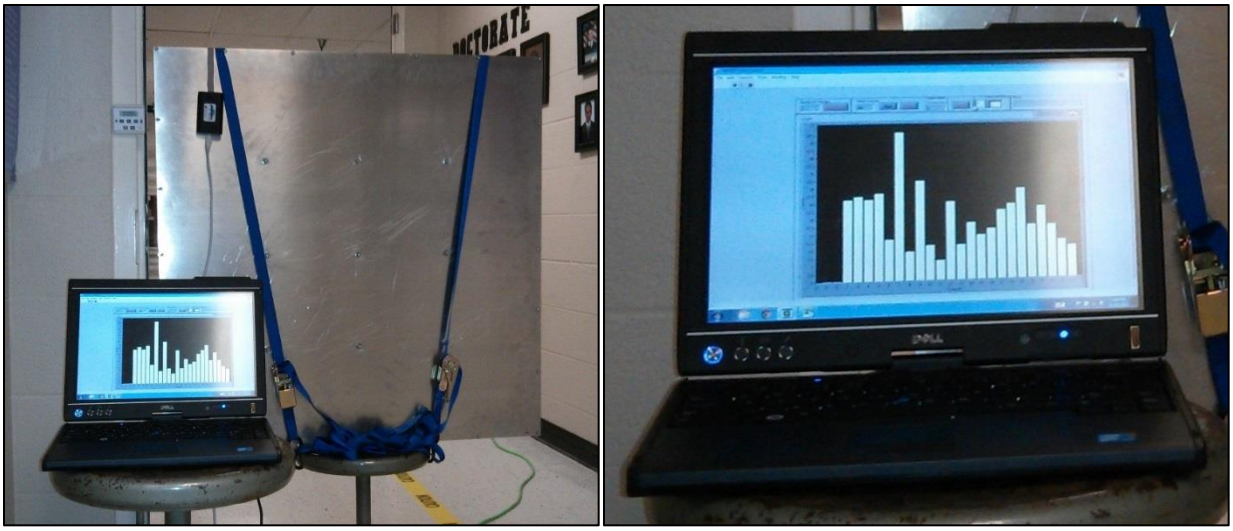

Fig. 6.4.4. The LabView program was developed to read out the string count rates by the Kansas State University Electronics Design Laboratory (left). The program utilizes an Aardvark I^2C USB adaptor to communicate with the Panel Array. The program displays the total counts recorded and the instantaneous count rate during the measurement.

Dominoes operated a 4 cm^2 MSNDs with an applied bias of -2.7 V and 100-kΩ threshold (160-mV output pulse equivalent), yielding an intrinsic thermal neutron detection efficiency of approximately 15% each. The Panel Array Mk II was tested for neutron sensitivity using two methods, a variable distance and variable attack angle. The TTL pulses generated by each Domino were fed through the string of Dominoes to the motherboard. The counts for a 1-s period were stored on on-board memory for that string. A LabView program was developed by the Electronics Design Laboratory (EDL) to read out the counts in each channel and display them in a user interface on a remote laptop via an Aardvark I^2C to USB adapter (Fig. 6.4.4).

The array was tested in a concrete hallway for neutron response at varying distances with a 54 ng ^{252}Cf spontaneous fission source (Fig. 6.4.5). The detector's response was first measured with the source located normally from the front face of the array, at distances of 1 m, 2 m, 5 m, and 10 m as plotted in Fig. 6.4.6. The detector yielded count rates of 79.57 ± 0.52 cts s^{-1} (1.45 ± 0.009 cts s^{-1} ng^{-1}) at a source distance of 2 m, a 10x improvement over the Panel Array Mk I. The Panel Array Mk II yielded an average background count rate of approximately 0.9 cts s^{-1} ng^{-1}. The count rates deviated from $1/r^2$ largely due to albedo neutrons from the concrete walls. It should also be noted that the count rate at 10 m was approximately 7 times the background count rate for the 54 ng source.

Fig. 6.4.5. The Panel Array Mk II was tested for neutron sensitivity in a concrete hallway at distances of 1 m, 2 m, 5 m, and 10 m. A 54 ng ^{252}Cf source with a neutron activity of approximately 125,000 n s^{-1} at 1 m above the floor was used for the sensitivity measurements.

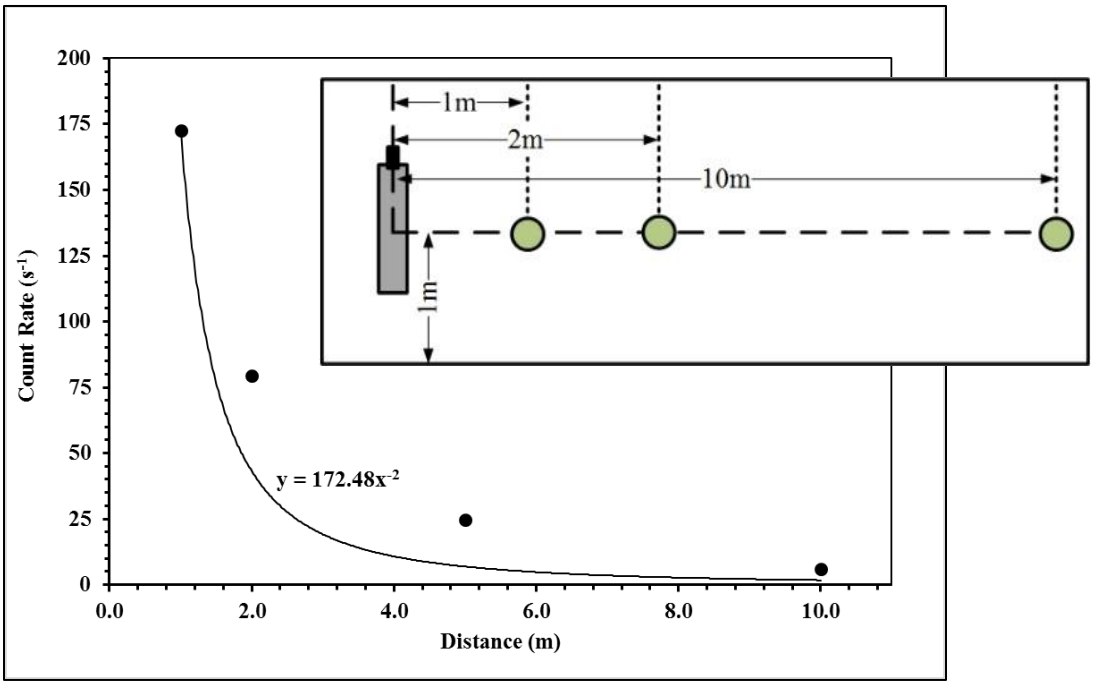

Fig. 6.4.6. Plotted is the measured count rate yielded by the Panel Array Mk II increasing source distance. The expected $1/r^2$ function is plotted for comparison.

Chapter 7 - *Conclusions*

The preceding decade saw intrinsic thermal neutron detection efficiencies of solid-state neutron detectors improve by a factor of 7x with the development of the single-sided MSND to replace common thin-film-coated diodes [6, 15]. However, the single-sided MSND is theoretically limited to 52% intrinsic thermal neutron detection efficiency due to neutron streaming paths, thereby, limiting the MSND's usefulness as a direct ^{3}He replacement [12]. Furthermore, achieving greater than 50% intrinsic thermal neutron detection efficiency requires manufacturing devices with exceedingly small features. Limitations in manufacture of such devices, due to mechanical strength of the substrate material and dopant diffusion depths, have realistically reduced detection efficiency to 35% for modern devices. This limitation was nullified with the production of the DS-MSNDs, where intrinsic thermal neutron detection efficiencies of greater than 50% are regularly achievable with the addition of a second set of trenches on the back-side of the diode, off-set from the front-side trenches, thereby, eliminating neutron streaming paths. The development of the dual-sided microstructured semiconductor (DS-MSND) represents the most significant advancement in solid-state neutron detection in this decade, exceeding the capabilities of all previous solid-state neutron detector sensors.

Previous attempts to increase the intrinsic thermal neutron detection efficiency of single-sided MSNDs, such as double-stacking single devices, allowed minimal success due to the difficulty in aligning the two devices [16]. Improper alignment of the front and back devices limited the effectiveness of the stack, and thus the technique was abandoned. However, the geometry produced by the double-stacked device (i.e. a set of front-side and back-side trenches) was ideal, therefore the idea was pursued for use in a single chip. A single-chip, DS-MSND design not only made alignment of the trenches straight forward, but also eliminated the concern that mismatched devices might not perform well, even if properly aligned.

The first-generation DS-MSNDs were produced on common 500-µm thick Si material with a front-side, semi-conformal *p*-type contact and a back-side, semi-conformal *n*-type contact, similar to the MSND. Trenches were etched to a depth of 175 µm and 20-µm wide, with a 20-µm pitch. The first significant achievement made with these first DS-MSNDs was in etching both sets of trenches simultaneously. Concerns over how the second set of trenches would be etched were

overcome through the use of a heated batch of KOH and proper alignment of the back-side pattern, thereby, allowing for both sets of trenches to be etched at the same time, thus etching times for DS-MSNDs were no greater than for single-sided MSNDs. Unfortunately, the application of the back-side *n*-type contacts restricted the depth of the depletion region and limiting intrinsic thermal neutron detection efficiencies of these first devices to roughly 20%, which is much less than single sided MSNDs of the time [19]. The effect was lessened by reducing the conformalness and the concentration of the back-side *n*-type contact. Second-generation DS-MSNDs were able to achieve nearly 30%, still well short of expected values.

The second major achievement of this work came in the form of changing the contact dopant structure; the back-side contact material was instead *p*-type (*pvp*-type DS-MSNDs), thus representing a change from the traditional contact doping profiles [20]. The formation of nearly-conformal *p*-type contacts on both the front- and the back-side fins greatly increased the detection efficiency of the devices with no other changes to their geometry. This feat was achieved due to the formation of self-depletion regions within the fins by the electrochemical potential between the heavily-doped *p*-type regions of the contact layers, and the *n*-type background-doped bulk material. The built-in potential established between these regions depleted the fins of free charge carriers, thereby, establishing an effective electric field. Electron-hole pairs produced by ionization from the charge-particle reaction products are drifted by the built-in potential and induce a signal on the contacts of the device. This phenomenon was nearly missed, until it was realized that events occurring in the front- or back-side of the device would produce different polarity pulses; the electric field points towards the contact for both the anode and the cathode, thus the charge motion always induces a positive pulse on the contact. The electronics system references the potential to the ground (very often the cathode side of the device), therefore, events occurring on the front-side of the device would produce a positive pulse from the anode, but a negative pulse from the cathode. Once both the positive and negative pulses were measured, devices regularly achieved greater than 50% intrinsic thermal neutron detection efficiency, with a world-record detection efficiency of 53.4% being achieved by a single device.

The expected detection efficiency for the final iteration of DS-MSNDs reported was nearly 60%, indicating that producing a fully-conformal contact was not achieved. However, it does show that producing these devices is possible, and that theoretical models are accurate. Geometries capable of greater than 70-80% intrinsic thermal neutron detection efficiency are possible if new

techniques for in-trench contact forming can be developed. Such devices would be directly comparable to many ^{3}He counters that are nearly 150x more expensive to manufacture. Furthermore, this method for producing DS-MSNDs has two additional unexpected benefits not possible in the single-sided MSNDs. First, formation of the *p*-type contacts on both sides of the device requires only a single diffusion process, unlike the MSND which requires and intermediate oxide-etch, drying, and then *n*-type diffusion process, requiring more than 2x the time to produce than the DS-MSND *pvp*-type contact profile. The second unexpected benefit was that the *pvp*-type DS-MSND operates on 0-V applied bias, therefore bias electronics are no longer necessary, thereby, reducing circuit complexity, power consumption, and cost. Overall, the DS-MSND technology reported here has improved intrinsic thermal neutron detection efficiency of solid-state neutron detectors from 35% to 54% while reducing cost and complexity of manufacture, and simplifying operation, thereby, reducing the cost and complexity of supporting electronics.

DS-MSND technology represents a form of solid-state neutron detectors never before demonstrated, and has achieved intrinsic thermal neutron detection efficiency records for single devices. Their low cost and mass producibility make them ideal for use in commercial instruments and will likely replace the single-sided MSND in the coming years. The future of the technology will likely see improvements in detection efficiency through improved trench and fin geometries and improved methods for doping fins deep within the trenches, thereby, ensuring full fin depletion. Detection efficiencies exceeding 70% will likely be achieved in the coming years with these improvements, by deploying the techniques learned and reported here. The importance of these achievements will be felt in the field of neutron detection as lower-cost, higher-efficiency, lower-profile instruments will now be possible by replacing ^{3}He proportional counters with DS-MSND sensors, at a small fraction of the size, cost, and power requirements. These instruments will allow for more flexibility and improved accuracy in national defense, space and celestial-body investigations, personal dosimetry, and reactor-physics applications.

Appendix A - *References*

[1] A. Rose, "Sputtered boron films on silicon surface barrier detectors," *Nucl. Instr. Meth.*, vol. 52, pp. 166-170, 1967.

[2] A. Mireshghi, G. Cho, J. Drewery, T. Jing, S. N. Kaplan, V. Perez-Mendez, and D. Wildermuth, "Amorphous silicon position sensitive neutron detector," *IEEE Trans. Nucl. Sci.*, vol. 39, pp. 635-640, 1992.

[3] A. Mireshghi, G. Cho, J. S. Drewery, W. S. Hong, T. Jing, H. Lee, S. N. Kaplan, and V. Perez-Mendez, "High efficiency neutron sensitive amorphous silicon pixel detectors," *IEEE Trans. Nucl. Sci.*, vol. 41, pp. 915-921, 1994.

[4] S. Pospisil, B. Sopko, E. Havrankova, Z. Janout, J. Konicek, I. Macha, and J. Pavlu, "Si diode as a small detector of slow neutrons," *Rad. Prot. Dosimetry*, vol. 46, pp. 115-118, 1993.

[5] D. S. McGregor, J. T. Lindsay, C. C. Brannon, and R. W. Olsen, "Semi-insulating bulk GaAs as a semiconductor thermal-neutron imaging device," *Nucl. Instr. Meth. Phys. Res. A*, vol. 380, pp. 271-275, 1996.

[6] D. S. McGregor, R. T. Klann, H. K. Gersch, and Y. H. Yang, "Thin-film-coated bulk GaAs detectors for thermal and fast neutron measurements," *Nucl. Instr. Meth.*, vol. 466, pp. 126-141, 2001.

[7] D. S. McGregor, R. T. Klann, H. K. Gersch, E. Ariesanti, J. D. Sanders, and B. VanDerElzen, "New surface morphology for low stress thin-film-coated thermal neutron detectors," *IEEE Trans. Nucl. Sci.*, vol. 49, pp. 1999-2004, 2002.

[8] D. S. McGregor and J. K. Shultis, "Spectral identification of thin-film-coated and solid-form semiconductor neutron detectors," *Nuclear Instruments and Methods in Physics Research A*, vol. 517, pp. 180-188, 2003.

[9] R. A. Muminov and L. D. Tsvang, "High-efficiency semiconductor thermal-neutron detectors," *Soviet Atomic Energy*, vol. 62, pp. 316-19, 1987.

[10] J. Schelten, M. Balzhauser, F. Hongesberg, R. Engels, and R. Reinartz, "A new neutron detector development based on silicon semiconductor and ^{6}LiF converter," *Physica B*, vol. 234-236, pp. 1084-1086, 1997.

[11] D. S. McGregor, S. L. Bellinger, and J. K. Shultis, "Present status of microstructured semiconductor neutron detectors," *J. of Crys. Growth*, vol. 379, pp. 99-110, 2013.

[12] J. K. Shultis and D. S. McGregor, "Design and performance considerations for perforated semiconductor thermal-neutron detectors," *Nucl. Instr. Meth. Phys. Res. A*, vol. 606, pp. 608-636, 2009.

[13] S. L. Bellinger, B. W. Cooper, R. G. Fronk, L. C. Henson, T. R. Ochs, T. J. Sobering, and D. S. McGregor, "Characterization of microstructured semiconductor neutron detectors," in *IEEE Nucl. Sci. Symp.*, Seoul, Korea, 2013, pp. 1-7.

[14] R. G. Fronk, S. L. Bellinger, L. C. Henson, D. E. Huddleston, T. R. Ochs, T. J. Sobering, and D. S. McGregor, "High-efficiency microstructured semiconductor neutron detectors for direct He-3 Replacement," *Nucl. Inst. Meth. Phys. Res. A*, vol. 779, pp. 25-32, 2015.

[15] D. S. McGregor, S. L. Bellinger, R. G. Fronk, L. Henson, D. Huddleston, T. Ochs, J. K. Shultis, T. J. Sobering, and R. D. Taylor, "Development of compact high efficiency microstructured semiconductor neutron detectors," *Rad. Phys. Chem.*, vol. 116, pp. 32-37,

2015.
[16] S. L. Bellinger, R. G. Fronk, W. J. McNeil, J. K. Shultis, T. J. Sobering, and D. S. McGregor, "Characteristics of the stacked microstructured solid-state neutron detector," in *Proc. of SPIE*, San Diego, CA USA, 2010.
[17] S. L. Bellinger, R. G. Fronk, T. J. Sobering, and D. S. McGregor, "High-efficiency microstructured semiconductor neutron detectors that are arrayed, dual-integrated, and stacked," *App. Rad. and Iso.*, vol. 79, pp. 1121-1124, 2012.
[18] S. L. Bellinger, R. G. Fronk, W. J. McNeil, T. J. Sobering, and D. S. McGregor, "Improved high effiiciency stacked microstructured neutron detectors backfilled with nanoparticle ^{6}LiF," *IEEE Trans. Nucl. Sci.*, vol. 59, pp. 167-173, 2012.
[19] R. G. Fronk, S. L. Bellinger, L. C. Henson, D. Huddleston, T. R. Ochs, C. T. Smith, T. J. Sobering, C. J. Rietcheck, R. D. Taylor, J. K. Shultis, and D. S. McGregor, "Development of the dual-sided microstructured semiconductor neutron detector," in *IEEE Nucl. Sci. Symp.*, Seattle, WA, 2014.
[20] R. G. Fronk, S. L. Bellinger, L. C. Henson, T. R. Ochs, C. T. Smith, J. K. Shultis, and D. S. McGregor, "Dual-sided microstructured semiconductor neutron detectors (DSMSNDs)," *Nucl. Inst. Meth. Phys. Res. A*, vol. 804, pp. 201-206, 2015.
[21] S. L. Bellinger, "Advanced Microstructured Semiconductor Neutron Detectors: Design, Fabrication, and Performance," Mech. & Nucl. Eng. Dept., Kansas State University, Manhattan, KS, 2011.
[22] W. J. McNeil, "Perforated Diode Neutron Sensors," Mech. & Nucl. Eng. Dept. , Kansas State University, Manhattan, KS, 2010.
[23] E. Rutherford, "Uranium radiation and the electrical conduction produced by it," *Philos. Mag.*, vol. 47, 1899.
[24] N. Tsoulfanidis, *Measurement and Detection of Radiation*, 2nd ed. Washington D.C., USA: Taylor & Francis, 1995.
[25] D. Griffiths, *Introduction to Elementary Particles*: John Wiley & Sons, Inc., 1987.
[26] G. F. Knoll, *Radiation Detection and Measurement*, 4th ed.: John Wiley & Sons, Inc., 2010.
[27] J. K. Shultis and R. E. Faw, *Fundamentals of Nuclear Science and Engineering*: CRC Press, 2008.
[28] W. N. Cottingham and D. A. Greenwood, *An Introduction to Nuclear Physics* vol. Cambridge, NY: Cambridge University Press, 2001.
[29] D. Reilly, N. Ensslin, J. H. Smith, and S. Kreiner, *Passive Nondestructive Assay of Nuclear Materials*. Los Alamos, NM: Nuclear Regulatory Commission, 1991.
[30] J. K. Shultis and R. E. Faw, *Radiation Shielding*, 1st ed. La Grange Park, Il., USA: American Nuclear Society, Inc., 2000.
[31] S. R. Bolding, "Design of a neutron spectrometer and simulations of neutorn multiplicity experiments with nuclear data perturbations," Masters of Science, Mechanical and Nuclear Engineering, Kansas State University, Manhattan, KS USA, 2013.
[32] B. o. R. Health, *Radiological Health Handbook*. Washington D.C., USA: U.S. Department of Health, Education, and Welfare, 1970.
[33] J. J. Duderstadt and L. J. Hamilton, *Nuclear Reactor Analysis*: John Wiley & Sons, Inc., 1976.
[34] G. Bertolini and A. Coche, *Semiconductor Detectors*, 1st ed. New York, NY, USA: American Elsevier Publishing Company, Inc., 1968.

[35] N. Bohr, "On the constitution of atoms and molecules," *Philos. Mag.*, vol. 6, pp. 1-25, 1913.
[36] R. F. Pierret, *Semiconductor Fundamentals*, 2nd ed. vol. 1. New York, NY, USA: Addison-Wesley Publishing Company, 1988.
[37] D. J. Griffiths, *Introduction to Quantum Mechanics*. Upper Saddle River, NJ, USA: Pearson Education, Inc., 2005.
[38] G. Dearnaley and D. C. Northrop, *Semiconductor Counters for Nuclear Radiations*. New York, NY USA: John Wiley, Inc., 1963.
[39] S. M. Sze and K. K. Ng, *Physics of Semiconductor Devices*. Hoboken, NJ: John Wiley & Sons, Inc., 2007.
[40] S. M. Sze, *Semiconductor Devices: Physics and Technology*, 2nd ed. Hoboken, NJ: John Wiley & Sons, Inc., 2002.
[41] D. S. McGregor and R. A. Rojeski, "Performance of CdZnTe Geometrically Weighted Semiconductor Frisch Grid Radiation Detectors," *IEEE Trans. Nucl. Sci.*, vol. 46, pp. 250-259, 1999.
[42] W. J. McNeil, D. S. McGregor, A. E. Bolotnikov, G. W. Wright, and R. B. James, "Single-charge-carrier-type sensing with an insulated Frisch ring CdZnTe semiconductor radiation detecdtor," *App. Phys. Letters*, vol. 84, pp. 1988-1990, 2004.
[43] D. J. Griffiths, *Introduction to Electrodynamics*, Fourth ed. New Jersey, USA: Pearson Education, Inc., 2013.
[44] S. L. Bellinger, R. G. Fronk, and D. S. McGregor, "Method of Fabricating A Neutron Detector Such As A Microstructured Semiconductor Neutron Detector," United States Patent 8778715, 2014.
[45] S. A. Campbell, *Fabrication Engineering at the Micro- and Nanoscale*, 3rd ed. New York, USA: Oxford University Press, 2008.
[46] K. A. Nelson, "An investigation of aerogels, foams, and foils for multi-wire proportional counter neutron detectors," Ph.D., Mechanical & Nuclear Engineering Dept., Kansas State University, Manhattan, KS, 2013.
[47] K. A. Nelson, N. S. Edwards, N. J. Hinson, C. D. Wayant, and D. S. McGregor, "A suspended boron foil multi-wire proportional counter neutron detector," *Nuclear Instruments and Methods in Physics Research A*, vol. 767, pp. 14-8, 2014.
[48] K. A. Nelson, M. R. Kusner, B. W. Montag, M. R. Mayhugh, A. J. Schmidt, C. D. Wayant, J. K. Shultis, P. B. Ugorowski, and D. S. McGregor, "Characterization of a mid-sized Li foil multi-wire proportional count neutron detector," *Nuclear Instruments and Methods in Physics Research A*, vol. 762, pp. 119-24, 2014.
[49] J. L. Lacy, A. Athanasiades, L. Sun, C. S. Martin, G. J. Vazquez-Flores, M. Regmi, and S. Croft, "Performance of a Neutron Coincidence Counter Based on Boron-Coated Straws," in *2014 IEEE Nuclear Science Symposium*, Seattle, WA, 2014.
[50] A. Geuorguiev, J. Glodo, J. Tower, R. Hawrami, U. Shirwadkar, P. O'Dougherty, and K. S. Shah, "Pulse Shape Discrimination for CLYC Based Handheld Instruments," in *IEEE Nuclear Sciency Symposium and Medical Imaging Conference*, Anaheim, CA, 2012, pp. 32-37.
[51] N. D'Olympia, P. Chowdhury, C. J. Lister, J. Glodo, R. Hawrami, K. Shah, and U. Shirwadkar, "Pulse-shape analysis of CLYC for thermal neutrons, fast neutrons, and gamma-rays," *Nuclear Instruments and Methods in Physics Research A*, vol. 714, pp. 121-7, 2013.

[52] M. Suffert, "Silicon photodiode readout of scintillators and associated electronics," *Nuclear Instruments and Methods in Physics Research A,* vol. A322, pp. 523-8, 1992.
[53] F. Rego and L. Peralta, "Si-PIN photodiode readout for a scintillating optical fiber dosimeter," *Radiation Measurements,* vol. 47, pp. 947-950, 2012.
[54] D. S. McGregor, R. T. Klann, H. K. Gersch, E. Ariesanti, J. D. Sanders, and B. VanDerElzen, "New surface morphology for low stress thin-film-coated thermal neutron detectors," *IEEE Transactions on Nuclear Science,* vol. 49, 2002.
[55] D. S. McGregor, M. D. Hammig, Y.-H. Yang, H. K. Gersch, and R. T. Klann, "Design considerations for thin film coated semiconductor thermal neutron detectors-I: basics regarding alpha particle emitting neutron reactive films," *Nucl. Instr. Meth. Phys. Res. A,* vol. 500, pp. 272-308, 2003.
[56] J. K. Shultis and D. S. McGregor, "Designs for micro-structured semiconductor neutron detectors," in *SPIE Hard X-ray, Gamma-ray, and Neutron Detector Physics X*, San Diego, CA USA, 2008.
[57] S. L. Bellinger, W. J. McNeil, T. C. Unruh, and D. S. McGregor, "Characteristics of 3D micro-structured semiconductor high efficiency neutron detectors," *IEEE Transactions on Nuclear Science,* vol. 56, pp. 742-746, 2009.
[58] D. S. McGregor, W. J. McNeil, S. L. Bellinger, T. C. Unruh, and J. K. Shultis, "Microstructured semiconductor neutron detectors," *Nuclear Instruments and Methods in Physics Research A,* vol. 608, pp. 125-131, 2009.
[59] S. L. Bellinger, W. J. McNeil, and D. S. McGregor, "Variant designs and characteristics of improved microstructured solid-state neutron detectors," in *IEEE Nuclear Science Symposium Conference Record*, Orlando, FL USA, 2009, pp. 986-989.
[60] S. L. Bellinger, R. G. Fronk, W. J. McNeil, T. J. Sobering, and D. S. McGregor, "Enhanced variant designs and characteristics of the microstructured solid-state neutron detector," *Nuclear Instruments and Methods in Physics Research A,* vol. 652, pp. 387-391, 2011.
[61] W. J. McNeil, S. L. Bellinger, T. C. Unruh, E. L. Patterson, J. K. Shultis, and D. S. McGregor, "Perforated diode fabrication for neutron detection," in *IEEE Nucl. Sci. Symp.*, San Diego, USA, 2006, pp. 3732-5.
[62] E. M. Baum, H. D. Knox, and T. R. Miller, *Chart of the Nuclides*, 16th ed.: KAPL, 2002.
[63] S. L. Bellinger, R. G. Fronk, W. J. McNeil, T. J. SObering, and D. S. McGregor, "Improved high efficiency stacked microstructured neutron detectors backfilled with nanoparticle ^{6}LiF," *IEEE Transactions on Nuclear Science,* vol. 59, pp. 167-173, 2011.
[64] S. L. Bellinger, R. G. Fronk, D. S. McGregor, and T. J. Sobering, "Arrayed high efficiency dual-integrated microstructured semiconductor neutron detectors," in *IEEE Nuclear Science Symposium*, Valencia, Spain, 2011, pp. 1281-1284.
[65] ORNL. (2013). *RSICC CODE PACKAGE CCC-810*. Available: https://rsicc.ornl.gov/codes/ccc/ccc8/ccc-810.html
[66] W. L. Dunn and J. K. Shultis, *Exploring Monte Carlo Methods*. Burlington, MA USA: Academic Press, 2012.
[67] D. S. McGregor and J. K. Shultis, "Reporting detection efficiency for semiconductor neutron detectors: A need for a standard," *Nuclear Instruments and Methods in Physics Research A,* vol. 632, pp. 167-174, 2011.
[68] J. K. Shultis and D. S. McGregor, "Calculation of Ion Energy-Deposition Spectra in Silicon, Lithium-Fluoride, Boron, and Boron Carbide," College of Engineering, Kansas State University, Manhattan, KS2007.

[69] C. J. Solomon, J. K. Shultis, W. J. McNeil, T. C. Unruh, B. B. Rice, and D. S. McGregor, "A hybrid method for coupled neutron-ion transport calculations for 10-B and 6-LiF coated and perforated detector efficiencies," *Nuclear Instruments and Methods in Physics Research A*, vol. 580, pp. 326-330, 2007.
[70] S. K. Ghandhi, *VLSI Fabrication Principles*, 1st ed.: Rensselaer Polytechnic Institute, 1983.
[71] K. Sato, M. Shikida, Y. Matsushima, T. Yamashiro, K. Asaumi, Y. Iriye, and M. Yamamoto, "Characterization of anisotropic etching properties of single-crystal silicon: effects of KOH concentration on etching profiles," in *IEEE Micro Electro Mechanical Systems*, Nagoya, Japan, 1997, pp. 406-411.
[72] L. E. Kassel, "KOH-Etch related defects on processed silicon wafers," in *Mat. Res. Soc. Symp. Proc.*, Pittsburgh, USA, 1992, pp. 187-192.
[73] K. P. Rola and I. Zubel, "Impact of alcohol additives concentration on etch rate and surface morphology of (100) and (110) Si substrates etched in KOH solutions," *Microsyst. Tech.*, vol. 19, pp. 635-643, 2013.
[74] S. Dutta, M. Imran, P. Kumar, R. Pal, P. Datta, and R. Chatterjee, "Comparison of etch characteristics of KOH, TMAH and EDP for bulk micromachining of silicon (110)," *Microsyst. Tech.*, vol. 17, pp. 1621-1628, 2011.
[75] W. C. Chien, C. O. Chang, P. Chen, and C. Chou, "On the determination of Si(110) convex corner undercut planes by the zoning model," *Journ. of the Electrochem. Soc.*, vol. 155, pp. D209-D222, 2008.
[76] R. G. Fronk, S. L. Bellinger, L. C. Henson, T. R. Ochs, C. T. Smith, and D. S. McGregor, "Zero-bias dual-sided microstructured semiconductor neutron detectors (DSMSNDs)," *Nucl. Inst. Meth. Phys. Res. A*, vol. Submitted., 2015.
[77] *CRC Handbook of Chemistry and Physics*, 87 ed. New York, USA: Taylor & Francis Group, 2006-2007.
[78] (2008). *Optimizing your diamond blade cutting operation*. Available: http://ukam.com/optimizing_diamond_blades.htm
[79] (2008). *Diamond blade sawing problem solving trouble shooting*. Available: http://ukam.com/blade_trouble_shooting.htm
[80] "American National Standard Performance Criteria for Backpack-Based Radiation-Detection Systems Used for Homeland Security," ed: Electrical and Electronics Engineers, Inc., 2013.
[81] S. L. Bellinger, B. W. Cooper, N. R. Crawford, R. G. Fronk, T. J. Sobering, R. D. Taylor, and D. S. McGregor, "Very large area multi-element microstructured semiconductor neutron detector panel array," in *IEEE Nuclear Science Symposium*, Anaheim, CA USA, 2012, pp. 215-218.
[82] R. G. Fronk, S. L. Bellinger, L. C. Henson, T. R. Ochs, M. A. Reichenberger, C. J. Rietcheck, C. T. Smith, J. K. Shultis, and D. S. McGregor, "Advancements in Microstructured Semiconductor Neutron Detector (MSND)-Based Instruments," in *IEEE Nucl. Sci. Symp.*, San Diego, CA, 2015.
[83] B. Semiconductors. (1991). *CAN Specification Version 2.0*. Available: http://www.bosch-semiconductors.de/media/ubk_semiconductors/pdf_1/canliteratur/can2spec.pdf
[84] S. L. Bellinger, R. G. Fronk, T. J. Sobering, T. R. Ochs, L. C. Henson, and D. S. McGregor, "Microstructured semiconductor neutron detector (MSND)-based helium-3 replacement technology," in *IEEE Nucl. Sci. Sym.*, Seattle, United States, 2014.

[85] J. Ziegler, "The Stopping and Range of Ions in Matter," 2008 ed, 2015.
[86] CANBERRA. (2016). *Model 2022A Spectroscopy Amplifier*. Available: http://www.canberra.com/products/radiochemistry_lab/pdf/Model-2022A-SS-C40488.pdf

Appendix B - *MCNP Input Cards*

MCNP Input Card Introduction

This section contains the MCNP6 input cards used throughout this work. These input cards are fed to MCNP in a terminal window using either (assuming that Windows is the host operating system):

```
mcnp6.exe i = [input_file_name].i o = [output_file_name].o
```

or

```
mcnp6.exe i = [input_file_name].i o = [output_file_name].o tasks [n]
```

where '*mcnp6.exe'* denotes which version of MCNP to run, '*i ='* defines the input card file, '*o =*' and *'tasks n'* instructs MCNP to split the problem and solve the problem as a multi-threaded process. Multi-threading is only available on analog-type problem, i.e. those that are solved using Monte Carlo methods (such as in neutron transport). The *tasks* option is disabled for charged-particle-tracking (CPT) problems.

The structure of a typical *input* file for MCNP goes as **Problem Title**, **Cell Cards**, **Surface Cards**, and **Data Cards**, where are filled in as follows:

Problem Title - A free line for titling of the MCNP problem to be solved.

```
Standard DSMSND Device - Mono-Energetic, Normally Incident Beam
…
```

Cell Cards – The Cell Cards section defines the bodies contained within the problem. Surface cards (defined in the next section) are filled with materials, given densities, and repeated in lattices (if used) in this section. The input parameters go as:

```
…
C ===================================================================
C --------------------CELL CARDS-------------------
C ===================================================================
[Cell Number] [Mat. ID] -[Mat. Density] [Surf.] [Lat] [Fill] [Universe]$ [Comments]
…
```

Cell Numbers are defined by the user and can be any value between 1 and 9999 and cannot be

reused in the same input file. The *Mat. ID* is defined later in the Data Cards section and defines what material the cell is comprised of. The *Mat. Density* is defined with a '-' symbol and is in units of g/cm^3. The *Surf.* definition determines how the cell fills the given surfaces. For macrobodies (complete shapes built by MCNP), a '-' denotes that the cell is within the surface, and a ' ' denotes that the cell is outside of the surface. The *Lat* parameter states which repeating structure (i.e. cubic, 1, or hexagonal, 2) a cell should take, should the problem call for cell to fill some volume in a repeating manor. *Fill* and *Universe* are used to define what 'universe' a cell contains and what 'universe' that cell is defined as, respectively.

Surface Cards – Surface Cards are used to define boundaries for cells and defines the world as it is seen by MCNP. The input parameters go as:

```
…
C ===========================================================================
C --------------------SURFACE CARDS----------------
C ===========================================================================
[Surf. Number] [Surf. Type] [Surface Boundaries] $ [Comments]
…
```

The *Surf. Number* is the identification number for that particular surface, as referenced by the Cell Card and can be any number between 1 and 9999. The *Surf. Type* defines the type of surface being constructed, such as a single plane or macrobody (fully enclosed surface, such as a hollow cube). *Surface Boundaries* are typically coordinates that position the surface within the MCNP world and typically take on a Cartesian-coordinate system.

Data Cards – With the Data Cards, the physics, materials, and problem parameters are defined for MCNP. The Data Cards can take on many forms, but for a majority of the cases of the problems defined in this work, the input parameters go as:

```
…
C ===========================================================================
C --------------------DATA CARDS-------------------
C ===========================================================================
MODE [Part.] – Defines what particles to consider for the given problem.
IMP: [Part.] [Importance] – Defines the weight a particle takes in a given cell.
PHYS:[Part.] [Parameters] – Sets options for MCNP's handling of given particle.
CUT: [Part.] [Parameters] – Sets lower-level energy at which the particle is killed.
M[N] [Isotope] [Atom/Weight Fraction] – Defines material used for cell.
SDEF POS=[x,y,z]  PAR=[Part.] ERG=[Energy] [Parameters] – Defines the source to be used by MCNP by
setting its position, what particles and at what energy it emits, etc. Each of these settings can
be further defined with sub-parameters to disperse the source across a surface or volume as well
as give the source some energy distribution or biasing.
F[MN]:[Part.] [Surf./Cell] – Defines what type of tally (N) and tally ID (M), what particle it is
tallying, and what surface or cell contains the area of interest.
```

MS-DOS Batch File to Run MCNP6

This file, titled MCNP.bat, is used to automatically set the environmental variables necessary to run MCNP6 in a plain MS-DOS environment. This file, named MCNP.bat, can be executed to run any desired MCNP file, MCNP is installed. The file was used in conjunction with Python to automate many of the optimization portions of the problem.

```
@ REM - Sets the MCNP Environment Variables for use in standard
@ REM - command prompt. This will help with MatLab functionality.
@ set MCNPPATH=C:\MCNP\MCNP_CODE\bin
@ PATH %MCNPPATH%;%PATH%
@ set DISPLAY=:0.0
@ set DATAPATH=C:\MCNP\MCNP_DATA
mcnp6.exe i=li_foil.i o=li_foil.o
erase run*
```

Here, the line mcnp6.exe `i=li_foil.i o=li_foil.o` can be amended to include multiple files, each with potentially a different problem condition and output file name.

Standard MSND MCNP6 Input File

Below is a complete, standard MCNP6 input file for a 0.5-mm thick MSND made from a Si *pvn*-junction diode, backfilled with nano-sized ^{6}LiF powder. Trenches are etched into the Si diode 350-μm deep and 20-μm wide with a 30-μm pitch. The device is irradiated with a 0.2-mm diameter collimated beam of thermal (0.0254 eV) neutrons. Charged-particle tracking has been turned on for this simulation as noted in the *Mode* input parameter. There are two tallies recorded for this simulation, each recording and binning energy deposition in the Si material. The first is intended to record the overall react-product pulse-height spectrum while the second is to output the overall intrinsic thermal neutron detection efficiency with LLD = 300 keV.

```
Standard MSND Device - Mono-Energetic, Normally Incident Beam
C ===========================================================================
C --------------------CELL CARDS-------------------
C ===========================================================================
C DSMSND
    10  2 -2.329 -10                    u=1 $ Front Sidewall
    11  1 -2.550  10                    u=1 $ Front Trench, 6-LiF
    12  0        -11       lat=1 fill=1 u=2 $ Front Unit Cell
    13  0        -12             fill=2     $ Front Diode
    14  2 -2.329 -13 12                     $ Bottom of Diode
C World
    100 0 #13 #14 -100        $ VOID IN WORLD
    101 0 100                    $ OUTSIDE WORLD

C ===========================================================================
C --------------------SURFACE CARDS----------------
C ===========================================================================
C DSMSND
    10 RPP 0.0000 0.0350  -0.50 0.50  -0.00075 0.00075 $ Front Sidewall
    11 RPP 0.0000 0.0350  -0.50 0.50  -0.00150 0.00150 $ Front Unit Cell
    12 RPP 0.0000 0.0350  -0.50 0.50  -0.50    0.50    $ Front Diode
    13 RPP 0.0350 0.0500  -0.50 0.50  -0.50    0.50    $ Bottom of Diode
C
    100 so 4 $ universe

C ===========================================================================
C --------------------DATA CARDS-------------------
C ===========================================================================
C
C ===========================================================================
C PHYSICS/CUT OFF
C ===========================================================================
MODE N T A
IMP:N 1 5R 0
IMP:T 1 4R 0 0
IMP:A 1 4R 0 0
PHYS:N 6J 3      $ NCIA, 3=ions are from neutron capture
CUT:N  2J 0
CUT:T  J 0.01 0 $ 10keV Energy Cut-off
CUT:A  J 0.01 0 $ 10keV Energy Cut-off
nps 2E6
C ===========================================================================
C  MATERIALS
C ===========================================================================
M1 $ 6-LITHIUM FLUORIDE, RHO = 2.635 (CRYSTALLINE)
```

```
      3006.70c  -0.225502
      3007.70c  -0.016789
      9019.70c  -0.757709
C
M2 $ NATURAL SILICON, RHO = 2.3290
     14028.70c  -9.2223E-01
     14029.70c  -4.6850E-02
     14030.70c  -3.0920E-02
C
C ===========================================================================
C SOURCE - COLL. 1CM DISK 0.0254eV ALONG THE X-AXIS.
C ===========================================================================
SDEF  POS= -0.1 0 0 PAR= N ERG= 0.0254E-6 VEC= 1 0 0  DIR= 1
      RAD= D1 AXS= 1 0 0 EXT= 0
SI1  0 0.1
SP1  -21 1
C ===========================================================================
C TALLY
C ===========================================================================
C --- SPECTRUM --------------
F6:A     (10 14)
SD6      1
F16:T    (10 14)
SD16     1
F8:A,T   (10 14)
FT8  phl 2 6 1 16 1 0
E8   0   100i  5
C --- EFFICIENCY ------------
F18:A,T   (10 14)
FT18  phl 2 6 1 16 1 0
E18   0   0.3  5
```

Standard DS-MSND MCNP6 Input File

Below is a complete, standard MCNP6 input file for a 1-mm thick DS-MSND made from a Si *pvp*-junction diode, backfilled with nano-sized ^{6}LiF powder. Trenches are etched into the Si diode 350-μm deep and 15-μm wide with a 30-μm pitch. The device is irradiated with a 0.2-mm diameter collimated beam of thermal (0.0254 eV) neutrons. Charged-particle tracking has been turned on for this simulation as noted in the *Mode* input parameter. This mode results in longer computational time, but more accurate results as the charged-particle reaction products are tracked for each neutron absorption event. There are two tallies recorded for this simulation, each recording and binning energy deposition in the Si material. The first is intended to record the overall react-product pulse-height spectrum while the second is to output the overall intrinsic thermal neutron detection efficiency with LLD = 300 keV.

```
Standard DSMSND Device - Mono-Energetic, Normally Incident Beam
C ===============================================================================
C --------------------CELL CARDS-------------------
C ===============================================================================
C DSMSND
    10  2 -2.329 -10                    u=1 $ Front Sidewall
    11  1 -2.550  10                    u=1 $ Front Trench, 6-LiF
    12  0        -11       lat=1 fill=1 u=2 $ Front Unit Cell
    13  0        -12             fill=2     $ Front Diode
    14  2 -2.329 -13 12 14                  $ Middle of Diode
    15  2 -2.329 -16                    u=3 $ Backside Sidewall
    16  1 -2.550  16                    u=3 $ Backside Trench, 6-LiF
    17  0        -15       lat=1 fill=3 u=4 $ Backside Unit Cell
    18  0        -14             fill=4     $ Backside Diode
C World
    100 0 #13 #14 #18 -100        $ VOID IN WORLD
    101 0 100                           $ OUTSIDE WORLD

C ===============================================================================
C --------------------SURFACE CARDS----------------
C ===============================================================================
C DSMSND
    10 RPP 0.0000 0.0350  -0.50 0.50  -0.00075 0.00075 $ Front Sidewall
    11 RPP 0.0000 0.0350  -0.50 0.50  -0.00150 0.00150 $ Front Unit Cell
    12 RPP 0.0000 0.0350  -0.50 0.50  -0.50    0.50    $ Front Diode
    13 RPP 0.0350 0.0650  -0.50 0.50  -0.50    0.50    $ Middle of Diode
    14 RPP 0.0650 0.1000  -0.50 0.50  -0.50    0.50    $ Backside Diode
    15 RPP 0.0650 0.1000  -0.50 0.50   0.00000 0.00300 $ Backside Unit Cell
    16 RPP 0.0650 0.1000  -0.50 0.50   0.00000 0.00150 $ Backside Sidewall
C
    100 so 4 $ universe

C ===============================================================================
C --------------------DATA CARDS-------------------
C ===============================================================================
C
C ===============================================================================
C PHYSICS/CUT OFF
C ===============================================================================
MODE N T A
```

```
IMP:N 1 9R 0
IMP:T 1 8R 0 0
IMP:A 1 8R 0 0
PHYS:N 6J 3      $ NCIA, 3=ions are from neutron capture
CUT:N  2J 0
CUT:T  J 0.01 0 $ 10keV Energy Cut-off
CUT:A  J 0.01 0 $ 10keV Energy Cut-off
nps 2E6
C ===========================================================================
C  MATERIALS
C ===========================================================================
M1 $ 6-LITHIUM FLUORIDE, RHO = 2.635 (CRYSTALLINE)
      3006.70c  -0.225502
      3007.70c  -0.016789
      9019.70c  -0.757709
C
M2 $ NATURAL SILICON, RHO = 2.3290
     14028.70c  -9.2223E-01
     14029.70c  -4.6850E-02
     14030.70c  -3.0920E-02
C
C ===========================================================================
C SOURCE - COLL. 1CM DISK 0.0254eV ALONG THE X-AXIS.
C ===========================================================================
SDEF  POS= -0.1 0 0 PAR= N ERG= 0.0254E-6 VEC= 1 0 0  DIR= 1
      RAD= D1 AXS= 1 0 0 EXT= 0
SI1  0 0.1
SP1  -21 1
C ===========================================================================
C TALLY
C ===========================================================================
C --- SPECTRUM --------------
F6:A     (10 14 15)
SD6      1
F16:T    (10 14 15)
SD16     1
F8:A,T   (10 14 15)
FT8  phl 2 6 1 16 1 0
E8   0   100i  5
C --- EFFICIENCY ------------
F18:A,T   (10 14 15)
FT18  phl 2 6 1 16 1 0
E18   0   0.3  5
```

Approximated DS-MSND MCNP6 Input File

Below is a complete, standard MCNP6 input file for a 1-mm thick DS-MSND made from a Si *pvp*-junction diode, backfilled with nano-sized ^{6}LiF powder. Trenches are etched into the Si diode 350-μm deep and 15-μm wide with a 30-μm pitch. The device is irradiated with a 0.2-mm diameter collimated beam of thermal (0.0254 eV) neutrons. Charged-particle tracking has been turned off for this simulation as noted in the *Mode* input parameter. This mode results in shorter computational time, but reduced accuracy for neutrons that vary from thermal energies. The tally is a modified F4 tally (denoted with the FM4 card) and is a simple multiplier of the neutron path length through the conversion material.

```
Standard DSMSND Device Approx. - Mono-Energetic, Normally Incident Beam
C ======================================================================
C --------------------CELL CARDS-------------------
C ======================================================================
C DSMSND
    10  2 -2.329  10                    u=1 $ Front Sidewall
    11  1 -2.540 -10                    u=1 $ Front Trench, 6-LiF
    12  0        -11       lat=1 fill=1 u=2 $ Front Unit Cell
    13  0        -12             fill=2     $ Front Diode
    14  2 -2.329 -13 12 14                  $ Middle of Diode
    15  2 -2.329  16                    u=3 $ Backside Sidewall
    16  1 -2.540 -16                    u=3 $ Backside Trench, 6-LiF
    17  0        -15       lat=1 fill=3 u=4 $ Backside Unit Cell
    18  0        -14             fill=4     $ Backside Diode
C World
    100 0 #13 #14 #18 -100        $ VOID IN WORLD
    101 0 100                           $ OUTSIDE WORLD

C ======================================================================
C --------------------SURFACE CARDS----------------
C ======================================================================
C DSMSND
    10 RPP 0.0000 0.0350  -0.50 0.50  -0.00075 0.00075 $ Front Sidewall
    11 RPP 0.0000 0.0350  -0.50 0.50  -0.00150 0.00150 $ Front Unit Cell
    12 RPP 0.0000 0.0350  -0.50 0.50  -0.50    0.50    $ Front Diode
    13 RPP 0.0350 0.0650  -0.50 0.50  -0.50    0.50    $ Middle of Diode
    14 RPP 0.0650 0.1000  -0.50 0.50  -0.50    0.50    $ Backside Diode
    15 RPP 0.0650 0.1000  -0.50 0.50   0.00000 0.00300 $ Backside Unit Cell
    16 RPP 0.0650 0.1000  -0.50 0.50   0.00075 0.00225 $ Backside Sidewall
C
    100 so 4 $ universe

C ======================================================================
C --------------------DATA CARDS-------------------
C ======================================================================
C
C ======================================================================
C PHYSICS/CUT OFF
C ======================================================================
MODE N
IMP:N 1 9R 0
PHYS:N 6J 3      $ NCIA, 3=ions are from neutron capture
CUT:N  2J 0
C ======================================================================
C  MATERIALS
```

```
C ===========================================================================
M1 $ 6-LITHIUM FLUORIDE, RHO = 2.635 (CRYSTALLINE)
      3006.70c  -0.225502
      3007.70c  -0.016789
      9019.70c  -0.757709
C
M2 $ NATURAL SILICON, RHO = 2.3290
     14028.70c  -9.2223E-01
     14029.70c  -4.6850E-02
     14030.70c  -3.0920E-02
C
C ===========================================================================
C SOURCE - COLL. 1CM DISK 0.0254eV ALONG THE X-AXIS.
C ===========================================================================
SDEF  POS= -0.1 0 0 PAR= N ERG= 0.0254E-6 VEC= 1 0 0  DIR= 1
      RAD= D1 AXS= 1 0 0 EXT= 0
SI1  0 0.1
SP1  -21 1
C ===========================================================================
C TALLY
C ===========================================================================
F4:N 11 16
FM4 4.9898E-6 1 105 $ 25%, FM4 2.33694E-6 (scales linearly)
C ===========================================================================
C Problem Stuff
C ===========================================================================
nps 2E6
```

Standard Modular Neutron Detector (MND) MCNP6 Input File

Below is a complete, standard MCNP6 input file for the Modular Neutron Detector (MND), as developed in 2015. The MND was populated with twenty-four single-sided MSNDs, arranged in a 4x6 array. The devices were mounted to ceramic disposable boards (CDBs) that measured 2-mm thick. The CDBs were then mounted directly to a 32-mil thick FR4 electronics board. No electronics components were modeled on the back-side of the MND. This particular card irradiates the MND with a large-diameter beam of collimated thermal neutrons.

```
Standard MND Device, Single-Sided MSNDs
C ===============================================================================
C --------------------CELL CARDS-------------------
C ===============================================================================
C ******************** MSNDS ************************************************
C First Row, MSND 1-1
    110  3 -2.329 -10              u=1 $ Sidewall
    111  1 -2.550  10              u=1 $ Trench, LiF
    112  0        -11 lat=1 fill=1 u=2 $ Unit Cell
    113  0        -12       fill=2     $ Diode
    114  3 -2.329 -13                  $ Diode bottom
C First Row, MSND 1-2
    120  3 -2.329 -20              u=3 $ Sidewall
    121  1 -2.550  20              u=3 $ Trench, LiF
    122  0        -21 lat=1 fill=3 u=4 $ Unit Cell
    123  0        -22       fill=4     $ Diode
    124  3 -2.329 -23                  $ Diode bottom
C First Row, MSND 1-3
    130  3 -2.329 -30              u=5 $ Sidewall
    131  1 -2.550  30              u=5 $ Trench, LiF
    132  0        -31 lat=1 fill=5 u=6 $ Unit Cell
    133  0        -32       fill=6     $ Diode
    134  3 -2.329 -33                  $ Diode bottom
C First Row, MSND 1-4
    140  3 -2.329 -40              u=7 $ Sidewall
    141  1 -2.550  40              u=7 $ Trench, LiF
    142  0        -41 lat=1 fill=7 u=8 $ Unit Cell
    143  0        -42       fill=8     $ Diode
    144  3 -2.329 -43                  $ Diode bottom
C Second Row, MSND 2-1, 2-2, 2-3, 2-4
    213 LIKE 113 BUT TRCL=(0 0 -1.2) $ MSND 2-1
    214 LIKE 114 BUT TRCL=(0 0 -1.2) $ MSND 2-1
    223 LIKE 123 BUT TRCL=(0 0 -1.2) $ MSND 2-2
    224 LIKE 124 BUT TRCL=(0 0 -1.2) $ MSND 2-2
    233 LIKE 133 BUT TRCL=(0 0 -1.2) $ MSND 2-3
    234 LIKE 134 BUT TRCL=(0 0 -1.2) $ MSND 2-3
    243 LIKE 143 BUT TRCL=(0 0 -1.2) $ MSND 2-4
    244 LIKE 144 BUT TRCL=(0 0 -1.2) $ MSND 2-4
C Third Row, MSND 3-1, 3-2, 3-3, 3-4
    313 LIKE 113 BUT TRCL=(0 0 -2.4) $ MSND 3-1
    314 LIKE 114 BUT TRCL=(0 0 -2.4) $ MSND 3-1
    323 LIKE 123 BUT TRCL=(0 0 -2.4) $ MSND 3-2
    324 LIKE 124 BUT TRCL=(0 0 -2.4) $ MSND 3-2
    333 LIKE 133 BUT TRCL=(0 0 -2.4) $ MSND 3-3
    334 LIKE 134 BUT TRCL=(0 0 -2.4) $ MSND 3-3
    343 LIKE 143 BUT TRCL=(0 0 -2.4) $ MSND 3-4
    344 LIKE 144 BUT TRCL=(0 0 -2.4) $ MSND 3-4
C Fourth Row, MSND 4-1, 4-2, 4-3, 4-4
    413 LIKE 113 BUT TRCL=(0 0 -3.6) $ MSND 4-1
```

```
    414 LIKE 114 BUT TRCL=(0 0 -3.6) $ MSND 4-1
    423 LIKE 123 BUT TRCL=(0 0 -3.6) $ MSND 4-2
    424 LIKE 124 BUT TRCL=(0 0 -3.6) $ MSND 4-2
    433 LIKE 133 BUT TRCL=(0 0 -3.6) $ MSND 4-3
    434 LIKE 134 BUT TRCL=(0 0 -3.6) $ MSND 4-3
    443 LIKE 143 BUT TRCL=(0 0 -3.6) $ MSND 4-4
    444 LIKE 144 BUT TRCL=(0 0 -3.6) $ MSND 4-4
C Fifth Row, MSND 5-1, 5-2, 5-3, 5-4
    513 LIKE 113 BUT TRCL=(0 0 -4.8) $ MSND 5-1
    514 LIKE 114 BUT TRCL=(0 0 -4.8) $ MSND 5-1
    523 LIKE 123 BUT TRCL=(0 0 -4.8) $ MSND 5-2
    524 LIKE 124 BUT TRCL=(0 0 -4.8) $ MSND 5-2
    533 LIKE 133 BUT TRCL=(0 0 -4.8) $ MSND 5-3
    534 LIKE 134 BUT TRCL=(0 0 -4.8) $ MSND 5-3
    543 LIKE 143 BUT TRCL=(0 0 -4.8) $ MSND 5-4
    544 LIKE 144 BUT TRCL=(0 0 -4.8) $ MSND 5-4
C Sixth Row, MSND 6-1, 6-2, 6-3, 6-4
    613 LIKE 113 BUT TRCL=(0 0 -6.0) $ MSND 6-1
    614 LIKE 114 BUT TRCL=(0 0 -6.0) $ MSND 6-1
    623 LIKE 123 BUT TRCL=(0 0 -6.0) $ MSND 6-2
    624 LIKE 124 BUT TRCL=(0 0 -6.0) $ MSND 6-2
    633 LIKE 133 BUT TRCL=(0 0 -6.0) $ MSND 6-3
    634 LIKE 134 BUT TRCL=(0 0 -6.0) $ MSND 6-3
    643 LIKE 143 BUT TRCL=(0 0 -6.0) $ MSND 6-4
    644 LIKE 144 BUT TRCL=(0 0 -6.0) $ MSND 6-4
C ******************** MSNDS ************************************************
C ******************** ELECTRONICS ******************************************
    100 4 -1.85 -100 $ FR4 DETECTOR BOARD
    101 5 -3.95  #113 #114 #123 #124 #133 #134 #143 #144 &
          #213 #214 #223 #224 #233 #234 #243 #244 &
          #313 #314 #323 #324 #333 #334 #343 #344 &
          #413 #414 #423 #424 #433 #434 #443 #444 &
          #513 #514 #523 #524 #533 #534 #543 #544 &
          #613 #614 #623 #624 #633 #634 #643 #644 &
          -101 $ VOID IN WORLD
C World
    900 0 100 101 -900  $ VOID IN WORLD
    901 0 900           $ OUTSIDE WORLD

C ===============================================================================
C --------------------SURFACE CARDS----------------
C ===============================================================================
C MSNDs COLUMN 1
    10 RPP 0.0000 0.0400  0.10 1.10  2.5010 2.5020  $ Fin, 10um thickness
    11 RPP 0.0000 0.0400  0.10 1.10  2.5000 2.5030  $ Unit Cell, 30um pitch
    12 RPP 0.0000 0.0400  0.10 1.10  2.5000 3.5000  $ Diode Cell
    13 RPP 0.0400 0.0500  0.10 1.10  2.5000 3.5000  $ Diode Bottom
C MSNDs COLUMN 2
    20 RPP 0.0000 0.0400  1.20 2.20  2.5010 2.5020  $ Fin, 10um thickness
    21 RPP 0.0000 0.0400  1.20 2.20  2.5000 2.5030  $ Unit Cell, 30um pitch
    22 RPP 0.0000 0.0400  1.20 2.20  2.5000 3.5000  $ Diode Cell
    23 RPP 0.0400 0.0500  1.20 2.20  2.5000 3.5000  $ Diode Bottom
C MSNDs COLUMN 3
    30 RPP 0.0000 0.0400  -1.10 -0.10  2.5010 2.5020  $ Fin, 10um thickness
    31 RPP 0.0000 0.0400  -1.10 -0.10  2.5000 2.5030  $ Unit Cell, 30um pitch
    32 RPP 0.0000 0.0400  -1.10 -0.10  2.5000 3.5000  $ Diode Cell
    33 RPP 0.0400 0.0500  -1.10 -0.10  2.5000 3.5000  $ Diode Bottom
C MSNDs COLUMN 4
    40 RPP 0.0000 0.0400  -2.20 -1.20  2.5010 2.5020  $ Fin, 10um thickness
    41 RPP 0.0000 0.0400  -2.20 -1.20  2.5000 2.5030  $ Unit Cell, 30um pitch
    42 RPP 0.0000 0.0400  -2.20 -1.20  2.5000 3.5000  $ Diode Cell
    43 RPP 0.0400 0.0500  -2.20 -1.20  2.5000 3.5000  $ Diode Bottom
C FR4 Detector Board
    100 RPP  0.15 0.28  -3.00 3.00 -4.00 4.00 $ Array Detector Board
    101 RPP -0.05 0.15  -2.60 2.60 -3.60 3.60 $ Ceramic Detector Board
C
    900 RCC -101 0 0  150 0 0  10 $ Universe, Cylinder 150-cm long, 10-cm radius.

C ===============================================================================
C --------------------DATA CARDS-------------------
C ===============================================================================
```

```
C
C ===========================================================================
C PHYSICS/CUT OFF
C ===========================================================================
MODE N T A
IMP:N 1 62R 0
IMP:T 1 60R 0 0 0
IMP:A 1 60R 0 0 0
PHYS:N 6J 3      $ NCIA, 3=ions are from neutron capture
CUT:N  2J 0
CUT:T  J 0.01 0 $ 10keV Energy Cut-off
CUT:A  J 0.01 0 $ 10keV Energy Cut-off
nps 1E6
C ===========================================================================
C MATERIALS
C ===========================================================================
M1 $ 6-LITHIUM FLUORIDE APPROXIMATION, RHO = 2.540
      3006.70c  -0.225502
      3007.70c  -0.016789
      9019.70c  -0.757709
C
M2 $ AIR, DRY, RHO = 0.001205
      6000.70c   -0.000124
      7014.70c   -0.755268
      8016.70c   -0.231781
      18040.70c  -0.012827
C
M3 $ NATURAL SILICON, RHO = 2.3290
     14028.70c  9.2223E-01
     14029.70c  4.685E-02
     14030.70c  3.092E-02
C
M4 $ FR4 Electronics board material, rho = 1.85
      1001   -0.010   $ Epoxy
      5010   -0.0053  $ Fiberglass
      5011   -0.0147  $ Fiberglass
      6000   -0.040   $ Epoxy
      8016   -0.390   $ Fiberglass/Epoxy
      13027  -0.010   $ Fiberglass
      14028  -0.230   $ Fiberglass
      29063  -0.140   $ Copper
      29065  -0.060   $ Copper
      35079  -0.050   $ Epoxy
      35081  -0.050   $ Epoxy
C
M5 $ Ceramic Detector Board Material, rho = 3.95
       8016  -0.471   $ Oxygen
      13027  -0.529   $ Aluminum
C
C ===========================================================================
C SOURCE - COLL. 20 CM DISK 0.0254eV ALONG THE X-AXIS.
C ===========================================================================
SDEF  POS= -100 0 0 PAR= N ERG= 0.0254E-6 VEC= 1 0 0  DIR= 1
      RAD= D1 AXS= 1 0 0 EXT= 0
SI1  0 10
SP1  -21 1
C Spectral Tally
C --- SPECTRUM --------------
F6:A     (110 114 120 124 130 134 140 144)
SD6      1
F16:T    (110 114 120 124 130 134 140 144)
SD16     1
F8:A,T   (110 114 120 124 130 134 140 144)
FT8  phl 2 6 1 16 1 0
E8   0   100i  5
C --- EFFICIENCY ------------
F18:A,T   (110 114 120 124 130 134 140 144)
FT18  phl 2 6 1 16 1 0
E18   0   0.3  5
```

Advanced Modular Neutron Detector (MND) MCNP6 Input File

Below is a complete, standard MCNP6 input file for the Advanced Modular Neutron Detector (AMND), expected to be developed in late 2017. The AMND will be populated with twenty-four double-sided MSNDs, arranged in a 4x6 array. The devices were mounted to ceramic disposable boards (CDBs) that measured 2-mm thick. The CDBs were then mounted directly to a 32-mil thick FR4 electronics board. No electronics components were modeled on the back-side of the MND. This particular card irradiates the MND with a large-diameter beam of collimated thermal neutrons.

```
Advanced MND Device, Double-Sided MSNDs
C ===============================================================================
C --------------------CELL CARDS-------------------
C ===============================================================================
C ******************* DSMSNDS ************************************************
C First Row, DSMSND 1-1
    110  3 -2.329 -10              u=1 $ Sidewall
    111  1 -2.550  10              u=1 $ Trench, LiF
    112  0        -11 lat=1 fill=1 u=2 $ Unit Cell
    113  0        -12       fill=2     $ Diode
    114  3 -2.329 -13 12 14            $ Diode bottom
    115  3 -2.329 -16              u=3 $ Backside Sidewall
    116  1 -2.550  16              u=3 $ Backside Trench, 6-LiF
    117  0        -15 lat=1 fill=3 u=4 $ Backside Unit Cell
    118  0        -14       fill=4     $ Backside Diode
C First Row, DSMSND 1-2
    120  3 -2.329 -20              u=5 $ Sidewall
    121  1 -2.550  20              u=5 $ Trench, LiF
    122  0        -21 lat=1 fill=5 u=6 $ Unit Cell
    123  0        -22       fill=6     $ Diode
    124  3 -2.329 -23 22 24                $ Diode bottom
    125  3 -2.329 -26              u=7 $ Backside Sidewall
    126  1 -2.550  26              u=7 $ Backside Trench, 6-LiF
    127  0        -25 lat=1 fill=7 u=8 $ Backside Unit Cell
    128  0        -24       fill=8     $ Backside Diode
C First Row, DSMSND 1-3
    130  3 -2.329 -30              u=9 $ Sidewall
    131  1 -2.550  30              u=9 $ Trench, LiF
    132  0        -31 lat=1 fill=9 u=10 $ Unit Cell
    133  0        -32       fill=10     $ Diode
    134  3 -2.329 -33 32 34                $ Diode bottom
    135  3 -2.329 -36               u=11 $ Backside Sidewall
    136  1 -2.550  36               u=11 $ Backside Trench, 6-LiF
    137  0        -35 lat=1 fill=11 u=12 $ Backside Unit Cell
    138  0        -34       fill=12      $ Backside Diode
C First Row, DSMSND 1-4
    140  3 -2.329 -40               u=13 $ Sidewall
    141  1 -2.550  40               u=13 $ Trench, LiF
    142  0        -41 lat=1 fill=13 u=14 $ Unit Cell
    143  0        -42       fill=14      $ Diode
    144  3 -2.329 -43 42 44              $ Diode bottom
    145  3 -2.329 -46               u=15 $ Backside Sidewall
    146  1 -2.550  46               u=15 $ Backside Trench, 6-LiF
    147  0        -45 lat=1 fill=15 u=16 $ Backside Unit Cell
    148  0        -44       fill=16      $ Backside Diode
C Second Row, DSMSND 2-1, 2-2, 2-3, 2-4
    213 LIKE 113 BUT TRCL=(0 0 -1.2) $ DSMSND 2-1
    214 LIKE 114 BUT TRCL=(0 0 -1.2) $ DSMSND 2-1
    218 LIKE 118 BUT TRCL=(0 0 -1.2) $ DSMSND 2-1
```

```
    223 LIKE 123 BUT TRCL=(0 0 -1.2) $ DSMSND 2-2
    224 LIKE 124 BUT TRCL=(0 0 -1.2) $ DSMSND 2-2
    228 LIKE 128 BUT TRCL=(0 0 -1.2) $ DSMSND 2-2
    233 LIKE 133 BUT TRCL=(0 0 -1.2) $ DSMSND 2-3
    234 LIKE 134 BUT TRCL=(0 0 -1.2) $ DSMSND 2-3
    238 LIKE 138 BUT TRCL=(0 0 -1.2) $ DSMSND 2-3
    243 LIKE 143 BUT TRCL=(0 0 -1.2) $ DSMSND 2-4
    244 LIKE 144 BUT TRCL=(0 0 -1.2) $ DSMSND 2-4
    248 LIKE 148 BUT TRCL=(0 0 -1.2) $ DSMSND 2-4
C Third Row, DSMSND 3-1, 3-2, 3-3, 3-4
    313 LIKE 113 BUT TRCL=(0 0 -2.4) $ DSMSND 3-1
    314 LIKE 114 BUT TRCL=(0 0 -2.4) $ DSMSND 3-1
    318 LIKE 118 BUT TRCL=(0 0 -2.4) $ DSMSND 3-1
    323 LIKE 123 BUT TRCL=(0 0 -2.4) $ DSMSND 3-2
    324 LIKE 124 BUT TRCL=(0 0 -2.4) $ DSMSND 3-2
    328 LIKE 128 BUT TRCL=(0 0 -2.4) $ DSMSND 3-2
    333 LIKE 133 BUT TRCL=(0 0 -2.4) $ DSMSND 3-3
    334 LIKE 134 BUT TRCL=(0 0 -2.4) $ DSMSND 3-3
    338 LIKE 138 BUT TRCL=(0 0 -2.4) $ DSMSND 3-3
    343 LIKE 143 BUT TRCL=(0 0 -2.4) $ DSMSND 3-4
    344 LIKE 144 BUT TRCL=(0 0 -2.4) $ DSMSND 3-4
    348 LIKE 148 BUT TRCL=(0 0 -2.4) $ DSMSND 3-4
C Fourth Row, DSMSND 4-1, 4-2, 4-3, 4-4
    413 LIKE 113 BUT TRCL=(0 0 -3.6) $ DSMSND 4-1
    414 LIKE 114 BUT TRCL=(0 0 -3.6) $ DSMSND 4-1
    418 LIKE 118 BUT TRCL=(0 0 -3.6) $ DSMSND 4-1
    423 LIKE 123 BUT TRCL=(0 0 -3.6) $ DSMSND 4-2
    424 LIKE 124 BUT TRCL=(0 0 -3.6) $ DSMSND 4-2
    428 LIKE 128 BUT TRCL=(0 0 -3.6) $ DSMSND 4-2
    433 LIKE 133 BUT TRCL=(0 0 -3.6) $ DSMSND 4-3
    434 LIKE 134 BUT TRCL=(0 0 -3.6) $ DSMSND 4-3
    438 LIKE 138 BUT TRCL=(0 0 -3.6) $ DSMSND 4-3
    443 LIKE 143 BUT TRCL=(0 0 -3.6) $ DSMSND 4-4
    444 LIKE 144 BUT TRCL=(0 0 -3.6) $ DSMSND 4-4
    448 LIKE 148 BUT TRCL=(0 0 -3.6) $ DSMSND 4-4
C Fifth Row, DSMSND 5-1, 5-2, 5-3, 5-4
    513 LIKE 113 BUT TRCL=(0 0 -4.8) $ DSMSND 5-1
    514 LIKE 114 BUT TRCL=(0 0 -4.8) $ DSMSND 5-1
    518 LIKE 118 BUT TRCL=(0 0 -4.8) $ DSMSND 5-1
    523 LIKE 123 BUT TRCL=(0 0 -4.8) $ DSMSND 5-2
    524 LIKE 124 BUT TRCL=(0 0 -4.8) $ DSMSND 5-2
    528 LIKE 128 BUT TRCL=(0 0 -4.8) $ DSMSND 5-2
    533 LIKE 133 BUT TRCL=(0 0 -4.8) $ DSMSND 5-3
    534 LIKE 134 BUT TRCL=(0 0 -4.8) $ DSMSND 5-3
    538 LIKE 138 BUT TRCL=(0 0 -4.8) $ DSMSND 5-3
    543 LIKE 143 BUT TRCL=(0 0 -4.8) $ DSMSND 5-4
    544 LIKE 144 BUT TRCL=(0 0 -4.8) $ DSMSND 5-4
    548 LIKE 148 BUT TRCL=(0 0 -4.8) $ DSMSND 5-4
C Sixth Row, DSMSND 6-1, 6-2, 6-3, 6-4
    613 LIKE 113 BUT TRCL=(0 0 -6.0) $ DSMSND 6-1
    614 LIKE 114 BUT TRCL=(0 0 -6.0) $ DSMSND 6-1
    618 LIKE 118 BUT TRCL=(0 0 -6.0) $ DSMSND 6-1
    623 LIKE 123 BUT TRCL=(0 0 -6.0) $ DSMSND 6-2
    624 LIKE 124 BUT TRCL=(0 0 -6.0) $ DSMSND 6-2
    628 LIKE 128 BUT TRCL=(0 0 -6.0) $ DSMSND 6-2
    633 LIKE 133 BUT TRCL=(0 0 -6.0) $ DSMSND 6-3
    634 LIKE 134 BUT TRCL=(0 0 -6.0) $ DSMSND 6-3
    638 LIKE 138 BUT TRCL=(0 0 -6.0) $ DSMSND 6-3
    643 LIKE 143 BUT TRCL=(0 0 -6.0) $ DSMSND 6-4
    644 LIKE 144 BUT TRCL=(0 0 -6.0) $ DSMSND 6-4
    648 LIKE 148 BUT TRCL=(0 0 -6.0) $ DSMSND 6-4
C ******************** MSNDS ************************************************
C ******************** ELECTRONICS ******************************************
    100 4 -1.85 -100   $ FR4 DETECTOR BOARD
    101 5 -3.95 #113 #114 #118 #123 #124 #128 #133 #134 #138 #143 #144 #148 &
          #213 #214 #218 #223 #224 #228 #233 #234 #238 #243 #244 #248 &
          #313 #314 #318 #323 #324 #328 #333 #334 #338 #343 #344 #348 &
          #413 #414 #418 #423 #424 #428 #433 #434 #438 #443 #444 #448 &
          #513 #514 #518 #523 #524 #528 #533 #534 #538 #543 #544 #548 &
          #613 #614 #618 #623 #624 #628 #633 #634 #638 #643 #644 #648 &
          -101 $ VOID IN WORLD
```

```
C World
    900 0 100 101 -900  $ VOID IN WORLD
    901 0 900           $ OUTSIDE WORLD

C ===============================================================================
C --------------------SURFACE CARDS----------------
C ===============================================================================
C MSNDs COLUMN 1
    10 RPP 0.0000 0.0400  0.10 1.10  2.5010 2.5020  $ Fin, 10um thickness
    11 RPP 0.0000 0.0400  0.10 1.10  2.5000 2.5030  $ Unit Cell, 30um pitch
    12 RPP 0.0000 0.0400  0.10 1.10  2.5000 3.5000  $ Diode Cell
    13 RPP 0.0400 0.0600  0.10 1.10  2.5000 3.5000  $ Diode Bottom
    14 RPP 0.0600 0.1000  0.10 1.10  2.5000 3.5000  $ Backside Diode
    15 RPP 0.0600 0.1000  0.10 1.10  2.5015 2.5045  $ Backside Unit Cell
    16 RPP 0.0600 0.1000  0.10 1.10  2.5025 2.5035  $ Backside Fin
C MSNDs COLUMN 2
    20 RPP 0.0000 0.0400  1.20 2.20  2.5010 2.5020  $ Fin, 10um thickness
    21 RPP 0.0000 0.0400  1.20 2.20  2.5000 2.5030  $ Unit Cell, 30um pitch
    22 RPP 0.0000 0.0400  1.20 2.20  2.5000 3.5000  $ Diode Cell
    23 RPP 0.0400 0.0600  1.20 2.20  2.5000 3.5000  $ Diode Bottom
    24 RPP 0.0600 0.1000  1.20 2.20  2.5000 3.5000  $ Backside Diode
    25 RPP 0.0600 0.1000  1.20 2.20  2.5015 2.5045  $ Backside Unit Cell
    26 RPP 0.0600 0.1000  1.20 2.20  2.5025 2.5035  $ Backside Fin
C MSNDs COLUMN 3
    30 RPP 0.0000 0.0400  -1.10 -0.10  2.5010 2.5020  $ Fin, 10um thickness
    31 RPP 0.0000 0.0400  -1.10 -0.10  2.5000 2.5030  $ Unit Cell, 30um pitch
    32 RPP 0.0000 0.0400  -1.10 -0.10  2.5000 3.5000  $ Diode Cell
    33 RPP 0.0400 0.0600  -1.10 -0.10  2.5000 3.5000  $ Diode Bottom
    34 RPP 0.0600 0.1000  -1.10 -0.10  2.5000 3.5000  $ Backside Diode
    35 RPP 0.0600 0.1000  -1.10 -0.10  2.5015 2.5045  $ Backside Unit Cell
    36 RPP 0.0600 0.1000  -1.10 -0.10  2.5025 2.5035  $ Backside Fin
C MSNDs COLUMN 4
    40 RPP 0.0000 0.0400  -2.20 -1.20  2.5010 2.5020  $ Fin, 10um thickness
    41 RPP 0.0000 0.0400  -2.20 -1.20  2.5000 2.5030  $ Unit Cell, 30um pitch
    42 RPP 0.0000 0.0400  -2.20 -1.20  2.5000 3.5000  $ Diode Cell
    43 RPP 0.0400 0.0600  -2.20 -1.20  2.5000 3.5000  $ Diode Bottom
    44 RPP 0.0600 0.1000  -2.20 -1.20  2.5000 3.5000  $ Backside Diode
    45 RPP 0.0600 0.1000  -2.20 -1.20  2.5015 2.5045  $ Backside Unit Cell
    46 RPP 0.0600 0.1000  -2.20 -1.20  2.5025 2.5035  $ Backside Fin
C FR4 Detector Board
    100 RPP  0.15 0.28  -3.00 3.00 -4.00 4.00 $ Array Detector Board
    101 RPP -0.05 0.15  -2.60 2.60 -3.60 3.60 $ Ceramic Detector Board
C
    900 RCC -101 0 0  150 0 0  10 $ Universe, Cylinder 150-cm long, 10-cm radius.

C ===============================================================================
C --------------------DATA CARDS-------------------
C ===============================================================================
C
C ===============================================================================
C PHYSICS/CUT OFF
C ===============================================================================
MODE N T A
IMP:N 1 98R 0
IMP:T 1 96R 0 0 0
IMP:A 1 96R 0 0 0
PHYS:N 6J 3      $ NCIA, 3=ions are from neutron capture
CUT:N  2J 0
CUT:T  J 0.01 0 $ 10keV Energy Cut-off
CUT:A  J 0.01 0 $ 10keV Energy Cut-off
nps 1E6
C ===============================================================================
C MATERIALS
C ===============================================================================
M1 $ 6-LITHIUM FLUORIDE APPROXIMATION, RHO = 2.540
      3006.70c  -0.225502
      3007.70c  -0.016789
      9019.70c  -0.757709
C
M2 $ AIR, DRY, RHO = 0.001205
      6000.70c   -0.000124
```

```
      7014.70c   -0.755268
      8016.70c   -0.231781
      18040.70c  -0.012827
C
M3 $ NATURAL SILICON, RHO = 2.3290
     14028.70c  9.2223E-01
     14029.70c  4.685E-02
     14030.70c  3.092E-02
C
M4 $ FR4 Electronics board material, rho = 1.85
      1001   -0.010   $ Epoxy
      5010   -0.0053  $ Fiberglass
      5011   -0.0147  $ Fiberglass
      6000   -0.040   $ Epoxy
      8016   -0.390   $ Fiberglass/Epoxy
      13027  -0.010   $ Fiberglass
      14028  -0.230   $ Fiberglass
      29063  -0.140   $ Copper
      29065  -0.060   $ Copper
      35079  -0.050   $ Epoxy
      35081  -0.050   $ Epoxy
C
M5 $ Ceramic Detector Board Material, rho = 3.95
       8016  -0.471   $ Oxygen
      13027  -0.529   $ Aluminum
C
C ===========================================================================
C SOURCE - COLL. 20 CM DISK 0.0254eV ALONG THE X-AXIS.
C ===========================================================================
SDEF  POS= -100 0 0 PAR= N ERG= 0.0254E-6 VEC= 1 0 0  DIR= 1
      RAD= D1 AXS= 1 0 0 EXT= 0
SI1  0 10
SP1  -21 1
C Spectral Tally
C --- SPECTRUM --------------
F6:A     (110 115 120 125 130 135 140 145)
SD6      1
F16:T    (110 115 120 125 130 135 140 145)
SD16     1
F8:A,T   (110 115 120 125 130 135 140 145)
FT8  phl 2 6 1 16 1 0
E8   0   100i  5
C --- EFFICIENCY ------------
F18:A,T   (110 118 120 128 130 138 140 148)
FT18  phl 2 6 1 16 1 0
E18   0   0.3  5
```

Appendix C - *DS-MSND Efficiency Values*

This section contains tables regarding the calculated intrinsic thermal neutron detection efficiency for DS-MSNDs of various designs. The section is organized into two DS-MSND variants, Off-Set type and Opaque Type, each with two groups; ^{6}LiF conversion-material-based detectors and ^{10}B conversion-material-based detectors. Within each group, the tables are further organized by the geometry of the microstructures; straight trenches, circular holes, and circular pillars for the Off-Set type, and straight trenches, front-side circular holes with back-side circular pillars, and front-side circular pillars with back-side circular holes as described in Chapter 4.3. The tables contain detection efficiency calculations for DS-MSNDs with varying unit-cell dimensions (*W_Cell*), trench depths (*H*), and trench width-to-unit cell ratio. These calculations were performed using MCNP6 and Python scripting languages. Example input cards and Python scripts can be found in Appendix B.

Off-Set Type, Straight Trench Pattern

Table D.1. Efficiencies for off-set straight trenches with ^{10}B and ^{6}LiF neutron converting material. Neutrons are incident normally on the detector surface and the LLD is 300 keV.

Off-Set Dual-Sided MSND, Straight Trench, 10-B					
T/W_Cell	*Cell width W_Cell (um)*				
	4	**6**	**8**	**10**	**12**
	Trench depth H = 10 um				
0.10	7.3%	7.2%	7.0%	6.8%	6.6%
0.20	13.9%	13.2%	12.5%	11.8%	11.3%
0.30	19.9%	18.2%	16.8%	15.4%	14.1%
0.40	25.1%	22.4%	19.9%	17.5%	15.0%
0.50	29.6%	25.6%	21.8%	18.2%	15.8%
0.60	31.1%	25.7%	20.3%	16.9%	14.7%
0.70	32.4%	25.6%	19.8%	16.6%	14.5%
0.80	24.2%	24.4%	19.8%	16.8%	14.8%
0.90	10.6%	12.1%	13.5%	14.4%	14.9%
	Trench depth H = 20 um				
0.10	11.9%	11.6%	11.3%	11.0%	10.7%
0.20	22.5%	21.4%	20.2%	19.1%	18.1%
0.30	32.1%	29.5%	27.0%	24.6%	22.2%
0.40	40.5%	36.0%	31.8%	27.4%	23.2%
0.50	47.8%	40.9%	34.3%	27.8%	23.7%
0.60	47.3%	38.2%	29.0%	23.3%	19.6%
0.70	47.4%	36.1%	26.6%	21.3%	18.0%
0.80	32.5%	32.7%	25.2%	20.6%	17.7%
0.90	10.5%	12.9%	15.2%	16.6%	17.3%
	Trench depth H = 40 um				
0.10	16.3%	15.9%	15.5%	15.1%	14.7%
0.20	31.0%	29.4%	27.8%	26.3%	24.8%
0.30	44.1%	40.6%	37.1%	33.7%	30.3%
0.40	55.7%	49.5%	43.4%	37.3%	31.2%
0.50	65.7%	56.1%	46.6%	37.4%	31.6%
0.60	61.5%	48.7%	36.0%	28.0%	23.0%
0.70	58.7%	43.6%	30.9%	23.9%	19.6%
0.80	37.2%	37.5%	27.9%	21.9%	18.5%
0.90	9.4%	12.4%	15.2%	16.9%	17.7%
	Trench depth H = 60 um				
0.10	18.0%	17.6%	17.1%	16.7%	16.3%
0.20	34.2%	32.5%	30.7%	29.0%	27.3%
0.30	48.7%	44.8%	40.9%	37.1%	33.3%
0.40	61.4%	54.6%	47.7%	41.0%	34.2%
0.50	72.4%	61.8%	51.2%	40.9%	34.5%
0.60	66.3%	52.3%	38.2%	29.5%	23.9%
0.70	62.1%	45.7%	32.0%	24.3%	19.7%
0.80	38.1%	38.4%	28.1%	21.8%	18.3%
0.90	8.7%	11.9%	14.8%	16.5%	17.3%

Off-Set Dual-Sided MSND, Straight Trench, 6-LiF					
T/W_Cell	*Cell width W_Cell (um)*				
	20	**40**	**60**	**80**	**100**
	Trench depth H = 90 um				
0.10	7.5%	7.3%	7.0%	6.8%	6.6%
0.20	14.5%	13.6%	12.7%	11.9%	11.0%
0.30	21.1%	19.1%	17.2%	15.3%	13.6%
0.40	27.2%	23.7%	20.4%	17.2%	14.4%
0.50	32.8%	27.6%	22.5%	18.0%	15.1%
0.60	35.4%	28.3%	21.4%	16.8%	14.1%
0.70	37.9%	29.0%	20.9%	16.5%	13.9%
0.80	36.2%	29.1%	20.6%	16.5%	14.1%
0.90	22.1%	22.2%	20.4%	16.8%	14.5%
	Trench depth H = 175 um				
0.10	12.0%	11.6%	11.2%	10.9%	10.4%
0.20	23.1%	21.7%	20.2%	18.8%	17.5%
0.30	33.6%	30.3%	27.2%	24.1%	21.0%
0.40	43.2%	37.6%	32.1%	26.6%	21.8%
0.50	52.2%	43.5%	34.9%	27.3%	22.4%
0.60	53.7%	42.1%	30.8%	23.3%	18.8%
0.70	55.5%	41.3%	28.4%	21.3%	17.2%
0.80	50.9%	40.0%	26.9%	20.3%	16.8%
0.90	28.2%	28.7%	25.7%	20.2%	16.9%
	Trench depth H = 350 um				
0.10	16.7%	16.2%	15.7%	15.1%	14.5%
0.20	32.2%	30.1%	28.1%	26.1%	24.1%
0.30	46.6%	42.0%	37.6%	33.1%	28.8%
0.40	59.9%	52.0%	44.1%	36.4%	29.5%
0.50	72.3%	59.9%	47.8%	36.9%	30.0%
0.60	70.8%	54.8%	39.1%	28.7%	22.4%
0.70	70.2%	51.3%	34.1%	24.4%	18.9%
0.80	61.3%	47.5%	30.5%	22.1%	17.8%
0.90	31.4%	32.3%	28.0%	21.5%	17.5%
	Trench depth H = 500 um				
0.10	18.4%	17.8%	17.3%	16.7%	16.0%
0.20	35.3%	33.1%	30.9%	28.7%	26.4%
0.30	51.2%	46.1%	41.2%	36.3%	31.5%
0.40	65.8%	57.0%	48.3%	39.7%	32.2%
0.50	79.2%	65.5%	52.1%	40.1%	32.6%
0.60	76.0%	58.4%	41.3%	29.9%	23.2%
0.70	74.0%	53.5%	35.1%	24.6%	18.8%
0.80	63.3%	48.8%	30.7%	21.7%	17.2%
0.90	31.4%	32.4%	27.6%	20.9%	16.8%

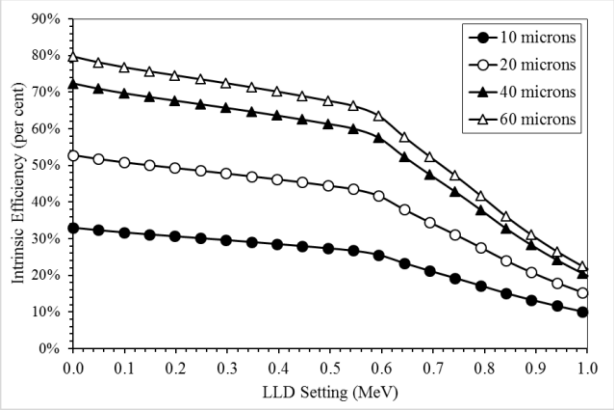

Fig. D.1. Plotted are intrinsic efficiencies for various perforation depths for straight-trench devices; 4 μm unit cell and 2 μm wide trenches backfilled with ^{10}B.

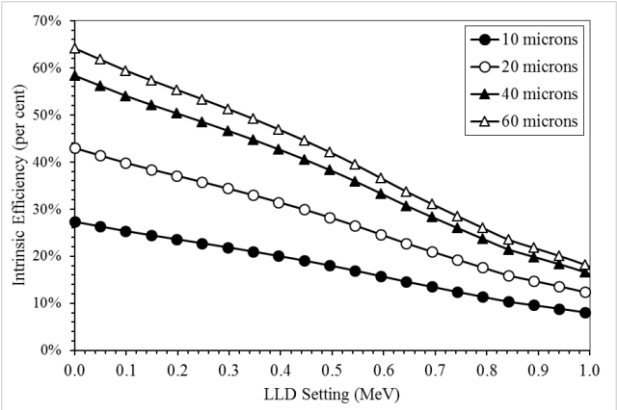

Fig. D.2. Plotted are intrinsic efficiencies for various perforation depths for straight-trench devices; 8 μm unit cell and 4 μm wide trenches backfilled with ^{10}B.

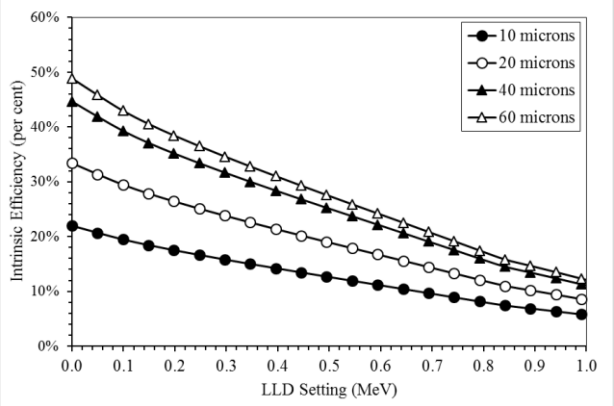

Fig. D.3. Plotted are intrinsic efficiencies for various perforation depths for straight-trench devices; 12 μm unit cell, 6 μm wide trenches backfilled with ^{10}B.

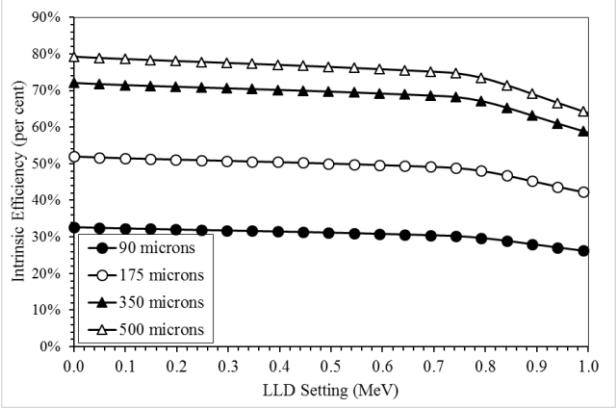

Fig. D.4. Plotted are intrinsic efficiencies for various perforation depths for straight-trench devices; 20 μm unit cell, 10 μm wide trenches backfilled with ^{6}LiF.

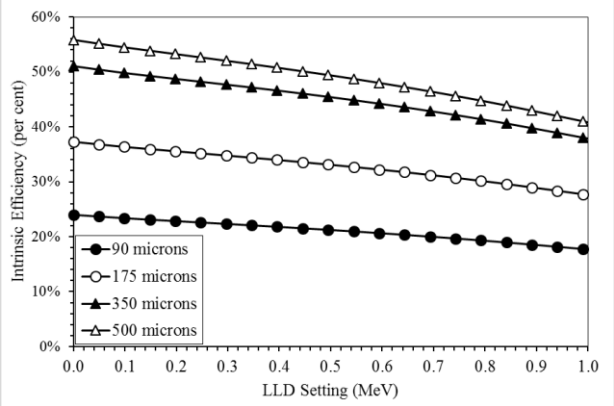

Fig. D.5. Plotted are intrinsic efficiencies for various perforation depths for straight-trench devices; 60 μm unit cell, 30 μm wide trenches backfilled with ^{6}LiF.

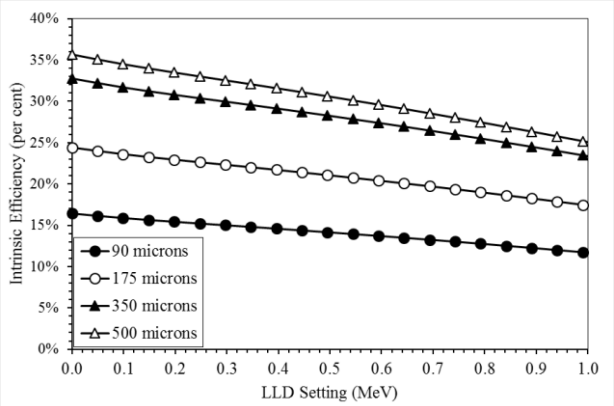

Fig. D.6. Plotted are intrinsic efficiencies for various perforation depths for straight-trench devices; 100 μm unit cell, 50 μm wide trenches backfilled with ^{6}LiF.

Off-Set Type, Circular Hole Pattern

Table D.2. Efficiencies for off-set circular holes with ^{10}B and ^{6}LiF neutron converting material. Neutrons are incident normally on the detector surface and the LLD is 300 keV.

Off-Set Dual-Sided MSND, Circular Hole, 10-B					
D/W_Cell	***Cell width W_Cell (um)***				
	4	**6**	**8**	**10**	**12**
	Trench depth H = 10 um				
0.10	0.6%	0.6%	0.6%	0.6%	0.6%
0.20	2.4%	2.4%	2.4%	2.3%	2.3%
0.30	5.4%	5.3%	5.1%	5.0%	4.8%
0.40	9.4%	9.1%	8.8%	8.3%	7.8%
0.50	14.5%	13.9%	13.1%	11.7%	10.3%
0.60	20.5%	19.3%	17.5%	14.8%	12.8%
0.70	27.4%	25.3%	21.1%	17.9%	15.6%
0.80	31.3%	29.6%	23.7%	20.0%	17.4%
0.90	30.2%	25.4%	22.9%	20.7%	18.6%
	Trench depth H = 20 um				
0.10	1.0%	1.0%	1.0%	1.0%	1.0%
0.20	3.9%	3.9%	3.8%	3.8%	3.7%
0.30	8.7%	8.6%	8.4%	8.1%	7.9%
0.40	15.3%	14.9%	14.4%	13.6%	12.6%
0.50	23.6%	22.7%	21.4%	18.9%	16.4%
0.60	33.5%	31.6%	28.3%	23.6%	20.3%
0.70	44.7%	41.1%	33.9%	28.3%	24.3%
0.80	49.6%	46.5%	36.4%	30.0%	25.5%
0.90	44.8%	36.7%	32.4%	28.8%	25.4%
	Trench depth H = 40 um				
0.10	1.4%	1.4%	1.4%	1.4%	1.3%
0.20	5.4%	5.4%	5.3%	5.2%	5.2%
0.30	12.0%	11.9%	11.6%	11.3%	11.0%
0.40	21.1%	20.6%	19.9%	18.8%	17.4%
0.50	32.6%	31.3%	29.5%	26.1%	22.5%
0.60	46.3%	43.6%	38.9%	32.3%	27.6%
0.70	61.9%	56.7%	46.5%	38.6%	32.9%
0.80	66.7%	62.2%	47.9%	38.9%	32.7%
0.90	56.5%	45.4%	39.5%	34.7%	30.1%
	Trench depth H = 60 um				
0.10	1.5%	1.5%	1.5%	1.5%	1.5%
0.20	6.0%	5.9%	5.9%	5.8%	5.7%
0.30	13.3%	13.1%	12.9%	12.5%	12.1%
0.40	23.4%	22.8%	22.0%	20.8%	19.2%
0.50	36.0%	34.6%	32.6%	28.8%	24.8%
0.60	51.1%	48.1%	42.9%	35.6%	30.4%
0.70	68.3%	62.6%	51.2%	42.4%	36.1%
0.80	72.9%	67.8%	52.0%	42.1%	35.2%
0.90	60.2%	48.1%	41.6%	36.4%	31.4%

Off-Set Dual-Sided MSND, Circular Hole, 6-LiF					
D/W_Cell	***Cell width W_Cell (um)***				
	20	**40**	**60**	**80**	**100**
	Trench depth H = 90 um				
0.10	0.6%	0.6%	0.6%	0.6%	0.6%
0.20	2.4%	2.4%	2.4%	2.3%	2.3%
0.30	5.5%	5.3%	5.2%	5.0%	4.8%
0.40	9.6%	9.4%	8.9%	8.4%	7.4%
0.50	14.9%	14.3%	13.4%	11.6%	9.9%
0.60	21.2%	20.1%	17.9%	14.7%	12.4%
0.70	28.7%	26.6%	22.0%	17.8%	15.1%
0.80	35.4%	32.1%	24.9%	19.9%	16.8%
0.90	38.5%	33.6%	27.0%	21.5%	18.0%
	Trench depth H = 175 um				
0.10	1.0%	1.0%	1.0%	0.9%	1.0%
0.20	3.9%	3.8%	3.8%	3.7%	3.7%
0.30	8.7%	8.5%	8.4%	8.1%	7.7%
0.40	15.4%	15.0%	14.3%	13.4%	11.8%
0.50	23.8%	22.9%	21.4%	18.4%	15.6%
0.60	34.0%	32.1%	28.4%	23.1%	19.3%
0.70	45.9%	42.5%	34.7%	27.7%	23.1%
0.80	55.4%	50.0%	37.8%	29.6%	24.3%
0.90	57.5%	49.9%	38.9%	30.0%	24.4%
	Trench depth H = 350 um				
0.10	1.4%	1.4%	1.4%	1.3%	1.3%
0.20	5.4%	5.4%	5.3%	5.3%	5.1%
0.30	12.1%	12.0%	11.7%	11.3%	10.8%
0.40	21.4%	20.9%	20.0%	18.7%	16.4%
0.50	33.1%	32.0%	29.7%	25.5%	21.5%
0.60	47.3%	44.7%	39.4%	31.8%	26.4%
0.70	63.8%	59.0%	47.9%	38.0%	31.4%
0.80	75.2%	67.5%	50.3%	38.8%	31.4%
0.90	74.2%	64.1%	49.0%	36.8%	29.3%
	Trench depth H = 500 um				
0.10	1.5%	1.5%	1.5%	1.5%	1.5%
0.20	6.0%	6.0%	5.9%	5.8%	5.7%
0.30	13.4%	13.2%	12.9%	12.5%	11.9%
0.40	23.6%	23.0%	22.0%	20.5%	18.0%
0.50	36.4%	35.1%	32.7%	28.0%	23.5%
0.60	51.9%	49.1%	43.2%	34.8%	28.9%
0.70	70.0%	64.7%	52.5%	41.5%	34.3%
0.80	81.7%	73.1%	54.3%	41.6%	33.5%
0.90	79.0%	68.0%	51.5%	38.4%	30.2%

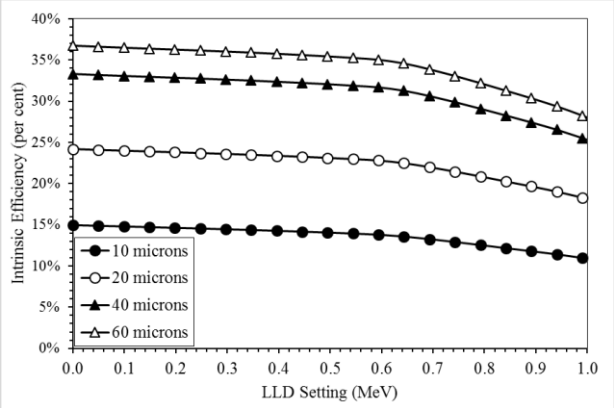

Fig. D.7. Plotted are intrinsic efficiencies for various perforation depths for circular-hole devices; 4 μm unit cell and 2 μm diameter holes backfilled with ^{10}B.

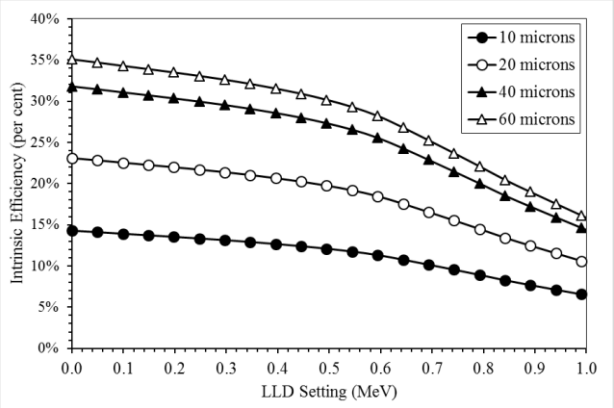

Fig. D.8. Plotted are intrinsic efficiencies for various perforation depths for circular-hole devices; 8 μm unit cell and 4 μm diameter holes backfilled with ^{10}B.

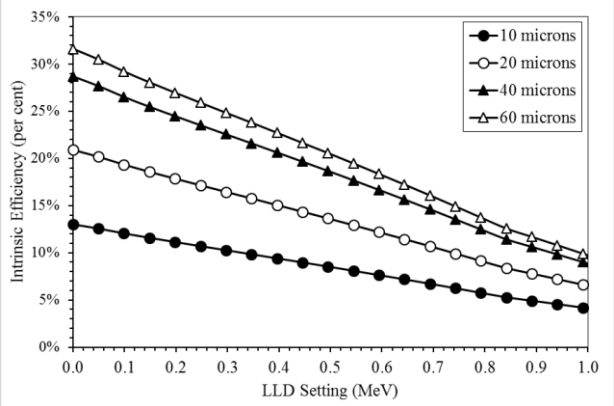

Fig. D.9. Plotted are intrinsic efficiencies for various perforation depths for circular-hole devices; 12 μm unit cell and 6 μm diameter holes backfilled with ^{10}B.

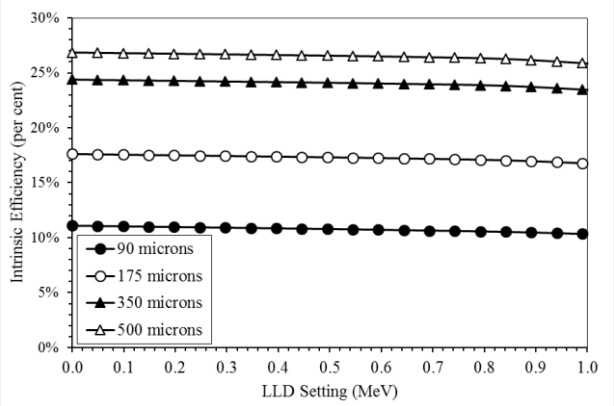

Fig. D.10. Plotted are intrinsic efficiencies for various perforation depths for circular-hole devices; 20 μm unit cell, 10 μm diameter holes backfilled with ^{6}LiF.

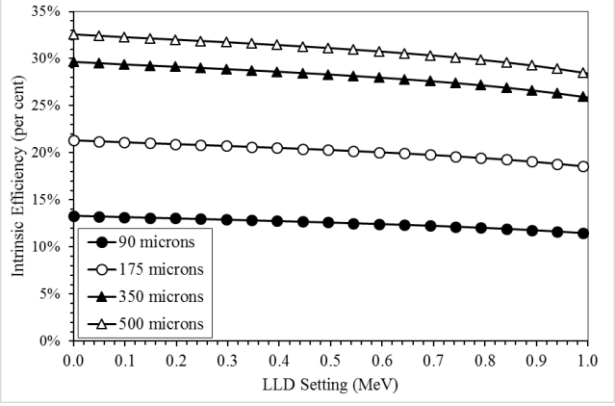

Fig. D.11. Plotted are intrinsic efficiencies for various perforation depths for circular-hole devices; 60 μm unit cell, 30 μm diameter holes backfilled with ^{6}LiF.

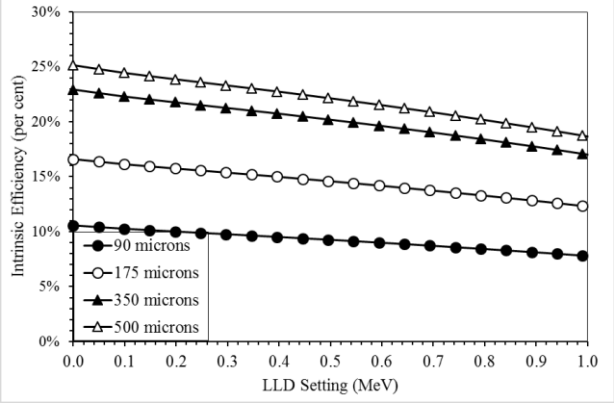

Fig. D.12. Plotted are intrinsic efficiencies for various perforation depths for circular-hole devices; 60 μm unit cell, 30 μm diameter holes backfilled with ^{6}LiF.

Off-Set Type, Circular Pillar Pattern

Table D.3. Efficiencies for off-set circular pillars with ^{10}B and ^{6}LiF neutron converting material. Neutrons are incident normally on the detector surface and the LLD is 300 keV.

Off-Set Dual-Sided MSND, Circular Pillar, 10-B						Off-Set Dual-Sided MSND, Circular Pillar, 6-LiF					
D/W_Cell	*Cell width W_Cell (um)*					*D/W_Cell*	*Cell width W_Cell (um)*				
	4	**6**	**8**	**10**	**12**		**20**	**40**	**60**	**80**	**100**
			Trench depth H = 10 um						***Trench depth H = 90 um***		
0.10	6.4%	6.5%	6.6%	6.8%	7.0%	**0.10**	6.7%	6.9%	7.2%	7.1%	6.9%
0.20	7.8%	9.2%	9.6%	9.2%	8.9%	**0.20**	10.8%	11.7%	10.0%	9.0%	8.3%
0.30	13.2%	13.5%	12.0%	11.0%	10.2%	**0.30**	19.3%	15.6%	12.4%	10.7%	9.6%
0.40	19.5%	16.7%	14.2%	12.6%	11.5%	**0.40**	26.7%	19.1%	14.8%	12.3%	10.9%
0.50	23.9%	19.6%	16.4%	14.2%	12.7%	**0.50**	31.6%	22.3%	17.2%	14.0%	12.1%
0.60	27.1%	22.0%	18.5%	16.1%	14.1%	**0.60**	34.6%	25.0%	19.4%	15.9%	13.5%
0.70	29.3%	24.4%	20.5%	18.0%	15.9%	**0.70**	35.4%	27.2%	21.5%	17.9%	15.3%
0.80	28.6%	24.9%	21.2%	18.8%	16.9%	**0.80**	32.4%	27.0%	22.1%	18.8%	16.4%
0.90	24.0%	22.1%	19.6%	17.3%	15.7%	**0.90**	25.9%	23.3%	20.3%	17.4%	15.3%
			Trench depth H = 20 um						***Trench depth H = 175 um***		
0.10	4.0%	4.1%	4.4%	4.6%	5.0%	**0.10**	5.1%	5.4%	5.9%	5.8%	5.4%
0.20	6.3%	8.4%	8.9%	8.4%	7.9%	**0.20**	11.3%	12.6%	10.1%	8.6%	7.6%
0.30	14.7%	15.0%	12.8%	11.2%	10.1%	**0.30**	24.0%	18.6%	13.8%	11.3%	9.8%
0.40	24.7%	20.3%	16.4%	14.0%	12.3%	**0.40**	35.4%	24.2%	17.6%	13.9%	11.8%
0.50	32.1%	25.3%	20.3%	16.8%	14.6%	**0.50**	43.7%	29.7%	21.7%	16.9%	14.0%
0.60	38.6%	30.3%	24.5%	20.5%	17.5%	**0.60**	49.8%	35.0%	26.0%	20.5%	16.7%
0.70	44.2%	36.1%	29.5%	25.1%	21.7%	**0.70**	53.4%	40.2%	30.8%	24.9%	20.7%
0.80	45.0%	38.8%	32.5%	28.3%	25.0%	**0.80**	50.5%	41.7%	33.5%	28.0%	24.0%
0.90	38.6%	35.4%	31.2%	27.1%	24.4%	**0.90**	41.0%	36.8%	31.7%	26.8%	23.4%
			Trench depth H = 40 um						***Trench depth H = 350 um***		
0.10	1.6%	1.8%	2.1%	2.4%	2.8%	**0.10**	3.2%	3.6%	4.2%	4.0%	3.6%
0.20	4.3%	6.9%	7.6%	6.9%	6.3%	**0.20**	10.7%	12.2%	9.2%	7.5%	6.3%
0.30	14.7%	14.9%	12.3%	10.4%	9.1%	**0.30**	26.2%	19.7%	13.7%	10.8%	8.9%
0.40	27.2%	21.6%	16.8%	13.8%	11.9%	**0.40**	40.8%	27.0%	18.6%	14.1%	11.5%
0.50	37.3%	28.5%	22.1%	17.7%	14.9%	**0.50**	52.2%	34.7%	24.2%	18.0%	14.4%
0.60	47.1%	36.0%	28.3%	23.0%	19.1%	**0.60**	62.0%	42.8%	30.8%	23.4%	18.5%
0.70	57.2%	46.1%	36.9%	30.8%	26.2%	**0.70**	69.9%	52.2%	39.0%	30.9%	25.1%
0.80	60.4%	51.9%	42.9%	37.0%	32.5%	**0.80**	68.4%	56.3%	44.7%	36.9%	31.3%
0.90	52.9%	48.4%	42.4%	36.7%	32.8%	**0.90**	56.6%	50.7%	43.5%	36.5%	31.7%
			Trench depth H = 60 um						***Trench depth H = 500 um***		
0.10	0.7%	0.9%	1.2%	1.5%	2.0%	**0.10**	2.1%	2.5%	3.1%	2.9%	2.5%
0.20	3.5%	6.2%	6.9%	6.2%	5.5%	**0.20**	9.8%	11.4%	8.3%	6.5%	5.3%
0.30	14.3%	14.4%	11.7%	9.8%	8.5%	**0.30**	26.0%	19.1%	12.9%	9.9%	8.0%
0.40	27.5%	21.6%	16.5%	13.4%	11.5%	**0.40**	41.3%	26.9%	18.0%	13.4%	10.8%
0.50	38.4%	29.1%	22.2%	17.6%	14.7%	**0.50**	53.8%	35.2%	24.1%	17.7%	13.9%
0.60	49.5%	37.5%	29.2%	23.5%	19.3%	**0.60**	65.1%	44.4%	31.5%	23.6%	18.4%
0.70	61.6%	49.4%	39.3%	32.6%	27.5%	**0.70**	74.9%	55.6%	41.2%	32.3%	26.1%
0.80	66.0%	56.7%	46.7%	40.1%	35.1%	**0.80**	74.3%	61.1%	48.4%	39.7%	33.6%
0.90	58.2%	53.2%	46.5%	40.2%	35.9%	**0.90**	61.9%	55.5%	47.5%	39.8%	34.5%

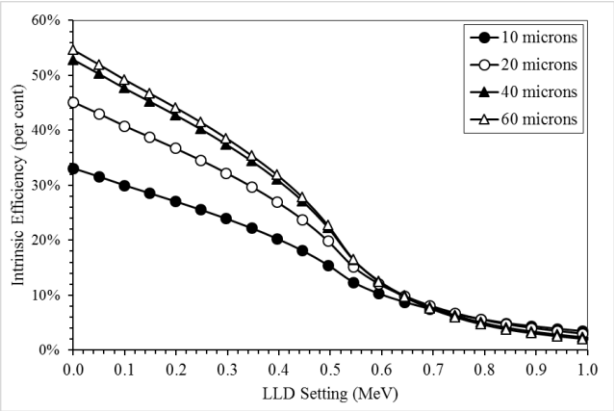

Fig. D.13. Plotted are intrinsic efficiencies for various perforation depths for circular-pillar devices; 4 μm unit cell, 2 μm diameter pillars surrounded with ^{10}B.

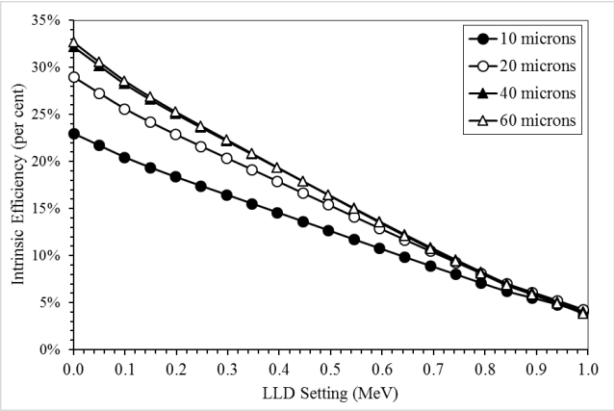

Fig. D.14. Plotted are intrinsic efficiencies for various perforation depths for circular-pillar devices; 8 μm unit cell, 4 μm diameter pillars surrounded with ^{10}B.

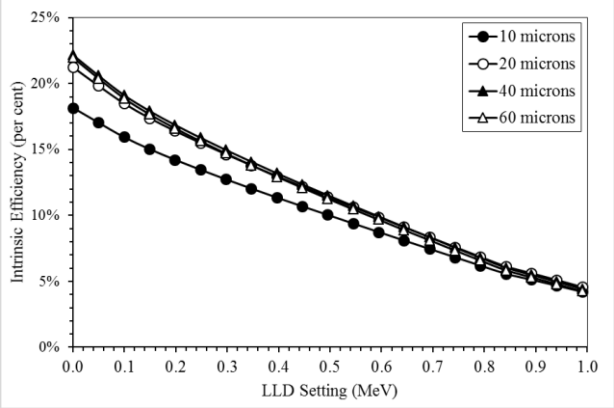

Fig. D.15. Plotted are intrinsic efficiencies for various perforation depths for circular-pillar devices; 12 μm unit cell, 6 μm diameter pillars surrounded with ^{10}B.

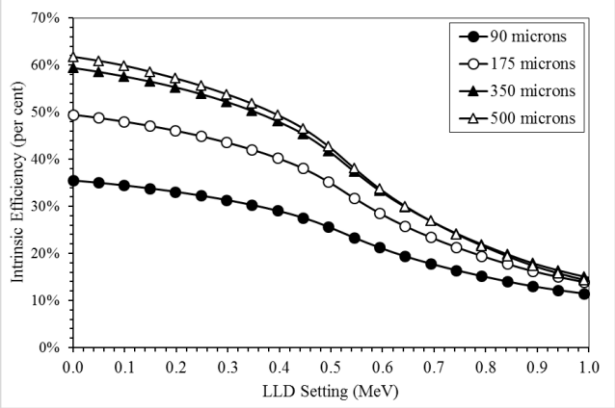

Fig. D.16. Plotted are intrinsic efficiencies for various perforation depths for circular-pillar devices; 20 μm unit cell, 10 μm diameter pillars surrounded with ^{6}LiF.

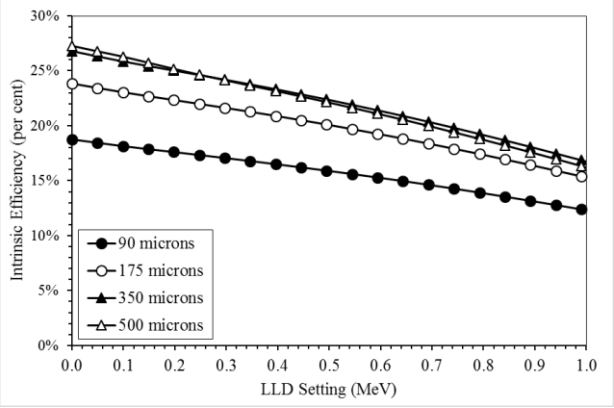

Fig. D.17. Plotted are intrinsic efficiencies for various perforation depths for circular-pillar devices; 60 μm unit cell, 30 μm diameter pillars surrounded with ^{6}LiF.

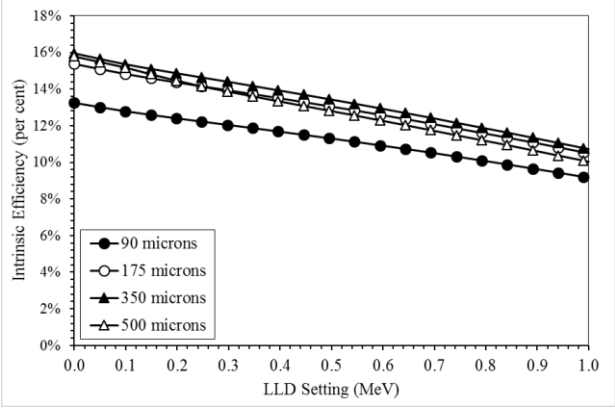

Fig. D.18. *Plotted are intrinsic efficiencies for various perforation depths for circular-pillar devices; 100 μm unit cell, 50 μm diameter pillars surrounded with ^{6}LiF.*

Opaque Type, Straight Trench Pattern

Table D.4. Efficiencies for opaque straight trenches with ^{10}B and ^{6}LiF neutron converting material. Neutrons are incident normally on the detector surface and the LLD is 300 keV.

Opaque Dual-Sided MSND, Straight Trench, 10-B						Opaque Dual-Sided MSND, Straight Trench, LiF					
T/W_Cell	*Cell width W_Cell (um)*					*T/W_Cell*	*Cell width W_Cell (um)*				
	4	**6**	**8**	**10**	**12**		**20**	**40**	**60**	**80**	**100**
	Trench depth H = 10 um						***Trench depth H = 90 um***				
0.10	11.0%	11.8%	12.6%	13.1%	13.3%	**0.10**	17.9%	17.7%	16.7%	14.3%	12.9%
0.20	22.1%	21.7%	18.7%	16.7%	15.2%	**0.20**	29.0%	24.4%	19.2%	16.4%	14.6%
0.30	28.7%	24.2%	20.3%	17.9%	16.0%	**0.30**	32.1%	26.3%	21.0%	17.6%	15.4%
0.40	29.5%	25.4%	21.4%	18.4%	15.9%	**0.40**	32.7%	27.3%	22.1%	18.1%	15.3%
0.50	29.6%	25.6%	21.8%	18.2%	15.8%	**0.50**	32.8%	27.6%	22.5%	18.0%	15.1%
0.60	29.2%	25.0%	21.1%	18.1%	15.6%	**0.60**	32.5%	27.1%	21.8%	17.8%	15.0%
0.70	28.1%	23.6%	19.7%	17.2%	15.4%	**0.70**	31.8%	25.7%	20.4%	17.1%	14.7%
0.80	21.0%	20.8%	17.8%	15.7%	14.2%	**0.80**	28.4%	23.7%	18.4%	15.6%	13.7%
0.90	9.5%	10.4%	11.3%	11.7%	12.0%	**0.90**	16.8%	16.7%	15.6%	13.3%	11.7%
	Trench depth H = 20 um						***Trench depth H = 175 um***				
0.10	15.3%	16.8%	18.2%	19.1%	19.4%	**0.10**	27.1%	26.9%	25.2%	21.2%	18.7%
0.20	34.7%	34.1%	28.9%	25.4%	22.8%	**0.20**	46.0%	38.1%	29.4%	24.6%	21.7%
0.30	46.2%	38.4%	31.7%	27.4%	24.2%	**0.30**	51.1%	41.3%	32.3%	26.7%	22.9%
0.40	47.5%	40.5%	33.5%	28.2%	24.0%	**0.40**	52.0%	43.0%	34.2%	27.5%	22.7%
0.50	47.8%	40.9%	34.3%	27.8%	23.7%	**0.50**	52.2%	43.5%	34.9%	27.3%	22.4%
0.60	47.0%	39.9%	32.9%	27.7%	23.5%	**0.60**	51.6%	42.5%	33.7%	27.0%	22.2%
0.70	45.1%	37.2%	30.5%	26.3%	23.1%	**0.70**	50.4%	40.3%	31.3%	25.8%	21.8%
0.80	32.8%	32.3%	27.2%	23.6%	21.0%	**0.80**	44.8%	36.7%	27.9%	23.2%	20.1%
0.90	12.6%	14.3%	15.8%	16.7%	17.1%	**0.90**	25.3%	25.1%	23.3%	19.3%	16.6%
	Trench depth H = 40 um						***Trench depth H = 350 um***				
0.10	19.4%	21.6%	23.7%	25.0%	25.5%	**0.10**	36.8%	36.5%	34.0%	28.3%	24.8%
0.20	47.2%	46.2%	38.9%	33.9%	30.3%	**0.20**	63.6%	52.3%	40.0%	33.2%	29.0%
0.30	63.4%	52.4%	42.9%	36.9%	32.3%	**0.30**	70.8%	56.8%	44.2%	36.2%	30.7%
0.40	65.3%	55.4%	45.5%	38.0%	32.0%	**0.40**	72.1%	59.3%	46.8%	37.2%	30.4%
0.50	65.7%	56.1%	46.6%	37.4%	31.6%	**0.50**	72.3%	59.9%	47.8%	36.9%	30.0%
0.60	64.5%	54.5%	44.6%	37.2%	31.2%	**0.60**	71.5%	58.6%	46.0%	36.5%	29.6%
0.70	61.8%	50.7%	41.2%	35.2%	30.6%	**0.70**	69.8%	55.4%	42.6%	34.7%	29.1%
0.80	44.4%	43.7%	36.4%	31.3%	27.7%	**0.80**	61.8%	50.2%	37.8%	31.1%	26.6%
0.90	15.5%	18.0%	20.3%	21.6%	22.1%	**0.90**	34.0%	33.7%	31.1%	25.6%	21.7%
	Trench depth H = 60 um						***Trench depth H = 500 um***				
0.10	21.0%	23.5%	25.8%	27.2%	27.7%	**0.10**	40.1%	39.8%	37.0%	30.7%	26.8%
0.20	51.9%	50.8%	42.7%	37.1%	33.1%	**0.20**	69.7%	57.1%	43.6%	36.1%	31.4%
0.30	69.9%	57.6%	47.1%	40.4%	35.3%	**0.30**	77.6%	62.1%	48.1%	39.4%	33.3%
0.40	72.0%	61.0%	50.0%	41.7%	35.0%	**0.40**	78.9%	64.8%	51.1%	40.5%	33.0%
0.50	72.4%	61.8%	51.2%	40.9%	34.5%	**0.50**	79.2%	65.5%	52.1%	40.1%	32.6%
0.60	71.1%	60.0%	49.0%	40.7%	34.1%	**0.60**	78.3%	64.1%	50.2%	39.7%	32.1%
0.70	68.1%	55.8%	45.2%	38.5%	33.5%	**0.70**	76.4%	60.4%	46.4%	37.8%	31.5%
0.80	48.8%	47.9%	39.9%	34.2%	30.3%	**0.80**	67.7%	54.8%	41.1%	33.8%	28.8%
0.90	16.6%	19.4%	22.0%	23.4%	24.0%	**0.90**	37.0%	36.7%	33.8%	27.7%	23.4%

Opaque Type, Circular Hole (front-side), Circular Pillar (back-side)

Table D.5. Efficiencies for opaque circular holes (back-side pillars) and ^{10}B and ^{6}LiF neutron converting material. Neutrons are incident normally on the detector surface and the LLD is 300 keV.

Opaque Dual-Sided MSND, Circular Hole, 10-B					
D/W_Cell	***Cell width W_Cell (um)***				
	4	**6**	**8**	**10**	**12**
	Trench depth H = 10 um				
0.10	5.2%	5.2%	5.2%	5.2%	5.2%
0.20	6.1%	6.1%	6.2%	6.2%	6.3%
0.30	7.7%	7.9%	8.1%	8.1%	8.0%
0.40	10.2%	10.6%	10.6%	10.2%	9.7%
0.50	13.5%	14.0%	13.3%	12.2%	11.1%
0.60	17.9%	17.4%	15.8%	13.9%	12.6%
0.70	22.6%	20.9%	17.9%	15.6%	14.0%
0.80	26.0%	24.1%	20.0%	17.3%	15.5%
0.90	26.9%	23.0%	20.5%	18.5%	16.8%
	Trench depth H = 20 um				
0.10	5.4%	5.4%	5.4%	5.4%	5.4%
0.20	6.8%	6.9%	7.0%	7.1%	7.3%
0.30	9.5%	9.8%	10.2%	10.2%	10.0%
0.40	13.5%	14.3%	14.3%	13.6%	12.7%
0.50	19.1%	19.8%	18.5%	16.7%	14.9%
0.60	26.2%	25.3%	22.5%	19.3%	17.0%
0.70	33.7%	30.8%	25.7%	21.8%	19.1%
0.80	38.9%	35.6%	28.8%	24.3%	21.1%
0.90	39.4%	33.0%	29.0%	25.7%	22.8%
	Trench depth H = 40 um				
0.10	5.5%	5.6%	5.6%	5.6%	5.6%
0.20	7.6%	7.7%	7.8%	7.9%	8.1%
0.30	11.2%	11.6%	12.1%	12.2%	11.8%
0.40	16.7%	17.8%	17.7%	16.7%	15.5%
0.50	24.3%	25.2%	23.3%	20.7%	18.3%
0.60	33.9%	32.6%	28.6%	24.1%	21.0%
0.70	43.8%	39.8%	32.7%	27.4%	23.6%
0.80	50.4%	45.9%	36.5%	30.4%	26.1%
0.90	49.8%	41.4%	36.1%	31.8%	28.0%
	Trench depth H = 60 um				
0.10	5.6%	5.6%	5.6%	5.6%	5.6%
0.20	7.8%	7.9%	8.1%	8.2%	8.4%
0.30	11.8%	12.2%	12.9%	12.9%	12.5%
0.40	17.9%	19.1%	18.9%	17.8%	16.5%
0.50	26.2%	27.1%	25.0%	22.2%	19.4%
0.60	36.7%	35.2%	30.8%	25.8%	22.3%
0.70	47.4%	43.0%	35.1%	29.3%	25.1%
0.80	54.4%	49.5%	39.1%	32.5%	27.8%
0.90	53.3%	44.1%	38.4%	33.9%	29.7%

Opaque Dual-Sided MSND, Circular Hole, LiF					
D/W_Cell	***Cell width W_Cell (um)***				
	20	**40**	**60**	**80**	**100**
	Trench depth H = 90 um				
0.10	4.7%	4.8%	4.8%	4.8%	4.8%
0.20	6.1%	6.2%	6.4%	6.3%	6.1%
0.30	8.3%	8.8%	8.5%	8.1%	7.7%
0.40	11.8%	12.1%	11.0%	10.2%	9.3%
0.50	16.3%	15.5%	13.7%	12.1%	10.7%
0.60	21.5%	19.2%	16.4%	13.9%	12.1%
0.70	26.8%	23.0%	18.8%	15.6%	13.5%
0.80	31.9%	26.9%	21.0%	17.3%	14.9%
0.90	35.1%	28.9%	23.2%	18.9%	16.2%
	Trench depth H = 175 um				
0.10	4.9%	5.0%	5.0%	5.1%	5.1%
0.20	7.1%	7.3%	7.6%	7.5%	7.2%
0.30	10.7%	11.6%	11.1%	10.4%	9.7%
0.40	16.3%	16.8%	15.0%	13.6%	12.1%
0.50	23.5%	22.2%	19.3%	16.5%	14.2%
0.60	31.7%	28.0%	23.4%	19.2%	16.2%
0.70	39.8%	34.0%	26.9%	21.8%	18.2%
0.80	47.4%	39.7%	30.2%	24.2%	20.2%
0.90	51.7%	42.3%	33.0%	26.2%	21.9%
	Trench depth H = 350 um				
0.10	5.2%	5.3%	5.3%	5.4%	5.5%
0.20	8.2%	8.5%	8.9%	8.7%	8.3%
0.30	13.2%	14.5%	13.6%	12.7%	11.7%
0.40	20.8%	21.5%	19.0%	17.0%	14.8%
0.50	30.6%	28.9%	24.7%	20.8%	17.6%
0.60	41.5%	36.6%	30.1%	24.3%	20.1%
0.70	52.1%	44.4%	34.6%	27.5%	22.7%
0.80	61.8%	51.8%	38.6%	30.4%	25.1%
0.90	66.3%	54.4%	41.9%	32.7%	27.0%
	Trench depth H = 500 um				
0.10	5.2%	5.4%	5.4%	5.5%	5.6%
0.20	8.6%	8.9%	9.3%	9.1%	8.6%
0.30	13.9%	15.4%	14.4%	13.3%	12.3%
0.40	22.3%	22.9%	20.1%	18.0%	15.6%
0.50	32.8%	30.8%	26.2%	22.0%	18.5%
0.60	44.5%	39.1%	32.0%	25.6%	21.1%
0.70	55.8%	47.4%	36.8%	29.0%	23.8%
0.80	66.0%	55.2%	40.9%	32.0%	26.3%
0.90	70.4%	57.7%	44.2%	34.3%	28.2%

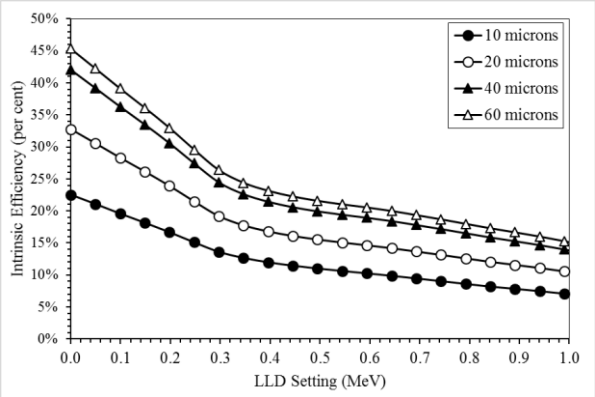

Fig. D.19. Plotted are intrinsic efficiencies for various perforation depths for front-side circular-hole, back-side pillar devices; 4 μm unit cell and 2 μm diameter, ^{10}B converter.

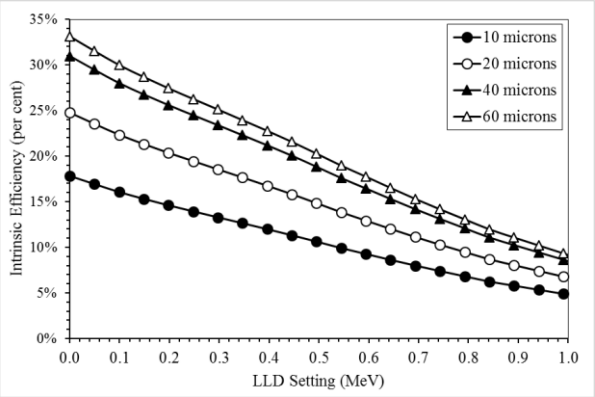

Fig. D.20. Plotted are intrinsic efficiencies for various perforation depths for front-side circular-hole, back-side pillar devices; 8 μm unit cell and 4 μm diameter, ^{10}B converter.

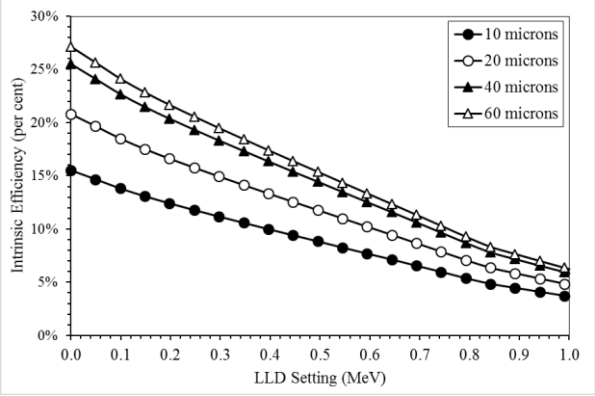

Fig. D.21. Plotted are intrinsic efficiencies for various perforation depths for front-side circular-hole, back-side pillar devices; 12 μm unit cell, 6 μm diameter, ^{10}B converter.

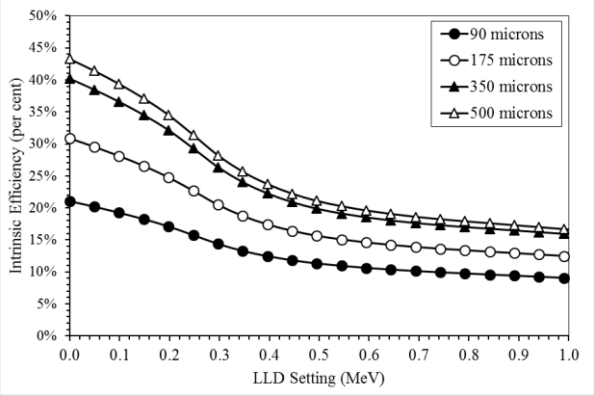

Fig. D.22. Plotted are intrinsic efficiencies for various perforation depths for front-side circular-hole, back-side pillar devices; 20 μm unit cell, 10 μm diameter, ^{6}LiF converter.

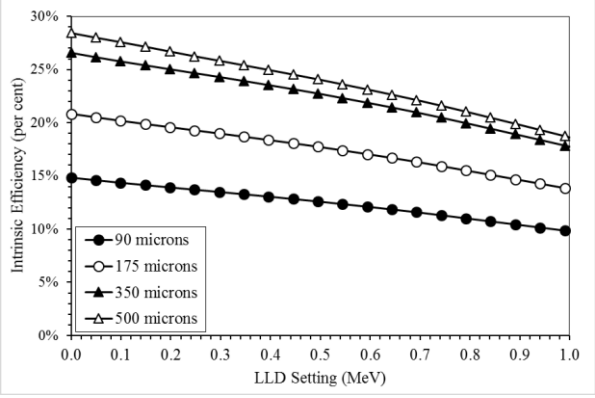

Fig. D.23. Plotted are intrinsic efficiencies for various perforation depths for front-side circular-hole, back-side pillar devices; 60 μm unit cell, 30 μm diameter, ^{6}LiF converter.

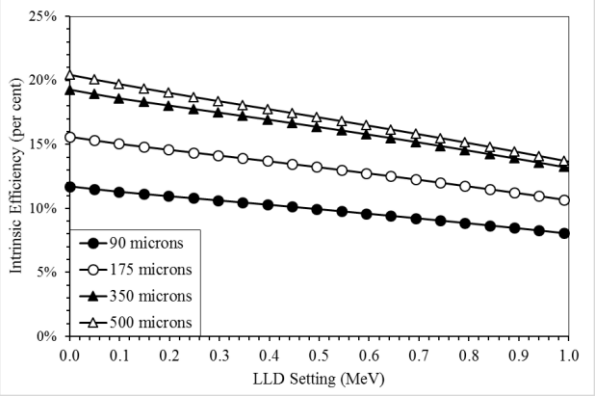

Fig. D.24. Plotted are intrinsic efficiencies for various perforation depths for front-side circular-hole, back-side pillar devices; 100 μm unit cell.50 μm diameter. ^{6}LiF converter.

Opaque Type, Circular Pillar (front-side), Circular Hole (back-side)

Table D.6. Efficiencies for opaque circular pillars (back-side holes) and ^{10}B and ^{6}LiF neutron converting material. Neutrons are incident normally on the detector surface and the LLD is 300 keV.

Opaque Dual-Sided MSND, Circular Pillar, 10-B					
D/W_Cell	***Cell width W_Cell (um)***				
	4	**6**	**8**	**10**	**12**
	Trench depth H = 10 um				
0.10	3.4%	3.5%	3.6%	3.7%	3.9%
0.20	4.6%	5.4%	5.7%	5.4%	5.2%
0.30	8.3%	8.4%	7.5%	6.9%	6.4%
0.40	12.5%	10.9%	9.4%	8.4%	7.7%
0.50	15.6%	13.1%	11.3%	10.0%	9.1%
0.60	17.9%	15.1%	13.1%	11.7%	10.5%
0.70	19.3%	16.6%	14.6%	13.2%	11.9%
0.80	19.5%	17.5%	15.5%	14.1%	12.8%
0.90	18.2%	17.1%	15.6%	14.1%	12.8%
	Trench depth H = 20 um				
0.10	2.2%	2.3%	2.5%	2.7%	3.0%
0.20	4.2%	5.8%	6.2%	5.8%	5.4%
0.30	10.8%	11.1%	9.6%	8.4%	7.6%
0.40	18.4%	15.5%	12.9%	11.2%	10.0%
0.50	23.9%	19.5%	16.4%	14.1%	12.5%
0.60	28.1%	23.1%	19.7%	17.2%	15.2%
0.70	30.7%	26.1%	22.5%	20.0%	17.8%
0.80	31.3%	27.8%	24.3%	21.9%	19.6%
0.90	29.3%	27.4%	24.8%	22.2%	19.9%
	Trench depth H = 40 um				
0.10	1.0%	1.2%	1.5%	1.7%	2.1%
0.20	3.9%	6.1%	6.7%	6.1%	5.6%
0.30	13.3%	13.7%	11.5%	9.9%	8.8%
0.40	24.1%	20.0%	16.3%	13.9%	12.2%
0.50	32.0%	25.8%	21.4%	18.1%	15.9%
0.60	38.1%	31.0%	26.2%	22.6%	19.7%
0.70	42.0%	35.4%	30.3%	26.7%	23.7%
0.80	43.0%	38.0%	33.0%	29.5%	26.3%
0.90	40.3%	37.6%	33.9%	30.1%	26.8%
	Trench depth H = 60 um				
0.10	0.6%	0.8%	1.1%	1.3%	1.8%
0.20	3.7%	6.3%	6.9%	6.3%	5.6%
0.30	14.2%	14.7%	12.3%	10.5%	9.2%
0.40	26.2%	21.7%	17.6%	14.9%	13.0%
0.50	35.0%	28.2%	23.2%	19.6%	17.1%
0.60	41.8%	34.0%	28.6%	24.6%	21.4%
0.70	46.2%	38.9%	33.2%	29.2%	25.8%
0.80	47.3%	41.9%	36.3%	32.3%	28.9%
0.90	44.5%	41.4%	37.3%	33.0%	29.4%

Opaque Dual-Sided MSND, Circular Pillar, LiF					
D/W_Cell	***Cell width W_Cell (um)***				
	20	**40**	**60**	**80**	**100**
	Trench depth H = 90 um				
0.10	3.7%	3.8%	4.0%	4.0%	3.8%
0.20	6.5%	7.0%	6.0%	5.4%	4.9%
0.30	12.1%	9.8%	7.9%	6.8%	6.1%
0.40	17.0%	12.3%	9.8%	8.3%	7.3%
0.50	20.3%	14.7%	11.7%	9.9%	8.6%
0.60	22.3%	16.7%	13.5%	11.5%	10.0%
0.70	22.7%	18.1%	15.0%	12.9%	11.3%
0.80	21.6%	18.5%	15.8%	13.8%	12.2%
0.90	19.2%	17.6%	15.7%	13.7%	12.2%
	Trench depth H = 175 um				
0.10	3.1%	3.3%	3.7%	3.6%	3.3%
0.20	7.9%	8.8%	7.1%	6.0%	5.3%
0.30	17.4%	13.5%	10.3%	8.5%	7.3%
0.40	25.8%	17.9%	13.6%	11.1%	9.5%
0.50	31.4%	22.0%	17.1%	13.9%	11.9%
0.60	35.0%	25.6%	20.4%	16.9%	14.4%
0.70	36.0%	28.2%	23.0%	19.6%	16.8%
0.80	34.3%	29.2%	24.7%	21.3%	18.6%
0.90	30.5%	27.9%	24.9%	21.5%	18.9%
	Trench depth H = 350 um				
0.10	2.5%	2.8%	3.4%	3.2%	2.8%
0.20	9.4%	10.6%	8.2%	6.6%	5.6%
0.30	23.0%	17.4%	12.8%	10.2%	8.6%
0.40	34.9%	23.8%	17.6%	14.1%	11.8%
0.50	43.1%	29.6%	22.6%	18.2%	15.3%
0.60	48.2%	34.9%	27.4%	22.5%	18.9%
0.70	49.8%	38.7%	31.4%	26.5%	22.5%
0.80	47.5%	40.4%	33.9%	29.1%	25.3%
0.90	42.4%	38.8%	34.4%	29.6%	25.8%
	Trench depth H = 500 um				
0.10	2.3%	2.7%	3.2%	3.1%	2.6%
0.20	9.9%	11.3%	8.5%	6.9%	5.7%
0.30	24.9%	18.7%	13.6%	10.8%	9.0%
0.40	38.1%	25.8%	19.0%	15.1%	12.6%
0.50	47.1%	32.3%	24.5%	19.6%	16.4%
0.60	52.8%	38.1%	29.8%	24.4%	20.4%
0.70	54.6%	42.4%	34.3%	28.9%	24.5%
0.80	52.1%	44.2%	37.1%	31.8%	27.5%
0.90	46.5%	42.5%	37.7%	32.3%	28.2%

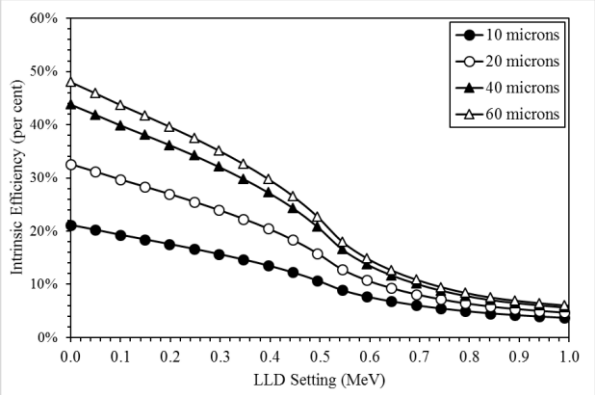

Fig. D.25. Plotted are intrinsic efficiencies for various perforation depths for front-side circular-pillar, back-side hole devices; 4 μm unit cell and 2 μm diameter, ^{10}B converter.

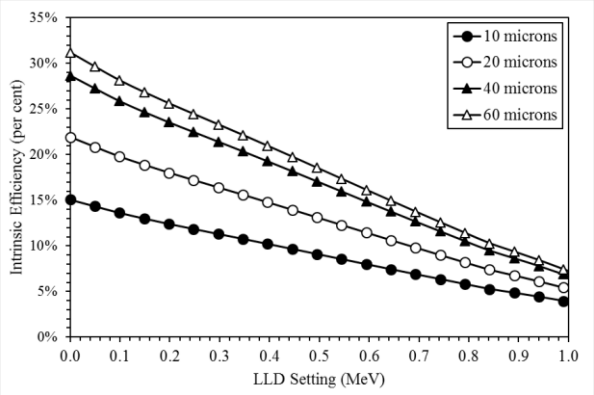

Fig. D.26. Plotted are intrinsic efficiencies for various perforation depths for front-side circular-pillar, back-side hole devices; 8 μm unit cell and 4 μm diameter, ^{10}B converter.

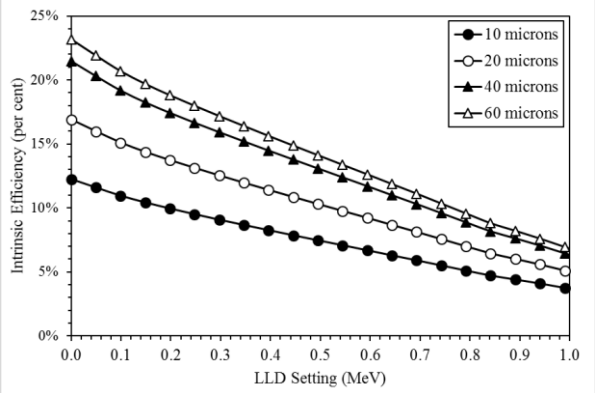

Fig. D.27. Plotted are intrinsic efficiencies for various perforation depths for front-side circular-pillar, back-side hole devices; 12 μm unit cell, 6 μm diameter, ^{10}B converter.

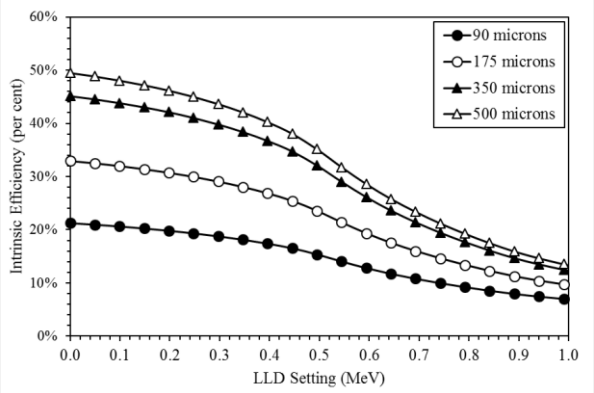

Fig. D.28. Plotted are intrinsic efficiencies for various perforation depths for front-side circular-pillar, back-side hole devices; 20 μm unit cell, 10 μm diameter, ^{6}LiF converter.

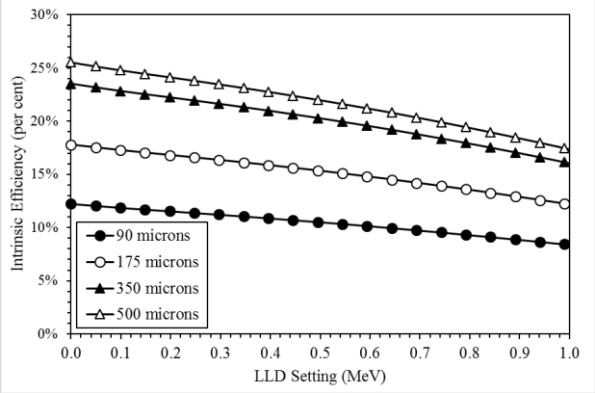

Fig. D.29. Plotted are intrinsic efficiencies for various perforation depths for front-side circular-pillar, back-side hole devices; 60 μm unit cell, 30 μm diameter, ^{6}LiF converter.

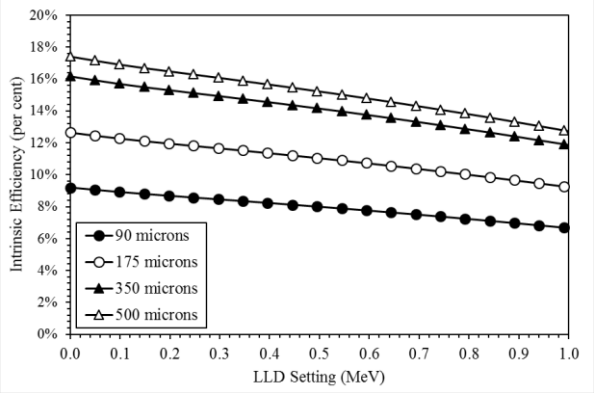

Fig. D.30. Plotted are intrinsic efficiencies for various perforation depths for front-side circular-pillar, back-side hole devices; 100 μm unit cell.50 μm diameter. ^{6}LiF converter.